A Novel Nonlocal Lattice Particle Framework for Modeling of Solids

by

Hailong Chen

A Dissertation Presented in Partial Fulfillment
of the Requirement for the Degree
Doctor of Philosophy

Approved July 2015 by the
Graduate Supervisory Committee:

Yongming Liu, Chair
Yang Jiao
Kiran Solanki
Marc Mignolet
Jay Oswald

ARIZONA STATE UNIVERSITY

August 2015

ABASTRACT

A NOVEL NONLOCAL LATTICE PARTICLE FRAMEWORK FOR MODELING OF SOLIDS

Fracture phenomena have been extensively studied in the last several decades. Continuum mechanics-based approaches, such as finite element methods and extended finite element methods, are widely used for fracture simulation. One well-known issue of these approaches is the stress singularity resulted from the spatial discontinuity at the crack tip/front. The requirement of guiding criteria for various cracking behaviors, such as initiation, propagation, and branching, also poses some challenges. Comparing to the continuum based formulation, the discrete approaches, such as lattice spring method, discrete element method, and peridynamics, have certain advantages when modeling various fracture problems due to their intrinsic characteristics in modeling discontinuities.

A novel, alternative, and systematic framework based on a nonlocal lattice particle model is proposed in this study. The uniqueness of the proposed model is the inclusion of both pair-wise local and multi-body nonlocal potentials in the formulation. First, the basic ideas of the proposed framework for 2D isotropic solid are presented. Derivations for triangular and square lattice structure are discussed in detail. Both mechanical deformation and fracture process are simulated and model verification and validation are performed with existing analytical solutions and experimental observations. Following this, the extension to general 3D isotropic solids based on the proposed local and nonlocal potentials is given. Three cubic lattice structures are discussed in detail. Failure predictions using the 3D simulation are compared with experimental testing results and very good agreement is observed. Next, a lattice rotation scheme is proposed to account for the material orientation in modeling anisotropic solids. The consistency and difference compared to the classical material tangent stiffness transformation method are discussed in detail. The implicit and explicit solution methods for the proposed lattice particle model are also discussed. Finally, some conclusions and discussions based on the current study are drawn at the end.

TO MY GRANDPARENTS

ACKNOWLEDGMENTS

I would like to express my sincere gratitude to my advisor, the chair of my dissertation supervisory committee, Professor Yongming Liu, for his guidance, enthusiasm and constant support throughout the entire study and research at Arizona State University. I would like to thank him for the numerous insights and help he has provided during every stage of the research. Without his support, assistance and patience, it would not have been possible to complete this work.

I would also like to thank Professor Yang Jiao, for his guidance and help has provided on some topics throughout the whole research. His enthusiasm and unique perspective on the research provided me much confidence and thrust, and exposed me to interdisciplinary research perspectives. Without his help, the current work would not have been so inclusive.

I would also like to thank the other members of my dissertation supervisory committee, Professor Marc Mignolet, Professor Jay Oswald and Professor Kiran Solanki. I'm grateful for their willingness to serve on the committee, for providing help whenever required, for precious time on reviewing this dissertation, and for valuable suggestions provided.

I would also like to thank all my group members, current or former. Without them, life and study couldn't be such joyful and meaningful at Arizona State University. Special thanks go to Fraaz Tahir and Tishun Peng, for their willingness and time on proofreading the manuscript.

Last but not least, I would like to thank my family members, my grandparents, parents, siblings, wife and two lovely children, for their constant love, understanding and support.

TABLE OF CONTENTS

Page

APPENDIX Page

LIST OF TABLES

LIST OF FIGURES

CHAPTER

1. INTRODUCTION

1.1 Overview

Existing numerical methods for mechanical analysis of solid materials can be generally categorized into two groups: continuum-based approaches and discrete approaches. The continuum-based approaches assume the material under study is continuous throughout the entire simulation domain. Thus, the spatial derivatives always exist at every material point. Numerical methods such as finite element methods (FEM), finite difference methods (FDM), and many other schemes belong to this category. On the other hand, the discrete approaches allow discontinuities to exist in the simulation domain and the concept of spatial derivative is not employed in their formulation. Numerical methods such as discrete element methods (DEM) [1], lattice spring methods (LSM) [2], Peridynamics [3], and other discrete formulations belong to this category. Another distinction between these two categories is the interaction range, i.e., local versus non-local. In classical Continuum Mechanics, the material points can only interact with its nearest surrounding material points. While in discrete formulations, the interaction can be nonlocal.

The continuum-based approaches have advantages in problems not involving discontinuities, such as elasticity and plasticity. They are usually computationally more efficient and close form solutions may be available [4]. On the other hand, the non-continuum-based approaches are usually less efficient and no analytical solution is available even for simple problems. Due to the intrinsic formulation difference, the non-continuum-based approaches usually have some other problems, such as fixed Poisson's ratio. But these types of issues can be solved with refined formulation mechanisms.

For problems involving discontinuities, such as defects in materials, the continuum-based approaches have the singularity issue due to the spatial derivative at the discontinuities. Some special treatments are required before these approaches can yield meaning simulation results.

The adaptive remeshing technique [5], cohesive element[6], the level set methods and crack tip/front enrichment [7] are among the most frequently used techniques in continuum-based approaches. With these schemes, the performance of the continuum-based approaches improves, but it is still heavily based on the requirement of externally developed failure criteria for various cracking behaviors, such as initiation and propagation. On the other hand, the non-continuum-based approaches are, in principle, more suitable for this type of problem [8]. The non-continuum-based methods represent the material as an assemblage of independent elements (also called units, particles or grains), which are interacting with each other with different types of interaction potentials. The fracture process in these types of approaches is the natural “loss of interaction” between “particles”. The crack propagation is the natural outcome of the breakage of the connecting bonds. Only a bond based crack initiation criterion is required and is usually simpler comparing to the continuum mechanics-based methods.

The lattice spring model is of special interest in this study. This approach was initially applied to atomic systems and later to larger scales as well. For isotropic materials, the restriction on effective Poisson’s ratio of materials is a well-known issue for models of this kind. For lattice spring model using only normal springs [9], due to the inefficiency of material characterization using only one spring parameter, the Poisson’s ratio in the limit of infinite numbers of particles is fixed to 1/4 for plane strain and 1/3 for plane stress. With the introduction of shear/angular springs [2], [10], the limitation on Poisson’s ratio can be removed, but the full range of Poisson’s ratio cannot be modeled with physically meaningful stiffness parameter for shear springs, i.e., the stiffness parameter of the shear springs become negative when the Poisson’s ratio greater than 1/4 for plane strain case and 1/3 for plane stress case. Alternative approaches have also been proposed to remove this restriction, such as the hybrid formulation using both particle methods and finite element method [11].

One intrinsic issue of the lattice models for fracture simulation is the crack path preference due to the regular lattice configuration [12], [13]. Two major approaches have been proposed to address this issue. One is to use the random/irregular network [14]. The irregular lattice models exhibit

less crack path preference and offer freedom in domain discretization, but require certain scaling technique to obtain elastic uniformity. Another possible solution is to use multiple neighbors [15]. By introducing multiple neighbors, the lattice symmetry will be enhanced and the crack path preference will be eliminated or reduced. This is similar to the concept of “horizon” used in Peridynamics [3].

After reviewing the pros and cons of current major numerical models for mechanical analysis of solid materials, it’s the objective of this work to develop a lattice based discrete model which can handle linear and nonlinear responses of isotropic and anisotropic materials under static and dynamic mechanical loadings.

1.2 Outlines

The content of this dissertation is organized as follows:

In Chapter 1, the frequently used numerical approaches for fracture simulation are briefly reviewed. The pros and cons of these various numerical approaches are briefly discussed. The motivation for current work is outlined. Some basic concepts from continuum mechanics are also reviewed in this chapter.

In Chapter 2, the details on the formulation of the lattice particle framework for both 2D and 3D homogeneous isotropic solid materials are discussed. The focus is on developing a nonlocal potential and deriving the relationship between the model parameters and the material constants. A one-dimensional spring based failure criterion for fracture simulation is proposed. Some numerical results to show the validity and performance of the proposed model are presented. Conclusions on modeling isotropic materials using the proposed model are drawn at the end.

In Chapter 3, the lattice particle model is extended to simulate anisotropic solids. The derivation procedure follows that of the isotropic case. A lattice structure rotation scheme is proposed to account for the material orientation. The extended spring based fracture criterion is also discussed. Simulation results are compared with both literature solutions and experimental findings. Conclusions on modeling anisotropic materials using the proposed model are drawn at the end.

In Chapter 4, the implicit and explicit solutions schemes to solve the proposed lattice particle method are discussed. The coupling between the lattice particle model and FEM based on the implicit solution method is briefly discussed. Application of the proposed lattice particle model to study the particle reinforced composite system is presented.

Chapter 5 is devoted to the conclusion and scope of future work. A brief comparison of the lattice particle model with other numerical approaches is given.

The analytical derivations on the equivalency between lattice structure rotation and material stiffness transformation to account for the material orientation of anisotropic materials is given in

APPENDIX A. The analytical proof of the frame independence of the 3D formulation for isotropic materials is given in APPENDIX B.

1.3 Basic Concepts from Continuum Mechanics

In this section, some basic concepts from continuum mechanics are reviewed, including the definition of strains, Hooke's law, and the strain energy. These concepts serve as the basis for the development of the lattice particle model.

1.3.1 Strains

For elastic material under small deformation, the components of strain vector are defined in terms of the displacements as

$$\varepsilon_{IJ} = \frac{1}{2}\left(\frac{\partial u_I}{\partial x_J} + \frac{\partial u_J}{\partial x_I} \right) = \frac{1}{2}\left(u_{I,J} + u_{J,I} \right) \tag{1.3.1}$$

By this definition, the strain tensor is symmetric. And its components with respect to the $\left(\overline{\mathbf{e}}_1, \overline{\mathbf{e}}_2, \overline{\mathbf{e}}_3\right)$ coordinate system can be expressed as

$$\left[\varepsilon\right] = \begin{bmatrix} \varepsilon_{11} & \varepsilon_{12} & \varepsilon_{31} \\ \varepsilon_{12} & \varepsilon_{22} & \varepsilon_{23} \\ \varepsilon_{31} & \varepsilon_{23} & \varepsilon_{33} \end{bmatrix} \tag{1.3.2}$$

The strain matrix can be transformed under the same rule of matrix transformation. For the rotation of axes, the transformed strains are

$$\left[\hat{\varepsilon}\right] = \left[Q\right]\left[\varepsilon\right]\left[Q\right]^T \tag{1.3.3}$$

where $\left[Q\right]$ is a transformation matrix.

The volumetric strain, or the dilatation, is the trace of the strain vector.

$$\varepsilon_v = \frac{\Delta V}{V_0} = \varepsilon_{11} + \varepsilon_{22} + \varepsilon_{33} \tag{1.3.4}$$

The strain vector $\left\{e\right\}$ across a surface with normal vector $\left\{n\right\}$ is

$$\begin{Bmatrix} e_1 \\ e_2 \\ e_3 \end{Bmatrix} = \begin{bmatrix} \varepsilon_{11} & \varepsilon_{12} & \varepsilon_{31} \\ \varepsilon_{12} & \varepsilon_{22} & \varepsilon_{23} \\ \varepsilon_{31} & \varepsilon_{23} & \varepsilon_{33} \end{bmatrix} \begin{Bmatrix} n_1 \\ n_2 \\ n_3 \end{Bmatrix} \tag{1.3.5}$$

The one dimensional engineering strain is defined as

$$\varepsilon = \frac{\Delta l}{l_0} \tag{1.3.6}$$

where Δl is the elongation, and l_0 is the original length.

Under plane strain assumption, the out-of-plane components of the strain matrix ε_{31}, ε_{23}, ε_{33} are assumed to be zero. Thus, the strain matrix reduces to an in-plane case.

$$[\varepsilon] = \begin{bmatrix} \varepsilon_{11} & \varepsilon_{12} & 0 \\ \varepsilon_{12} & \varepsilon_{22} & 0 \\ 0 & 0 & 0 \end{bmatrix} \tag{1.3.7}$$

The transformed strains for plane strain case are

$$\begin{aligned} \hat{\varepsilon}_{11} &= \left(\frac{\varepsilon_{11}+\varepsilon_{22}}{2}\right) + \left(\frac{\varepsilon_{11}-\varepsilon_{22}}{2}\right)\cos 2\theta + \varepsilon_{12}\sin 2\theta \\ \hat{\varepsilon}_{11} &= \left(\frac{\varepsilon_{11}+\varepsilon_{22}}{2}\right) - \left(\frac{\varepsilon_{11}-\varepsilon_{22}}{2}\right)\cos 2\theta - \varepsilon_{12}\sin 2\theta \\ \hat{\varepsilon}_{12} &= -\left(\frac{\varepsilon_{11}-\varepsilon_{22}}{2}\right)\sin 2\theta + \varepsilon_{12}\cos 2\theta \end{aligned} \tag{1.3.8}$$

where θ is the rotation angle.

1.3.2 Hooke's Law

The general constitutive relationship between the stresses and strains of a linear elastic material is

$$\sigma_{IJ} = C_{IJKL}\varepsilon_{KL} \tag{1.3.9}$$

where C_{IJKL} is the 6×6 stiffness matrix which is a fourth-order tensor. The number of independent material constant for determination of C_{IJKL} is dependent on the material symmetry.

Triclinic Linearly Elastic Solids

If a linearly elastic solid has no plane of material symmetry, it is called a triclinic material. For material of this kind, there are 21 independent coefficients. The expression of the stiffness matrix can be generally written as

$$\mathbf{C}=\begin{bmatrix} C_{11} & C_{12} & C_{13} & C_{14} & C_{15} & C_{16} \\ & C_{22} & C_{23} & C_{24} & C_{25} & C_{26} \\ & & C_{33} & C_{34} & C_{35} & C_{36} \\ & & & C_{44} & C_{45} & C_{46} \\ & sym & & & C_{55} & C_{56} \\ & & & & & C_{66} \end{bmatrix} \tag{1.3.10}$$

Monoclinic Linearly Elastic Solids

If a linearly elastic solid has one plane of material symmetry, it is called a monoclinic material. For materials of this kind, there are 13 independent coefficients.

In terms of the compliance matrix, the constitutive relationship between the stresses and strains for the case where $\mathbf{e}_1$ plane is the plane of symmetry is

$$\begin{Bmatrix} \varepsilon_{11} \\ \varepsilon_{22} \\ \varepsilon_{33} \\ \gamma_{23} \\ \gamma_{13} \\ \gamma_{12} \end{Bmatrix} = \begin{bmatrix} 1/E_1 & -\nu_{21}/E_2 & -\nu_{31}/E_3 & \eta_{41}/G_4 & 0 & 0 \\ -\nu_{12}/E_1 & 1/E_2 & -\nu_{32}/E_3 & \eta_{42}/G_4 & 0 & 0 \\ -\nu_{13}/E_1 & -\nu_{23}/E_2 & 1/E_3 & \eta_{43}/G_4 & 0 & 0 \\ \eta_{14}/E_1 & \eta_{24}/E_2 & \eta_{34}/E_3 & 1/G_4 & 0 & 0 \\ 0 & 0 & 0 & 0 & 1/G_5 & \mu_{65}/\mathrm{G}_6 \\ 0 & 0 & 0 & 0 & \mu_{56}/\mathrm{G}_5 & 1/\mathrm{G}_6 \end{bmatrix} \begin{Bmatrix} \sigma_{11} \\ \sigma_{22} \\ \sigma_{33} \\ \sigma_{23} \\ \sigma_{13} \\ \sigma_{12} \end{Bmatrix} \tag{1.3.11}$$

The 13 independent constants are E_1, E_2, E_3, G_4, G_5, G_6, ν_{12}, ν_{23}, ν_{13}, η_{14}, η_{24}, η_{34}, and μ_{56}.

Orthotropic Linearly Elastic Solids

If a linearly elastic solid has two mutually perpendicular planes of material symmetry, then automatically the third plane is also a plane of material symmetry. The material is called orthotropic elastic material. For material of this kind, there are only 9 independent elastic coefficients.

In terms of the compliance matrix, the constitutive relationship between the stresses and strains is

$$\begin{Bmatrix} \varepsilon_{11} \\ \varepsilon_{22} \\ \varepsilon_{33} \\ \gamma_{23} \\ \gamma_{13} \\ \gamma_{12} \end{Bmatrix} = \begin{bmatrix} 1/E_1 & -\nu_{21}/E_2 & -\nu_{31}/E_3 & 0 & 0 & 0 \\ -\nu_{12}/E_1 & 1/E_2 & -\nu_{32}/E_3 & 0 & 0 & 0 \\ -\nu_{13}/E_1 & -\nu_{23}/E_2 & 1/E_3 & 0 & 0 & 0 \\ 0 & 0 & 0 & 1/G_{23} & 0 & 0 \\ 0 & 0 & 0 & 0 & 1/G_{31} & 0 \\ 0 & 0 & 0 & 0 & 0 & 1/\mathrm{G}_{12} \end{bmatrix} \begin{Bmatrix} \sigma_{11} \\ \sigma_{22} \\ \sigma_{33} \\ \sigma_{23} \\ \sigma_{13} \\ \sigma_{12} \end{Bmatrix} \tag{1.3.12}$$

The nine independent constants are E_1, E_2, E_3, G_{12}, G_{23}, G_{31}, ν_{12}, ν_{23}, and ν_{13}.

Transverse Linearly Elastic Solids

If there exists a plane such that every plane perpendicular to it is a plane of symmetry, then the material is called a transversely isotropic material. That plane is called plane of isotropy. For material of this kind, the number of independent coefficients reduces to 5.

In terms of the compliance matrix, the constitutive relationship between the stresses and strains is

$$\begin{Bmatrix} \varepsilon_{11} \\ \varepsilon_{22} \\ \varepsilon_{33} \\ \gamma_{23} \\ \gamma_{13} \\ \gamma_{12} \end{Bmatrix} = \begin{bmatrix} 1/E_1 & -\nu_{21}/E_1 & -\nu_{31}/E_3 & 0 & 0 & 0 \\ -\nu_{21}/E_1 & 1/E_2 & -\nu_{31}/E_3 & 0 & 0 & 0 \\ -\nu_{13}/E_1 & -\nu_{13}/E_1 & 1/E_3 & 0 & 0 & 0 \\ 0 & 0 & 0 & 1/\mathrm{G}_{13} & 0 & 0 \\ 0 & 0 & 0 & 0 & 1/\mathrm{G}_{13} & 0 \\ 0 & 0 & 0 & 0 & 0 & 1/G_{12} \end{bmatrix} \begin{Bmatrix} \sigma_{11} \\ \sigma_{22} \\ \sigma_{33} \\ \sigma_{23} \\ \sigma_{13} \\ \sigma_{12} \end{Bmatrix} \tag{1.3.13}$$

where $G_{12} = \dfrac{E_1}{2(1+\nu_{21})}$.

The five independent constants are E_1, E_3, G_{12}, G_{13}, and ν_{13}.

Isotropic Linearly Elastic Solids

If the material's property is independent of the direction, then the materials is called an isotropic material. For an isotropic material, the number of independent coefficients reduces to 2. The compliance matrix has the simplest form as

$$\begin{Bmatrix}\varepsilon_{11}\\ \varepsilon_{22}\\ \varepsilon_{33}\\ \lambda_{23}\\ \gamma_{31}\\ \gamma_{12}\end{Bmatrix}=\frac{1}{E}\begin{bmatrix}1 & -\nu & -\nu & 0 & 0 & 0\\ -\nu & 1 & -\nu & 0 & 0 & 0\\ -\nu & -\nu & 1 & 0 & 0 & 0\\ 0 & 0 & 0 & 2(1+\nu) & 0 & 0\\ 0 & 0 & 0 & 0 & 2(1+\nu) & 0\\ 0 & 0 & 0 & 0 & 0 & 2(1+\nu)\end{bmatrix}\begin{Bmatrix}\sigma_{11}\\ \sigma_{22}\\ \sigma_{33}\\ \sigma_{23}\\ \sigma_{31}\\ \sigma_{12}\end{Bmatrix} \tag{1.3.14}$$

The reverse relation is

$$\begin{Bmatrix}\sigma_{11}\\ \sigma_{22}\\ \sigma_{33}\\ \sigma_{23}\\ \sigma_{31}\\ \sigma_{12}\end{Bmatrix}=\frac{E}{(1+\nu)(1-2\nu)}\begin{bmatrix}1-\nu & \nu & \nu & 0 & 0 & 0\\ \nu & 1-\nu & \nu & 0 & 0 & 0\\ \nu & \nu & 1-\nu & 0 & 0 & 0\\ 0 & 0 & 0 & (1-2\nu)/2 & 0 & 0\\ 0 & 0 & 0 & 0 & (1-2\nu)/2 & 0\\ 0 & 0 & 0 & 0 & 0 & (1-2\nu)/2\end{bmatrix}\begin{Bmatrix}\varepsilon_{11}\\ \varepsilon_{22}\\ \varepsilon_{33}\\ \lambda_{23}\\ \gamma_{31}\\ \gamma_{12}\end{Bmatrix} \tag{1.3.15}$$

Under plane stress and plane strain conditions, the Hooke's law for isotropic material has following distinct form as

for plane stress:

$$\begin{Bmatrix}\sigma_{11}\\ \sigma_{22}\\ \sigma_{12}\end{Bmatrix}=\frac{E}{1-\nu^2}\begin{bmatrix}1 & \nu & 0\\ \nu & 1 & 0\\ 0 & 0 & (1-\nu)/2\end{bmatrix}\begin{Bmatrix}\varepsilon_{11}\\ \varepsilon_{22}\\ \gamma_{12}\end{Bmatrix} \tag{1.3.16}$$

for plane strain:

$$\begin{Bmatrix}\sigma_{11}\\ \sigma_{22}\\ \sigma_{12}\end{Bmatrix}=\frac{E}{(1+\nu)(1-2\nu)}\begin{bmatrix}1-\nu & \nu & 0\\ \nu & 1-\nu & 0\\ 0 & 0 & (1-2\nu)/2\end{bmatrix}\begin{Bmatrix}\varepsilon_{11}\\ \varepsilon_{22}\\ \gamma_{12}\end{Bmatrix} \tag{1.3.17}$$

1.3.3 Strain Energy

For elastic materials, the strain energy is defined as the area under the stress-strain curve.

$$U=\frac{1}{2}\int_V\{\sigma\}^T\{\varepsilon\}\,dV \tag{1.3.18}$$

The strain energy density is the strain energy per unit volume,

$$U_s=\frac{U}{V}=\frac{\frac{1}{2}\int_V\{\sigma\}^T\{\varepsilon\}\,dV}{V} \tag{1.3.19}$$

Since the strain energy of an elastic material is conservative, the stresses can be derived given the strain energy and strains as

$$\sigma_{IJ} = \frac{\partial U_s}{\partial \varepsilon_{IJ}} \tag{1.3.20}$$

And the same is for the strains given the strain energy and the stresses.

The stiffness matrix C_{IJKL} can be further obtained from the strain energy as

$$C_{IJKL} = \frac{\partial^2 U_s}{\partial \varepsilon_{IJ} \partial \varepsilon_{KL}} \tag{1.3.21}$$

1.3.4 Plastic strains

The first and fundamental assumption of plasticity theory is that the strains can be additively decomposed into elastic and plastic parts:

$$\varepsilon_{IJ} = \varepsilon_{IJ}^e + \varepsilon_{IJ}^p \tag{1.3.22}$$

The elastic strains ε_{IJ}^e can be specified by the displacements as described in Eq. (1.3.1). The plastic strains are of a different nature, and are defined in quite a different way.

1.3.5 Yield Criteria

Two frequently used yield criteria are the von Mises and the Tresca yield criteria. The von Mises yield criterion suggests that the yielding of materials begins when the second deviatoric stress invariant J_2 reaches a critical value. It applies best to ductile materials, such as metals. The yield function for von Mises yield criterion in terms of the stress matrix is

$$f\left(\sigma_{IJ}\right) = \frac{1}{2}\left[\left(\sigma_{11}-\sigma_{22}\right)^2 + \left(\sigma_{22}-\sigma_{33}\right)^2 + \left(\sigma_{11}-\sigma_{33}\right)^2 + 6\left(\sigma_{23}^2+\sigma_{31}^2+\sigma_{12}^2\right)\right] - \sigma_Y^2 \tag{1.3.23}$$

The Tresca, or maximum shear stress, criterion specifies that a material would flow plastically if the maximum shear stress reaches a critical value. The yield function for Tresca yield criterion in terms of the principal stresses is

$$f\left(\sigma_I\right) = \frac{1}{2}\max\left(\left|\sigma_1-\sigma_2\right|,\left|\sigma_2-\sigma_3\right|,\left|\sigma_3-\sigma_1\right|\right) - \frac{1}{2}\sigma_Y \tag{1.3.24}$$

1.3.6 Yield Surface and Strain Hardening

A yield surface is a surface in the stress space, defined through the yield function by $f(\sigma_{IJ},\cdots)=0$. The yield function indicates that it's not only depend on the stress but also some other variables. Changes in plastic strain can occur only if the stress point lies on the yield surface, i.e., $f(\sigma_{IJ},\cdots)=0$. If the stress point falls within the yield surface ($f(\sigma_{IJ},\cdots)<0$), then there is no plastic strain increments as within the yield surface. The 2D von Mises and Tresca yield surfaces for plane stress ($\sigma_3=0$) are shown in Fig. 1.3.1.

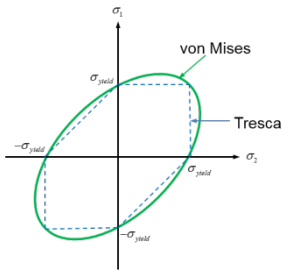

Figure 1.3.1. The Von Mises and Tresca Yield Surface in Plane Stress

If the yield surface expands (or contracts) but does not translate as plastic straining occurs, then this is said to be isotropic hardening (or softening). See Fig. 1.3.2(a).

On the other hand, if the yield surface translates, but does not change in size, as plastic strain occurs, then this is said to be kinematic hardening. See Fig. 1.3.2(b).

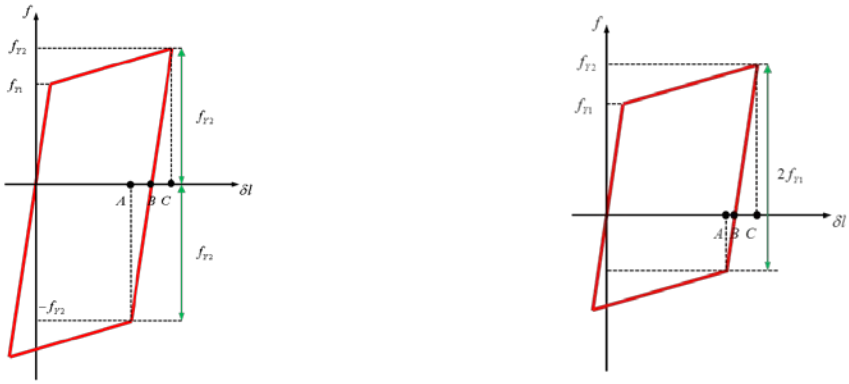

a). Isotropic hardening b). Kinematic hardening

Figure 1.3.2. One Dimensional Strain Hardening Laws

CHAPTER

2. THE LATTICE PARTICLE MODEL FOR ISOTROPIC SOLIDS

2.1 Introduction

The idea of employing discrete one-dimensional bonds, e.g., springs or beams, to study the different phenomena of solids dates back to the work of Hrennikoff [16], in which the elastic properties of solids is firstly investigated using the lattice method. Successive studies can be found, e.g., in [17], [2], [18], [19]. The lattice models can be classified into different categories according to how the lattice sites interact via the connecting bonds. The simplest and one of the most popular forms of interaction is through the central force (or axial) springs [9]. This type of model has the issue of the fixed Poisson's ratio. With the introduction of the bond rotation as additional degree of freedom [20], the Poisson's ratio can be modified. The Born model [21] introduces a non-central two-body interaction, but this model is not rotationally invariant. Keating [10] discussed the rotationally invariant requirement and proposed a bond-bending model, in which the angle change between two adjacent connecting bonds is considered as an additional component of the system energy. The beam model [12] removes the limitation on the Poisson's ratio by considering both the forces and the moments (i.e., rotational degrees of freedom) at each lattice site. Another lattice model introduces a volumetric term in the potential which can avoid the Poisson's ratio issue and the rotational invariant requirement is guaranteed [22].

One of the intrinsic issue of the lattice models for fracture simulation is the crack path preference due to the regular lattice configuration [12], [13]. This directional preference of the crack path is also related to the anisotropy of the failure surface that has been investigated in [15]. Two major approaches have been proposed to address this issue. One is to use the random/irregular network. The irregular lattice models exhibit less crack path preference and offer freedom in domain discretization, but require certain scaling technique [14] to obtain elastic uniformity. Another possible solution is to use multiple neighbors. By introducing multiple neighbors, the lattice symmetry will be enhanced and the crack path preference will be eliminated or reduced.

In this chapter, a novel nonlocal lattice particle is proposed to overcome the challenges while using lattice spring model for homogeneous isotropic materials. The content of this chapter is organized as follows: in Section 2.2, detailed formulations of the proposed lattice particle model based on triangular and square packing for two dimensional homogeneous isotropic solids is presented. The concept of energy equivalency between discrete element and its continuum counterpart is introduced. Extension of the elastic framework to model elasto-plastic materials is discussed. The validity of the proposed model is verified against classical solution and FEM solution. In Section 2.3, a detailed study on fracture modeling using the proposed model is investigated. The bond dependency of the crack path is studied by rotating the underlying topological lattice structure. A generalized lattice particle framework including arbitrary neighbors is proposed for triangular packing to remove or reduce the bond dependency for fracture modeling. The validity of the generalized lattice particle model is verified with experimental findings. Section 2.4 is devoted to the formulation of the three-dimensional lattice particle model. Three cubic lattice structures are used and the corresponding model parameters are derived in terms of materials constants following the same procedure as in 2D case. The 3D lattice model is verified with analytical and numerical solution from the literature whenever available. The fracture modeling using the 3D lattice particle model is verified with experimental findings.

2.2 2D Elasticity and Plasticity

The study of the deformation and fracture of two dimensional solids using the proposed lattice particle model is presented in this section. In this proposed lattice particle model, two potentials are introduced to model the interactions between material particles, i.e., a local pair-wise potential and a non-local multi-body potential. The local pair-wise potential is utilized to account for the constitutive relationship within the connecting bonds between particles while the non-local multi-body potential is employed for considering the volumetric effects under general mechanical loadings. The potential coefficients are determined by matching the potential energy stored in a discrete unit cell to the strain energy at the classical continuum level. A volume conservation scheme is proposed to model the plastic deformation. The validity of the proposed model is verified against the classical elasticity and elasto-plasticity solutions before it was applied to fracture problems. Several conclusions are drawn based on the proposed study.

2.2.1. Introduction

Existing numerical methods for analysis of solid mechanics can be generally grouped into two categories: the continuum-based approach and the discontinuous approach. The continuum-based approach includes classical finite element methods, extended finite element method, and many other schemes based on the continuum mechanics. The discontinuous approach includes discrete element method, lattice methods, particle methods, and other non-continuum-based methods. For discontinuous problems, such as cracking in materials, the classical continuum-based theories have the singularity issue, while the discontinuous approach is, in principle, more suitable for this type of problem. Before the application to general fracture and damage analysis of solids, the discontinuous approach must be verified to be consistent with classical continuum theory for general elasticity and plasticity analysis, which is the focus of the present study. Since the proposed method belongs to the discontinuous approach and the following discussion is mainly made for the discontinuous approaches.

One of the most common discontinuous methods is the lattice model. The idea of introducing lattice models, or spring network models, to simulate elastic solids dates back to Hrennikoff [16]. Many subsequent developments have been done by researchers in engineering and material science, e.g., [23] [24] [22] [25] [26] [27] [28]. This approach was initially applied to atomic systems and later to larger scales as well. The restriction on Poisson's ratio of materials is a well-known issue for lattice spring models. For 2D model employing only the normal springs, the Poisson's ratio in the limit of infinite numbers of particles is fixed to 1/4 for plane strain and 1/3 for plane stress. With the introduction of additional shear springs [2], the limitation on Poisson's ratio can be removed, but it still cannot model the full range of Poisson's ratio with positive stiffness parameter for shear springs, i.e., the stiffness parameter of the shear springs become negative when the Poisson's ratio greater than 1/4 for plane strain case and 1/3 for plane stress case. For 3D regular lattices model with normal and shear springs, it can only represents isotropic materials with zero Poisson's ratio [26]. Jivkov and Yates [28] proposed a specific bi-regular lattice model which can be calibrated for a wide range of Poisson's ratios with beam elements. Alternative approaches have also been proposed for removing this restriction, such as Lattice Discrete Particle Model (LDPM) [27] [29], Confinement-Shear Lattice model (CSL) [24] and Distinct Lattice Spring Model (DLSM) [11].

Another well cited discontinuous approach is the Virtual Internal Bond method (VIB) proposed by Gao and Klein [30]. In the VIB method, the continuum is treated as a randomized network of material points, interconnected by bonds, which obeys a cohesive law. The macroscopic collective behavior of this random bond network is obtained through the Cauchy-Born rule[21] of crystal elasticity and theory of hyper-elasticity. The key element in VIB method is the determination of the function for the cohesive force law, which is calibrated in a phenomenological sense from the stress-strain curve in a uniaxial tensile experiment. The original VIB model only considered the bond stretching effect and thus also has a fixed Poisson's ratio issue, i.e., 1/4 for plane strain case and 1/3 for plane stress case. In order to make VIB applicable to a wider range of materials, Volokh and Gao [31] proposed a decomposition of the Green-

Lagrangian strain tensor into spherical and deviatoric parts with separate contributions to the strain energy of the bonds. Another recently developed discontinuous method is the peridynamics method proposed by Silling [3]. The peridynamics uses the interaction among a group of particles (e.g., within the horizon radius) to describe the mechanical behaviors of solids. In peridynamics, an iterative trial-and-error calibration process is required to determine the model parameters for the force density function. The original peridynamics formulation also has the restriction of the applicable Poisson's ratios. With the introduction of the state-based formulation, the restriction on the Poisson's ratio can be removed but the computation process is complex [3].

Most existing discontinuous methods have been mostly applied to model brittle/quasi brittle fracture problems. For some materials, such as concrete and rocks, the plastic deformation can be ignored and simulation assuming brittle or quasi-brittle behavior is sufficient. But the plastic deformation plays an important role for many other engineering materials and thus cannot be ignored in order to obtain a fully understanding of failure mechanism of these materials. Although several attempts to include plasticity have been made [32] [33] [34], relatively few studies have been made for general plasticity analysis using the discontinuous approach compared to its wide applications to elastic problems. Buxton [32] included plasticity into the classical Born spring model and Thiagarajan and Huang [33] extended the hyperelastic to elasto-viscoplastic material modeling using the VIB method by incorporating the continuum-based plasticity theories. Both above attempts are based on the classical lattice theories and the restriction on the Poisson's ratio still exists. Foster [34] extended the peridynamics to model viscoplastic material, which is also based on the classical continuum-based plasticity theories. As can be observed, most existing implementation of plastic deformation into the discontinuous approach still relies on the continuum-based plasticity theory, which requires the transformation between the particle system and the continuum domain throughout the analysis (i.e., transformation between the particle displacement/force to continuum strain/stress). To the best knowledge of the authors', no systematic studies have been proposed to simultaneously consider the arbitrary Poisson's ratio in

elastic and elastic-plastic deformations by only employing the pair-wise particle interactions in the open literature.

Lattice models have been dominantly applied to model fracture phenomenon of brittle materials due to its easiness of simulating crack initiation and propagation by bond breaking and removal [4, 35]. Several bond breaking rules can be applied at the bond level, such as the critical energy, critical force and critical elongation criteria. For regular lattice based models, however, it's shown that the lattice regularity results in the preference of certain crack propagation direction [13] [12]. This directional preference intrinsically comes from the anisotropy of the failure surface [15]. Based on the work of Monette and Anderson [15], the degree of anisotropy of the failure surface can be decreased by employing more particles as the neighbors of the centered particle, which essentially is the same as the concept of horizon used in peridynamics [3]. In this paper, the major objectives are to propose a new discrete simulation framework under elasticity and plasticity, which is of critical importance before a comprehensive fracture study using the proposed framework. One demonstration example for fracture is shown to see the capability of the proposed new framework.

Based on the above discussions, the objectives of the proposed study is to develop a novel lattice particle model, which can handle the arbitrary Poisson's ratio effect and the plastic deformation which does not rely on the classical plasticity theories. The key idea in the proposed lattice particle model is to include two potential descriptions for the particle system interaction. In addition to the local pair-wise potential used in the classical lattice spring models, a non-local multi-body potential is introduced to account for the volume change of particles. The restriction on the Poisson's ratio is completely removed by using the volumetric potential term, i.e., the non-local multi-body potential. The proposed model is capable of simulating elastic-plastic deformation by considering the conservation of volume under the general plastic deformation. The content of this section is organized as follows. First, details on the formulation of the proposed lattice particle model is given, includes particle packing selection, derivation of the coefficients of potential functions. Next, the proposed methodology is extended to model elastic-

plastic materials according to the volume conservation during the plastic deformation. Following this, a critical elongation failure criterion is proposed and used for fracture modeling. Then, some benchmark problems of solid mechanics are used to verify the validity of the proposed methodology. Some discussions and conclusions are presented based on the current study at the very end.

2.2.2. Lattice Particle Model: formulation

In this section, detailed formulation of the proposed lattice particle model is given, including particle packing selection, determination of potential coefficients for elasticity and plasticity, and failure criterion. The solution methods used to obtain the final solution in lattice particle model is presented in Chapter 4.

Particle packing

Similar to all particle-based simulation methods, particle packing also directly affects the formulation and model parameter determination in lattice particle model. Two possible packing types, e.g., the hexagonal packing and the square packing are investigated in detail in this study. The schematic plots for different packing are shown in Fig. 2.2.1.

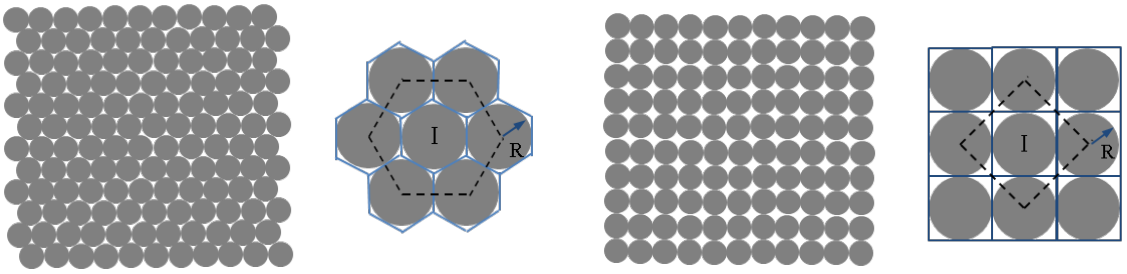

a). Hexagonal packing b). Square packing

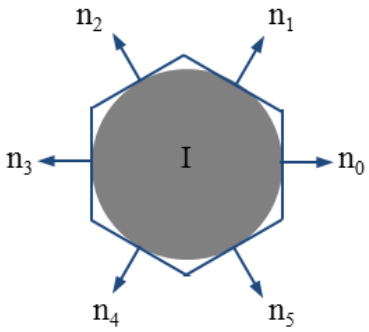

c). Unit cell for hexagonal packing

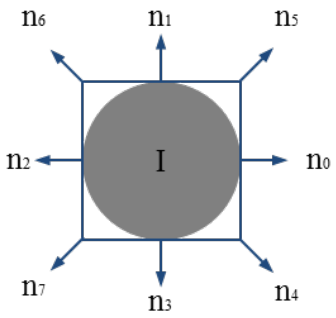

d). Unit cell for square packing

Figure 2.2.1. Schematic Illustration for 2D Particle Packing

In classical lattice models, both packing (Fig. 2.2.1) have been investigated and the restriction on Poisson's ratio exists in both cases [36]. For these two packing only considering the nearest neighbors, they both satisfy the isotropic condition which is required for modeling isotropic homogeneous materials. But for the square packing, there is no shear contribution from the nearest neighbors. By taking the second nearest neighbors into consideration, shear can be introduced into the square packing. More details are shown in section 2.2.1.

Once the particle packing is selected, a unit cell that periodically repeating in the discrete model is chosen to calculate the potential energy. Two typical unit cells for both hexagonal and square packing are shown in Fig. 2.2.1 c) and Fig. 2.2.1 d), respectively. The strain energy of a unit cell can be calculated based on the classical lattice theory, in which the normal vectors of each pair of particles are required. A normal vector is the direction vector between a centered particle and its neighboring particles. The normal vectors of a typical unit cell are listed in Table 2.2.1 for both packing. These definitions will be used in the derivation shown in the next section.

Table 2.2.1. Normal Vectors Associated with a Typical Unit Cell for Two Packing

Normal vector	Hexagonal packing	Square packing
n_0	$(1,0,0)$	$(1,0,0)$
n_1	$(1/2,\sqrt{3}/2,0)$	$(0,1,0)$
n_2	$(-1/2,\sqrt{3}/2,0)$	$(-1,0,0)$
n_3	$(-1,0,0)$	$(0,-1,0)$

n_4	$\left(-1/2,-\sqrt{3}/2,0\right)$	$\left(\sqrt{2}/2,\sqrt{2}/2,0\right)$
n_5	$\left(1/2,-\sqrt{3}/2,0\right)$	$\left(-\sqrt{2}/2,\sqrt{2}/2,0\right)$
n_6	N/A	$\left(-\sqrt{2}/2,-\sqrt{2}/2,0\right)$
n_7	N/A	$\left(\sqrt{2}/2,-\sqrt{2}/2,0\right)$

Model development and potential coefficients determination

The key idea of the proposed lattice particle model is that two potential terms are used to describe the strain energy U_{cell} stored in a unit cell: the energy stored in the local pair-wise neighboring springs U_s and the energy associated with the volume change of a unit cell U_v. Note that only a half spring is used in each unit cell while calculating the strain energy, which avoids overlapping. Mathematically, the above hypothesis can be expressed as

$$U_{cell} = U_s + U_v \tag{2.2.1}$$

Both hexagonal packing and square packing share the same derivation process. Without loss of generality, following derivation is based on the hexagonal packing. Some specific issues related to square packing will be addressed later. The local pair-wise potential function U_s of the hexagonal packing is

$$U_s^h = \frac{1}{2}\sum_{J=0}^{5} k_1^h (\delta l_{IJ})^2 \tag{2.2.2}$$

where superscript h indicates hexagonal packing. δl_{IJ} is the length change of a half spring, k_1^h is the stiffness parameter for springs connecting the center particle with its nearest neighbor.

$$\delta L_{IJ} = \sqrt{\left(x_I - x_J\right)^2 + \left(y_I - y_J\right)^2} - L_{IJ}^0 \tag{2.2.3}$$

where $\left(x_I, y_I\right)$ is the position vector of particle I for 2D case and L_{IJ}^0 is the original length of the connecting bond.

Based on the assumption that the displacement field of a spring is linearly distributed, the strain of a spring connecting particle I and J can be expressed as

$$\varepsilon_{IJ} = \frac{\delta L_{IJ}}{2R} = \frac{\delta l_{IJ}}{R} \tag{2.2.4}$$

where δL_{IJ} is the length change of an entire spring, i.e., $\delta L_{IJ} = 2\delta l_{IJ}$.

The relationship between the strain ε_{IJ} of a spring and the strain tensor of a unit cell in the Cartesian coordinate system is

$$\varepsilon_{IJ} = \varepsilon_{ij} n_j n_i \tag{2.2.5}$$

with $i, j = 1,2,3$.

Based on Eq. (2.2.5), the strain energy stored in the springs of a unit cell can be further formulated as

$$U_s^h = \frac{1}{2} R^2 \sum_{J=0}^{5} k_1^h \left(\frac{\delta l_{IJ}}{R} \right)^2 = \frac{1}{2} R^2 k_1^h \sum_{J=0}^{5} \varepsilon_{IJ}^2 = \frac{1}{2} R^2 k_1^h \sum_{N=0}^{5} n_i^N \varepsilon_{ij} n_j^N n_m^N \varepsilon_{mn} n_n^N \tag{2.2.6}$$

with $i, j, m, n = 1,2,3$, n_i^J indicates the ith component of the normal vector N listed in Table 2.2.1. I, J is the particle indices.

From Eq. (2.2.6) and the normal vectors listed in Table 2.2.1, the strain energy stored in springs associated with a unit cell can be obtained as

$$U_s^h = \frac{1}{2} R^2 k_1^h \left(\frac{9}{4}\varepsilon_{11}^2 + \frac{9}{4}\varepsilon_{22}^2 + \frac{3}{4}\gamma_{12}^2 + \frac{3}{2}\varepsilon_{11}\varepsilon_{22} \right) \tag{2.2.7}$$

Unlike the local pair-wise potential energy, the energy of volume change is introduced via the volumetric strain of a unit cell. For 2D case, the volumetric strain is different in the plane strain and plane stress cases. The general formula for the non-local multi-body potential function U_v is

$$U_v^h = \frac{1}{2} V^h T^h \left(\varepsilon_v^h \right)^2 \tag{2.2.8}$$

where V^h is the volume of a unit cell, T^h is the non-local multi-body potential parameter and ε_v^h is the volumetric strain of a unit cell. For hexagonal packing, the volume of a unit cell is $V^h = 2\sqrt{3}R^2$, where R is the radius of a particle as shown in Fig. 2.2.1(a).

Under the plane strain assumption (i.e., the out-of-plane strains are all zeros), the volumetric strain in terms of the normal strains under Cartesian Coordinates is

$$\varepsilon_v = \varepsilon_{11} + \varepsilon_{22} \tag{2.2.9}$$

Thus, the non-local multi-body potential for volume change of a unit cell is,

$$U_v^h = \frac{1}{2} V^h T^h \left(\varepsilon_v^h\right)^2 = \sqrt{3} R^2 T^h \left(\varepsilon_{11}^2 + 2\varepsilon_{11}\varepsilon_{22} + \varepsilon_{22}^2\right) \tag{2.2.10}$$

Given Eqs. (2.2.7) and (2.2.10), the total strain energy of a unit cell in terms of the strains in the Cartesian Coordinates can be expressed as

$$U_{cell}^h = R^2\left(\frac{9}{8}k_1^h + \sqrt{3}T^h\right)\varepsilon_{11}^2 + R^2\left(\frac{9}{8}k_1^h + \sqrt{3}T^h\right)\varepsilon_{22}^2 + R^2\left(\frac{3}{4}k_1^h + 2\sqrt{3}T^h\right)\varepsilon_{11}\varepsilon_{22} + R^2\left(\frac{3}{8}k_1^h\right)\gamma_{12}^2 \tag{2.2.11}$$

Using the characteristic of elastic material that the strain energy is conservative, the stiffness tensor can be obtained in the Voigt form as

$$C_{ijkl} = \frac{1}{V^h}\frac{\partial^2 U_{cell}^h}{\partial\varepsilon_{ij}\partial\varepsilon_{kl}} \tag{2.2.12}$$

Expanding terms using Eq. (2.2.11), the stiffness matrix can be further expressed as

$$\mathbf{C} = \begin{bmatrix} \frac{3\sqrt{3}k_1^h}{8} + T^h & \frac{\sqrt{3}k_1^h}{8} + T^h & 0 \\ \frac{\sqrt{3}k_1^h}{8} + T^h & \frac{3\sqrt{3}k_1^h}{8} + T^h & 0 \\ 0 & 0 & \frac{\sqrt{3}k_1^h}{8} \end{bmatrix} \tag{2.2.13}$$

Comparing this stiffness matrix with that of 2D isotropic homogeneous material, the parameters of the potential function k_1^h and T^h can be solved in terms of the material constants E (Young's modulus) and ν (Poisson's ratio) uniquely as

$$k_1^h = \frac{4E}{\sqrt{3}(1+\nu)},\ T^h = \frac{E(4\nu-1)}{2(1+\nu)(1-2\nu)} \tag{2.2.14}$$

Eq. (2.2.14) is the expression of the coefficients of the potential function. Next, the interaction force within each spring needs to be calculated which will be used for the particle dynamics

simulation. The interaction force within a spring given certain length change δl_{IJ} can be obtained by taking derivative of the totally energy of a unit cell U_{cell}^{h} with respect to the length change of such spring δl_{IJ} as

$$f_{IJ} = \frac{\partial U_{cell}^{h}}{\partial(\delta l_{IJ})} \tag{2.2.15}$$

In order to do so, the potential energy needs to be expressed as a function of the spring length change δl_{IJ}. By definition, the volumetric strain of a unit cell can be approximated by the strains of all the neighboring springs as

$$\varepsilon_{v}^{h} = \frac{\Delta V}{V} \approx \frac{\frac{2\sqrt{3}R}{3}\sum_{J=0}^{5}\delta l_{IJ}}{2\sqrt{3}R^{2}} = \frac{\sum_{J=0}^{5}\delta l_{IJ}}{3R} \tag{2.2.16}$$

Given Eq. (2.2.16), the total strain energy of a unit cell can be rewritten in terms of the spring length change δl_{IJ} as

$$U_{cell}^{h} = \frac{1}{2}\sum_{J=0}^{5}k_{1}^{h}(\delta l_{IJ})^{2} + \frac{\sqrt{3}}{9}T^{h}\left(\sum_{J=0}^{5}\delta l_{IJ}\right)^{2} \tag{2.2.17}$$

It is shown in Eq. (2.2.17) that the potential energy stored within the springs is a local pair-wise potential and that of the volume change is a non-local multi-body potential.

Based on Eqs. (2.2.15) and (2.2.17), the interaction force within a half spring given certain length change δl_{IJ} can be obtained as

$$f_{IJ} = k_{1}^{h}\delta l_{IJ} + \frac{2\sqrt{3}}{9}T^{h}\sum_{J=0}^{5}\delta l_{IJ} \tag{2.2.18}$$

For plane stress case, the volumetric strain can be expressed using the in-plane normal strains in the Cartesian Coordinates as

$$\varepsilon_{v} = \varepsilon_{11} + \varepsilon_{22} + \varepsilon_{33} = \frac{1-2\nu}{1-\nu}(\varepsilon_{11} + \varepsilon_{22}) \tag{2.2.19}$$

Follow the same procedure as that in the plane strain case, the potential coefficients can be obtained as

$$k_1^h = \frac{4E}{\sqrt{3}(1+\nu)},\ T^h = \frac{E(3\nu-1)(1-\nu)}{2(1+\nu)(1-2\nu)^2} \tag{2.2.20}$$

Comparing Eq. (2.2.14) with Eq. (2.2.20), the spring stiffness parameters are the same while the multi-body potential parameters are different for plane strain and plane stress cases.

The volumetric strain of a unit cell in the plane stress condition can be approximated from its definition as

$$\varepsilon_v^h = \frac{\Delta V}{V} \approx \frac{\left(2\sqrt{3}R^2 - \frac{2\sqrt{3}}{3}R\sum_{J=0}^{5}\delta l_{IJ}\right)(1+d_{33}) - 2\sqrt{3}R^2}{2\sqrt{3}R^2} = \left(1 - \frac{1}{3R}\sum_{J=0}^{5}\delta l_{IJ}\right)(1+\varepsilon_{33}) - 1 \tag{2.2.21}$$

where d_{33} is the thickness change.

Using Eqs. (2.2.19) and (2.2.21), the strain in the thickness direction ε_{33} can be solved as

$$\varepsilon_{33} = \frac{\frac{1}{3R}\sum_{J=0}^{5}\delta l_{IJ}}{\frac{1}{\nu} - 1 - \frac{1}{3R}\sum_{J=0}^{5}\delta l_{IJ}} \tag{2.2.22}$$

Thus, the interaction force for half spring can be obtained as

$$f_{IJ} = k_1^h \delta l_{IJ} + 2\sqrt{3}T^h e^h \tag{2.2.23}$$

where

$$e^h = \left(\frac{(2\nu-1)R\sum_{J=0}^{5}\delta l_{IJ}}{3(1-\nu)R - \nu\sum_{J=0}^{5}\delta l_{IJ}}\right)\left(\frac{3(2\nu-1)R^2(1-\nu)}{\left(3(1-\nu)R - \nu\sum_{J=0}^{5}\delta l_{IJ}\right)^2}\right) \tag{2.2.24}$$

The above discussion is for the parameters of the potential functions for hexagonal packing. For those parameters of square packing, the same derivation scheme can be applied. For simplicity, the results are directly given with some special notes.

The strain energy stored in the springs has a different form from the hexagonal packing since two types of spring is adopted in square packing. The strain energy U_s^s is

$$U_s^s = \frac{1}{2}\sum_{J=0}^{3} k_1^s \left(\delta l_{IJ}\right)^2 + \frac{1}{2}\sum_{J=4}^{7} k_2^s \left(\delta l_{IJ}\right)^2 \tag{2.2.25}$$

where superscript s indicated the square packing, k_1^s and k_2^s are the spring stiffness parameters for springs connecting a center particle with the nearest and the second nearest neighbors, respectively.

The strain energy with the volume change of a unit cell is the same as that of the hexagonal packing, except the volume of a unit cell is $V^s = 4R^2$ for square packing.

For plane strain case, the strain energy of volume change of a unit cell is

$$U_v^s = \frac{1}{2} V^s T^s \left(\varepsilon_v^s\right)^2 = 2R^2 T^s \left(\varepsilon_{11}^2 + 2\varepsilon_{11}\varepsilon_{22} + \varepsilon_{22}^2\right) \tag{2.2.26}$$

Using Eq. (2.2.12), the stiffness matrix for square packing under plane strain assumption is

$$\mathbf{C} = \begin{bmatrix} \frac{k_1^s + k_2^s}{2} + T^s & \frac{k_2^s}{2} + T^s & 0 \\ \frac{k_2^s}{2} + T^s & \frac{k_1^s + k_2^s}{2} + T^s & 0 \\ 0 & 0 & \frac{k_2^s}{2} \end{bmatrix} \tag{2.2.27}$$

Comparing the components with the stiffness matrix of 2D isotropic homogeneous materials, the potential coefficients can be determined uniquely as

$$k_1^s = \frac{2E}{1+\nu},\ k_2^s = \frac{E}{1+\nu},\ T^s = \frac{E\left(4\nu - 1\right)}{2\left(1+\nu\right)\left(1-2\nu\right)} \tag{2.2.28}$$

By definition, the volumetric strain of a unit cell in square packing can be approximated as

$$\varepsilon_v^s = \frac{\Delta V}{V} \approx \frac{2\left(\sqrt{2}-1\right)R\sum_{J=0}^{7}\delta l_{IJ}}{4R^2} = \frac{\left(\sqrt{2}-1\right)\sum_{J=0}^{7}\delta l_{IJ}}{2R} \tag{2.2.29}$$

Thus, the total strain energy of a unit cell in square packing can be rewritten in terms of the length change of a half spring as

$$U_{cell}^s = \frac{1}{2}\sum_{J=0}^{3} k_1^s \left(\delta l_{IJ}\right)^2 + \frac{1}{2}\sum_{J=4}^{7} k_2^s \left(\delta l_{IJ}\right)^2 + \left(\frac{3-2\sqrt{2}}{2}\right) T^s \left(\sum_{J=0}^{7}\delta l_{IJ}\right)^2 \tag{2.2.30}$$

From Eq. (2.2.15), the interaction force within half spring can be obtained as

$$f_{IJ}=\begin{cases} k_1^s\delta l_{IJ}+\left(2\sqrt{2}-3\right)T^s\left(\sum_{J=0}^{7}\delta l_{IJ}\right) & J=0,1,2,3 \\ k_2^s\delta l_{IJ}+\left(2\sqrt{2}-3\right)T^s\left(\sum_{J=0}^{7}\delta l_{IJ}\right) & J=4,5,6,7 \end{cases} \tag{2.2.31}$$

For plane stress case of the square packing, the derived expression of the potential coefficients is

$$k_1^s=\frac{2E}{1+\nu},\ k_2^s=\frac{E}{1+\nu},\ T_s=\frac{E\left(3\nu-1\right)\left(1-\nu\right)}{2\left(1+\nu\right)\left(1-2\nu\right)^2} \tag{2.2.32}$$

The volumetric strain for the square packing under plane stress condition can be approximated as

$$\varepsilon_v^s=\frac{\Delta V}{V}\approx\frac{\left(4R^2-2\left(\sqrt{2}-1\right)\sum_{J=0}^{7}\delta l_{IJ}\right)\left(1+d_{33}\right)-4R^2}{4R^2}=\left(1-\frac{\sqrt{2}-1}{2R}\sum_{J=0}^{7}\delta l_{IJ}\right)\left(1+\varepsilon_{33}\right)-1 \tag{2.2.33}$$

The strain in the thickness direction can be solved from Eqs. (2.2.19) and (2.2.33) as

$$\varepsilon_{33}=\frac{\frac{\sqrt{2}-1}{2R}\sum_{J=0}^{7}\delta l_{IJ}}{\frac{1}{\nu}-1-\frac{\sqrt{2}-1}{2R}\sum_{J=0}^{7}\delta l_{IJ}} \tag{2.2.34}$$

Thus, the interaction force for half spring can be obtained as

$$f_{IJ}=\begin{cases} k_1^s\delta l_{IJ}+T^s e^s & J=0,1,2,3 \\ k_2^s\delta l_{IJ}+T^s e^s & J=4,5,6,7 \end{cases} \tag{2.2.35}$$

where

$$e^s=\left(\frac{2R\left(\sqrt{2}-1\right)\left(2\nu-1\right)\sum_{J=0}^{7}\delta l_{IJ}}{2\left(1-\nu\right)R-\left(\sqrt{2}-1\right)\nu\sum_{J=0}^{7}\delta l_{IJ}}\right)\left(\frac{4R^2\left(\sqrt{2}-1\right)\left(2\nu-1\right)\left(1-\nu\right)}{\left(2\left(1-\nu\right)R-\left(\sqrt{2}-1\right)\nu\sum_{J=0}^{7}\delta l_{IJ}\right)^2}\right) \tag{2.2.36}$$

As a short summary, the model parameters under 2D elastic cases have been derived for both packing. In the following section, the developed model is extended to elastic-plastic deformations.

Extension to plasticity

Plastic deformation is a path-dependent problem from the perspective of energy, which means the parameters derived by equating the strain energy between the discrete model and the continuum model is no longer valid for the case of elastic-plastic deformation. It is known that the plastic deformation is primarily a distortion and the volume change is negligible. From this perspective, instead of equating the strain energies, a volume conservation scheme is proposed to extend the lattice particle model from elastic to plastic deformations.

Volume conservation

The interaction force between a particle pair for an elastic media has been derived as shown in Eqs. (2.2.18) and (2.2.31). A modified equation is proposed to model general elastic-plastic materials and can be expressed as

$$f_{IJ} = \begin{cases} k_e \delta l_{IJ}^e + T_e Q\left(\delta l_{IJ}^e\right) & \delta l_{IJ} \le \delta l_{IJ}^Y \\ k_e \delta l_{IJ}^e + T_e Q\left(\delta l_{IJ}^e\right) + T_p Q\left(\delta l_{IJ}^p\right) & \delta l_{IJ} > \delta l_{IJ}^Y \end{cases} \tag{2.2.37}$$

where k_e is the spring stiffness parameter of the elastic deformation and k_p is that of plastic deformation, as shown in Fig. 2.2.2, δl_{IJ}^e is the elastic part of the length change of a half spring and δl_{IJ}^p is the plastic part, δl_{IJ}^Y is the yielding displacement of the connecting bond, T_e is the multi-body potential parameter for elastic deformation, T_p is the multi-body potential parameter for plastic deformation, and $Q(\cdot)$ is a function of the strains as shown in Eq. (2.2.18). It should be noted that Eq. (2.2.37) is for bi-linear plastic model (see Fig. 2.2.2) and more complex plastic models can be developed based on the similar procedures.

In the Eq. (2.2.37), the length change of a typical bond is additively decomposed into two parts, the elastic part and the plastic part, in a similar way as have been done in classical continuum mechanics for strains.

$$\delta l_{IJ} = \delta l_{IJ}^e + \delta l_{IJ}^p \tag{2.2.38}$$

For plastic deformation, parameters of the potential function, as shown in Eqs. (2.2.17) and (2.2.30), are calculated based on the Poisson's ratio and the tangent modulus at the

corresponding plastic deformation. Given the material's tangent modulus and Poisson's ratio at the plastic deformation stage, the model parameters (in the case of hexagonal packing) can be determined as

$$\left(k_1^h\right)_p = \frac{4E_p}{\sqrt{3}(1+\nu_p)},\ \left(T^h\right)_p = \frac{E_p(4\nu_p - 1)}{2(1+\nu_p)(1-2\nu_p)} \tag{2.2.39}$$

in which the subscript p indicates the plastic deformation. The same model parameters updating is for square packing. If the elastic deformation at the plastic deformation stage is negligible, then $\nu_p = 0.5$. Given the updated model parameters, the interaction force within each bond can be calculated from the elastic and plastic deformations using Eq. (2.2.37). The remaining question is to determine the yielding condition of the bond, i.e., δl_{IJ}^Y in Eq. (2.2.37). Details are shown below.

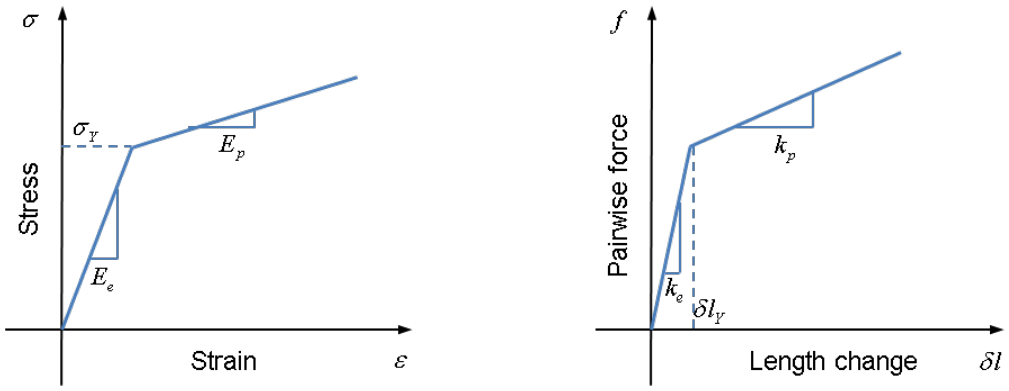

a). A typical bilinear stress-strain curve in continuum model

b). A typical pairwise force vs. length change curve for a bond

Figure 2.2.2. Bilinear Constitutive Model in Lattice Particle Model

Equivalent yield condition

Classical continuum-based plasticity theory needs to define the yield surface for the general plasticity analysis. The proposed lattice particle only uses the one-dimensional bond potential to describe the plastic deformation. The yielding condition is derived by considering the force exerted on a unit cell. The force state is shown in Fig. 2.2.3 for both packing.

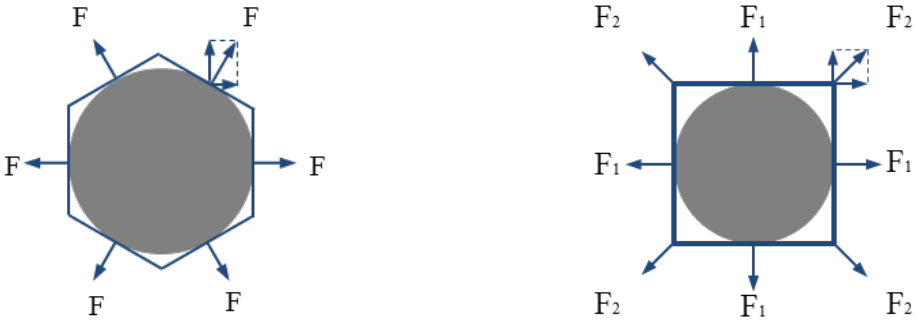

Figure 2.2.3. Forces Exerted on a Unit Cell from Neighboring Springs

As shown in Fig. 2.2.3, for hexagonal packing, the force on a unit cell in the horizontal direction is

$$F_h = 2 \times F \sin\left(60^\circ\right) = \sqrt{3}F \tag{2.2.40}$$

Equating the above net forces with the yielding force in the continuum model, the following equation can be obtained,

$$\sqrt{3}\left(k_1^h \delta l_{IJ} + \frac{\sqrt{3}}{9} T^h \sum_{M=0}^{5} \delta l_{IM} \right) = \sigma_Y 2R \tag{2.2.41}$$

Using Eq. (2.2.14), and Eq. (2.2.41), the yielding length change of a bond can be obtained as,

$$\delta l_{IJ}^Y = \frac{2}{\sqrt{3}\left(1 + \frac{(4\nu - 1)}{24(1-2\nu)} \sum_{M=0}^{5} \frac{\delta l_{IM}}{\delta l_{IJ}} \right)} \frac{\sigma_Y}{k_1^h} R \tag{2.2.42}$$

The same procedure is applied to the square packing, and the critical length change of a spring can be obtained as, for the springs connecting the nearest neighbors and the center particle,

$$\delta l_{IJ}^Y = \frac{2}{\left(\left(1 + \left(3 - 2\sqrt{2}\right) \frac{4\nu - 1}{4(1-2\nu)} \sum_{M=0}^{7} \frac{\delta l_{IM}}{\delta l_{IJ}} \right) + \frac{\sqrt{2}}{2} \left(1 + \left(3 - 2\sqrt{2}\right) \frac{4\nu - 1}{2(1-2\nu)} \sum_{M=0}^{7} \frac{\delta l_{IM}}{\delta l_{IK}} \right) \frac{\delta l_{IK}}{\delta l_{IJ}} \right)} \frac{\sigma_Y}{k_1^s} R \tag{2.2.43}$$

and for the springs connecting the second nearest neighbors and the center particle,

$$\delta l_{IJ}^{Y}=\frac{2}{\left(\left(2+\left(3-2\sqrt{2}\right)\frac{4\nu-1}{2\left(1-2\nu\right)}\sum_{M=0}^{7}\frac{\delta l_{IM}}{\delta l_{IJ}}\right)\frac{\delta l_{IJ}}{\delta l_{IK}}+\left(\sqrt{2}+\left(3-2\sqrt{2}\right)\frac{4\nu-1}{\sqrt{2}\left(1-2\nu\right)}\sum_{M=0}^{7}\frac{\delta l_{IM}}{\delta l_{IK}}\right)\right)}\frac{\sigma_Y}{k_2^s}R \tag{2.2.44}$$

As can be seen, elastic-plastic material modeling in the proposed lattice particle model only uses the modified bond potentials. For general plastic analysis, no stresses and strains transformation to the continuum and the determination of yielding surface are needed, which differentiates the lattice particle model from most existing discontinuous approaches as discussed in the first section.

Fracture criterion

As discussed at the beginning, the fracture simulation if one of the most important advantages of the discrete approach. Detailed study on the fracture simulation needs significant future study. In the current study, only a simple scheme is used to demonstrate the capability of the proposed methodology. The fracture criterion used in the proposed lattice particle model is bond-based, which make the simulation process much easier. Critical energy/force/elongation criteria can be derived based on different material properties, such as fracture toughness and material strength. For demonstration purpose, a bond-based critical elongation criterion is given below.

For springs of triangular packing, the critical elongation can be expressed as

$$\delta l_{IJ}^{critical}=\left(\frac{2}{\sqrt{3}\left(1+\frac{\left(4\nu-1\right)}{24(1-2\nu)}\sum_{M=0}^{5}\frac{\delta l_{IM}}{\delta l_{IJ}}\right)}\frac{\sigma_R}{k_1^h}+2\right)R \tag{2.2.45}$$

For the springs connecting the nearest neighbors and the center particle in square packing, the critical elongation can be expressed as

$$\delta l_{IJ}^{critical} = \left(\frac{2}{\left(\left(1+\left(3-2\sqrt{2}\right)\frac{4\nu-1}{4(1-2\nu)}\sum_{M=0}^{7}\frac{\delta l_{IM}}{\delta l_{IJ}} \right) + \frac{\sqrt{2}}{2}\left(1+\left(3-2\sqrt{2}\right)\frac{4\nu-1}{2(1-2\nu)}\sum_{M=0}^{7}\frac{\delta l_{IM}}{\delta l_{IK}} \right)\frac{\delta l_{IK}}{\delta l_{IJ}} \right)} \frac{\sigma_R}{k_1^s} + 2 \right) R \tag{2.2.46}$$

For the springs connecting the second nearest neighbors and the center particle in the square packing, the critical elongation can be expressed as

$$\delta l_{IJ}^{critical} = \left(\frac{2}{\left(\left(2+\left(3-2\sqrt{2}\right)\frac{4\nu-1}{2(1-2\nu)}\sum_{M=0}^{7}\frac{\delta l_{IM}}{\delta l_{IJ}} \right)\frac{\delta l_{IJ}}{\delta l_{IK}} + \left(\sqrt{2}+\left(3-2\sqrt{2}\right)\frac{4\nu-1}{\sqrt{2}(1-2\nu)}\sum_{M=0}^{7}\frac{\delta l_{IM}}{\delta l_{IK}} \right) \right)} \frac{\sigma_R}{k_2^s} + 2\sqrt{2} \right) R \tag{2.2.47}$$

where σ_R is the rupture strength of a material. Once the critical elongation is reached by a bond during the simulation step, the bond is considered broken and removed from future simulation steps. The entire fracture process can be tracked by the bond breaking process as used in most existing discrete approaches.

2.2.3. Numerical Examples

Elasticity and elastic-plasticity

The benchmark problems used in this section to examine the validity of the proposed lattice particle model share two types of geometric dimensions: one rectangular plate with centered hole and one without. The dimensions of the two plates are shown in Fig. 2.2.4. The unit for the geometric dimension is meter (*m*). Several different loading conditions are considered. The boundary conditions are specified in each example. The material properties are listed in Table 2.2.2.

Table 2.2.2. Material Constants for 2D Elasticity and Plasticity

Material constants	Value
Young's modulus (E) (*Pa*)	6.9 x10^{10}
Mass density (ρ) (*kg/m*^{3})	2.7 x10^3

Yielding strength (σ_Y) (*Pa*)	2.0 x10^8
Poisson's ratio (v)	Vary

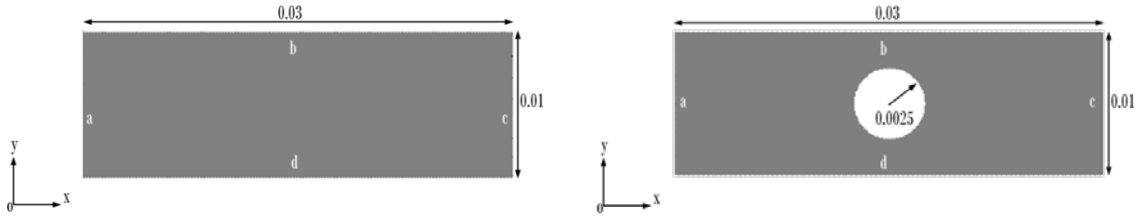

Rectangular plate 1 Rectangular plate 2, with centered hole

Figure 2.2.4. The Dimensions of the Two Plates

Elastic problems

Various loading conditions are utilized to test the validity of lattice particle model for modeling the elastic deformation of isotropic materials. The physical model used for all elastic examples is the rectangular plate 1, without centered hole. The boundary conditions for each example may different. A more detailed specification is given in each example.

Verification of Poisson's Ratio

The plate left edge (edge *a*) is fixed in the *x* direction while free in the *y* direction. A displacement boundary condition is applied on the right edge (edge *c*) in the positive *x* direction, with value of 1.0 x10^{-5} *m*. The testing results are shown in Fig. 2.2.5, in which the fixed Poisson's ratios in classical lattice models are also provided for comparison.

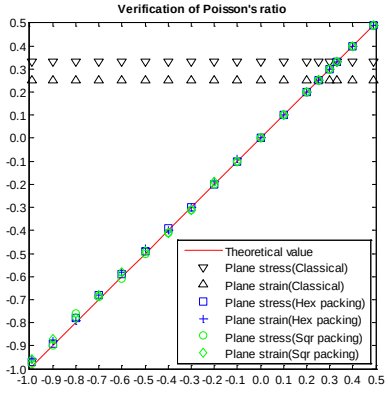

Figure 2.2.5. The Verification of Poisson's Ratio for 2D Isotropic Materials

Clamped plate under tension

The rectangular plate 1 is stretched in the positive *x* direction with force of value 2000 newton. The left edge (edge *a*) is clamped, i.e., the motions in both *x* and *y* directions are fixed. Due to symmetry, only a half model is used. The plane stress assumption is adopted. The Poisson's ratio is 0.25. The results for the displacement distribution are compared in Fig. 2.2.6. The simulation results using two different packing and the solution from FEM using ABAQUS are compared.

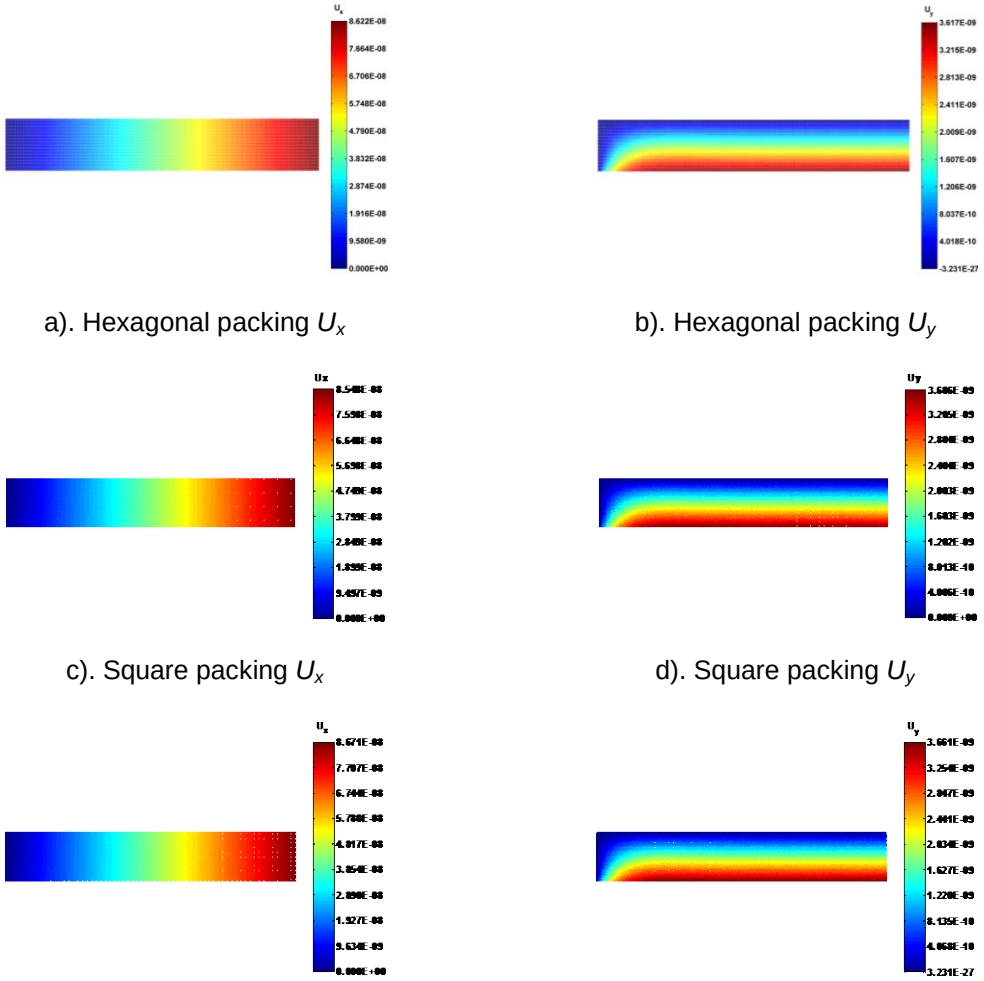

a). Hexagonal packing U_x b). Hexagonal packing U_y

c). Square packing U_x d). Square packing U_y

e). FEM U_x f). FEM U_y

Figure 2.2.6. Displacements Distribution for Tensile Loading

Cantilever beam 1

For the beam in this case, the left edge (edge *a*) is clamped. An external shear force with value of 2000 newton is applied on the right edge (edge *c*) in the negative *y* direction. Due to symmetry of

the physical model, only a half model is used. The plane strain assumption is made for this example. The Poisson's ratio is 0.33. The deformation results are shown in Fig. 2.2.7.

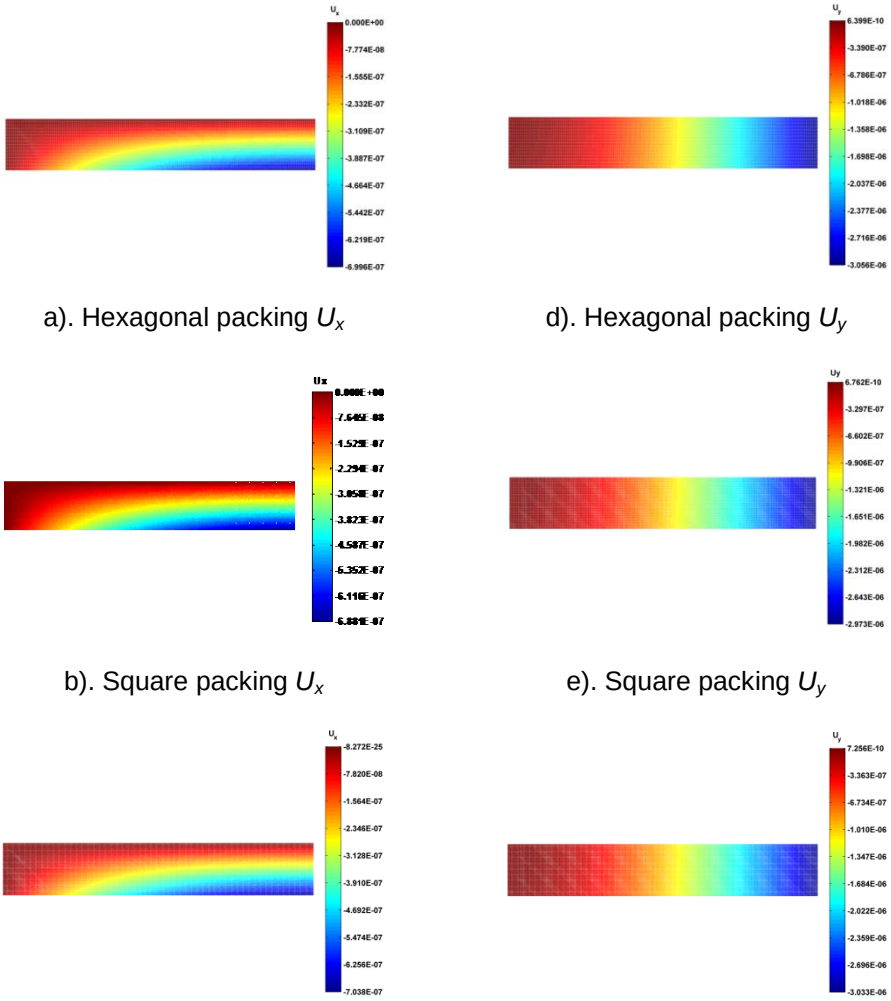

a). Hexagonal packing U_x d). Hexagonal packing U_y

b). Square packing U_x e). Square packing U_y

c). FEM U_x f). FEM U_y

Figure 2.2.7. Displacements Distribution for Shear Loading

A convergence study is also performed using this example. The L2 norm error is defined as

$$e_{L_2} = \frac{\left\| u^{ex} - u^h \right\|_{L_2}}{\left\| u^{ex} \right\|_{L_2}} = \frac{\left(\sum_{i=1}^{N_p} \left(u_i^{ex} - u_i^h \right)^2 \right)^{1/2}}{\left(\sum_{i=1}^{N_p} \left(u_i^{ex} \right)^2 \right)^{1/2}} \tag{2.2.48}$$

where N_p is the total number of particles and the exact solution from Timoshenko [37] under plane stress assumption is

$$u = -\frac{P(L-x)^2 y}{2EI} - \frac{vPy^3}{6EI} + \frac{Py^3}{6GI} + \left(\frac{PL^2}{2EI} - \frac{PD^2}{8GI}\right)y$$
$$v = \frac{vP(L-x)y^2}{2EI} + \frac{P(L-x)^3}{6EI} - \frac{PL^2(L-x)}{2EI} + \frac{PL^3}{3EI} \tag{2.2.49}$$

with the plate length $L = 0.03$ and height $D = 0.01$, and the moment of inertia of the cross section of the plate $I = \frac{D^3}{12}$.

The convergence plot is shown in Fig. 2.2.8. As can be seen, a good convergence rate is achieved in the proposed model.

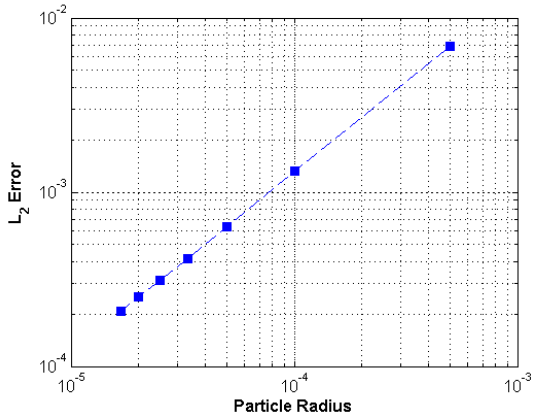

Figure 2.2.8. The Convergence Characteristic of Hexagonal Packing

Cantilever beam 2

For this example, the left edge (edge *a*) is clamped. A uniformly distributed force is applied on the top edge (edge *b*) with a resultant force of 2000 newton in the negative *y* direction. The plane strain assumption is also made for this case. The Poisson's ratio for this case is 0.3. The results are shown in Fig. 2.2.9.

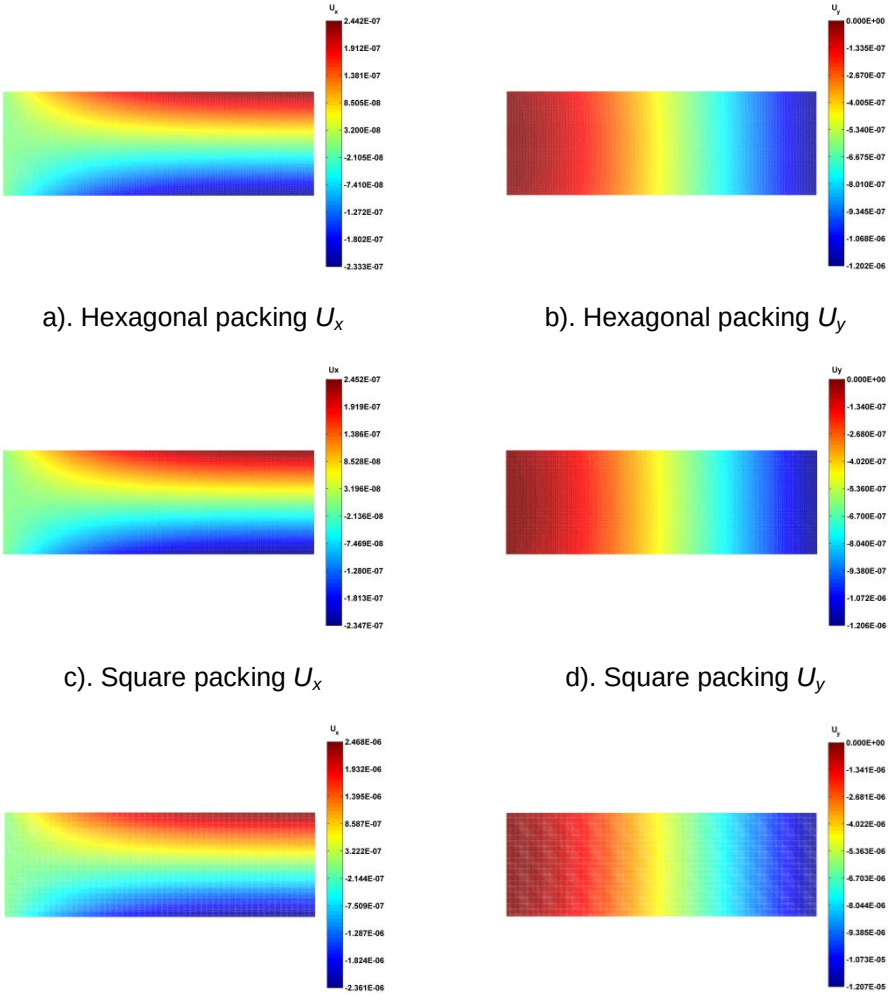

a). Hexagonal packing U_x b). Hexagonal packing U_y

c). Square packing U_x d). Square packing U_y

e). FEM U_x f). FEM U_y

Figure 2.2.9. Displacements Distribution for Uniformly Distributed Loading

Based on the above verification for linear elastic cases, it is observed that the proposed lattice particle model can accurately predict the deformation behavior for different Poisson's ratios under different loading conditions. The two different packing give similar results compared to the classical FEM results.

Elastic-plastic problems

For problems in this section, the displacement boundary conditions are used and applied at a very low speed so as to obtain a quasi-static solution. Dynamic solution method is used and no damping strategy is used in this section.

As mentioned in the previous section, the strain measures adopted in the lattice particle model have the meaning of engineering strains. In order to compare the results with FEM results obtained from the ABAQUS package, the engineering stress-strain curve needs to be translated into the true stress-strain curve. For the bilinear engineering stress-strain curve shown in Fig. 2.2.10, the tangent moduli are 6.9 x10^{10} *Pa* and 6.9 x10^{8} *Pa* for elastic and plastic stages, respectively. The yielding strength of the material is 2.0 x10^{8} *Pa*, as listed in Table 2.2.2. The engineering stress-strain curve and the converted true stress-strain curve are shown in Fig. 2.2.10. These curves are used for both examples in this section.

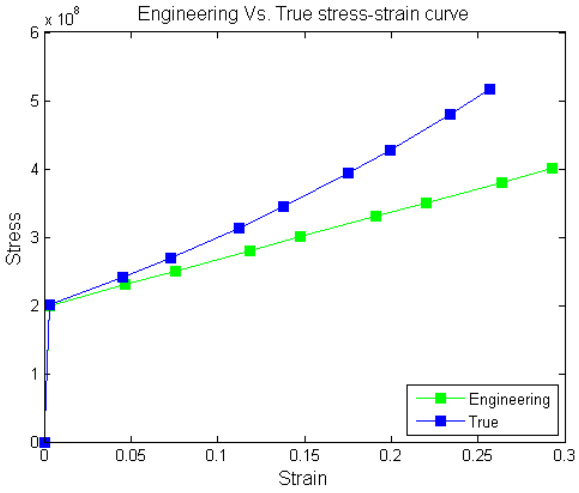

Figure 2.2.10. Engineering and Translated True Stress-Strain Curves

Uniaxial tension

The rectangular plate with a center-hole is used in this example. Both geometrical and material nonlinearities are involved. The left edge (edge *a*) is clamped. A displacement boundary condition is applied on the right edge (edge *c*) in the positive *x* direction, with value of 5.0 x10^{-4} *m*. The example is tested for various Poisson's ratio so as to show the validity of the proposed lattice particle model for elastic-plastic materials. The Poisson's ratios for all cases are assumed to be 0.499 at the plastic deformation. For simplicity, the plots are made only for the case of initial Poisson's ratio of 0.4. The lateral deformation results are shown in Fig. 2.2.11 a)-c), with d) is the history of the reaction force at the right edge (edge *c*). The results for other cases are listed in Table 2.2.3.

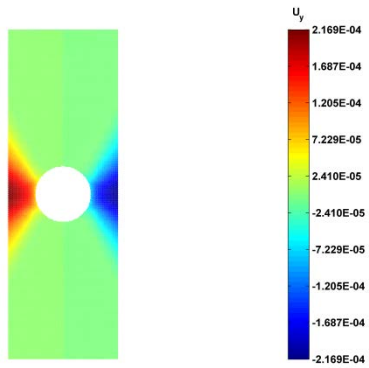

a). Hexagonal packing U_y

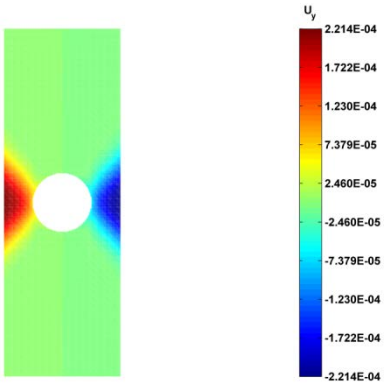

b). Square packing U_y

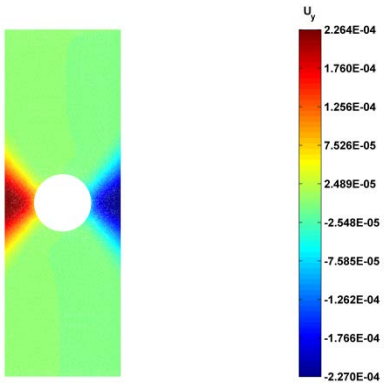

c). FEM U_y

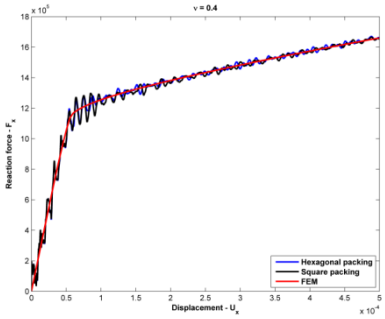

d). Reaction force on the right edge (edge *c*)

Figure 2.2.11. Distribution of Uy and Reaction Force Fx

Table 2.2.3. Displacement Uy and Reaction Force Fx for Various Poisson's Ratio

Poisson's Ratio	U_y (x10^{-4} *m*)			F_x (x10^{6} *N*)		
	Hexagonal	Square	FEM	Hexagonal	Square	FEM
0.40	+2.169 -2.169	+2.214 -2.214	+2.264 -2.270	-1.663	-1.661	-1.660
0.33	+2.158 -2.158	+2.194 -2.194	+2.229 -2.234	-1.656	-1.656	-1.652
0.30	+2.152 -2.152	+2.191 -2.191	+2.215 -2.220	-1.651	-1.650	-1.650
0.25	+2.164 -2.164	+2.187 -2.187	+2.193 -2.197	-1.649	-1.648	-1.646

Cantilever beam 1: shear loading

The physical model used in this example is the rectangular plate without the hole. The left edge (edge *a*) is clamped and a displacement boundary condition is applied on the right edge (edge *c*) in the negative *y* direction with value of -2.0 x10^{-3} *m*. The stress-strain curve is the same as the one used in the uniaxial tension test. Comparing to the geometrical dimension, the model used in

this example undergoes a large deformation. For simplicity, only the results for Poisson's ratio of 0.4 are given here. The final displacement distributions and the reaction force history on the right edge (edge *c*) are shown in Fig. 2.2.12.

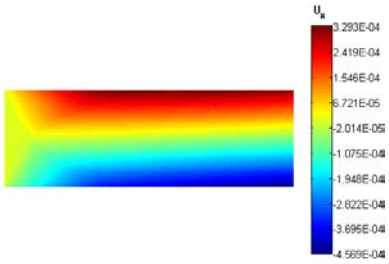

a). Hexagonal Packing U_x

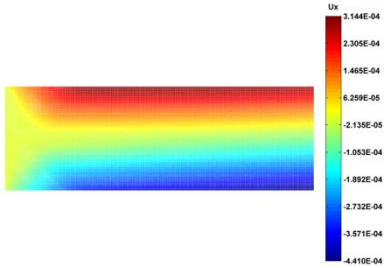

b). Square packing U_x

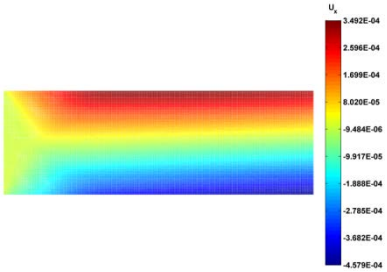

c). FEM U_x

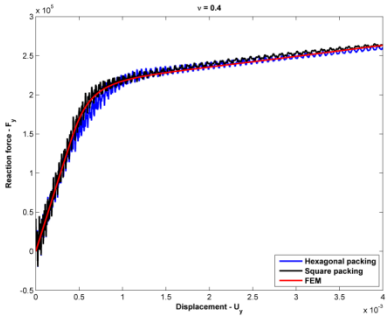

d). Reaction force on the right edge (edge *c*)

Figure 2.2.12. Distribution of Ux and Reaction Force Fy

Uniaxial tension, Unloading

In order to differentiate the elastic-plastic response from the nonlinear elastic response of materials, an unloading case is studied here, i.e., elastic unloading forward plastic reloading. The model used in this subsection is the same as the one in the uniaxial tension test, except that an unloading process is applied after the plate is loaded to certain plastic deformation. Only the results of the hexagonal packing are provided. The history of the external applied displacement boundary conditions and the reaction force on edge *C* are shown in Fig. 2.2.13. The oscillation during the elastic unloading and reloading is due to the nature of dynamic formulation. The final displacements distributions are shown in Fig. 2.2.14.

Based the above verification for elastic-plastic analysis, it is observed that the proposed lattice particle model and volume conservation scheme can successfully predict the elastic-plastic

deformation under loading and geometry induced plasticity (i.e., due to bending and stress concentration). The results agree well with classical FEM results based on von-Misses yielding criterion. Both packing have similar results compared to the FEM results, which indicates that the proposed lattice particle model is independent of the packing selection, at least for the investigated two packing patterns. It should be noted that the above plastic analysis using the lattice particle model only depends on the one dimensional pair-wise bond potentials and no yield surface as used in the classical continuum-based plasticity theory is required. This greatly facilitates the implementation of nonlinear material behavior in the proposed lattice particle model, e.g., damage-induced stiffness degradation. Future study is required to fully verify this for general 3D cases under general loading conditions.

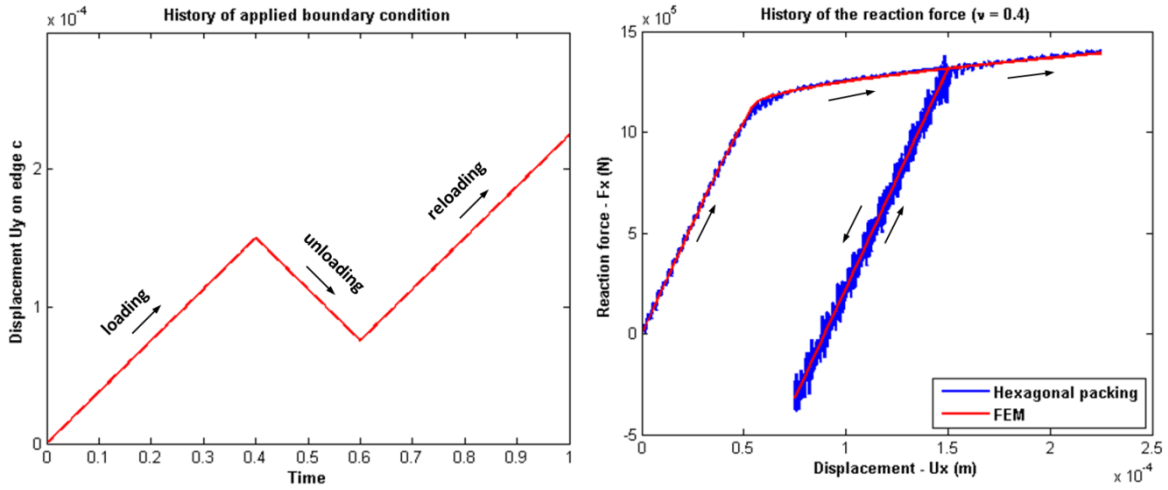

a). Applied displacement b). Reaction force

Figure 2.2.13. History of the Applied Displacement and Reaction Force on Edge c

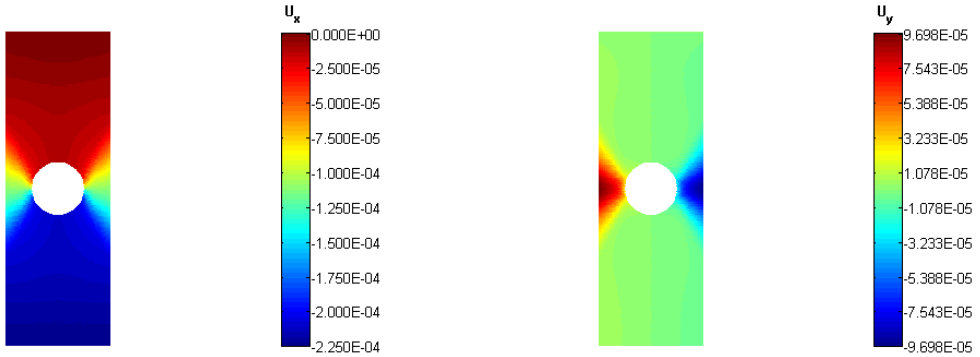

a). Hexagonal packing U_x

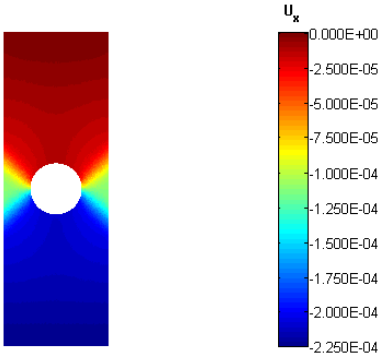

b). Hexagonal packing U_y

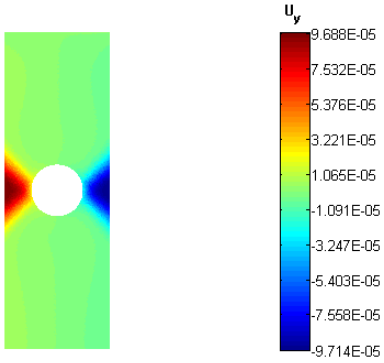

c). FEM U_x

b). FEM U_y

Figure 2.2.14. Displacements Distribution for 2D Elasto-Plastic Materials

Fracture simulation

A three-point-bending test is simulated in this section to show the capability of the proposed model for fracture modeling using the triangular packing lattice. The geometry and the loading condition of the specimen are shown in Fig. 2.2.15. A centered point loading is applied on the top edge of the specimen and the crack length is 0.002 *m*. Two points, 0.028 *m* away from each other, on the bottom edge are fixed in the *y*-direction. The material property in this problem is the same as those listed in the Table 2.2.2. The Poisson's ratio is 0.2. The simulation results using the triangular packing are given in Fig. 2.2.16.

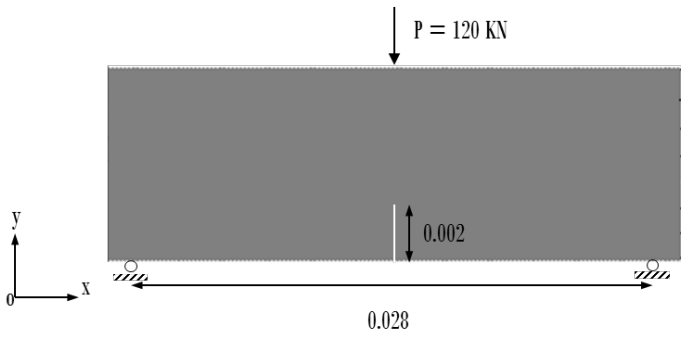

Figure 2.2.15. Configurations of the Three-Point-Bending Test Specimen

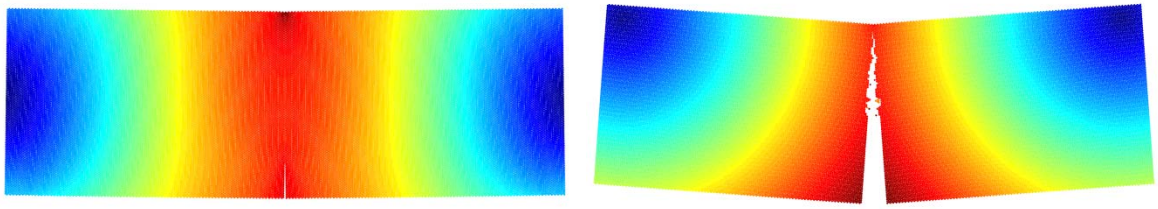

t_1 t_2

Figure 2.2.16. Snapshots of the Fracture Processes at Two Different Time Steps

It can be observed that a typical mode I crack growth is simulated in this example, which is expected from the continuum theory. It should be noted that this demonstration example is only used to illustrate the feasibility of fracture simulation using the proposed new framework. Detailed investigation of fracture analysis using the proposed approach needs further study.

2.2.4. Discussion and Conclusion

A novel lattice particle model is proposed for the general analysis of 2D isotropic solids, i.e., elasticity, elastic-plasticity and fracture. The proposed method is verified with the classical continuum-based solutions.

For some discrete approach using both normal and shear springs, the stiffness of the shear spring will become negative for some special Poisson's ratios [2]. In this approach, both springs are physical springs corresponding to different displacements. It is hard to justify the negative stiffness for a macro level spring element under elastic deformation, although some physical explanations have been given in [11]. In the proposed approach, the volumetric parameter *T* will be negative for certain range of Poisson's ratio, i.e. smaller than 0.25 for plane strain and 0.33 for plane stress. This parameter does not have any physical meaning and is used to compensate the energy representation in the classical axial spring model. For the plane strain case, when the Poisson's ratio is larger than 0.25, the strain energy stored in a unit cell will become smaller than that of the corresponding continuum theory. The volumetric energy term is introduced to compensate this difference such that the energy equivalence can be achieved for arbitrary Poisson's ratios.

In the plasticity examples, the maximum strain level is about 10% which is considered large for most engineering materials and structures. As long as the lattice distortion is not significant, the proposed framework can be directly applied to large displacement problems. If the lattice distortion is significant, a geometric nonlinearity tracking algorithm needs to be used to update the lattice configuration at each simulation step, which is similar to classical FEM implementations to include the geometric nonlinearity. Thus, the proposed framework is possible for large displacement, but needs additional studies for highly distorted particle systems.

The lattice beam model introduces “micropolarity” and can improve the Poisson’s ratio limitations of the classical lattice spring model. There are two distinct differences between the beam element approach and the proposed model. First, the degree of freedom of the proposed framework is very different from the beam element method since only nodal displacement at the particle locations are considered as DOF (i.e., no rotational DOF). This difference can be significant for large particle systems and can impact the solution efficiency. Second, the fracture simulation for beam elements needs to consider the multi-axial force/displacement while the proposed method only uses the axial force/displacement. This difference will have very different effects in the fracture simulations. Detailed comparison between the proposed framework and the beam element method will be very interesting and needs further study. The pros and cons of each method should be investigated in detail. Nevertheless, the proposed framework offers a new, systematic, and alternative way for the discrete method simulation of solids.

Several major conclusions are drawn based on the current investigation:

1). Introducing the local pair-wise and non-local multi-body volumetric potentials successfully reproduces all Poisson’s ratios using the proposed particle method;

2). The volume conservation scheme in the proposed lattice particle model is able to analyze the nonlinear elastic-plastic deformation of 2D solids;

3). Only one-dimensional pair-wise potential needs to be determined for the plastic deformation and general plasticity analysis can be performed, which greatly facilitates the plasticity analysis;

4). Fracture phenomenon can be simulated using the proposed model with suitable bond breaking rules;

5). Both hexagonal packing and square packing yield similar results compared to the classical continuum-based methods;

6). For the modeling of continuous materials, the proposed lattice particle model is not computational as efficient as the classical finite elements.

The current study focuses on the 2D analysis and is extendable to general 3D cases. Future work on the theoretical development and model validation on 3D conditions is ongoing. More detailed study on the damage and fracture modeling using the proposed lattice particle model is also required. Applications of the proposed methodology to complex loadings and anisotropic and non-homogeneous materials need additional theoretical and experimental studies.

2.3 2D Generalized Lattice Particle Model for Fracture Simulation

In this section, a generalized 2D non-local lattice particle model is presented for the study of fracture phenomena of homogeneous isotropic solids. In the proposed model, both the pairwise local and the multi-body non-local interaction force among particles are considered. Special focus is on the investigation of the failure anisotropy or directional preference of the crack path while modeling fracture phenomena within the framework of regular lattice spring models. Different from random network models, a generalized regular lattice framework to include multiple non-local forces from neighboring particles is proposed to eliminate/reduce this well-known failure anisotropy issue. Several benchmarks are tested to assess the performance of the proposed methodology. Discussions and conclusions are drawn based on the current study.

2.3.1. Introduction

The idea of employing discrete one-dimensional bonds, e.g., springs or beams, to study the different phenomena of solids dates back to the work of Hrennikoff [16], in which the elastic properties of solids is firstly investigated using the lattice method. Successive studies can be found, e.g., in [17], [2], [18], [19]. The lattice models can be classified into different categories according to how the lattice sites interact via the connecting bonds. The simplest and one of the most popular forms of interaction is through the central force (or axial) springs [9]. This type of model has the issue of the fixed Poisson's ratio. With the introduction of the bond rotation as additional degree of freedom [20], the Poisson's ratio can be modified. The Born model [21] introduces a non-central two-body interaction, but this model is not rotationally invariant. Keating [10] discussed the rotationally invariant requirement and proposed a bond-bending model, in which the angle change between two adjacent connecting bonds is considered as an additional component of the system energy. The beam model [12] removes the limitation on the Poisson's ratio by considering both the forces and the moments (i.e., rotational degrees of freedom) at each lattice site. Another lattice model introduces a volumetric term in the potential which can avoid the Poisson's ratio issue and the rotational invariant requirement is guaranteed [22]. Similar to

Grassl's work [22], Chen et al. [38] proposed a lattice particle method by introducing a non-local particle potential term in addition to the pairwise potential. Unlike the elastic formulation proposed by Grassl's [22], both elasticity and plasticity of isotropic solids using the regular lattice framework were proposed using the non-local particle interactions [38].

Fracture phenomena have been extensively studied and many numerical simulation approaches have been proposed, such as the Finite Element Methods (FEM) with adaptive remeshing technique [5] and cohesive elements [39], the XFEM [40], the Peridynamics [3], [41], [42], and the Lattice Models [17], [12], [2]. The Lattice Models have some advantages when handling the fracture problems. For instance, Lattice Models are based on discontinuous formulation which avoids singularity related issues while handling problems with discontinuity. The crack initiation and propagation processes can be modelled via bond breaking and removal rules.

One of the intrinsic issue of the lattice/particle method for fracture simulation is the crack path preference due to the regular lattice configuration [13], [12]. This directional preference of the crack path is also related to the anisotropy of the failure surface that has been investigated in [15]. Two major approaches have been proposed to address this issue. One is to use the random/irregular network. The irregular lattice models exhibits less crack path preference and offers freedom in domain discretization, but require certain scaling technique [14] to obtain elastic uniformity. Another possible solution is to use multiple neighbors. By introducing multiple neighbors, the lattice symmetry will be enhanced and the crack path preference will be eliminated or reduced. A similar idea has been used in Peridynamics [3] and is termed as "horizon".

Many non-local lattice models can be found in the literature, such as [10], [11], but the systematic study of the effects of multiple neighbor non-local interaction on fracture simulation is rarely found. Thus, one of the major objectives of the proposed study is to investigate the effect of multiple neighbors' effects on the crack path preference for a newly developed lattice particle model [38]. The article is organized as follows. First, a brief review of the basic concepts and major derivations of the proposed lattice particle model employing the nearest neighbors is given. Following this, the generalized cases with multiple different neighbors are considered. The

fracture criterion based on the critical stress is discussed in detail. Next, the performance of the proposed framework up to the 4th-nearest neighbors is assessed by studying several benchmark problems, e.g., the quasi-static mode-I fracture, the dynamic mode-II cracking [43], and the dynamic crack branching [44]. Detailed discussion on the crack path preference is given. Several conclusions are drawn based on the proposed study.

2.3.2. Theory and Formulation

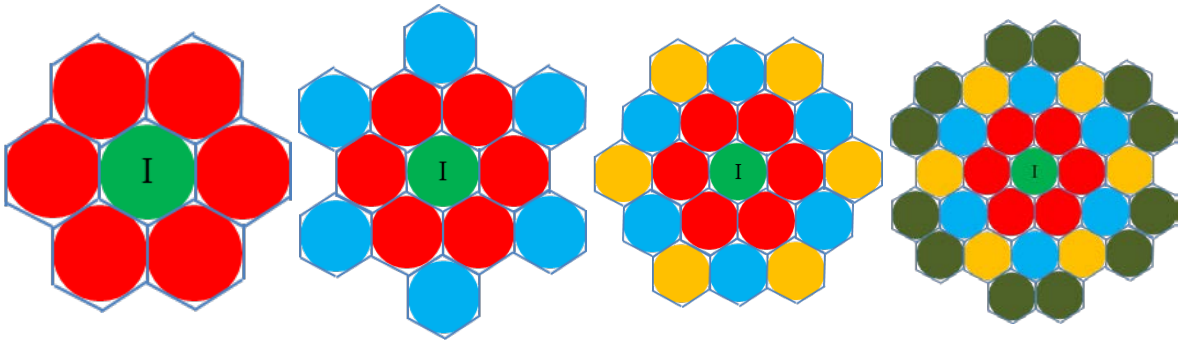

(a) 1st neighbor **(b)** 2nd neighbor **(c)** 3rd neighbor **(d)** 4th neighbor

Figure 2.3.1. Different Packing Using Different Numbers of Neighboring Particles

In this section, a brief review of the lattice particle model is given first. The lattice particle model proposed in [38] only considers the 1st-nearest six neighboring particles (Fig. 2.3.1(a)). Following that, new development for multiple neighboring particles (see Fig. 2.3.1) is proposed. The derivation is first illustrated for the 2nd-nearest, 3rd-nearest and 4th-nearest neighboring particles and is generalized to the N^{th}-nearest neighboring particles case. Without loss of generality, only the hexagonal packing is studied in this paper (Fig. 2.3.1). For other packing, e.g., square packing, the same methodology can be applied. Next, the generalized failure criterion is discussed in detail.

Lattice particle model using only the 1st-nearest-neighbor: a review

In the regular lattice models, a unit cell is identified from the discretization to derive the model parameters in terms of the material properties. The unit cell for this 1st-nearest-neighor packing is

shown in Fig. 2.3.2(a) with associated six normal vector directions. The values of these normal vectors are listed in Table 2.3.1. A brief derivation is given here and a more detailed formulation can be found in the previous work [38].

Table 2.3.1. The Normal Vectors for the 1st-Nearest Neighbors

n_1	n_2	n_3	n_4	n_5	n_6
$(1,0)$	$\left(1/2,\sqrt{3}/2\right)$	$\left(-1/2,\sqrt{3}/2\right)$	$(-1,0)$	$\left(-1/2,-\sqrt{3}/2\right)$	$\left(1/2,-\sqrt{3}/2\right)$

The total energy of a unit cell is composed of two parts, the pair-wise (local) energy and the volumetric (non-local) energy:

$$U_{cell}^{(1)} = U_s^{(1)} + U_v^{(1)} \tag{2.3.1}$$

where the pair-wise energy stored in a unit cell in terms of the elongation of the associated six springs is

$$U_s^{(1)} = \frac{1}{2} k^{(1)} \sum_{J=1}^{6} \left(\delta l_{IJ}\right)^2 \tag{2.3.2}$$

and the volumetric energy is

$$U_v^{(1)} = \frac{1}{2} T^{(1)} \left(\sum_{J=1}^{6} \delta l_{IJ} \right)^2 \tag{2.3.3}$$

where δl_{IJ} is half of the length change of the whole bond. $k^{(1)}$ and $T^{(1)}$ are the model parameters. The superscription indicates these quantities are for the 1st-nearest neighbor. It should be noted that the volumetric energy is a generalized form of the one proposed in [22] and [38].

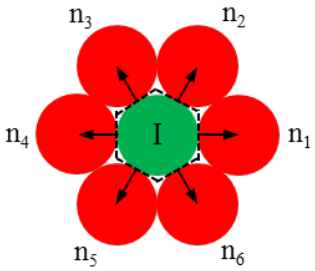

Figure 2.3.2. The Unit Cell and Normal Vectors for the 1st-Nearest Neighbors

In terms of the strain tensor, Eq. (2.3.1) can be rewritten using Eqs. (2.3.2)-(2.3.3) as

$$U_{cell}^{(1)} = \frac{1}{2}k^{(1)}R_1^2\sum_{b=1}^{6} n_i^b n_j^b n_k^b n_l^b \varepsilon_{ij}\varepsilon_{kl} + \frac{1}{2}T^{(1)}R_1^2\left(\sum_{b=1}^{6} n_i^b n_j^b \varepsilon_{ij}\right)\left(\sum_{b=1}^{6} n_k^b n_l^b \varepsilon_{kl}\right) \tag{2.3.4}$$

where R_1 is the radius of the inscribed circle of the unit cell, which is half value of the particle spacing and superscript b is the number of normal vectors given in Table 2.3.1.

The total energy of a unit cell in terms of the components of the strain tensor can be obtained as

$$U_{cell}^{(1)} = \frac{1}{2}R_1^2\left(\left(\frac{9}{4}k^{(1)} + 9T^{(1)}\right)\varepsilon_{11}^2 + \left(\frac{9}{4}k^{(1)} + 9T^{(1)}\right)\varepsilon_{22}^2 + \left(\frac{3}{4}k^{(1)}\right)\gamma_{12}^2 + \left(\frac{3}{2}k^{(1)} + 18T^{(1)}\right)\varepsilon_{11}\varepsilon_{22}\right) \tag{2.3.5}$$

The stiffness tensor of an equivalent continuum can be obtained as

$$C_{ijkl} = \frac{1}{V_1}\frac{\partial^2 U_{cell}^{(1)}}{\partial\varepsilon_{ij}\partial\varepsilon_{kl}} \tag{2.3.6}$$

where V_1 is the volume of the unit cell and $V_1 = \frac{1}{2}\cdot\frac{2\sqrt{3}}{3}R_1\cdot R_1\cdot 6\cdot h = 2\sqrt{3}hR_1^2$. To be dimensional consistent, the unit thickness h is kept in all the derivations.

Comparing the stiffness matrix with the ones of 2D isotropic homogeneous Hookean material, the following correspondence can be obtained:

Plane strain case:

$$\begin{aligned}
&\frac{3\sqrt{3}k^{(1)}}{8h} + \frac{9}{2\sqrt{3}h}T^{(1)} = \frac{E(1-\nu)}{(1+\nu)(1-2\nu)}\\
&\frac{\sqrt{3}k^{(1)}}{8h} + \frac{9}{2\sqrt{3}h}T^{(1)} = \frac{E\nu}{(1+\nu)(1-2\nu)}\\
&\frac{\sqrt{3}k^{(1)}}{8h} = \frac{E}{2(1+\nu)}
\end{aligned} \tag{2.3.7}$$

Plane stress case:

$$\frac{3\sqrt{3}k^{(1)}}{8h}+\frac{9}{2\sqrt{3}h}T^{(1)}=\frac{E}{1-\nu^2}$$
$$\frac{\sqrt{3}k^{(1)}}{8h}+\frac{9}{2\sqrt{3}h}T^{(1)}=\frac{E\nu}{1-\nu^2} \tag{2.3.8}$$
$$\frac{\sqrt{3}k^{(1)}}{8h}=\frac{E}{2(1+\nu)}$$

Therefore, the model parameters $k^{(1)}$ and $T^{(1)}$ for 1st-nearest neighbors can be uniquely solved as

Plane strain case:

$$k^{(1)}=\frac{4hE}{\sqrt{3}(1+\nu)}$$
$$T^{(1)}=\frac{\sqrt{3}}{9}\frac{hE(4\nu-1)}{(1+\nu)(1-2\nu)} \tag{2.3.9}$$

Plane stress case:

$$k^{(1)}=\frac{4hE}{\sqrt{3}(1+\nu)}$$
$$T^{(1)}=\frac{\sqrt{3}}{9}\frac{hE(3\nu-1)}{(1+\nu)(1-\nu)} \tag{2.3.10}$$

From Eqs. (2.3.9) and (2.3.10), the model parameters are functions of the bulk material constants, i.e., the Young's modulus (*E*) and the Poisson's ratio (*v*). And the model parameters are uniquely determined.

Given the model parameters $k^{(1)}$ and $T^{(1)}$, the interaction force within each connecting bond can be calculated by differentiating the total energy as

$$F_{IJ}^{(1)}=-\frac{\partial U_{cell}^{(1)}}{\partial \delta l_{IJ}}=-k^{(1)}\delta l_{IJ}-T^{(1)}\sum_{J=1}^{6}\delta l_{IJ} \tag{2.3.11}$$

Eqs. (2.3.1)-(2.3.10) are the derivations of the model parameters for the 1st-nearest neighbors. A generalized scheme to introduce more neighboring particles is discussed in next section.

Generalized lattice particle model using multiple neighbors

2nd-nearest-neighbor packing

The 2nd-nearest-neighboring particles are considered as the interacting neighbors with the center particles in this subsection. The center particle *I*, shown in Fig. 2.3.3, has two types of neighboring particles, i.e., the 1st-nearest neighbors and the 2nd-nearest neighbors. The schematic plot is shown in Fig. 2.3.4 to show the interactions between the neighbors with the center particle. For each type of neighbor, it has its own unit cell. The unit cell for the center particle packed with the 1st-nearest neighbors is the same as the one in the 1st-nearest-neighbor packing shown in Fig. 2.3.2. The unit cell for the 2nd-nearest neighbors is shown in Fig. 2.3.3. The normal vectors for the 2nd-nearest neighbors are given in Table 2.3.2.

Table 2.3.2. The Normal Vectors for the 2nd-Nearest Neighbors

n_7	n_8	n_9	n_{10}	n_{11}	n_{12}
$\left(\sqrt{3}/2,1/2\right)$	$(0,1)$	$\left(-\sqrt{3}/2,1/2\right)$	$\left(-\sqrt{3}/2,-1/2\right)$	$(0,-1)$	$\left(\sqrt{3}/2,-1/2\right)$

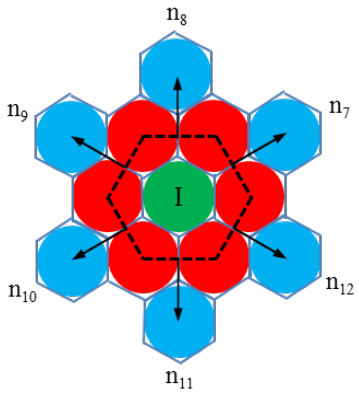

Figure 2.3.3. The Unit Cell for the 2nd-Nearest Neighbors

The total energy of the unit cell for the 2nd-nearest neighbors has the same form as the 1st-nearest neighbors as

$$U_{cell1}^{(2)} = U_{s1}^{(2)} + U_{v1}^{(2)} = \frac{1}{2}\sum_{J=1}^{6} k^{(2)} \left(\delta l_{IJ}\right)^2 + \frac{1}{2} T^{(2)} \left(\sum_{J=1}^{6} \delta l_{IJ}\right)^2 \tag{2.3.12}$$

$$U_{cell2}^{(2)} = U_{s2}^{(2)} + U_{v2}^{(2)} = \frac{1}{2}\sum_{J=7}^{12} k^{(2)} \left(\delta l_{IJ}\right)^2 + \frac{1}{2} T^{(2)} \left(\sum_{J=7}^{12} \delta l_{IJ}\right)^2 \tag{2.3.13}$$

where $k^{(2)}$ and $T^{(2)}$ are the model parameters. It's assumed that the stiffness parameters are the same for all springs and the volumetric parameters are the same for both unit cells.

The energies in Eqs. (2.3.12)-(2.3.13) can be rewritten in terms of the strain tensor as

$$U_{cell1}^{(2)} = \frac{1}{2} k^{(2)} R_1^2 \sum_{b=1}^{6} n_i^b n_j^b n_k^b n_l^b \varepsilon_{ij} \varepsilon_{kl} + \frac{1}{2} T^{(2)} R_1^2 \left(\sum_{b=1}^{6} n_i^b n_j^b \varepsilon_{ij}\right)\left(\sum_{b=1}^{6} n_k^b n_l^b \varepsilon_{kl}\right) \tag{2.3.14}$$

$$U_{cell2}^{(2)} = \frac{1}{2} k^{(2)} R_2^2 \sum_{b=7}^{12} n_i^b n_j^b n_k^b n_l^b \varepsilon_{ij} \varepsilon_{kl} + \frac{1}{2} T^{(2)} R_2^2 \left(\sum_{b=7}^{12} n_i^b n_j^b \varepsilon_{ij}\right)\left(\sum_{b=7}^{12} n_k^b n_l^b \varepsilon_{kl}\right) \tag{2.3.15}$$

Eq. (2.3.14) is exactly the same as Eq. (2.3.4), except the model parameters are different. These two energies in Eqs. (2.3.14)-(2.3.15) can be obtained given the normal vectors shown in Tables 2.3.1 and 2.3.2.

Assuming the energy densities are the same for both unit cells, the stiffness matrix for the 2-neighbor case has following form as

$$C_{ijkl} = C_{ijkl}^{(1)} + \frac{V_2}{V_1} C_{ijkl}^{(2)} = \frac{1}{V_1} \frac{\partial^2 U_{cell}^{(1)}}{\partial \varepsilon_{ij} \partial \varepsilon_{kl}} + \frac{V_2}{V_1}\left(\frac{1}{V_2} \frac{\partial^2 U_{cell}^{(2)}}{\partial \varepsilon_{ij} \partial \varepsilon_{kl}}\right) = \frac{1}{V_1}\left(\frac{\partial^2 U_{cell}^{(1)}}{\partial \varepsilon_{ij} \partial \varepsilon_{kl}} + \frac{\partial^2 U_{cell}^{(2)}}{\partial \varepsilon_{ij} \partial \varepsilon_{kl}}\right) \tag{2.3.16}$$

where $C_{ijkl}^{(1)}$ is the tangent stiffness matrix for unit cell 1 and $C_{ijkl}^{(2)}$ is for unit cell 2, V_2 is the volume of the second unit cell and $V_2 = \frac{1}{2} \cdot \frac{2\sqrt{3}}{3} R_2 \cdot R_2 \cdot 6 \cdot h = 2\sqrt{3} h R_2^2$.

Thus, the model parameters in this 2-neighbor case can be uniquely determined as

Plane strain case:

$$\begin{aligned} k^{(2)} &= \frac{hE}{\sqrt{3}(1+\nu)} \\ T^{(2)} &= \frac{\sqrt{3}}{9} \frac{hE(4\nu - 1)}{4(1+\nu)(1-2\nu)} \end{aligned} \tag{2.3.17}$$

Plane stress case:

$$k^{(2)} = \frac{hE}{\sqrt{3}(1+\nu)}$$
$$T^{(2)} = \frac{\sqrt{3}}{9}\frac{hE(3\nu-1)}{4(1+\nu)(1-\nu)} \qquad (2.3.18)$$

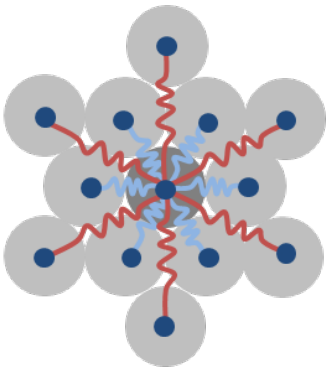

Figure 2.3.4. The Interaction between Particle and Its 1st and 2nd Neighbors

3rd-nearest-neighbor packing

The case of 3rd-nearest neighbors packing is briefly discussed in this subsection. The derivation procedure follows the case of 2nd-nearest neighbors. Each neighbor has a unique unit cell and thus three unit cells are identified from the discretization. The unit cells for the 1st-nearest neighbors and the 2nd-nearest neighbors are the same as the 2-neighbor case. The unit cell for the 3rd-nearest neighbors is shown in Fig. 2.3.5. The normal vectors for this unit cell are the same as that of the 1st-nearest neighbors, as shown in Table 2.3.1.

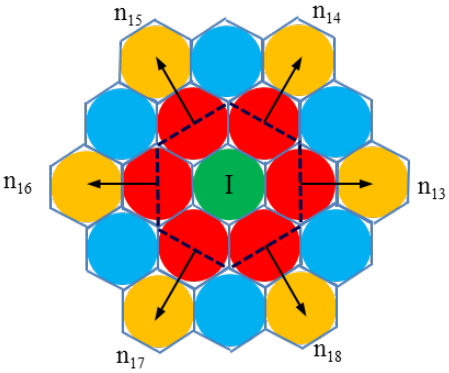

Figure 2.3.5. The Unit Cell for the 3rd-Nearest Neighbors

Under the same assumption, the tangent stiffness matrix has following form

$$C_{ijkl} = C_{ijkl}^{(1)} + \frac{V_2}{V_1} C_{ijkl}^{(2)} + \frac{V_3}{V_1} C_{ijkl}^{(3)} = \frac{1}{V_1}\left(\frac{\partial^2 U_{cell}^{(1)}}{\partial \varepsilon_{ij} \partial \varepsilon_{kl}} + \frac{\partial^2 U_{cell}^{(2)}}{\partial \varepsilon_{ij} \partial \varepsilon_{kl}} + \frac{\partial^2 U_{cell}^{(3)}}{\partial \varepsilon_{ij} \partial \varepsilon_{kl}} \right) \tag{2.3.19}$$

where $C_{ijkl}^{(1)}$ is the tangent stiffness matrix for unit cell 1, $C_{ijkl}^{(2)}$ is for unit cell 2 and $C_{ijkl}^{(3)}$ is for unit cell 3, V_3 is the volume of the second unit cell and $V_3 = \frac{1}{2} \cdot \frac{2\sqrt{3}}{3} R_3 \cdot R_3 \cdot 6 \cdot h = 2\sqrt{3} h R_3^2$. R_3 is the radius of the inscribed circle of unit cell 3.

The model parameters can be uniquely solved as

Plane strain case:

$$\begin{aligned} k^{(3)} &= \frac{4hE}{8\sqrt{3}(1+\nu)} \\ T^{(3)} &= \frac{\sqrt{3}}{9} \frac{hE(4\nu-1)}{8(1+\nu)(1-2\nu)} \end{aligned} \tag{2.3.20}$$

Plane stress case:

$$\begin{aligned} k^{(3)} &= \frac{4hE}{8\sqrt{3}(1+\nu)} \\ T^{(3)} &= \frac{\sqrt{3}}{9} \frac{hE(3\nu-1)}{8(1+\nu)(1-\nu)} \end{aligned} \tag{2.3.21}$$

4th-nearest-neighbor packing

The case of 4-neighbor is considered in this subsection. The unit cells for the 4th-nearest neighbors are shown in Fig. 2.3.6. The normal vectors for the 4th-nearest neighbors are given in Table 2.3.3. It should be noted that there are twelve 4th-nearest neighbors and two unit cells are identified, each assigned with six neighbors.

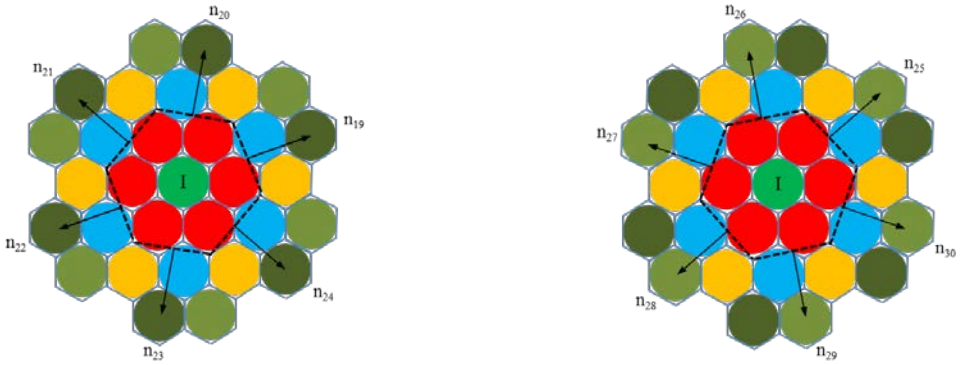

Figure 2.3.6. The Unit Cells for 4th-Nearest Neighbors

Table 2.3.3. The Normal Vectors for the 4th-Nearest Neighbor Packing

(a)

n_{19} $\left(5/2\sqrt{7},\sqrt{3}/2\sqrt{7}\right)$	n_{20} $\left(1/2\sqrt{7},3\sqrt{3}/2\sqrt{7}\right)$	n_{21} $\left(-4/2\sqrt{7},2\sqrt{3}/2\sqrt{7}\right)$
n_{22} $\left(-5/2\sqrt{7},-\sqrt{3}/2\sqrt{7}\right)$	n_{23} $\left(-1/2\sqrt{7},-3\sqrt{3}/2\sqrt{7}\right)$	n_{24} $\left(4/2\sqrt{7},-2\sqrt{3}/2\sqrt{7}\right)$

(b)

n_{25} $\left(4/2\sqrt{7},2\sqrt{3}/2\sqrt{7}\right)$	n_{26} $\left(-1/2\sqrt{7},3\sqrt{3}/2\sqrt{7}\right)$	n_{27} $\left(-5/2\sqrt{7},\sqrt{3}/2\sqrt{7}\right)$
n_{28} $\left(-4/2\sqrt{7},-2\sqrt{3}/2\sqrt{7}\right)$	n_{29} $\left(1/2\sqrt{7},-3\sqrt{3}/2\sqrt{7}\right)$	n_{30} $\left(5/2\sqrt{7},-\sqrt{3}/2\sqrt{7}\right)$

The tangent stiffness matrix has the following form as

$$C_{ijkl}=C_{ijkl}^{(1)}+\frac{V_2}{V_1}C_{ijkl}^{(2)}+\frac{V_3}{V_1}C_{ijkl}^{(3)}+2\frac{V_4}{V_1}C_{ijkl}^{(4)}=\frac{1}{V_1}\left(\frac{\partial^2U_{cell}^{(1)}}{\partial\varepsilon_{ij}\partial\varepsilon_{kl}}+\frac{\partial^2U_{cell}^{(2)}}{\partial\varepsilon_{ij}\partial\varepsilon_{kl}}+\frac{\partial^2U_{cell}^{(3)}}{\partial\varepsilon_{ij}\partial\varepsilon_{kl}}+2\frac{\partial^2U_{cell}^{(4)}}{\partial\varepsilon_{ij}\partial\varepsilon_{kl}}\right) \quad (2.3.22)$$

where $C_{ijkl}^{(1)}$ is the tangent stiffness matrix for unit cell 1, $C_{ijkl}^{(2)}$ is for unit cell 2, $C_{ijkl}^{(3)}$ is for unit cell 3 and $C_{ijkl}^{(4)}$ is for unit cell 4, V_4 is the volume of the second unit cell and $V_4=\frac{1}{2}\cdot\frac{2\sqrt{3}}{3}R_4\cdot R_4\cdot 6\cdot h=2\sqrt{3}hR_4^2$. R_4 is the radius of the inscribed circle of unit cell 4.

Comparing the components of the tangent stiffness matrix with the one obtained using solid mechanics, the model parameters can be uniquely obtained as

Plane strain case:

$$k^{(4)} = \frac{4hE}{22\sqrt{3}(1+\nu)}$$
$$T^{(4)} = \frac{\sqrt{3}}{9}\frac{hE(4\nu-1)}{22(1+\nu)(1-2\nu)} \tag{2.3.23}$$

Plane stress case:

$$k^{(4)} = \frac{4hE}{22\sqrt{3}(1+\nu)}$$
$$T^{(4)} = \frac{\sqrt{3}}{9}\frac{hE(3\nu-1)}{22(1+\nu)(1-\nu)} \tag{2.3.24}$$

Nth-nearest-neighbor packing

For the case of a particle has *N*-neighbor, a generalized formula for the model parameters within the lattice particle model framework can be obtained. Under the assumption that all springs have the same stiffness and all unit cells have the same volumetric parameter, the expressions for the model parameters can be uniquely determined given the neighbor number *N*.

Plane strain case:

$$k^{(N)} = \frac{4hE}{\sqrt{3}H(1+\nu)}$$
$$T^{(N)} = \frac{\sqrt{3}}{9}\frac{hE(4\nu-1)}{H(1+\nu)(1-2\nu)} \tag{2.3.25}$$

Plane stress case:

$$k^{(N)} = \frac{4hE}{\sqrt{3}H(1+\nu)}$$
$$T^{(N)} = \frac{\sqrt{3}}{9}\frac{hE(3\nu-1)}{H(1+\nu)(1-\nu)} \tag{2.3.26}$$

where the coefficient H is defined as

$$H = \frac{\sum_{i=1}^{N} V_i}{V_1} \tag{2.3.27}$$

For the cases considered in previous sections, this coefficient has following values as

$$H = \begin{cases} \dfrac{V_1}{V_1} = 1 & , N = 1 \\ \dfrac{V_1 + V_2}{V_1} = 4 & , N = 2 \\ \dfrac{V_1 + V_2 + V_3}{V_1} = 8 & , N = 3 \\ \dfrac{V_1 + V_2 + V_3 + V_4 + V_4}{V_1} = 22 & , N = 4 \end{cases} \tag{2.3.28}$$

Note that in the above Eq. (2.3.28), for the case of 4-neighbor, i.e., $N = 4$, there are two unit cells identified and thus two V_4 s is used. Using the radii of the inscribed circle of the unit cells, the coefficient H can be rewritten as

$$H = \frac{\sum_{i=1}^{N} R_i^2}{R_1^2} \tag{2.3.29}$$

where R_1 is the radius of the inscribed circle of the unit cell for the 1st-nearest neighbors, i.e., $R_1 = R$, R_i is of the i^{th}-nearest neighbors.

Eqs. (2.3.25)-(2.3.29) is the analytical solution for the model parameters of the generalized framework. The interaction forces between particles can be calculated using Eq.(2.3.11) for different interacting neighbors. Several numerical integration algorithms, such as Velocity Verlet and Central Difference integration schemes, can be used to solve the dynamic response of the particle system. More details can be found in [38].

Failure criterion and crack propagating rule

The critical force criterion [45], [46] derived based on the critical stress from a uniaxial tension experiment is used to simulate the crack initiation and propagation in this study. Other failure criterion can be used, such as the critical elongation [47], the cohesive energy [14]. First, the

derivation of the critical force for the 1st-nearest neighbors is presented. After that, the critical force criterion is generalized to the case of N-neighbor.

For the 1st-nearest neighbors, the length of the six edges of the unit cell is $L_1 = \frac{2}{\sqrt{3}} R_1$, as can be seen in Fig. 2.3.2. Thus, the equivalent stress in any of the six bonds can be calculated as

$$\sigma_{IJ} = \frac{F_{IJ}^{(1)}}{hL_1} \tag{2.3.30}$$

where $F_{IJ}^{(1)}$ is the forces of the six connecting bonds given in Eq. (2.3.11).

The critical force of a connecting bond can be obtained given the critical stress from a uniaxial tensile test as, for plane strain case,

$$F_{critical}^{(1)} = hL_1\sigma_{critical} = \frac{2}{\sqrt{3}} hR_1\sigma_{critical} \tag{2.3.31}$$

For the entire bond, the critical force is twice of the value calculated in Eq. (2.3.31). For plane stress case, the same criterion is applied. The bond breaking criterion for *N*-neighbor case can be generalized as

$$F_{critical}^{(N)} = \frac{2}{H\sqrt{3}} hR_N\sigma_{critical} \tag{2.3.32}$$

where H is the coefficient defined in Eq. (2.3.27), R_N is the radius for the inscribed circle of the N^{th} unit cell.

The crack propagation process is simulated in the proposed framework as follows: at each simulation time step, the force of the bonds are calculated and compared with the corresponding critical value. If the calculated force is larger than the critical value, then the bond is considered as broken and it cannot sustain any tensile forces in the following simulation steps. This process continues until the simulation ends.

2.3.3. Simulation results

Several benchmark problems, i.e., quasi-static mode I cracking, dynamic mode II cracking and the dynamic crack branching, are used to check the fracture anisotropy of the lattice spring model and to assess the performance of the proposed methodology. The fracture anisotropy is tested by rotating the lattice structure to different angles, but maintaining the same geometry and loading conditions. The definition of the rotation of the lattice structure is shown in Fig. 2.3.7. Considering the six-fold symmetry of a unit cell, four rotations are investigated, i.e., 0, *Pi*/12, *Pi*/6, *Pi*/4.

For a fixed lattice rotation, the same discretization is applied to all 4 packing. The particle densities for different lattice rotations are kept almost identical for each benchmark. The pre-existing notches/cracks are inserted by removing the particles.

All the simulation in this section is based on the dynamic formulation, i.e., the Newton's second law of motion. The critical time step can be determined using the Courant-Friedrichs-Lewy condition. For simplicity and best stability, a time step of 1.0e-9 s is used in all the simulations. The total numbers of time steps are given in each example. The computational efficiency is studied in the case of dynamic branching.

All simulations were done on a dual 2.8 GHz Intel Xeon E5-2680 v2 CPUs system using Ubuntu operating system. Double-precision floating-point number type is specified for all real data.

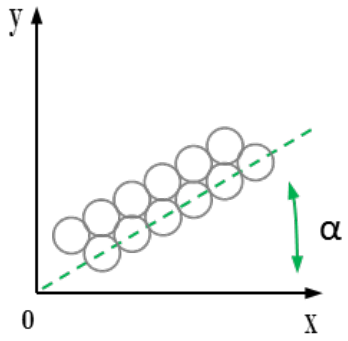

Figure 2.3.7. Lattice Rotation Scheme in Lattice Particle Model

Quasi-static Mode-I cracking

The single-edge-notched specimen, whose dimensions and loading conditions are shown in Fig. 2.3.8, is used in this example. A plane stress condition is assumed. The material properties are: Young's modulus E = *69 GPa*, Poisson's ratio ν = *0.3*, the mass density ρ = *2700 Kg/m*^{3}, and the tensile strength is assumed to be $\sigma_{critical}$ = *200 MPa*.

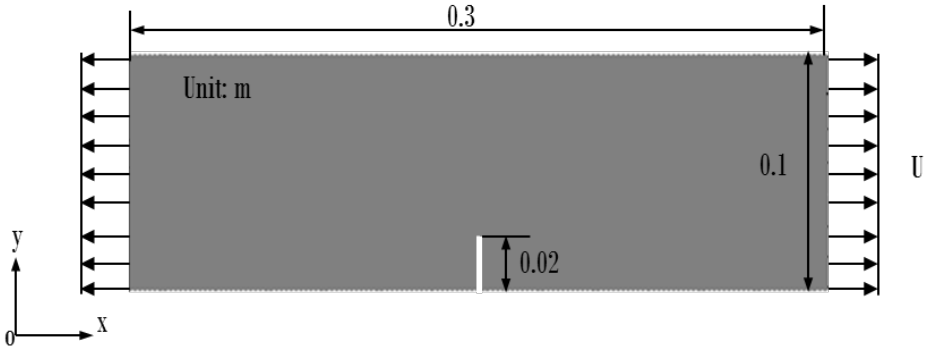

Figure 2.3.8. The Configuration of the SEN Specimen

In order to simulate a quasi-static loading condition, the left and right edges of the specimen are applied with a very small constant kinetic boundary condition. From Linear Elastic Fracture Mechanics (LEFM), the crack will propagates in its original crack plane (i.e., pure mode I) until the specimen fracture occurs. The total number of particles used for the domain decomposition for all rotations is about 70,000. The total number of simulation steps for this example is 600,000.

1st-nearest-neighbor packing

The plots of the crack path results for the 1-neighbor packing at different lattice orientations are shown in Fig. 2.3.9. As can be seen from Fig. 2.3.9(a), when the lattice orientation coincident with the crack path, the directional preference is not obvious thus the simulated crack propagation path is the same as analytical solution. When the lattice is rotated to different orientations, i.e., *Pi/12*, *Pi/6*, and *Pi/4*, the directional preference of the crack path is apparent, as can be seen in Fig. 2.3.9(b)-(d). This fracture anisotropy can also been seen from the load-displacement curve shown in Fig. 2.3.10. The peak loads varies with different rotation angles.

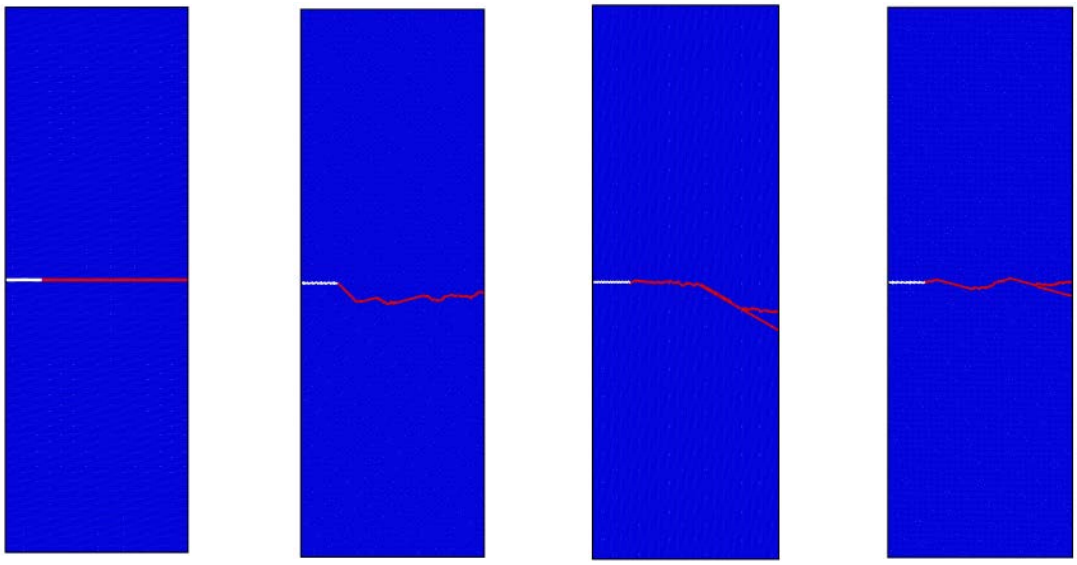

(a) α = 0 **(b)** α = Pi/12 **(c)** α = Pi/6 **(d)** α = Pi/4

Figure 2.3.9. The Crack Paths for Packing 1, Static Mode I

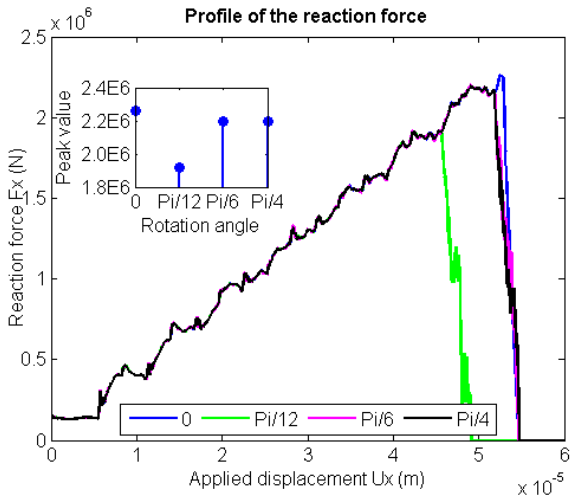

Figure 2.3.10. The Force-Displacement Curve for the Packing 1, Static Mode I

2nd-nearest-neighbor packing

The crack paths for this case are shown in Fig. 2.3.11. The load-displacement curves are shown in Fig. 2.3.12. As can be seen from the crack path results, the directional preference is significantly improved as both the crack paths are very close to the analytical solution and the difference between the peak loads is very small.

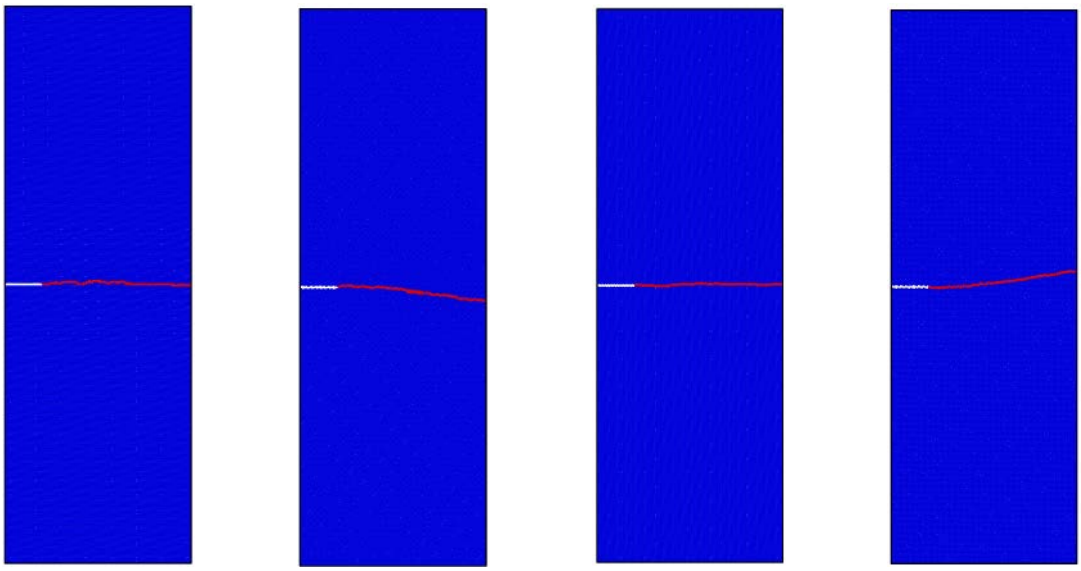

(a) α = 0 **(b)** α = Pi/12 **(c)** α = Pi/6 **(d)** α = Pi/4

Figure 2.3.11. The Crack Paths for Packing 2, Static Mode I

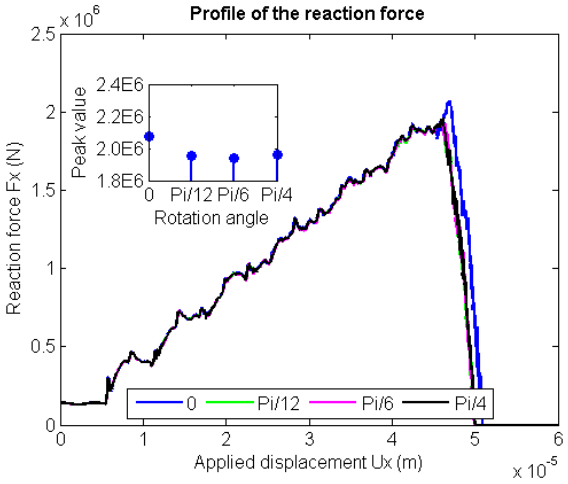

Figure 2.3.12. The Force-Displacement Curve for Packing 2, Static Mode I

3rd-nearest-neighbor packing

The crack paths for this case are shown in Fig. 2.3.13. And the load-displacement curves are shown in Fig. 2.3.14. The crack path preference is further reduced compared to the paths of 2 neighbor cases. The crack path for the cases of rotation *0*, *Pi/6*, and *Pi/4* is the same as the analytical solution. The variance of the peak loads becomes smaller.

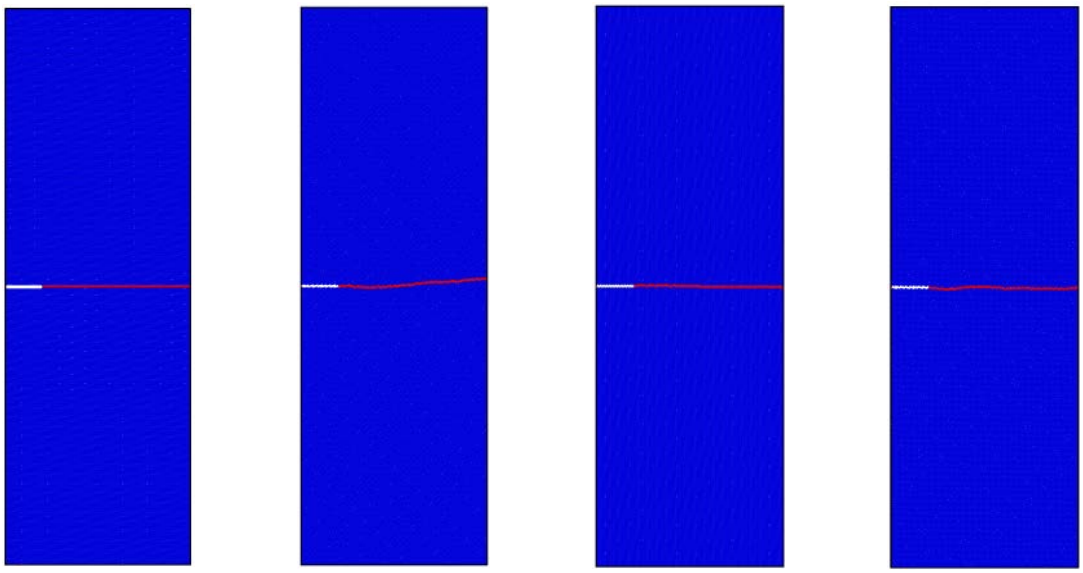

(a) α = 0 **(b)** α = Pi/12 **(c)** α = Pi/6 **(d)** α = Pi/4

Figure 2.3.13. The Crack Paths for Packing 3, Static Mode I

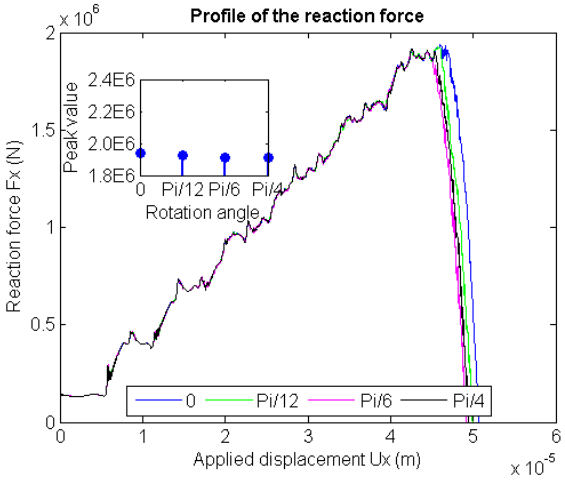

Figure 2.3.14. The Force-Displacement Curve for Packing 3, Static Mode I

4th-nearest-neighbor packing

The crack paths for this case are shown in Fig. 2.3.15. And the load-displacement curves are shown in Fig. 2.3.16. The crack paths for all lattice orientation rotations are identical to the analytical solution. And the peak load variance is the smallest among all four cases.

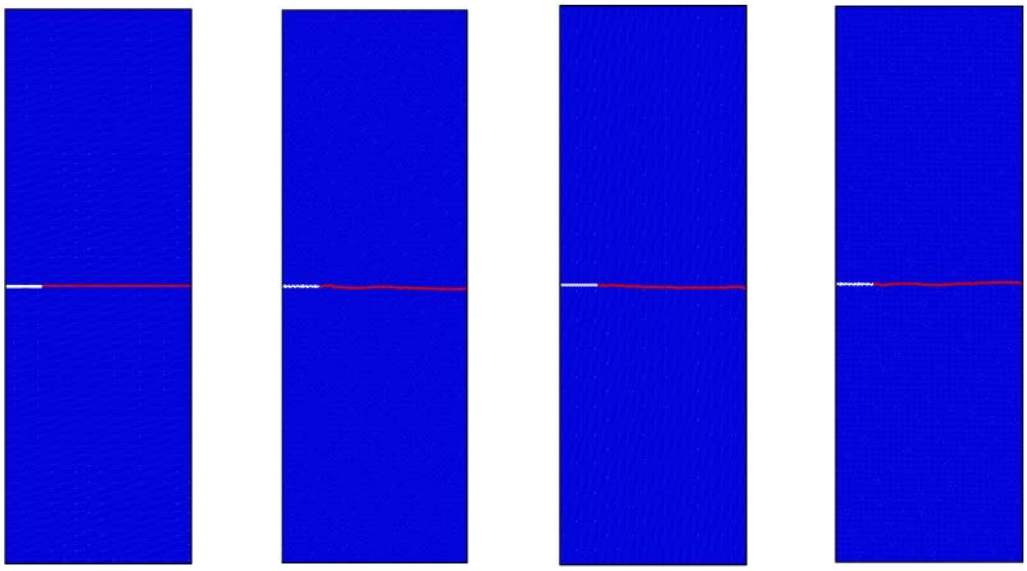

(a) α = 0 **(b)** α = Pi/12 **(c)** α = Pi/6 **(d)** α = Pi/4

Figure 2.3.15. The Crack Paths for Packing 4, Static Mode I

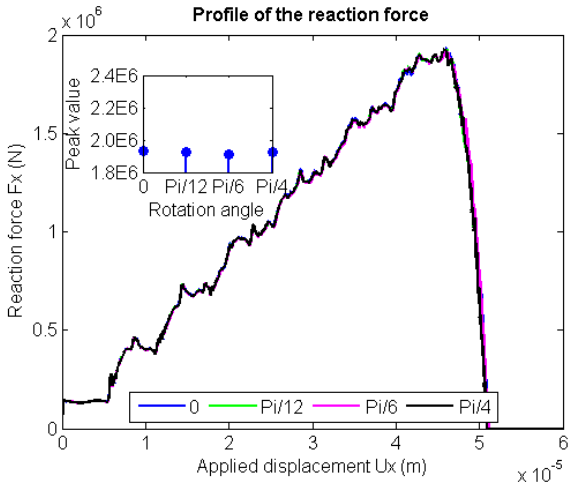

Figure 2.3.16. The Force-Displacement Curve for Packing 4, Static Mode I

From the simulation results in this subsection, it is observed that the directional preference of the crack propagation path can be weakened or eliminated by introducing more neighbors. For quasi-static mode-I fracture problem, the crack path preference can be eliminated by employing the 4^{th}-nearest or more neighbors. In next subsections, the proposed framework is applied to model dynamic fracturing problems.

Dynamic mode-II cracking

In this subsection, a modified Kalthoff's experiment [43] which has been extensively studied using the XFEM [48], [49], [50] is modelled to test the validity of the proposed framework. In the experiment, a plate with two edge notches, shown in Fig. 2.3.17, is impacted by a projectile with different strain rates. Two typical fracture patterns were observed from the experiments. At higher strain rates, a negative angle of about -10^o due to the shear localization mode was observed. On the other hand, at lower strain rates, a brittle fracture mode with a propagation angle of about 70^o was observed. In this study, we focus on the brittle fracture. Plane strain condition is assumed.

The configuration of the plate is shown in Fig. 2.3.17. To simplify the simulation, a constant velocity which is chosen as v_0 = 10 *m/s* is applied on the left cracked edge. The material properties are: Young's modulus E = *190 GPa*, Poisson's ratio ν = *0.3*, mass density ρ = *8000 kg/m^3*, and the material strength is assumed to be $\sigma_{critical}$ = *2.02 GPa*. The experimental result for the top half plate is shown in Fig. 2.3.18. It should be noted that due to the regularity of the lattice structure, the discretized domain may not reproduce the two-fold symmetry of the testing specimen exactly. The total number of particles used for the domain decomposition for all rotations is about 90,000. The total number of simulation steps for this example is 90,000.

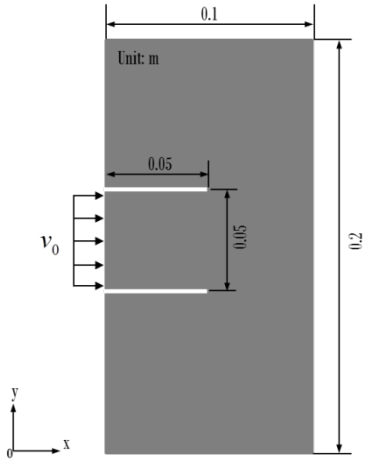

Figure 2.3.17. Configuration for the Dynamic Shear Cracking Test

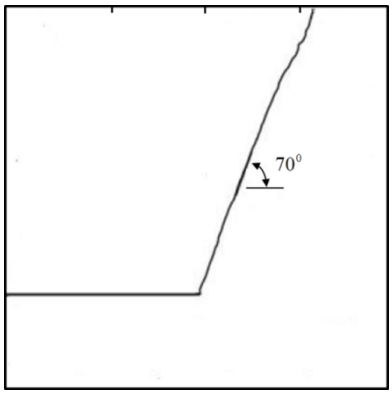

Figure 2.3.18. Experimental Observation (Top Half Plate for Dynamic Mode II)

1st-nearest-neighbor packing

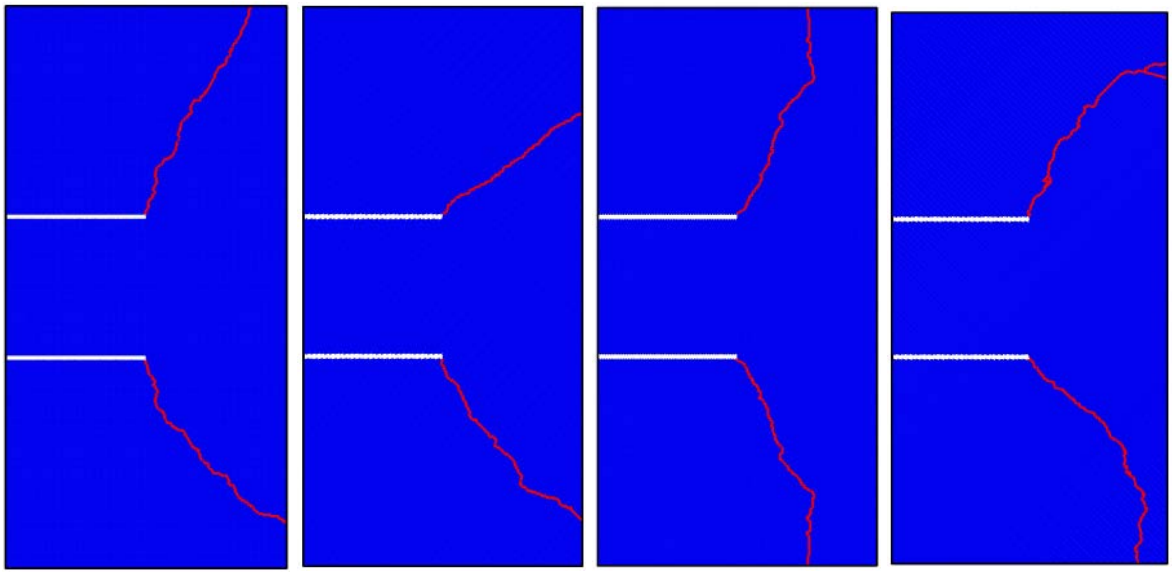

(a) α = 0 **(b)** α = Pi/12 **(c)** α = Pi/6 **(d)** α = Pi/4

Figure 2.3.19. The Crack Paths for Packing 1, Dynamic Mode II

The simulation results for the 1-neighbor case are shown in Fig. 2.3.19. As can be seen, the results for different rotations are very different, which indicates the fracture anisotropy in the 1st-nearest-neighbor packing is very crucial to the propagation path.

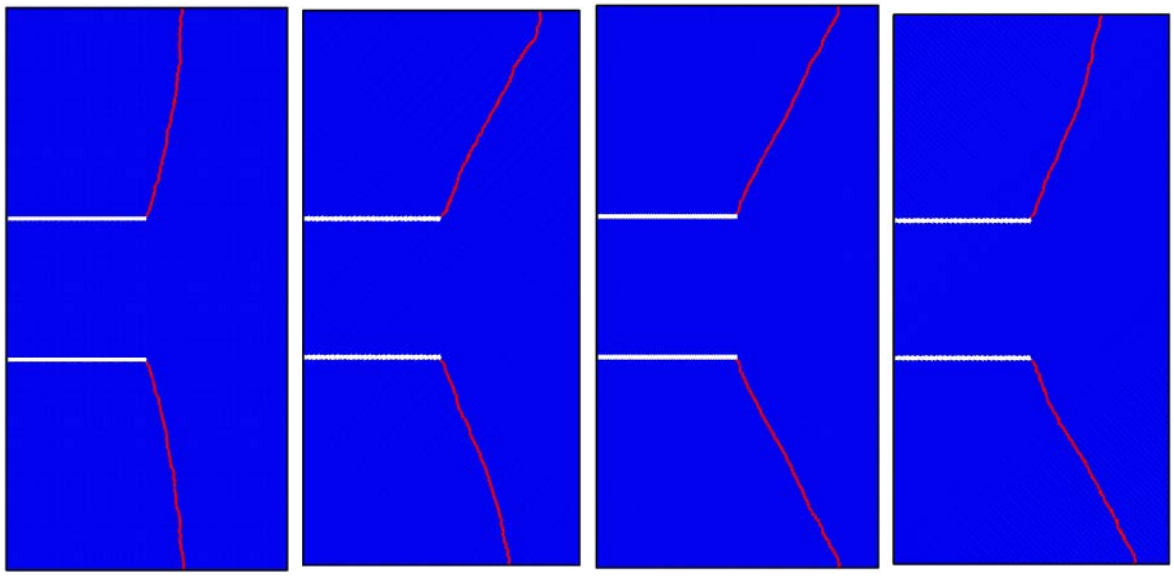

(a) α = 0 **(b)** α = Pi/12 **(c)** α = Pi/6 **(d)** α = Pi/4

Figure 2.3.20. The Crack Paths for Packing 2, Dynamic Mode II

2nd-nearest-neighbor packing

The simulated crack paths for the 2-neighbor case are shown in Fig. 2.3.20. Compared with the results of the 1-neighbor case, the crack paths are greatly improved. The crack angles, except $\alpha = 0$, are very close to the experiment results.

3rd-nearest-neighbor packing

The simulated crack paths for the 3-neighbor case are shown in Fig. 2.3.21. The results for different rotations are more consistent than the 2-neighbor case.

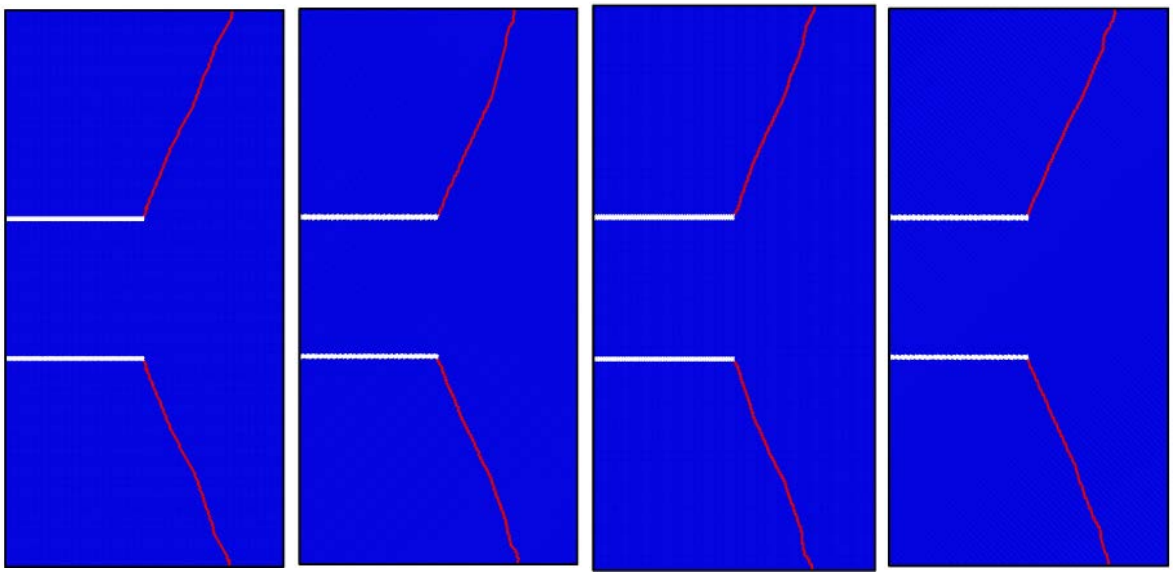

(a) $\alpha = 0$ **(b)** α = Pi/12 **(c)** α = Pi/6 **(d)** α = Pi/4

Figure 2.3.21. The Crack Paths for Packing 3, Dynamic Mode II

4th-nearest-neighbor packing

The simulation results for the 4-neighbor case are shown in Fig. 2.3.22. As can be seen, the crack paths for different rotations are approximately identical and very close to 70^{o}, which indicates the fracture anisotropy is almost eliminated.

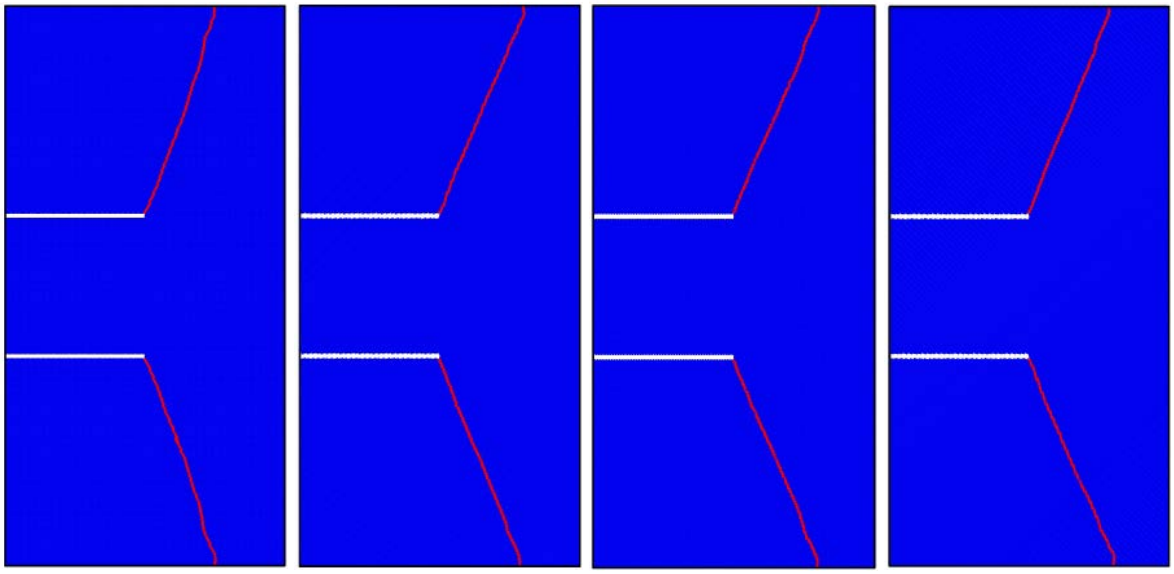

(a) α = 0 **(b)** α = Pi/12 **(c)** α = Pi/6 **(d)** α = Pi/4

Figure 2.3.22. The Crack Paths for Packing 4, Dynamic Mode II

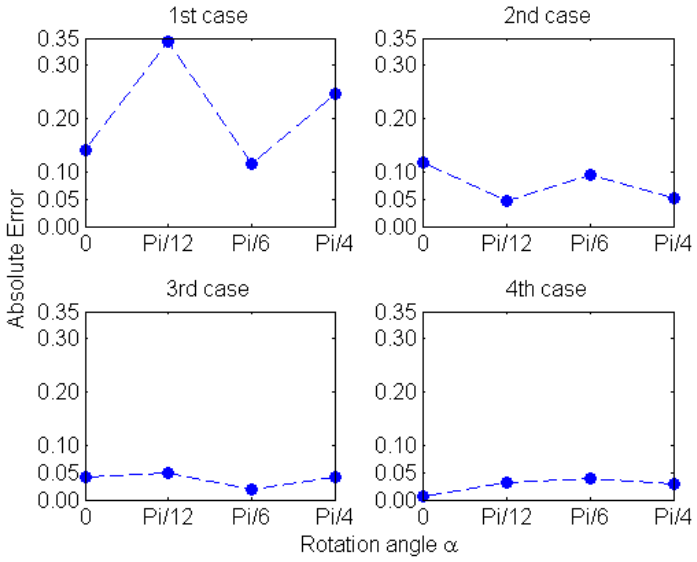

Figure 2.3.23. Comparison of the Crack Angle vs. Rotation Angle

A quantitative study on the average crack angles of different packing under different rotations are shown in Fig. 2.3.23. The case of 4-neighbor provides the best simulation results compared to the experiment observations.

This example shows the capability of the proposed framework for modeling of dynamic pure mode-II fracture problems. In next section, the proposed framework is used to model a dynamic crack branching problem.

Dynamic crack branching

The dynamic crack branching of brittle materials has been investigated extensively in the past. In this example, a pre-notched rectangular specimen, shown in Fig. 2.3.24, is simulated using the proposed framework. Similar experiments have been done by many researchers, such as [44]. A typical experiment result for the branching path is shown in Fig. 2.3.25. The analytical predicted branching angle is 27^o [51].

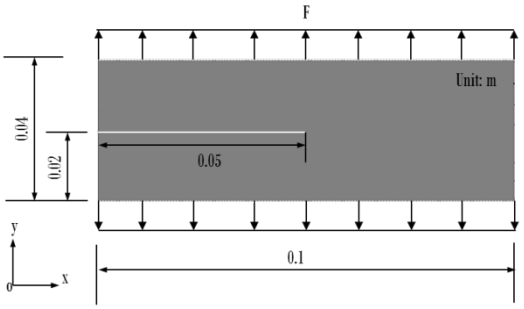

Figure 2.3.24. The Configuration of the Pre-notched Plate

Figure 2.3.25. Experimental Observation (Dynamic Branching)

The configuration of the plate is shown in Fig. 2.3.24. Tensile forces of value F = *10^5 Newton* are applied on both the top and the bottom edges. A plane stress condition is assumed. The materials properties are: Young's modulus E = *32 GPa*, Poisson's ratio ν = *0.2*, mass density ρ = *2450 kg/m^3*, and the material strength is assumed to be $\sigma_{critical}$ = 1*2 MPa*. The total number of particles used for the domain decomposition for all rotations is about 80,000. The total number of simulation steps for this example is 60,000.

The simulated crack paths are shown in Figs. 2.3.26-29 for different packing. For the 1-neighbor case, the lattice particle model cannot simulate the crack branching phenomenon. With the introduction of more neighbors, the fracture anisotropy is reduced or eliminated and the crack branching can be accurately captured. The branching angles for the cases of 3-neighbor and 4-

neighbor are shown in Fig. 2.3.30. The variance of the branching angle for the case of 4-neighbor is very small and is close to the experimental observations. The comparison of computation efficiency for different packing cases is shown in Fig. 2.3.31. For cases in which more neighbors are included, the computational time will be further increased. For dynamic simulation based on solution of the Equation of Motion, the relationship for the computation time and the number of neighbors is linear.

1st-nearest-neighbor packing

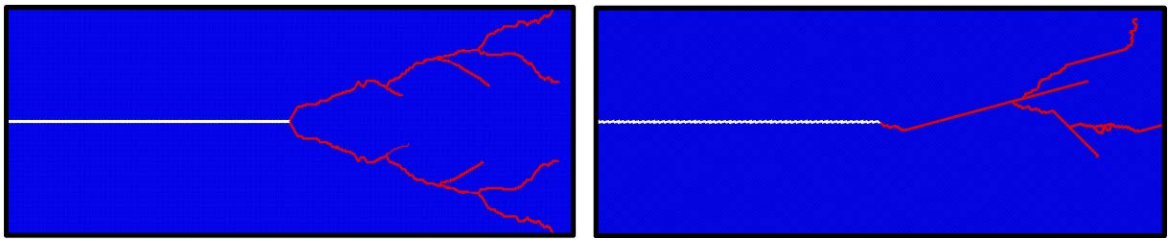

(a) α = 0 **(b)** α = Pi/12

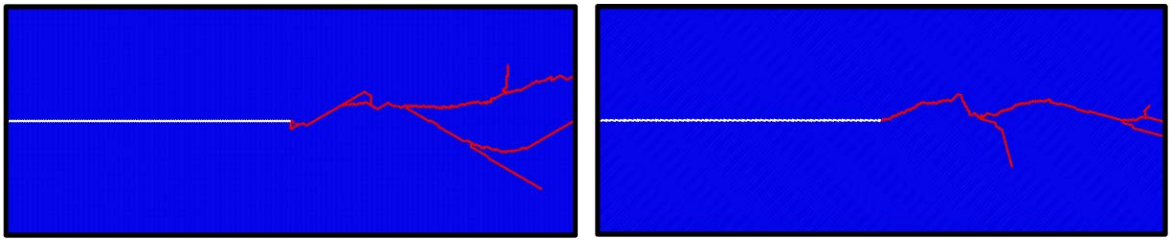

(c) α = Pi/6 **(d)** α = Pi/4

Figure 2.3.26. The Crack Paths for Packing 1, Dynamic Branching

2nd-nearest-neighbor packing

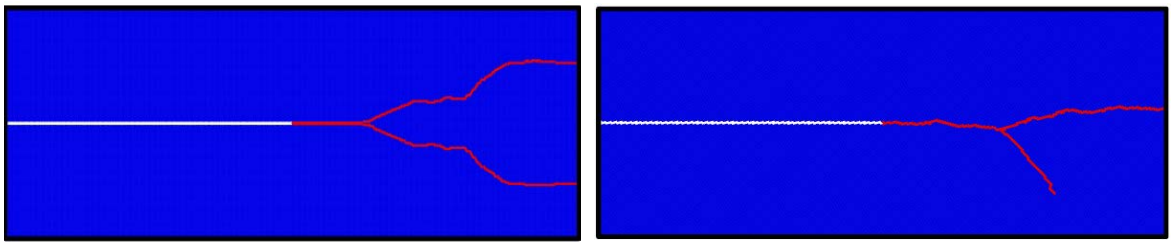

(a) α = 0 **(b)** α = Pi/12

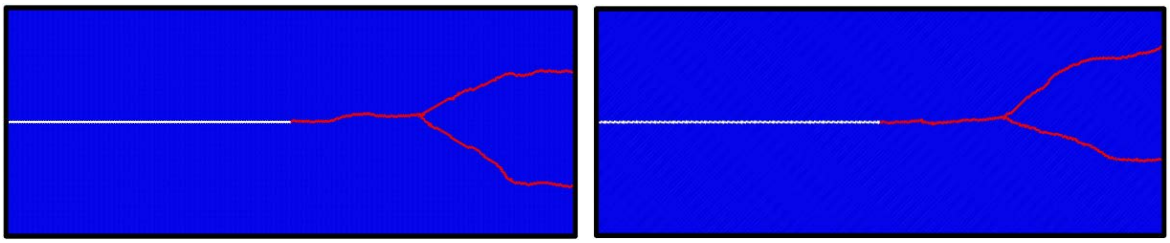

(c) α = Pi/6 **(d)** α = Pi/4

Figure 2.3.27. The Crack Paths for Packing 2, Dynamic Branching

3rd-nearest-neighbor packing

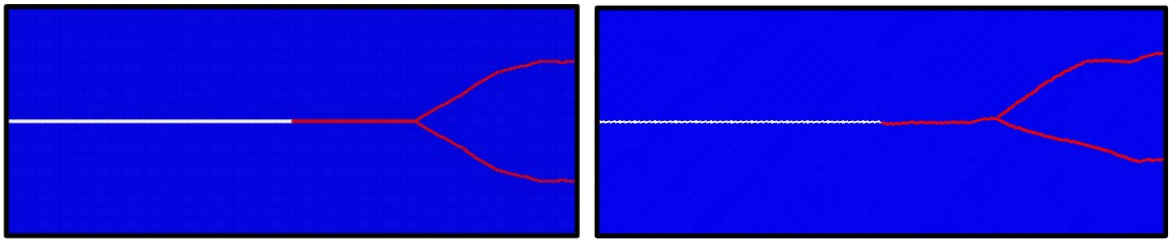

(a) α = 0 **(b)** α = Pi/12

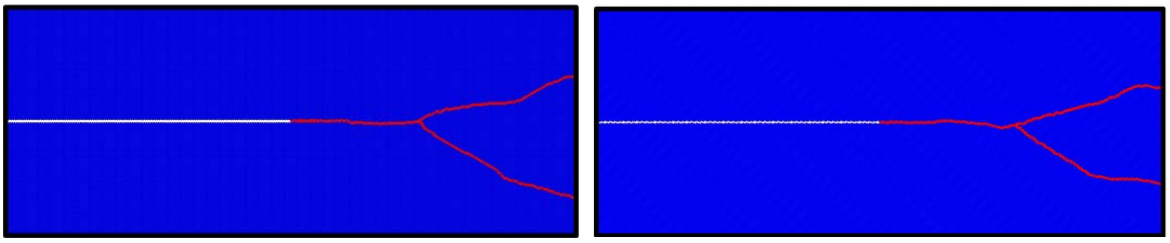

(c) α = Pi/6 **(d)** α = Pi/4

Figure 2.3.28. The Crack Paths for Packing 3, Dynamic Branching

4th-nearest-neighbor packing

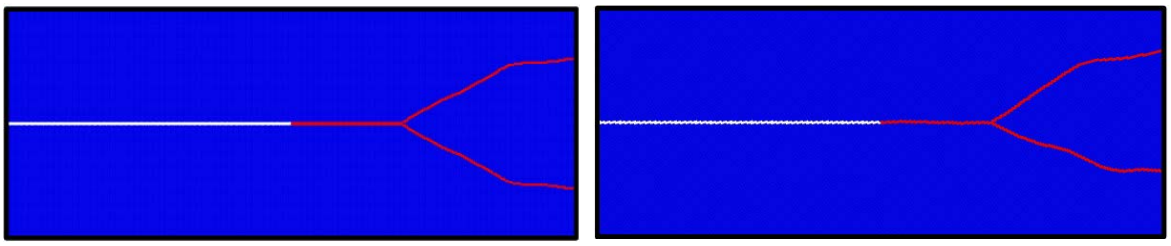

(a) α = 0 **(b)** α = Pi/12

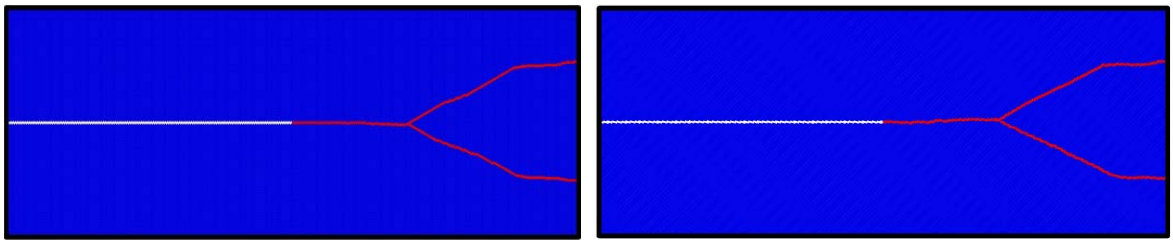

(c) α = Pi/6 **(d)** α = Pi/4

Figure 2.3.29. The Crack Paths for Packing 4, Dynamic Branching

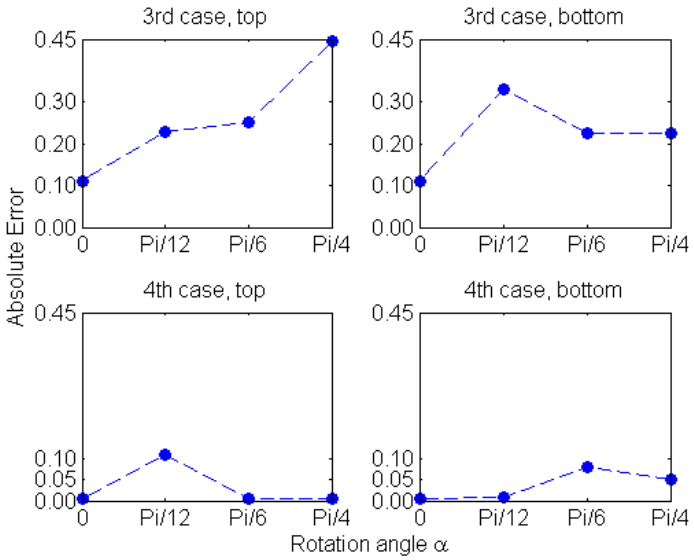

Figure 2.3.30. The Variations of the Branching Angle for Packing 3 and 4

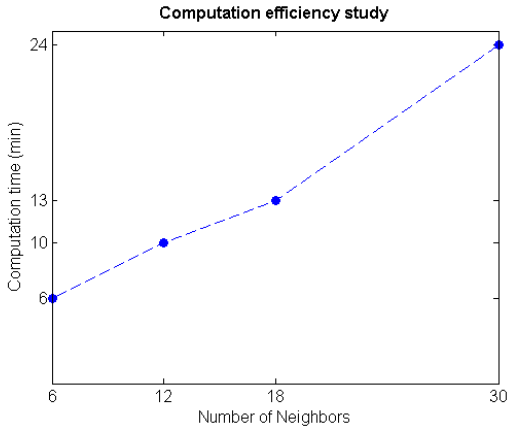

Figure 2.3.31. Computation Efficiency Comparison between Different Packing

2.3.4. Discussion and conclusions

In this section, a generalized regular lattice spring framework for modeling fracture phenomenon of homogeneous isotropic solids was proposed. Analytical solutions for the arbitrary number of neighbors are obtained under the assumption that all springs have the same stiffness and all unit cells have the same volumetric parameters. The performance of the proposed lattice particle model was assessed by modeling several benchmarks, i.e., the quasi-static mode-I fracture, the dynamic mode-II fracture and the dynamic fracturing problems.

From the simulation results, the fracture anisotropy intrinsically exists in the regular lattice models employing only the nearest neighbors. The effect of fracture anisotropy is more severe for dynamic problems than quasi-static problems. This fracture anisotropy can be reduced or eliminated by using random network models or introducing more neighbors to the center particle. There are several differences between these two approaches:

1). In the random network models, since each connecting bond has different properties, certain scaling technique is required to achieve the elastic uniformity. And some other type of interactions, such as shear spring or using beam element, must introduced so as to remove the limitation on the effective Poisson's ratio. In the proposed lattice particle framework, a volumetric energy term is introduced which facilitates the simulation process since only axial or normal spring is used. The non-locality serves as a path to reduce/eliminate the intrinsic fracture anisotropy in regular lattice model while preserving the elastic uniformity and can be generalized into arbitrary neighbor case.

2). The inclusion of more neighbors in lattice particle model is eventually results in a more uniform energy at a comparatively larger area or volume. The boundary effect, or skin effect, still exists in the proposed framework. At the particle level, the introduction of more neighbors will not increase or decrease the boundary effect. While at the global level, since the energy is more uniform at a larger area or volume, the more neighbors are considered, the more severe the boundary effect is. In order to reduce the boundary effect on the simulation results, one possible way is to increase the particle density. The computational cost will also increase. Thus, there should be

some balance between the simulation accuracy and the computational cost while considering including more neighbors in the proposed lattice particle model.

3). The assumptions that all springs have the same stiffness and all unit cells have the same volumetric parameters ensure that the model parameters can be uniquely determined. By these assumptions, there are only two model parameters irrespective of neighbor numbers, which can be uniquely solved using the two independent material constants for an isotropic solid. Some other ways to assign the spring stiffness are possible.

Several major conclusions are drawn based on the current investigation:

1). The inclusion of multiple neighbors for lattice spring model based on regular domain decomposition can reduce/eliminate the crack path preference in fracture simulation;

2). For the investigated cases, the inclusion of 4^{th}-nearest neighbors is shown to be able to maintain the computational variance within in 5% for crack path and failure loads;

3). The computational time increases as the number of neighbors increases, which show a linear relationship in the current investigation from 1^{st} to 4^{th} nearest neighbors;

4). The failure criterion was used in this study is the critical force criterion. No cohesive type behavior was assigned to the springs. The influence of different failure criteria on the fracture anisotropy needs further study.

Future work is required to extend this methodology to general 3D problems. Also, additional work on bond failure criterion, e.g., considering post-peak softening effect, is required to fully investigate its influence on fracture anisotropy of the lattice particle model.

2.4 3D Elasticity and Fracture

The lattice particle model for three-dimensional elasticity and fracture simulation of isotropic solids is presented in this section. First, the basic concept and detailed derivation of the proposed method is given. Various particles packing are investigated using the proposed method and the simulation results are compared with classical finite element method solution. The rotational invariance or frame independence of the formulation is showed both analytically and numerically. The performance of these lattice structures are assessed using several benchmark problems, for both mechanical deformation and fracture problems. From the simulation results, good agreements with both analytical solution and experimental observations are observed. Conclusions and future work are drawn based on this study.

2.4.1. Introduction

Modeling of various fracture phenomena using the classical Finite Element Method (FEM) has been investigated extensively in the past several decades, such as the mesh matching and remeshing [5] and the cohesive elements [6]. By employing the enrichment functions and using the level set method, the eXtended Finite Element Method (XFEM) [7] eliminates the requirement of mesh matching and remeshing significantly. In either approaches, certain external criteria, such as on crack initiation, propagation, branching and coalesce, are needed. These requirements for arbitrary 3D crack tracking become very tedious and difficult.

As alternatives, numerous discrete approaches have been proposed to avoid the intrinsic singularity related difficulties in the continuum-based fracture simulations. Some examples of these discrete approaches are the Lattice Spring Models (LSM) [2], [52], the Smoothed Particle Hydrodynamics (SPH) [53], [54], the Discrete Element Method (DEM) [55], Meshfree Particle Method [56], and the Peridynamics [57]. The discrete-based methods represent the material as an assemblage of independent elements (also called units, particles or grains), which are interacting with each other with different types of interaction potentials. The fracture process in

these types of approaches is the natural “loss of interaction” between “particles”. In this paper, the proposed method belongs to the category of the Lattice Spring Model (LSM).

The idea of using lattice model to simulate solids dates back to Hrennikoff [16]. Successive developments have been made since then, such as [19], [24], [58], [28], [38]. A well-known issue of the LSM is the restriction on the effective Poisson’s ratio if only the pair-wise axial interaction is assumed among particles. In order to overcome this limitation, various models have been proposed by introducing local non-axial interactions, such as the Born model [21], the shear/angular spring model [10], [11], the beam/strut model [59], [22]. Another different methodology to handle this issue is to introduce non-local axial interaction terms into the system potential. Grassl et al. [22] proposed a non-local irregular truss model based on the volumetric strain under the plane strain assumption for brittle materials. Starting from a similar concept, Chen et al. [38] developed a lattice particle model which utilizing a regular lattice structure under both plane stress and plane strain conditions.

In this paper, the developed non-local 2D lattice particle model is extended to the 3D cases and a family of 3D lattice structures is investigated using the proposed formulation. The performance of the proposed 3D framework is assessed by modeling the elastic and fracture response of the homogeneous isotropic solids. The content of this paper is organized as follows. First, a brief review on the non-local lattice particle model formulation is given. Following this, a detailed derivation of the model parameters for three different lattice structures, i.e., the simple cubic, face-centered cubic and body-centered cubic, is presented. Next, a spring-based failure criterion for fracture modeling in the proposed framework is formulated. After that, several benchmarks are employed to assess the performance of the proposed 3D lattice particle model. Discussions and conclusions are drawn based on the current study at the end of this section. Analytical derivations for all three packing to show the rotational invariance of the lattice particle formulation is given in the APPENDIX A.

2.4.2. Lattice particle model for isotropic materials: review

The formulation of lattice particle model is analogue to the classical lattice spring model, which is based on the Cauchy-Born Rule [60] and Theory of Hyper-elasticity. In the lattice particle model, the domain of interest is decomposed into regular unit cells, or particles, which located at the lattice sites and connected via springs. Since regular lattice packing are utilized in the proposed lattice particle model, the Cauchy-Born Rule can be broken down to energy equivalency at the unit cell level. In this section, a review on the formulation of the non-local lattice particle model is briefly presented.

Assuming there are generally *n* unit cells associated with a particle, the total potential energy of a particle is the sum of all the energies of these unit cells, which can be written as

$$U_{particle} = \sum_{I=1}^{n} U_{cell}^{I} \tag{2.4.1}$$

and

$$U_{cell}^{I} = U_{s}^{I} + U_{v}^{I} \tag{2.4.2}$$

where

$$U_{s}^{I} = \frac{1}{2} k_I \sum_{J=1}^{N_I} \left(\delta l_{IJ}\right)^2 \tag{2.4.3}$$

is the pair-wise potential energy stored within all the connecting springs associated with unit cell *I*, and

$$U_{v}^{I} = \frac{1}{2} T_I \left(\sum_{J=1}^{N_I} \delta l_{IJ} \right)^2 \tag{2.4.4}$$

is the non-local multi-body energy used to compensate the energy difference between the above pairwise energy with the continuum counterpart for the unit cell *I* [38].

In Eqs. (2.4.3)-(2.4.4), k_I and T_I are the pairwise and multi-body parameters for the springs associated with unit cell *I*; N_I is the total number of neighbors and δl_{IJ} are the half length of the spring elongation for neighbor *J* of unit cell *I*.

Relating the spring elongation to the strain at continuum level, the total potential energy of unit cell *I* can be rewritten in terms of the components of the strain tensor as

$$U_{cell}^{I}=\frac{1}{2}k_I\left(l_I\right)^2\sum_{b=1}^{N_I}\left(n_I^b n_J^b n_K^b n_L^b \varepsilon_{IJ}\varepsilon_{KL}\right)+\frac{1}{2}T_I\left(l_I\right)^2\left(\sum_{b=1}^{N_I}n_I^b n_J^b \varepsilon_{IJ}\right)\left(\sum_{b=1}^{N_I}n_K^b n_L^b \varepsilon_{KL}\right) \tag{2.4.5}$$

where l_I is the half length of the distance between the reference particle with its neighbors and n^b is the unit normal vector in the direction of the reference particle with the *b*th neighbor for unit cell *I*.

By the conservation of the potential energy, the tangent stiffness tensor according to the Theory of Hyper-elasticity for the reference particle, can be obtained as

$$\begin{aligned}C_{IJKL}&=\frac{1}{V_1}\frac{\partial^2 U_{cell}^1}{\partial\varepsilon_{IJ}\partial\varepsilon_{KL}}+\cdots+\frac{V_n}{V_1}\left(\frac{1}{V_n}\frac{\partial^2 U_{cell}^n}{\partial\varepsilon_{IJ}\partial\varepsilon_{KL}}\right)=\frac{1}{V_1}\frac{\partial^2\left(U_{cell}^1+\cdots+U_{cell}^n\right)}{\partial\varepsilon_{IJ}\partial\varepsilon_{KL}}\\&=\frac{1}{V_1}\left(\sum_{I=1}^{n}\left(\frac{1}{2}k_I\left(l_I\right)^2\sum_{b=1}^{N_I}\left(n_I^b n_J^b n_K^b n_L^b\right)+\frac{1}{2}T_I\left(l_I\right)^2\left(\sum_{b=1}^{N_I}n_I^b n_J^b\right)\left(\sum_{b=1}^{N_I}n_K^b n_L^b\right)\right)\right)\end{aligned} \tag{2.4.6}$$

For Hookean isotropic material, the model parameters can be solved uniquely by matching the components of the material tangent stiffness tensors. In next section, the three 3D lattice structures are presented and the explicit form of the model parameters are given for each structure.

2.4.3. 3D cubic lattice structures

Many lattice systems have been studied in the Lattice Theory. In the current study, the three commonly used lattice structures in cubic systems are employed, namely, the simple cubic (SC), the body-centered cubic (BCC) and the face-centered cubic (FCC). For each structure, two types of neighbors are considered, i.e., the first and the second nearest neighbors. Other cases introducing more neighbors can be formulated using a similar idea proposed in [52].

Simple cubic lattice

The unit cells identified from the discretization using the simple cubic structure is cube for the first neighbors and rhombic dodecahedron for the second neighbors, as shown in Fig. 2.4.1. It is

shown that there are 6 springs connecting the reference particle with its first nearest neighbors and 12 springs for the second nearest neighbors. The corresponding unit normal vectors for all connecting springs are given in Table 2.4.1.

Given the unit normal vectors, the total energy of a reference particle, in terms of the strain components, can be written as

$$U_{particle} = \frac{R^2}{2}\begin{pmatrix}(2k_1+4k_2+36T)\left(\varepsilon_{11}^2+\varepsilon_{22}^2+\varepsilon_{33}^2\right)+2k_2\left(\gamma_{12}^2+\gamma_{13}^2+\gamma_{23}^2\right)\\+\left(4k_2+72T\right)\left(\varepsilon_{11}\varepsilon_{22}+\varepsilon_{11}\varepsilon_{33}+\varepsilon_{22}\varepsilon_{33}\right)\end{pmatrix} \tag{2.4.7}$$

According to Eq. (2.4.6), matching the tangent stiffness matrix with a homogeneous isotropic Hookean solids, the model parameters can be uniquely determined as

$$k_1 = \frac{2RE}{1+v}, \qquad k_2 = \frac{2RE}{1+v}$$
$$T = \frac{RE(4v-1)}{9(1+v)(1-2v)} \tag{2.4.8}$$

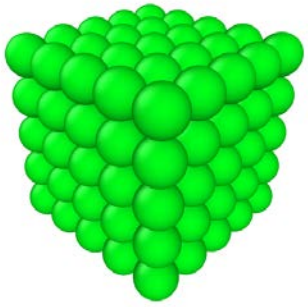

Simple cubic lattice

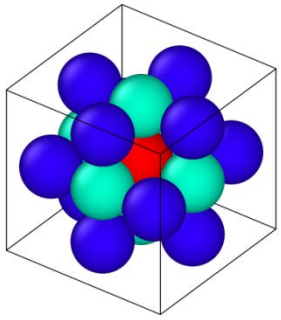

18 neighbors

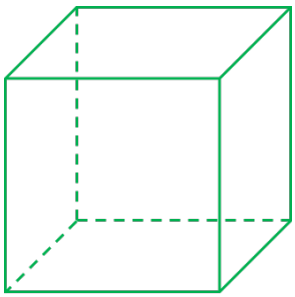

Unit cell 1: Cube

$(V_1 = 8R^3)$

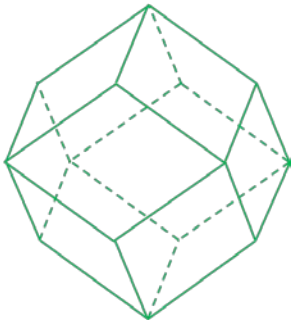

Unit cell 2: Rhombic dodecahedron

$(V_2 = 16R^3)$

Figure 2.4.1. The Simple Cubic Structure and Its Unit Cells

Table 2.4.1. The Unit Normal Vectors for Simple Cubic Structure

Neighbors 1		
$(1,0,0)$	$(0,1,0)$	$(0,0,1)$
$(-1,0,0)$	$(0,-1,0)$	$(0,0,-1)$
Neighbors 2		
$1/\sqrt{2}(1,1,0)$	$1/\sqrt{2}(1,0,1)$	$1/\sqrt{2}(0,1,1)$
$1/\sqrt{2}(-1,-1,0)$	$1/\sqrt{2}(-1,0,-1)$	$1/\sqrt{2}(0,-1,-1)$
$1/\sqrt{2}(1,-1,0)$	$1/\sqrt{2}(1,0,-1)$	$1/\sqrt{2}(0,1,-1)$
$1/\sqrt{2}(-1,1,0)$	$1/\sqrt{2}(-1,0,1)$	$1/\sqrt{2}(0,-1,1)$

Body-centered cubic lattice

The unit cell for the body-centered cubic structure is shown in Fig. 2.4.2, and there are 14 springs connecting the center reference particle with its neighbors. The unit cells for this lattice structure is a truncated octahedron and a cube with volume $V_1 = 32\sqrt{3}/9\,R^3$ and $V_2 = 64\sqrt{3}/9\,R^3$, respectively. R is the particle size. The corresponding 14 unit normal vectors are given in Table 2.4.2.

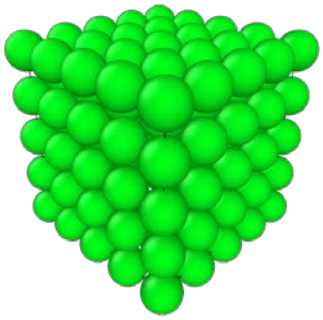

Body-centered cubic lattice

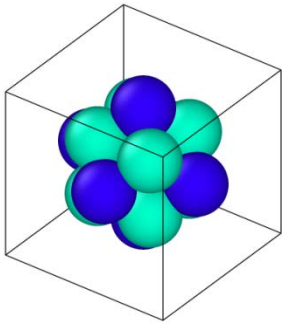

14 neighbors

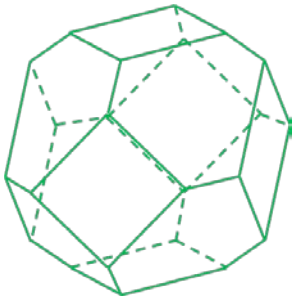

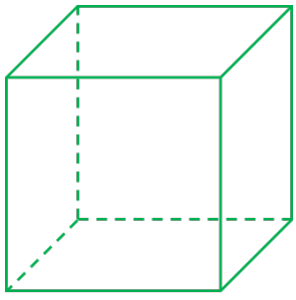

Unit cell 1: Truncated octahedron

$(V_1 = 32\sqrt{3}/9\,R^3)$

Unit cell 2: Cube

$(V_2 = 64\sqrt{3}/9\,R^3)$

Figure 2.4.2. The Body-Centered Cubic Structure and Its Unit Cells

Table 2.4.2. The Unit Normal Vectors for Body-Centered Cubic Structure

Neighbors 1			
$1/\sqrt{3}(1,1,1)$	$1/\sqrt{3}(1,1,-1)$	$1/\sqrt{3}(1,-1,-1)$	$1/\sqrt{3}(1,-1,1)$
$1/\sqrt{3}(-1,-1,-1)$	$1/\sqrt{3}(-1,-1,1)$	$1/\sqrt{3}(-1,1,1)$	$1/\sqrt{3}(-1,1,-1)$
Neighbors 2			
$(1,0,0)$	$(0,1,0)$	$(0,0,1)$	
$(-1,0,0)$	$(0,-1,0)$	$(0,0,-1)$	

The total energy of a reference particle for this lattice structure is

$$U_{particle} = \frac{R^2}{2}\left(\begin{array}{l}\left(\frac{8}{9}k_1+\frac{8}{3}k_2+\frac{112}{9}T\right)\left(\varepsilon_{11}^2+\varepsilon_{22}^2+\varepsilon_{33}^2\right)+\frac{8}{9}k_1\left(\gamma_{12}^2+\gamma_{23}^2+\gamma_{13}^2\right)\\ +\left(\frac{16}{9}k_1+\frac{224}{9}T\right)\left(\varepsilon_{11}\varepsilon_{22}+\varepsilon_{22}\varepsilon_{33}+\varepsilon_{11}\varepsilon_{33}\right)\end{array}\right) \tag{2.4.9}$$

Thus, the model parameters can be uniquely determined by matching the material tangent stiffness matrix as

$$\begin{aligned} k_1 &= \frac{2\sqrt{3}RE}{1+\nu},\quad k_2 = \frac{2}{3}\frac{2\sqrt{3}RE}{1+\nu}\\ T &= \frac{\sqrt{3}RE(4\nu-1)}{7(1+\nu)(1-2\nu)}\end{aligned} \tag{2.4.10}$$

Face-centered cubic lattice

The unit cells for this lattice structure are shown in Fig. 2.4.3. The volume of the unit cells in terms of the particle size are $V_1 = 4\sqrt{2}R^3$ and $V_1 = 16\sqrt{2}R^3$, respectively. There are 18 springs connecting the reference particle with all its neighbors, i.e., 12 for the first neighbors and 6 for the second neighbors. And the corresponding unit normal vectors are given in Table 2.4.3.

The total energy of a reference particle for FCC lattice structure is

$$U_{particle} = \frac{R^2}{2}\left(\begin{array}{l}\left(2k_1+4k_2+24T\right)\left(\varepsilon_{11}^2+\varepsilon_{22}^2+\varepsilon_{33}^2\right)+k_1\left(\gamma_{12}^2+\gamma_{23}^2+\gamma_{13}^2\right)\\ +\left(2k_1+48T\right)\left(\varepsilon_{11}\varepsilon_{22}+\varepsilon_{22}\varepsilon_{33}+\varepsilon_{11}\varepsilon_{33}\right)\end{array}\right) \tag{2.4.11}$$

Matching the material tangent stiffness matrix, the model parameters for this lattice structure can be determined as

$$k_1 = \frac{2\sqrt{2}RE}{1+v}, \quad k_2 = \frac{1}{4}\frac{2\sqrt{2}RE}{1+v}$$
$$T = \frac{\sqrt{2}RE(4v-1)}{12(1+v)(1-2v)} \tag{2.4.12}$$

It should be noted that in all the above derivations, the non-local parameters T are assumed to be identical for both unit cells.

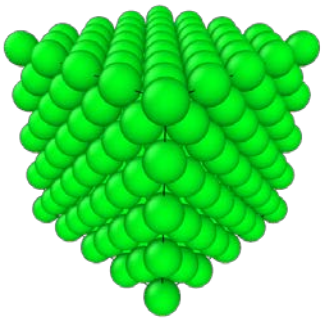

Face-centered cubic lattice

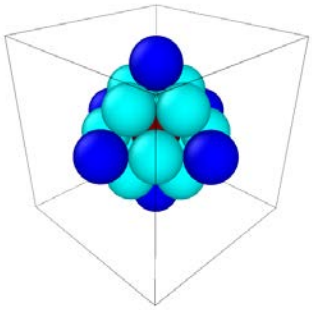

18 neighbors

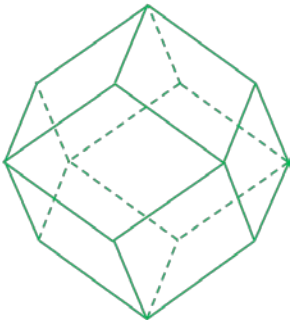

Unit cell 1: Rhombic dodecahedron

$(V_1 = 4\sqrt{2}R^3)$

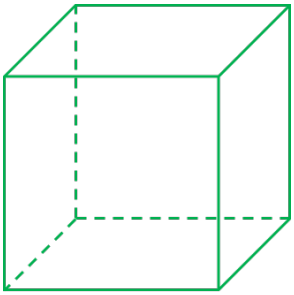

Unit cell 2: Cube

$(V_2 = 16\sqrt{2}R^3)$

Figure 2.4.3. The Face-Centered Cubic Structure and Its Unit Cells

Table 2.4.3. The Unit Normal Vectors for Face-Centered Cubic Structure

Neighbors 1		
$1/\sqrt{2}(1,1,0)$	$1/\sqrt{2}(1,0,1)$	$1/\sqrt{2}(0,1,1)$
$1/\sqrt{2}(-1,-1,0)$	$1/\sqrt{2}(-1,0,-1)$	$1/\sqrt{2}(0,-1,-1)$
$1/\sqrt{2}(1,-1,0)$	$1/\sqrt{2}(1,0,-1)$	$1/\sqrt{2}(0,1,-1)$

$1/\sqrt{2}(-1,1,0)$	$1/\sqrt{2}(-1,0,1)$	$1/\sqrt{2}(0,-1,1)$
Neighbors 2		
$(1,0,0)$	$(0,1,0)$	$(0,0,1)$
$(-1,0,0)$	$(0,-1,0)$	$(0,0,-1)$

Non-local Interactions

In the previous part, the model parameters for each lattice structure have been derived based on the energy equivalency between the discrete model and the corresponding continuum counterpart. In this part, some details on how to calculate the net force exerted on each particle from all its neighbors are presented. And the nonlocality of the model is explained.

Given the potential of each unit cell, the interaction force between particle I and its neighbors can be calculated by differentiating the potential energy with respect to the length change of each spring as

$$F_{IJ} = -\frac{\partial U_{cell}}{\partial(\delta l_{IJ})} = \begin{cases} -k_1(\delta l_{IJ}) - T\left(\sum_{M=1}^{N_1} \delta l_{IM}\right) & \text{for the first neighbors} \\ -k_2(\delta l_{IJ}) - T\left(\sum_{M=1}^{N_2} \delta l_{IM}\right) & \text{for the second neighbors} \end{cases} \tag{2.4.13}$$

Rewritten the nonlocal interaction force, an effective spring stiffness can be obtained as

$$k_{IJ} = \begin{cases} k_1 + T\left(\sum_{M=1}^{N_1} \frac{\delta l_{IM}}{\delta l_{IJ}}\right) & \text{for the first neighbors} \\ k_2 + T\left(\sum_{M=1}^{N_2} \frac{\delta l_{IM}}{\delta l_{IJ}}\right) & \text{for the second neighbors} \end{cases} \tag{2.4.14}$$

From Eq. (2.4.14), it is clear that the effective spring stiffness for each spring in the proposed lattice particle is non-local. It depends not only on the deformation the spring itself, but also on the deformation of its neighboring springs.

2.4.4. Spring-based failure criterion and crack propagation rule

A spring-based critical elongation failure criterion is utilized to simulation the cracking problem in the proposed framework. Some other bond-based failure criteria are available in the literature, such as critical force [46], [52], critical cohesive energy [14]. The advantage of the bond-based

failure criteria is that only the bond breaking rule is required to fully simulate various fracturing problems.

The critical elongation criterion in the proposed lattice particle framework has following expression:

$$\delta l_i^{critical} = \alpha_i \cdot \delta l_i^o \tag{2.4.15}$$

with $i = 1, 2$ for spring connecting with the first and second neighbors, δl_i^o is the original spring length, and α_i is the threshold coefficient, which is calibrated using experimental data.

For isotropic materials, there exists a relationship between α_1 and α_2. In the strain mapping used in Eq.(2.4.5), the relationship between the directional strains of the springs connecting the first neighbors and the second neighbors is, using the normal unit vector given in Table 2.4.1 – 2.4.3,

for simple cubic lattice structure,

$$\varepsilon_{ij,\, j=1,\ldots,6} = \sqrt{2}\varepsilon_{ij,\, j=7,\ldots,18} \tag{2.4.16}$$

Thus,

$$\alpha_1^{sc} = \sqrt{2}\alpha_2^{sc} \tag{2.4.17}$$

for body-centered cubic lattice structure,

$$\varepsilon_{ij,\, j=1,\ldots,8} = \frac{\varepsilon_{ij,\, j=9,\ldots,14}}{\sqrt{3}} \tag{2.4.18}$$

Thus,

$$\alpha_1^{bcc} = \frac{\alpha_2^{bcc}}{\sqrt{3}} \tag{2.4.19}$$

for face-centered cubic lattice structure,

$$\varepsilon_{ij,\, j=1,\ldots,12} = \frac{\varepsilon_{ij,\, j=13,\ldots,18}}{\sqrt{2}} \tag{2.4.20}$$

Thus,

$$\alpha_1^{fcc} = \frac{\alpha_2^{fcc}}{\sqrt{2}} \tag{2.4.21}$$

Using the above derived relationship between the critical elongation for the two types of springs, these is only one threshold coefficient needs to be calibrated from the experimental data for each packing case. And this concept will be illustrated in the numerical results section.

The crack propagation process in the proposed framework is simulated as follows: at each simulation time step, the elongation of the springs are calculated and compared with the corresponding critical values. If the calculated elongation is larger than the critical value, the spring is considered as broken and it cannot sustain any tensile force in the following simulation steps. This process continues until the whole specimen fractures.

2.4.5. Benchmarks

Several benchmarks are used to examine the performance of the proposed 3D lattice particle model for different lattice structures, including the testing of elastic properties, modeling elastic 3D thin plates and shells, and mixed-mode fracture problems. First, the frame-independence of the lattice particle formulation is examined by testing the directional Young's modulus and compared to the input material properties. The convergence characteristic and the applicability to arbitrary Poisson's ratio are also examined in this example. Following this, several thin plate and shell structures with different thickness under bending load are modeled. The numerical results are compared with the FEM solutions and literature results for all three lattice structures whenever available. The last benchmark is a mixed mode fracture simulation of a brittle material. A center-cracked specimen under uniaxial tension is modeled. The center crack is rotated with arbitrary in-plane angle to create the mixed-mode fracture scenarios. Both the fracture path and peak loading are compared with experimental observations.

Testing of the elastic properties

As shown in the APPENDIX A, the proposed model formulation is frame independent for all three cubic lattice structures. In this example, we numerically show the frame independence of the

model formulation by calculating the directional Young's modulus while rotating the underlying lattice structure. The Young's modulus on two planes are examined, the <010> and <110> planes. A convergence study is also performed for all three lattice structures when the lattice rotation is zero, i.e., the lattice coordinates coincide with the global coordinate.

The tests are performed using a cube with edge length of 0.01 *m*. The material constants used are: Young's modulus $E = 64\ GPa$ and Poisson's ratio $v = 0.36$. The simulation is repeated for different lattice rotations (i.e., rotation angle β in Fig. 2.4.5). The rotational invariance can be checked using this series of simulations. The numerical results for the directional Young's modulus are shown in Fig. 2.4.5. As can be seen, the numerical calculated Young's modulus for all three lattice structures are rotational invariant. The numerical simulation is consistent with the analytical derivation given in the APPENDIX A.

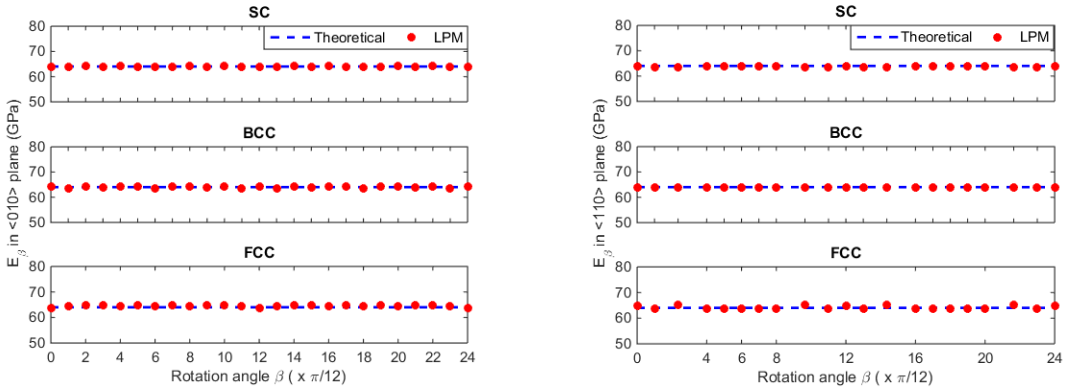

Figure 2.4.5. The Rotation Invariance of the Three Lattice Structures

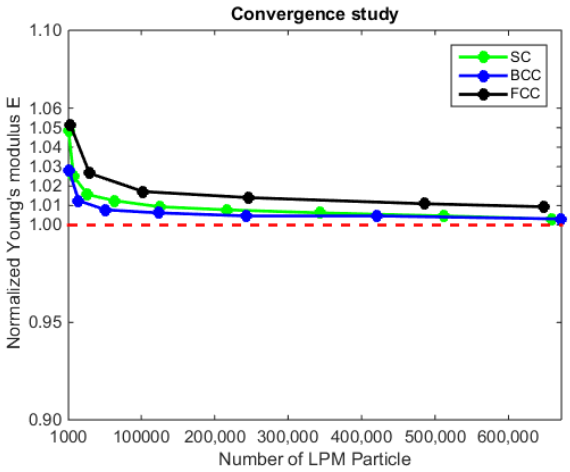

Figure 2.4.6. The Convergence Study for the Three Lattice Structures

The convergence study of the Young's modulus versus the particle number when the lattice rotation is zero on the <010> plane is shown in Fig. 2.4.6. From the results, all three lattice structures converge to the 2% error bound very fast. Among these three lattice structures, the body center cubic structure performs the best, while the face centered cubic structure needs a denser particle density in order to obtain the same accuracy as other two lattice structures.

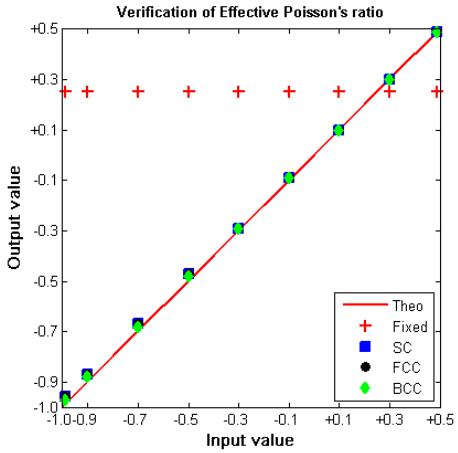

Figure 2.4.7. The Verification of Effective Poisson's Ratio

The isotropic materials with arbitrary Poisson's ratio can be modeled within the proposed framework. The verification results on effective Poisson's ratio are shown in Fig. 2.4.7. The x-axis is the actual material's Poisson's ratio and the y-axis is the simulated Poisson's ratio. Lattice particle model with only local axial spring will produce a fixed Poisson's ratio irrespective of the

input values (see red markers in Fig. 2.4.7). From the verification results, it is clear that the proposed framework removes the limitation on Poisson's ratio. It is also shown that among all three cubic lattice structures, the body centered cubic structure performs slightly better than the other two lattice structures.

3D thin plate and shell structures

Extensive researches have been done in modeling thin structures, such as [61], [62]. In this subsection, the deflections of 3D thin structures are simulated to evaluate the performance of the proposed framework for elastic thin structures. In this example, only the body-centered lattice structure is used.

Clamped circular plate under concentrated loading

A clamped circular plate is studied in this subsection. The radius of the plate is 0.05 *m*, with concentrated force of 10 *N* applied on the center region of radius 0.005 *m*. Two scenarios of different thickness of the plate are considered, i.e., the diameter to thickness ratio *d/h* is 10 and 100. Different Poisson's ratios $(\nu = 0.2,\ 0.3)$ are used in this example.

The results are compared with FEM solution from ABAQUS using 3D stress analysis employing C3D8R element. The typical deformation distributions are shown in Fig. 2.4.8. The extreme displacement components are given in Table 2.4.4. The error is defined as the absolute error with respect to the FEM solution. A detailed comparison for the displacement U_3 along the radial direction is shown in Fig. 2.4.9.

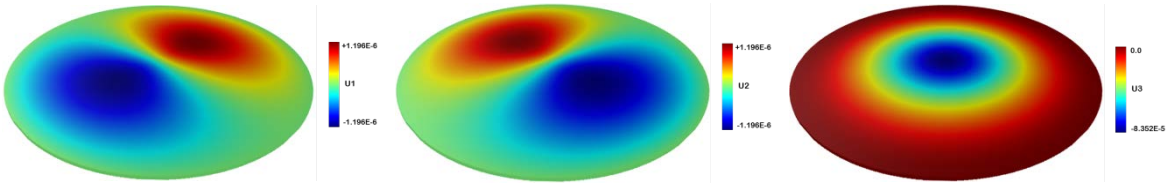

Figure 2.4.8. The Displacement Distribution for the Case of v = 0.3, d/h = 100

Table 2.4.4. The Extreme Displacements Values

d/h	Poisson's ratio	Displacement	BCC	FEM	Error (%)
10	0.2	$U_{1/2}$ (E-8)	±1.293	±1.325	2.42
		U_3 (E-7)	-1.085	-1.105	1.81
	0.3	$U_{1/2}$	±1.223	±1.254	2.47

		U_3	-1.033	-1.049	1.53
100	0.2	$U_{1/2}$ (E-6)	±1.271	±1.323	3.93
		U_3 (E-5)	-8.865	-8.874	0.10
	0.3	$U_{1/2}$	±1.196	±1.254	4.63
		U_3	-8.352	-8.412	0.71

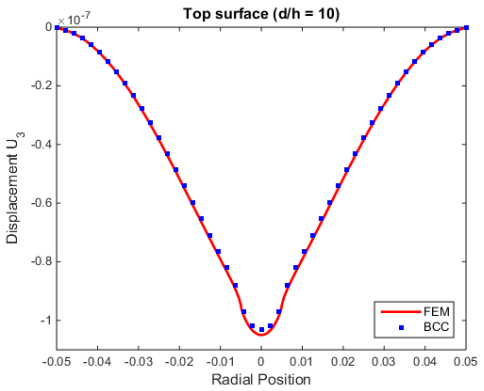

Top surface (d/h = 10)

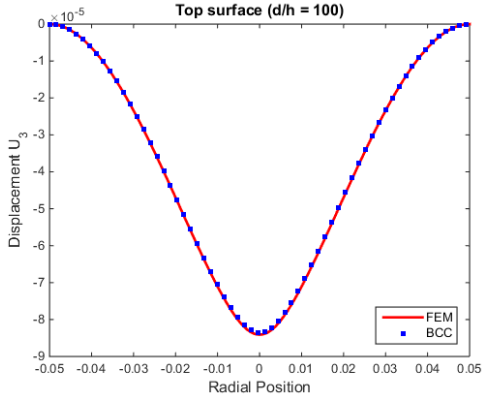

Top surface (d/h = 100)

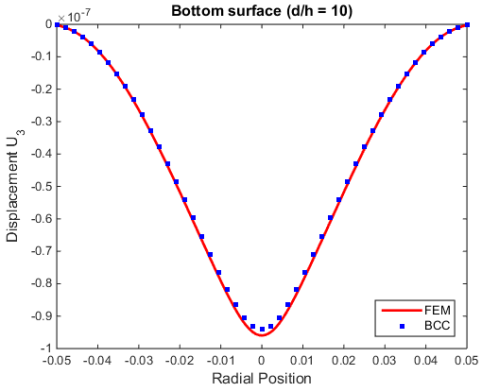

Bottom surface (d/h = 10)

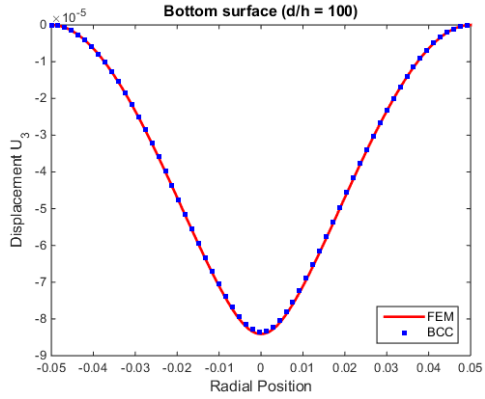

Bottom surface (d/h = 100)

Figure 2.4.9. The Detailed Deformation (w) Comparison (v = 0.3)

Simply-supported square plate under uniform loading

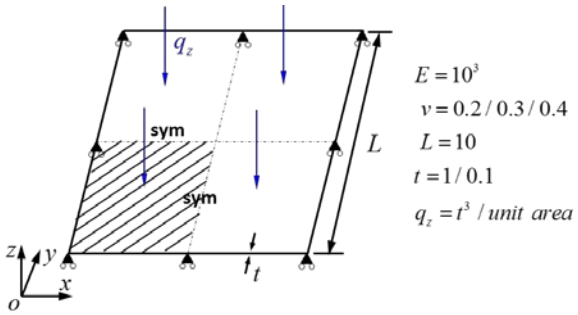

Figure 2.4.10. The Dimension and Configuration of the Square Plate

A simply-supported square plate under uniform distributed load is studied in this example. The dimensions and configuration of the plate are shown in Fig. 2.4.10. Due to symmetry, only a quadrant of the plate is modeled, as highlighted in Fig. 2.4.10. Two cases of length-to-thickness ratio L/t are studied. The literature results and Kirchhoff's analytical solution from [62] are used as reference solutions. For the case of $L/t = 100$, the effect of Poisson's ratio on the deflection is studied.

Table 2.4.5. The Deflection Uz at the Center of the Plate

L/t	Poisson's ratio	Deflection U_z		
		Lattice particle	Kirchhoff	Elasticity[a]
10	0.3	-0.4955	-0.4429	-0.4936
	0.2	-0.4556	-0.4672	--
100	0.3	-0.4279	-0.4429	-0.4429
	0.4	-0.3913	-0.4088	--

[a]: 7-parameter 3D shell model from [62]

The comparison of the deflection at the plate center is given in Table 2.4.5. The deflection distribution for the case of $v = 0.3$ and $L/t = 100$ is shown in Fig. 2.4.11.

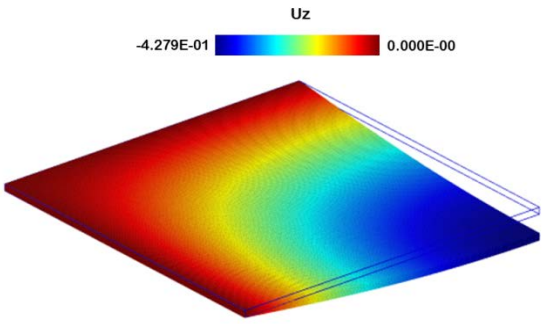

Figure 2.4.11. The Deformation Uz the Square Plate for the Case of v = 0.3, L/t = 100

Clamped cylindrical shell strip under concentrated loading

A cylindrical strip is studied in this example. As shown in Fig. 2.4.12, the strip is clamped at one end with a concentrated line load applied on the other end. Two thicknesses are considered. Due to symmetry, only half of the strip is modeled.

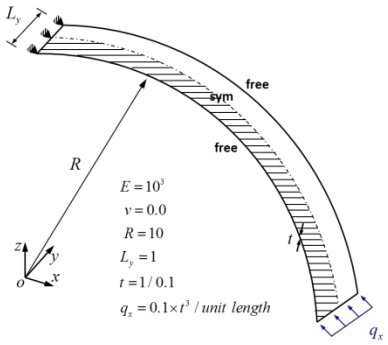

Figure 2.4.12. The Dimension and Configuration of the Cylindrical Strip

The comparison between the results from the proposed model with the literature results are shown in Table 2.4.6. The deformation distribution of Ux is shown in Fig. 2.4.13.

Table 2.4.6. The Displacement Ux at End Tip with Applied Force

L/t	Deflection U_z		
	Lattice particle	Bernoulli	Elasticity[a]
10	-0.947	-0.942	-0.945
100	-0.937	-0.942	-0.945

[a]: 7-parameter 3D shell model with discrete strain gap concept from [62]

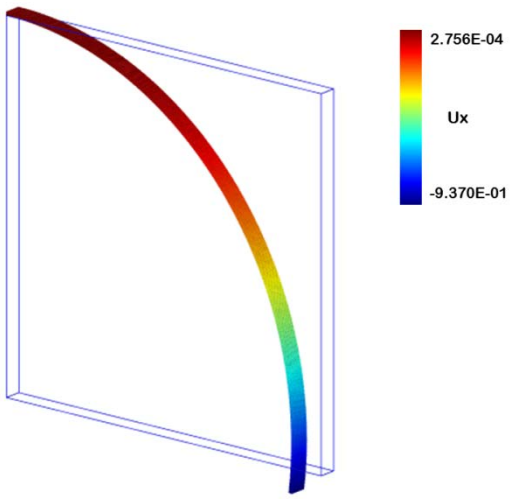

Figure 2.4.13. The Deformation Ux of the Cylindrical Shell Strip for R/t = 100

Scordelis-Lo roof example

The famous benchmark for testing the formulation for cylindrical shell structure, the Scordelis-Lo roof [63] problem, is modeled in this example. The roof dimension and configuration are shown in Fig. 2.4.14. As indicated, only a quadrant of the roof is modeled using the proposed model.

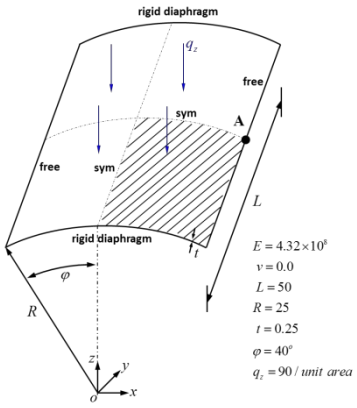

Figure 2.4.14. The Dimension and Configuration of the Scordelis-Lo Roof

The reference solution of the deflection at point A reported by [64] is 0.3024. The result obtained using the proposed model at point A is 0.3015, which is in good agreement with the reported result. A deformation distribution of Uz is shown in Fig. 2.4.15.

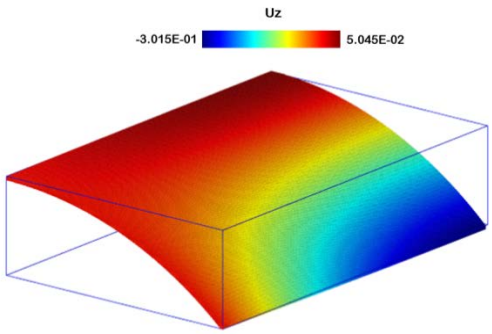

Figure 2.4.15. The Deformation Uz of the Scordelis-Lo Roof

From the simulation results of all three benchmarks, the proposed model can capture the deformation to certain accuracy for both relative thick and thin plate and shell structures. The proposed model is a discrete formulation of 3D elasticity, thus has the same issue while modeling very thin structures. And usually extensive computation is required for this type of structures.

Mixed mode fracture

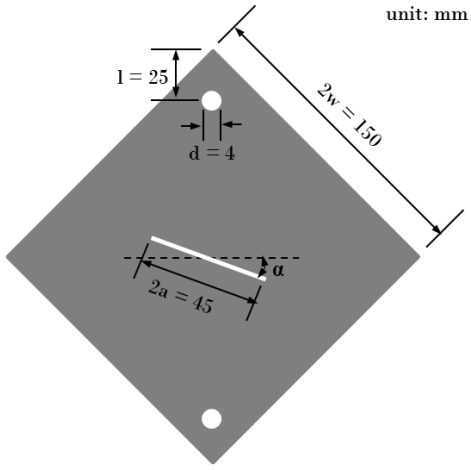

Figure 2.4.16. The Diagonally Loaded Square Plate

Brittle fracture is one of the common types of mechanical failure of cracked engineering components and structures. Extensive researches have been done, both analytically and experimentally, to investigate the different fracture modes, i.e., pure mode I, pure mode II and mixed mode. In this section, we adopt the diagonally loaded square plate specimen from [65] to test the performance of the proposed lattice particle framework for fracture modeling using the simple cubic lattice structure. All the crack angles are studied in this section. When $\beta = 0^o$, the plate is subjected to pure mode I loading . When $\beta = 62.5^o$, the plate is subjected to pure mode II loading. Other crack angles are corresponding to mixed mode loading.

The dimension of the specimen is shown in Fig. 2.4.16. The thickness of the plate is 5 *mm*. The initial crack width is 0.7 *mm*. The material properties of the PMMA material is: Young's modulus $E = 2940\text{MPa}$, Poisson's ratio $v = 0.38$, tensile strength $\sigma_T = 48\text{MPa}$ and the mass density $\rho = 1.18 \times 10^3 \text{kg/m}^3$. Instead of removing the particle to create the hole feature at the top and bottom parts of the specimen, we define two sets for the particles confined to the hole geometries and apply the constant velocity to these sets to simulate a uniaxial tensile loading cases. The particle set can only move upward or downward. The dynamic solution scheme [38] is used in this example. In the experiment [65], the constant loading rate is 1 *mm/min*, i.e., 1.7×10^{-5} *m/sec*. While in the simulation, we have used 0.17 *m/sec* and the time step is 10^{-8} *sec* for all cases. In

order to avoid singularity related issues around the hole, the threshold coefficients for springs around the holes were set to unity.

As pointed out in the Section 4, the failure parameters α_i ($i=1,2$) needs to be calibrated using the experimental data. And since there is certain relationship between α_1 and α_2, only one failure parameter needs to be calibrated. In this example, the case of initial crack angle $\beta=0^o$ is used to calibrate the threshold coefficients. And the other two cases are used to verify the model. The calibrated failure parameter for the simple cubic lattice structure is:

$$\begin{aligned}\alpha_1^{sc} &= 1.25\frac{\sigma_T R}{k_1^{sc}}\\ \alpha_1^{bcc} &= 1.2\frac{\sigma_T R}{k_1^{bcc}}\\ \alpha_1^{fcc} &= 1.2\frac{\sigma_T R}{k_1^{fcc}}\end{aligned} \tag{2.4.22}$$

where R is the particle radius and σ_T is the material tensile strength, k_1 is the spring stiffness parameter for the springs connecting with the first nearest neighbors.

The simulation results using the simple cubic lattice structure is compared with the experimental observation from [65]. The crack paths for various initial crack angles using the body centered cubic structure are shown in Fig. 2.4.17. The white lines indicate the final crack paths. The predicted peak reaction forces are shown in Fig. 2.4.18.

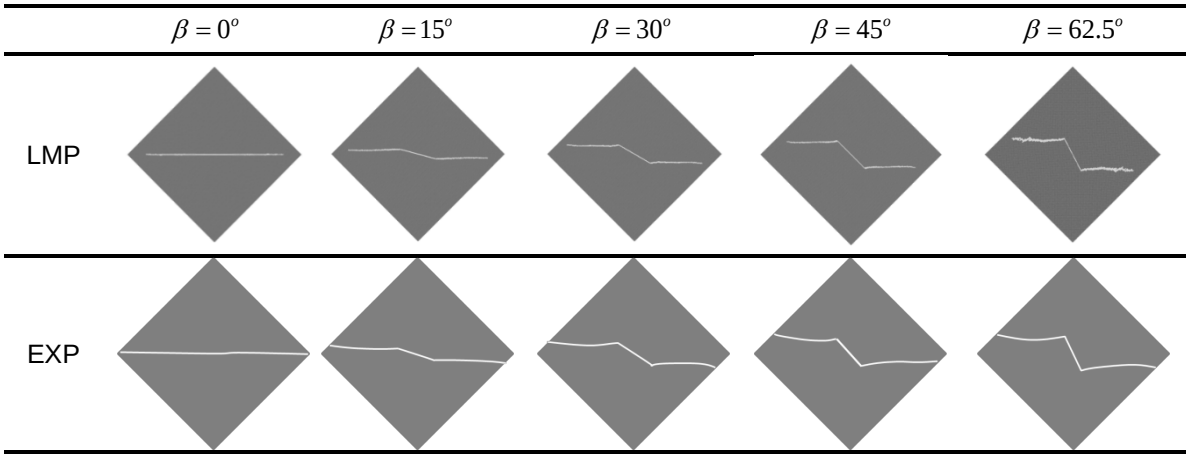

Figure. 2.4.17. The Final Crack Paths Compared with Experimental Results

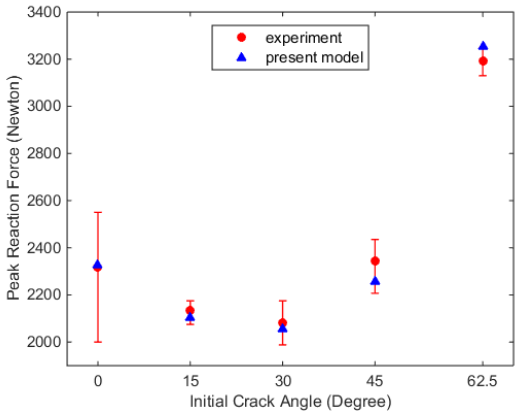

Figure 2.4.18. The Peak Force on the Top Hole Using bcc Lattice Structure

As can be seen from the comparisons in Fig. 2.4.17 and Fig. 2.4.18, there prediction using the body centered cubic lattice structure matches well with the experimental observations.

2.4.6. Discussion and conclusions

A family of 3D lattice structures for the Lattice Particle Model was proposed and their performances were studied by modeling several benchmark problems in this section. The simulation results are compared to both FEM solutions and experimental observations. Good agreements are found and the validity of the proposed model is verified. The proposed model is different from other lattice models at least in following two aspects:

1). In addition to the pair-wise potential in the classical lattice models, a non-local energy balancing term is introduced. From the functionality viewpoint, this term serves as a balance between the potential energy stored within all springs associated with a unit cell in the classical axial spring model and the strain energy of a corresponding continuum. This is completely different from the other shear/angular springs introduced in some lattice spring models;

2). The discrete elements, i.e., particles, not only communicate with its nearest neighbors but also interact with the second and even further neighbors in lattice particle model. This nonlocal interaction results in a non-uniform varying effective spring stiffness;

Based on the current investigation, the following conclusions can be drawn:

1). The proposed 3D lattice particle model is capable of modeling elasticity and fracture problems of solid materials under general mechanical loadings;

2). The proposed failure simulation criterion is valid for this 3D lattice particle model. The threshold coefficients can be calibrated using the experimental data, as illustrated in the benchmark section;

3). All three lattice structures have satisfactory accuracy and the BCC lattice produces the best simulation results in the investigated problems.

Further investigation on the capacity of modeling brittle fracture using the proposed model is required. Extending this framework to elasto-plastic materials and anisotropic materials requires additional research.

CHAPTER

3. THE LATTICE PARTICLE MODEL FOR ANISOTROPIC SOLIDS

3.1 Introduction

Anisotropic materials are the materials of non-isotropic, which means the property of material depends on the directions. Different directions have different properties. Anisotropic materials are more practical meaningful than isotropic materials due to its diversity in nature.

Anisotropic materials are widely used in engineering, such as laminated composites. The behaviors of composite laminates can be characterized by complex 3D states of stress. Full 3D elasticity analyses [66], [67], [68], [69], [70], [71] reveal that the interlaminar continuity of transverse normal and shear stresses as well as the layerwise continuous displacement field through the thickness of the laminated structures are the essential requirements for the accurate analysis of laminated structures. The inherent anisotropy and mismatch of material properties, particularly the Poisson's ratio, between plies result in high interlaminar stresses [72], [73], [74], [75], [76], which is critical to the delamination failure mechanism [77]. These requirements can only be partially fulfilled by other reduced formulations [78]. A drawback of the 3D models is their computational expensiveness. However, these models are essential for an accurate evaluation of the interlaminar stresses at locations such as cutouts, delamination fronts and regions of intense loading. Damage initiation and propagation are likely to occur at such locations, which might lead to the failure of laminate [79]. Moreover, owing to the advent of high-speed computers and the use of parallel computing and GPU computing, this drawback can be underestimated and will not be of concern in the near future.

Polycrystalline material is an aggregate of microstructural crystallites of various size, shape and crystallographic orientation. Its macroscopic properties are affected by the underlying microstructures. At the crystallite level, the material properties are anisotropic and orientation dependent. The macroscopic behavior of polycrystalline materials can be regarded as statistically isotropic when the materials have random crystallographic and morphologic texture. The

influence of individual crystallite on the overall macroscopic behavior of the aggregate is negligible. In practice, an ideally randomly oriented crystalline aggregate is very difficult to obtain. Initial deviation from this randomness may occur during the solidification process due to differences in crystal growth along different directions. Subsequent metal working processes, such as rolling, extrusion and annealing, provide other mechanisms for the formation of preferred orientation textures. This non-random distribution of crystallographic orientation influences the macroscopic properties of crystalline aggregates. The applicability of the aforementioned analyses for this type of polycrystal texture becomes very limited. It should be noted that perfect grain boundaries are assumed in all the theoretical predictions for effective elastic constants of a polycrystalline material with or without texture. Grain boundary also plays a significant role on the fracture behavior of the polycrystalline materials. Different grain boundary properties may result in different fracture mode, e.g., intergranular or transgranular fracture.

The development and application of lattice models has been mainly focused on isotropic materials. Grah et al. [45] has used a general αβ-model [10] to investigate the fracture behavior of 2D brittle polycrystalline materials. In their formulation, both the α-spring and β-spring, i.e., axial and angular springs, respectively, have been utilized. Various grain orientations were represented by the transformation of the material stiffness matrix. Although the spring stiffness can be easily assigned using the transformed materials stiffness, the shear springs suffers from the negative value for most of the grain orientations. In addition, the intrinsic fracture anisotropy of the lattice structure still persist [52]. Another effort to apply the lattice model to polycrystalline materials was done by Rindaldi et al. [80]. In this model, the effective elastic properties, i.e., Young's modulus and Poisson's ratio, were estimated using a novel mapping procedure between the FEM and the lattice spring formulations. According to their results, the estimated average Young's modulus is consistent with the experimental results. However, the Poisson's ratio could not be matched and its value is fixed around 0.33 for all simulation cases.

In this chapter, the lattice particle model for anisotropic materials is presented. A lattice rotation scheme is proposed to represent the material orientation which is consistent but different from the

classical tangent stiffness matrix transformation scheme in continuum mechanics. The content of this chapter is organized as follows. In Section 3.2, the lattice particle model based on triangular packing for general 2D anisotropic materials is presented. Different from the case of isotropic materials, the six springs associated with each particle not necessary to have the same local and nonlocal parameters. But due to symmetry, the local and nonlocal parameters are identical for springs in the opposite directions. Similar conditions apply to the spring based failure criterion. Several numerical examples used to verified the validity and test the performance of the proposed 2D anisotropic lattice particle model. Discussions and conclusions are drawn based on the current study. In Section 3.3, the anisotropic lattice particle model is applied to study the microstructural effect on the response of polycrystalline materials. The effects of the crystallographic orientation and interface properties are studied in detail, on both effective elastic properties and fracture mode and strength. In Section 3.4, the 3D anisotropic lattice particle model based on the simple cubic lattice structure is presented. The focus is on the modeling of the deformation of cross-ply laminated composite plates. Systematic study with other laminated plate theories is performed. Conclusions and future work are given based on the current study.

3.2 2D Anisotropic Composites

A novel nonlocal lattice particle framework for fracture simulation of general anisotropic materials is proposed in this paper. The key idea is that the material anisotropy is handled by the rotation of the underlying topological lattice structure, rather than the transformation of material stiffness matrix, which is commonly used in the finite element scheme. One major advantage of the proposed model is that the crack path preference of the anisotropic materials is naturally incorporated by the underlying lattice structure. First, the analytical derivation and formulation of the proposed nonlocal lattice particle method is given for general anisotropic materials. The equivalency of the lattice rotation and stiffness transformation using the proposed formulation is discussed in detail. Following this, numerical examples are used to demonstrate the capability of the proposed methodology for 2D anisotropic solids. Special focus is on the orthotropic materials widely used for structural applications, e.g., fiber-reinforced composite laminates. Numerical simulations are validated by comparing with observations from open literatures. Finally, discussions and future work are given based on the current investigation.

3.2.1 Introduction

Unlike isotropic materials, the properties of anisotropic materials are orientation dependent. Thus, modeling of various phenomena in anisotropic materials, such as fracture, is more complicated compared to that in isotropic solids. The modelling of fracture behavior of isotropic brittle materials can be traced back to Griffith [81]. One important issue in the fracture simulation is the propagation path determination. Under quasi-static loading, several popular criteria have been used along with the Griffith's theory to determine the crack path, such as the maximum energy release rate [82], the minimum strain energy density [83], and the maximum circumferential stress [84]. These criteria are generally not accurate if the anisotropy of the material properties are considered [85].

Anisotropic materials are widely used in engineering, such as fiber-reinforced composites (FRC). For FRC, various failure criteria have been proposed during the last several decades, such as the maximum stress criterion, the Tsai-Wu criterion [86] and the Tsai-Hill criterion [87]. These criteria try to determine the failure strength of anisotropic materials. The crack path prediction still poses a great challenge [88].

The discrete formulation of fracture mechanics, such as lattice particle method, is different from the continuum-based fracture mechanics. This approach dates back to the work of Hrennikoff [16]. Vast successive development of this approach can be found in the literature, e.g., [10], [89], [12], [90], [52]. The lattice models can be generally grouped into four categories based on the proposed potential functions among particles: (1) the local axial spring model [9]; (2) the axial-bending/axial-shear spring model, such as the bond-bending model [10] and the angular shear spring model [2]; (3) the micro-polar lattice model with axial, shear, and rotation degree of freedoms, such as [91]; (4) the model consider both local pairwise potential and nonlocal multi-body potential among particles, such as [22] and [38].

The Lattice Models have some intrinsic advantages when handling the fracture behavior of materials. For instance, Lattice Models are based on the discontinuous formulation which avoids singularity related issues in continuum-based numerical simulation methods. The crack initiation and propagation processes can be modelled via bond breaking rules [4]. No external crack path determination rule is required and the crack propagation is a natural outcome of the breakage of the connecting bonds. The development and application of Lattice Models has been mainly focused on isotropic materials. Grah et al. [45] developed a axial-shear spring model for simulating the fracture behavior of anisotropic materials (i.e., polycrystals). In the proposed model [45], a transformation of material stiffness tensor is performed according to the rotation of the material coordinate. The transformed material stiffness matrix is then used to evaluate the corresponding spring stiffness for each grain. This approach leads to the negative shear spring stiffness when mapping the lattice model to the transformed stiffness tensor matrix. The lattice

structure is independent of the grain orientation and the simulated the crack path deviates from the experimental observations [45].

The main objective of this study is to extend the lattice particle model developed by Chen et al. [38] for isotropic materials to general anisotropic elastic solids. The arbitrary material orientation of a general anisotropic material is accounted by rotating the topological lattice structure rather than the stiffness matrix transformation as in most existing approaches. Thus, the anisotropy of solids is naturally incorporated with the topological lattice structure. The content of this paper is organized as follows. First, the background theory and formulation of the proposed lattice particle model is presented. The unique mapping relationship between the model parameters and the components of the material stiffness matrix is derived based on the equivalence of the strain energy between the discrete model and the continuum model. Following this, a lattice rotation scheme to account for the material anisotropy is presented. A detailed derivation on the equivalency between the lattice rotation and the stiffness matrix transformation is given in the APPENDIX. Next, discussion on the failure criterion used in the proposed framework for modeling fracture phenomena of anisotropic materials is given. After that, several numerical benchmarks to test the performance of the proposed framework for modeling composite materials are presented. Conclusions and future work are given based on this study at the end.

3.2.2 The lattice particle model: theory and formulation

In the proposed lattice particle model (Fig. 3.2.1(a)), the domain of interest is decomposed into discrete particles, which are connected by springs. A unit cell can be identified from the decomposed domain, which is a hexagon for triangular packing as shown in Fig. 3.2.1(b). One of the main differences between the proposed framework and other lattice spring model is the introduction of the non-local potential among particles. This is achieved by balancing the system energy between the classical axial spring models with corresponding continuum model. The interaction force between a typical pair of particle (such as *I* and *J* shown in Fig. 3.2.1(c)) not only

depends on the particle pair themselves, but also has contributions from all its surrounding neighbors.

Thus, the total energy of a unit cell can be formulated into two parts, the local pairwise energy associated with the connecting springs and the non-local multi-body energy of all its neighboring springs.

$$U_{cell} = \frac{1}{2}\left(\sum_{J=1}^{6} k_J \left(\delta l_{IJ}\right)^2\right) + \frac{1}{2}\left(\sum_{J=1}^{6} T_J \delta l_{IJ}\right)\left(\sum_{K=1}^{6} \delta l_{IK}\right) \tag{3.2.1}$$

where the first term is the local pairwise energy of the connecting springs and the second term is the non-local multi-body energy of all its neighboring springs, δl_{IJ} is half of the length change of a connecting spring, k_J and T_J are the local and non-local spring stiffness parameters.

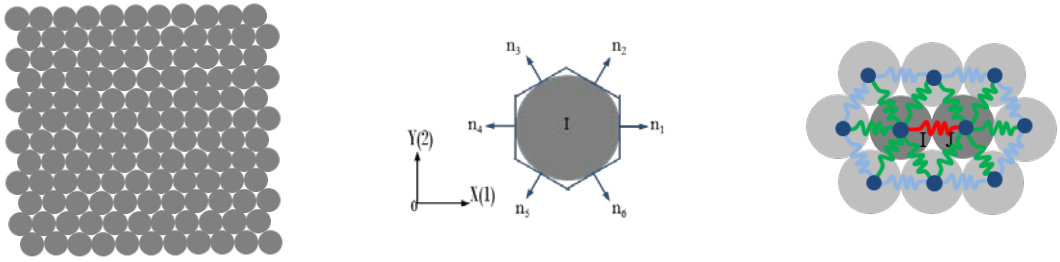

a). Domain decomposition b). Unit cell c). non-local interaction

Figure 3.2.1. The Discretization Scheme Used in the Proposed Model

Due to the symmetry of the material stiffness matrix $\mathbf{C}$ of the corresponding continuum, the springs in opposite directions should have the same local and non-local stiffness parameters. Thus, the following assumptions are used,

$$\begin{aligned} &k_1 = k_4; \quad k_2 = k_5; \quad k_3 = k_6 \\ &T_1 = T_4; \quad T_2 = T_5; \quad T_3 = T_6 \end{aligned} \tag{3.2.2}$$

In terms of the components of the strain tensor, Eq.(3.2.1) can be rewritten as

$$U_{cell} = \frac{1}{2}R^2 \sum_{b=1}^{6} k_b n_i^b n_j^b n_k^b n_l^b \varepsilon_{ij}\varepsilon_{kl} + \frac{1}{2}R^2\left(\sum_{b=1}^{6} T_b n_i^b n_j^b \varepsilon_{ij}\right)\left(\sum_{b=1}^{6} n_k^b n_l^b \varepsilon_{kl}\right) \tag{3.2.3}$$

where R is the radius of the particle, $n^{b}_{i,j,k,l}$ is the component of the normal vectors of spring b given in Table 3.2.1. $i, j, k, l = 1, 2$ for two dimensional formulations.

Table 3.2.1. The Normal Vectors for the Six Nearest Neighbors of a Unit Cell

n_1	n_2	n_3	n_4	n_5	n_6
$(1,0)$	$\left(1/2, \sqrt{3}/2\right)$	$\left(-1/2, \sqrt{3}/2\right)$	$(-1,0)$	$\left(-1/2, -\sqrt{3}/2\right)$	$\left(1/2, -\sqrt{3}/2\right)$

Note that the normal vectors given in Table 3.2.1 is with respect to the material coordinate *1O2*, as shown in Fig. 3.2.1(b) in which the material coordinate *1O2* is coincident with the global coordinate *XOY*. This is chosen for the convenience of calculating the normal vectors associated with each unit cells. More general case, where the material coordinates and global coordinate are different, will be discussed in Section 3.

Given the normal vectors in Table 3.2.1, the total energy stored in a unit cell can be calculated from Eq.(3.2.3). Due to the conservative of the potential energy, the material stiffness matrix can be obtained by the Theory of Hyper-elasticity as

$$C_{ijkl} = \frac{1}{V} \frac{\partial^2 U_{cell}}{\partial \varepsilon_{ij} \partial \varepsilon_{kl}} \tag{3.2.4}$$

where V is the volume of a unit cell, $V = \frac{1}{2} \cdot \frac{2\sqrt{3}}{3} R \cdot R \cdot 6 \cdot h = 2\sqrt{3} h R^2$. For dimensional consistency, the unit thickness h is used. In following derivation, the unit thickness h is usually omitted unless ambiguity arises.

According to the Hooke's law, the material stiffness tensor for a general anisotropic elastic material in 2D can be expressed as

$$\mathbf{C} = \begin{bmatrix} C_{11} & C_{12} & C_{16} \\ & C_{22} & C_{26} \\ sym & & C_{66} \end{bmatrix} \tag{3.2.5}$$

Comparing the components of the material stiffness matrices solved from Eq.(3.3.4) with Eq.(3.2.5), the following unique mapping relationship between the proposed model parameters and the component of material stiffness matrix can be obtained as

$$\begin{Bmatrix} k_1 \\ k_2 \\ k_3 \\ T_1 \\ T_2 \\ T_3 \end{Bmatrix} = \begin{bmatrix} \sqrt{3} & \sqrt{3} & -\frac{4\sqrt{3}}{3} & 0 & 0 & -2\sqrt{3} \\ 0 & 0 & \frac{8\sqrt{3}}{3} & 4 & -4 & 0 \\ 0 & 0 & \frac{8\sqrt{3}}{3} & -4 & 4 & 0 \\ 0 & -\frac{4\sqrt{3}}{9} & \frac{2\sqrt{3}}{3} & 0 & 0 & \frac{2\sqrt{3}}{3} \\ 0 & \frac{2\sqrt{3}}{9} & -\frac{2\sqrt{3}}{3} & -\frac{2}{3} & 2 & 0 \\ 0 & \frac{2\sqrt{3}}{9} & -\frac{2\sqrt{3}}{3} & \frac{2}{3} & -2 & 0 \end{bmatrix} \begin{Bmatrix} C_{11} \\ C_{22} \\ C_{66} \\ C_{26} \\ C_{16} \\ C_{12} \end{Bmatrix} \tag{3.2.6}$$

Eq. (3.3.5) is the exact mapping relationship between the model parameters and the components of the material stiffness matrix in 2D. Given any material constants, the six model parameters can be uniquely determined. When the material is isotropic, the solutions reduce to the one shown in [38].

Given the model parameters k_J and T_J ($J=1,\cdots,6$), the interaction force within each connecting spring can be calculated by differentiating the total energy with respect to the spring elongation as

$$F_{IJ} = -\frac{\partial U_{cell}}{\partial\left(\delta l_{IJ}\right)} = -k_J\left(\delta l_{IJ}\right) - \frac{1}{2}\sum_{K=1}^{6} T_K \delta l_{IK} - \frac{1}{2} T_J \sum_{K=1}^{6} \delta l_{IK} \tag{3.2.7}$$

The interaction force between a typical particle pair can be rewritten as

$$F_{IJ} = -\left(k_J + \frac{1}{2}\sum_{K=1}^{6} T_K \frac{\delta l_{IK}}{\delta l_{IJ}} + \frac{1}{2} T_J \sum_{K=1}^{6} \frac{\delta l_{IK}}{\delta l_{IJ}} \right)\left(\delta l_{IJ}\right) \tag{3.2.8}$$

Thus, the effective pairwise spring stiffness in an axial spring model is

$$k_J^{eff} = k_J + \frac{1}{2}\sum_{K=1}^{6} T_K \frac{\delta l_{IK}}{\delta l_{IJ}} + \frac{1}{2} T_J \sum_{K=1}^{6} \frac{\delta l_{IK}}{\delta l_{IJ}} \tag{3.2.9}$$

3.2.3 Material orientation represented by lattice rotation

In the above discussion in Section 3.2.2, the formulation is based on the coincidence of the material coordinate, the lattice orientation and the global coordinate. The definition of the lattice orientation and how to rotate the lattice according to the material orientation is schematically shown in Fig. 3.2.2. The lattice orientation is always coincident with the material coordinate (not with the global coordinate). Thus, the material coordinate orientation can be represented by the underlying lattice orientation. The material stiffness matrix is not transformed in the proposed method which is generally the case for Finite Element Methods. As shown in Fig. 3.2.2, the underlying lattice is rotated according to the rotation of the material coordinate *1O2*.

The equivalency between the rotation of the underlying lattice structure and the transformation of material stiffness matrix to accommodate the rotation of the material coordinate is shown in the APPENDIX. One benefit for the rotation of lattice structure is that the anisotropic fracture preference is included naturally by the topological lattice structure.

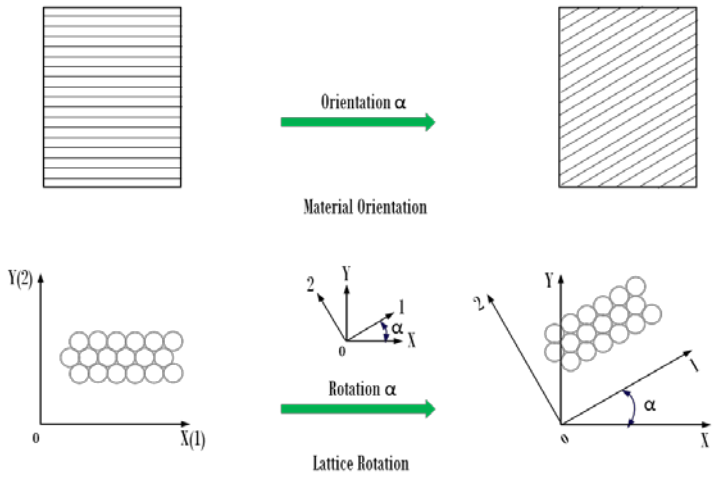

Figure 3.2.2. Correspondence between Material Orientation and Lattice Rotation

3.2.4 Failure criterion

A spring-based failure criterion is proposed in this study to model the fracture phenomenon of anisotropic materials. Various bond-based failure criteria exist in the literature, such as critical

force [12], critical strain energy [35] and critical elongation [8]. Cohesive type failure criteria are also used [14]. In this study, a critical elongation criterion is proposed.

For homogeneous isotropic materials, the connecting bonds in different directions have the same critical elongation. For anisotropic materials, the critical elongation for different connecting bonds is different. The critical elongation $s_j^{critical}$ in the three directions, i.e., $j=1,2,3$, is dependent on the particle radius and the off-axis material strength which can be obtained from the experimental testing. It is proposed that

$$s_j^{critical} = \alpha_j \cdot R \tag{3.2.10}$$

where R is particle radius. α_j is calibrated from experimental testing.

For general anisotropic materials, the calibrated failure parameters α_j should have six different values, i.e., three for tension tests and three for compression tests. For orthotropic materials, such as fiber-reinforced composites, the calibrated failure parameters α_j only have four different values, since bond 2 and bond 3 should have the same stiffness due to orthotropic symmetry of the material. Thus, only two set of tension and compression tests on the two principal material directions are needed for the calibration of the failure parameters α_j. This process will be demonstrated in the numerical results section.

3.2.5 Numerical results

Several simulation results using the proposed model are presented in this section. First, the proposed model is verified against the analytical solution for the off-axis Young's modulus of general orthotropic solids. The convergence study is carried out to test the performance of the proposed model. Following this, a comparison of the deformation calculated from FEM for a center-hole specimen is performed. After that, the crack propagation path prediction capability using the proposed framework is demonstrated using an orthotropic plate with center-crack. Parametric study of the effect of the material strength on the crack path is also performed. Two

frequently studied delamination benchmarks in the literature, such as [92] and [93], are also modeled using the proposed framework. The solution method proposed in [94] is used in all the simulations in this section.

Example 1: calculation of the off-axis Young's modulus

An orthotropic rectangular plate is modeled to calculate the off-axis Young's modulus in this section. The configuration of the plate is shown in Fig. 3.2.3. The top edge of the plate is constrained in the vertical direction while the center point is fixed. An evenly distributed force with the value of 20,000 *N* is applied on the bottom edge in the negative *y* direction. The elastic properties of the material in form of the stiffness matrix is

$$\mathbf{C} = \begin{bmatrix} 281 & 133 & 0 \\ 133 & 200 & 0 \\ 0 & 0 & 114 \end{bmatrix} \text{GPa} \tag{3.2.11}$$

The global coordinate of the plate is fixed while the local material coordinate is rotated at different angles α with respect to the global coordinate system. As mentioned in Section 3.2.3, the material coordinate orientation is represented by rotating the underlying lattice structure accordingly. The calculated off-axis Young's modulus for each rotation angle α are compared with the analytical solution provided by Jones [75].

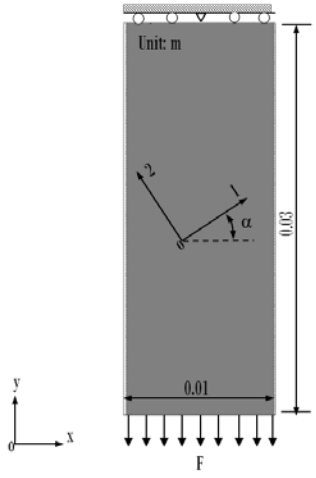

Figure 3.2.3. The Configuration of the Orthotropic Rectangular Plate for Off-Axis Test

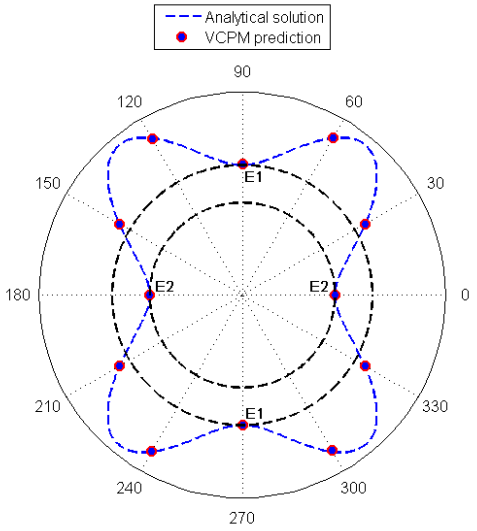

Figure 3.2.4. The Comparison of the Model Prediction and the Analytical Solution

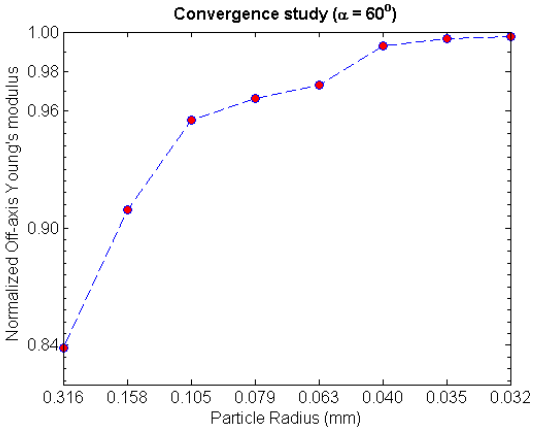

Figure 3.2.5. The Convergence Study for the Case of 60 Degree Rotation

The comparison of the predicted off-axis Young's modulus between the analytical solution and the results from the lattice particle model are shown in Fig. 3.2.4. As can be seen, the predictions match the analytical solution very well. The material anisotropy is accurately captured by the proposed lattice rotation scheme.

The convergence study of the 60^{o} lattice rotation is shown in Fig. 3.2.5. The predicted off-axis Young's moduli are normalized with the analytical solution from Jones [75]. As can be seen from the results in Fig. 3.2.5, the proposed model converges very fast to the analytical solution and the final converged result is within 0.1% error.

Example 2: comparison of the elastic deformation

In this example, the accuracy of the elastic deformation prediction is further examined for complex stress case. The same rectangular plate is used while a hole is introduced at the center of the specimen. The diameter of the hole is half of the horizontal edge length.

The displacements distributions predicted using the proposed framework are compared with the FEM solutions, which are shown in Fig. 3.2.6. As can be seen from the results, the predicted patterns and values of the displacement fields match quite well with the FEM solutions.

Proposed Lattice Particle Method FEM

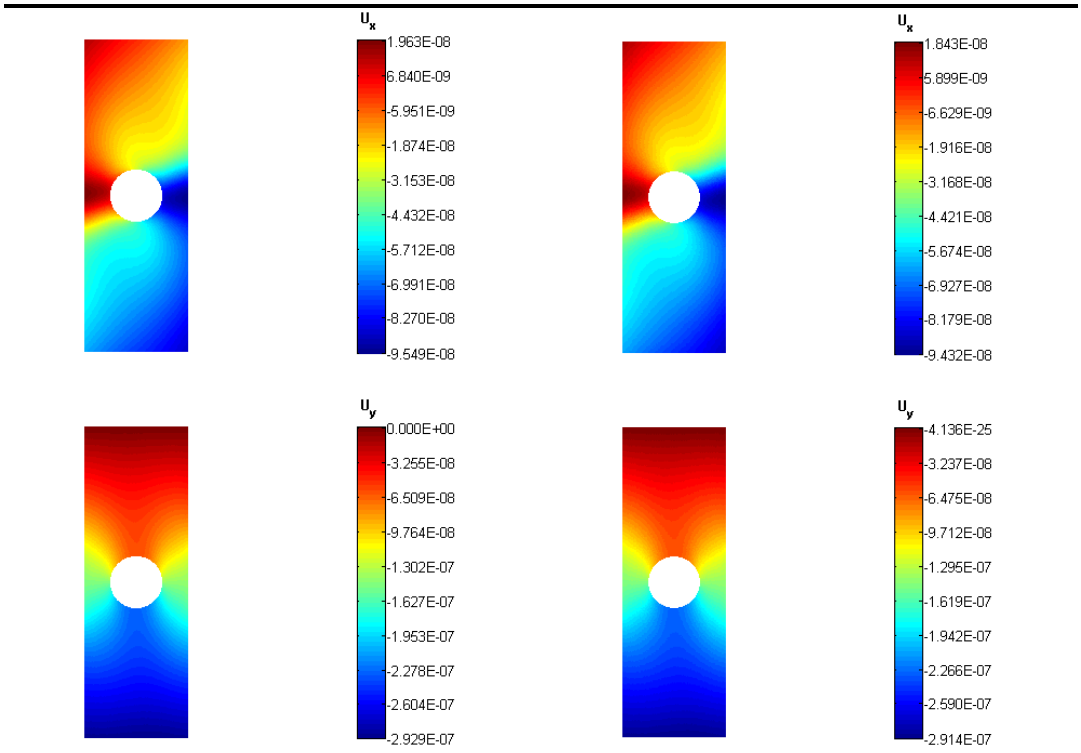

Figure 3.2.6. Comparison of Displacement Fields between Lattice Particle Model and FEM

A detailed quantitative comparison of the two displacement components at the right edge of the specimen is shown in Fig. 3.2.7. It further verifies the accuracy of the proposed framework for modeling of anisotropic elasticity problems.

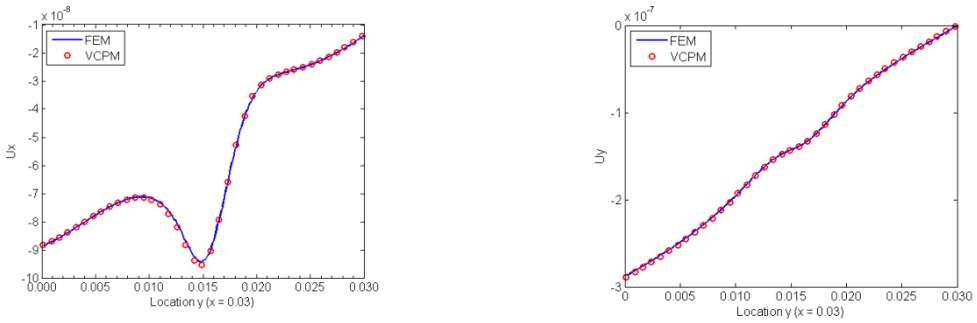

Figure 3.2.7. The Comparison of the Displacements at the Right Edge

Example 3: fracture of an orthotropic plate with pre-existing center crack

In this example, the fracture of an orthotropic lamina plate with a center through crack under uniaxial tensile loading is modeled. The plate has the same dimensions as shown in Fig. 3.2.3. The length of the crack is 4 mm. As discussed in Section 3.2.4, the failure parameters α_j can be

calibrated using the material tensile strength in the two principal directions from experiment. For demonstration purpose, the assumed values are used in the current simulation. Five different material rotations are considered, i.e., 0 ^{o}, 30 ^{o}, 45 ^{o}, 60 ^{o}, 90^{o}. All these material orientations are represented using the proposed lattice rotation scheme.

Case I:

In this case, the critical elongations of the springs are assumed to be

$$\begin{aligned} S_1^{critical} &= 0.016R \\ S_2^{critical} &= S_3^{critical} = 0.008R \end{aligned} \tag{3.2.12}$$

The final crack paths for five different rotations are shown in Fig. 3.2.8. The red lines indicate the crack paths. As can be seen, the crack path is different from that of isotropic material under pure mode I loading. When the loading is along with the material principal directions, i.e., α = 0 ^{o}, the crack path is perpendicular to the loading direction. When the loading direction is inclined with the material principal direction at different angles, e.g., 30 ^{o}, 45 ^{o} and 60 ^{o}, the crack path is perpendicular to the weak principal strength direction. This is usually observed in the experiment for some fiber-reinforced laminates [95].

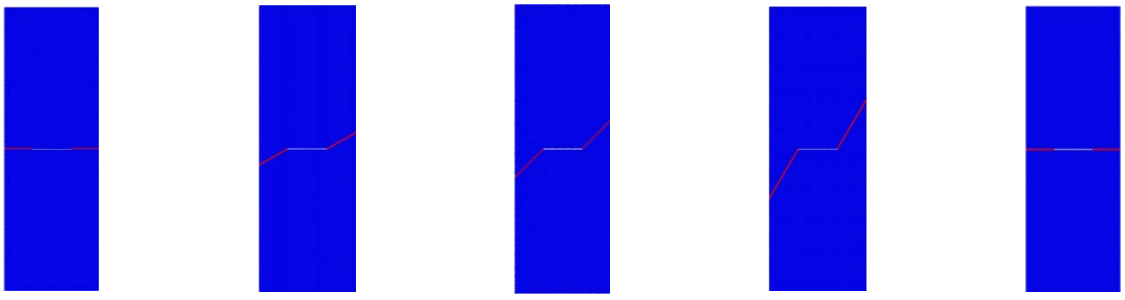

Figure 3.2.8. The Final Crack Path for Case I Material Strength

Case II:

In this case, the strength along different directions are assumed to be

$$\begin{aligned} S_1^{critical} &= 0.016R \\ S_2^{critical} &= S_3^{critical} = 0.004R \end{aligned} \tag{3.2.13}$$

The simulation results for this case are shown in Fig. 3.2.9. The crack paths for the rotations of 0 ^{o}, 30 ^{o}, 45 ^{o} and 60 ^{o} are the same as in case *I*. But for the case of 90 ^{o} rotation, the crack path is parallel to the loading direction. This is known as the crack splitting and usually observed for some composite laminates [96].

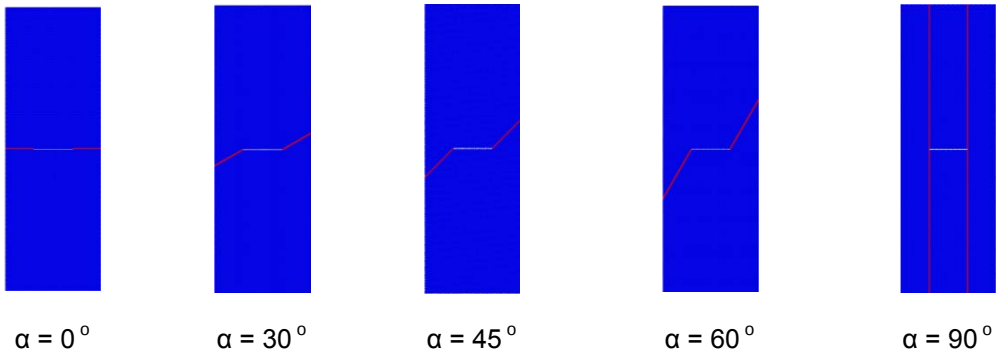

Figure 3.2.9. The Final Crack Path for Case II Material Strength

Example 4: delamination of CFRP with initial transverse crack

In this example, the delamination failure mode of an initially damaged cross-ply CFRP (Carbon Fiber-Reinforced Polymer) is studied. This model has been studied by other researchers, such as [97] and [92]. The stacking sequence for the case considered here is $[90/0]_s$. The configuration is shown in Fig. 3.2.10. The material properties are listed in Table 3.2.2.

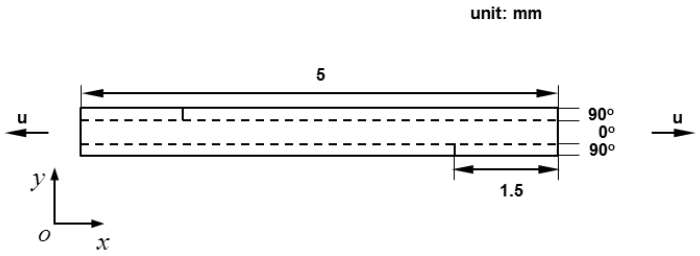

Figure 3.2.10. The Configuration of the CFRP Specimen

Table 3.2.2. The Orthotropic Material Constants for Example 4

Material constants	E_1	$E_2 = E_3$	$G_{12} = G_{13}$	G_{23}	$v_{12} = v_{13}$	v_{23}
Value (GPa)	144	9.7	4.5	3.4	0.35	0.43

Under 2D plane strain assumption, the 90^{o} ply is isotropic and has following material constants

$$\mathbf{C}_{90} = \begin{bmatrix} 12.2 & 5.4 & 0 \\ 5.4 & 12.2 & 0 \\ 0 & 0 & 3.4 \end{bmatrix} \text{GPa} \tag{3.2.14}$$

while the 0^o ply is orthotropic and has following material constants

$$\mathbf{C}_{0} = \begin{bmatrix} 148.3 & 6.1 & 0 \\ 6.1 & 12.2 & 0 \\ 0 & 0 & 4.5 \end{bmatrix} \text{GPa} \tag{3.2.15}$$

Similar to the experiment [97], a constant displacement rate is loaded at the two ends of the specimen. The initial damages are built by removing connecting springs between two pairs of neighboring particles. Since the orientation of the 0^o ply is coincident with the global coordinate, there is no need to rotate the underlying lattice structure in this example.

For the isotropic 90^o ply, all springs have the same critical elongation. For the orthotropic 0^o ply, two critical elongations are required for two different types of springs. For the interface springs, i.e., springs connecting particles belong to two different plies, they are assumed to have the same critical elongation independent of the direction. Thus, four critical elongations are required in this modeling example. The following values are used

$$\begin{aligned} S_{90}^{critical} &= 0.01R \\ S_{0-90}^{critical} &= 0.0002R \\ S_{0,1}^{critical} &= 0.016R \\ S_{0,2}^{critical} &= S_{0,3}^{critical} = 0.008R \end{aligned} \tag{3.2.16}$$

The model parameters for interface springs are taken as the arithmetic average. Justification on how to determine the interface spring properties requires additional investigation. The final delamination pattern is shown in Fig. 3.2.11. This result is consistent with the experimental observation from [92].

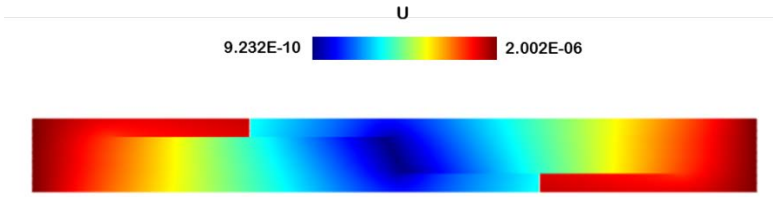

Figure 3.2.11. The Final Delamination Pattern of the CFRP Specimen

Example 5: delamination of L shaped composite panel with a fillet

The delamination analysis of the *L* shaped composites panel with fillet has been intensively studied in the literature, such as [93], [98]. In this example, we investigate the response of a simplified three-ply composite panel under monotonic constant displacement loading condition. The configuration of the composite panel is shown in Fig. 3.2.12. The corresponding material constants are given in Table 3.2.3.

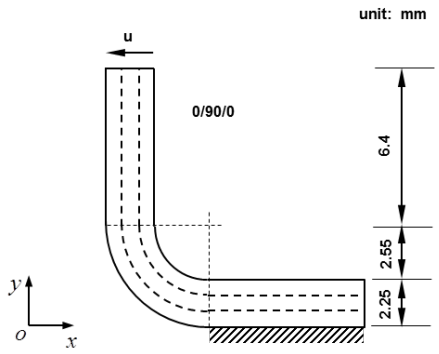

Figure 3.2.12. The Configuration of the L Shaped Composite Panel with Fillet

Table 3.2.3. The Orthotropic Material Constants for Example 5

Material constants	E_{11}	$E_{22}=E_{33}$	$G_{12}=G_{13}$	G_{23}	$\nu_{12}=\nu_{13}$	ν_{23}
Value (GPa)	139.3	9.72	5.59	3.45	0.29	0.40

Plane strain condition is assumed in this simulation. The 90^o ply is isotropic and the material stiffness matrix is

$$\mathbf{C}_{90}=\begin{bmatrix} 11.7 & 4.8 & 0 \\ 4.8 & 11.7 & 0 \\ 0 & 0 & 3.45 \end{bmatrix} \text{GPa} \tag{3.2.17}$$

while the 0^o ply is orthotropic and the material stiffness matrix is

$$\mathbf{C}_0 = \begin{bmatrix} 11.7 & 4.8 & 0 \\ 4.8 & 142.1 & 0 \\ 0 & 0 & 5.59 \end{bmatrix} \text{GPa} \tag{3.2.18}$$

In this case, the underlying lattice structure was rotated by 90 ^{o} to account for the material longitude direction along the *y* axis. For the critical elongations, the same values have been used in this example as the previous one, i.e., Eq. (3.2.16).

Figure 3.2.13. The Delamination Initiation Location and the Final Delamination Pattern

The initial and final delamination patterns are shown in Fig. 3.2.13. The reaction-displacement curve is shown in Fig. 3.2.14. Due to the applied constraint, the delamination initiates between the 90 ^{o}/0 ^{o} plies at the horizontal direction (point A in Fig. 3.2.14). With increase of the loading, this horizontal delamination is frozen while the delamination between the 0 ^{o}/90 ^{o} plies at the fillet area develops (point B in Fig. 3.2.14). Further increase of the displacement results in a fast delamination propagation and hence a sharp drop down in the reaction force. A snap through response occurs. Stable state is regained (point C in Fig. 3.2.14) and the delamination starts to propagate vertically (point D in Fig. 3.2.14). This reaction-displacement curve is consistent with experimental observations [93].

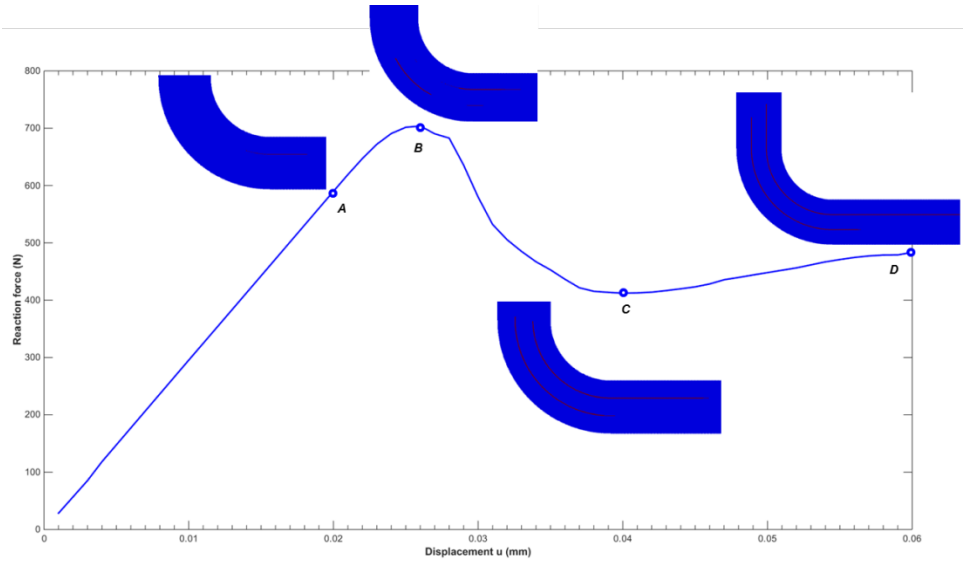

Figure 3.2.14. The Reaction-Displacement Curve with Details on the Delamination

3.2.6 Discussion and conclusion

A non-local lattice particle framework for modeling 2D general anisotropic elastic material was proposed in this section. The proposed lattice particle framework represents the material anisotropy by rotating the underlying lattice structure rather than transforming the material stiffness matrix which is generally used in some other numerical methods, such as FEM. The equivalency between this lattice rotation scheme and the traditional matrix transformation scheme was shown analytically and numerically. Several benchmark problems have been employed to verify and test the performance of the proposed framework. From the simulation results, both elastic and fracture response of composite materials can be accurately captured using the proposed framework. Several conclusions can be drawn based on the proposed study:

1). The proposed non-local lattice model is able to model arbitrary 2D anisotropic solids with a unique mapping relationship between the model parameters and the material constants;

2). The proposed lattice rotation scheme can handle the fracture path in anisotropic materials naturally without transforming the material stiffness matrix;

3). Fracture path simulation using the topological lattice structure agrees with many existing numerical and experimental observations in the current investigation for 2D orthotropic composite laminates.

Future work is required to further quantitatively validate the model predictions with experimental testing data for composite materials. Additional work is also required to extend the proposed framework to general 3D cases. The extension to anisotropic plasticity, such as the crystal plasticity, needs further study.

3.3 2D Polycrystalline Materials

In this section, the anisotropic lattice particle model is applied to investigate the microstructural effects, such as the crystallographic orientation distribution and grain boundary properties, on the mechanical performance of 2D polycrystalline materials. The classical approach of treating material anisotropy in other numerical methods, such as finite element method, is by transforming the material stiffness matrix for each crystallite. In the lattice particle model, the polycrystalline microstructures are constructed by rotating the underlying topological lattice structure consistently with the material crystallographic orientation while keeping the material stiffness matrix intact. By rotating the underlying lattice structure, the grain boundaries between different grains are naturally generated at locations where two crystallites meet. Thus, the grain boundary effect on the performance of the crystalline aggregates can be naturally incorporated. Parametric studies on the effects of crystallographic orientation distribution on both elastic and fracture behavior of polycrystalline materials are performed. The simulation results are compared with both analytical solutions and experimental observations in the open literature. Conclusions and discussions are drawn based on the current study.

3.3.1. Introduction

Polycrystalline material is an aggregate of microstructural crystallites of various size, shape and crystallographic orientation. Its macroscopic properties are affected by the underlying microstructures. At the crystallite level, the material properties are anisotropic and orientation dependent. The macroscopic behavior of polycrystalline materials can be regarded as statistically isotropic when the materials have random crystallographic and morphologic texture. The influence of individual crystallite on the overall macroscopic behavior of the aggregate is negligible. Under these assumptions, various theoretical prediction approaches have been proposed for the estimation of the effective elastic properties of materials of this kind, such as the

representative work of Voigt [99], Reuss [100], Hill [101], Kröner [102] and Hashin and Shtrikman [103], [104].

In practice, an ideally randomly oriented crystalline aggregate is very difficult to obtain. Initial deviation from this randomness may occur during the solidification process due to differences in crystal growth along different directions. Subsequent metal working processes, such as rolling, extrusion and annealing, provide other mechanisms for the formation of preferred orientation textures. This non-random distribution of crystallographic orientation influences the macroscopic properties of crystalline aggregates. The applicability of the aforementioned analyses for this type of polycrystal texture becomes very limited. Many theoretical works on extension of the Voigt-Reuss type analyses to materials with certain degree of texture exist in the literature, such as [105], [106], [107], [108], [109], [110]. It should be noted that perfect grain boundaries are assumed in all the theoretical predictions for effective elastic constants of a polycrystalline material with or without texture.

Grain boundary also plays a significant role on the fracture behavior of the polycrystalline materials [111], [112]. Different grain boundary properties may result in different fracture mode, e.g., intergranular or transgranular fracture. Numerous models have been developed to simulate the fracture behavior of polycrystalline materials, such as FEM with cohesive zone [113], [114], XFEM [115], [116], Geometric models [117], [118], Monte Carlo model [119], [120] and Molecular Dynamics [121], [122]. A detailed review on computational modeling of fracture in polycrystalline materials can be found in [123].

Lattice models have been widely used in the field of computational solid mechanics, such as [89], [38], [52]. It has advantages over the other numerical methods in fracture modeling, such as easiness of cracking presentation and no requirement of external rule to guide the crack growth. Grah et al. [45] has used a general αβ-model [10] to investigate the fracture behavior of 2D brittle polycrystalline materials. In their formulation, both the α-spring and β-spring, i.e., axial and angular springs, respectively, have been utilized. Various grain orientations were represented by the transformation of the material stiffness matrix. Although the spring stiffness can be easily

assigned using the transformed materials stiffness, the shear springs suffers from the negative value for most of the grain orientations. In addition, the intrinsic fracture anisotropy of the lattice structure still persist [52]. Another effort to apply the lattice model to polycrystalline materials was done by Rindaldi et al. [80]. In this model, the effective elastic properties, i.e., Young's modulus and Poisson's ratio, were estimated using a novel mapping procedure between the FEM and the lattice spring formulations. According to their results, the estimated average Young's modulus is consistent with the experimental results. However, the Poisson's ratio could not be matched and its value is fixed around 0.33 for all simulation cases.

Recently, Chen et al. [124] have proposed a lattice particle model for modeling elastic and fracture behavior of two-dimensional general anisotropic materials. Unlike transforming the materials stiffness matrix in other numerical approaches, the material anisotropy is represented by rotating the underlying lattice structures consistently with the local material's frame in lattice particle model. By doing this, the occurrence of negative spring stiffness is avoided and the intrinsic lattice fracture anisotropy is incorporated into the material anisotropy. The simulated results for both elastic and fracture problems match well with the analytical solutions and experimental observations. In this paper, we apply the two-dimensional anisotropic lattice particle formulation proposed by Chen et al. [124] to model polycrystalline materials. The grain boundary and the crystallographic orientation distribution effects on the elastic and fracture behaviors are investigated in detail. The content of this paper is organized as follows. First, a brief review on the background theory and formulation of the lattice particle model is presented. Then, details on how to apply lattice particle model to model polycrystalline materials are discussed. Special focus is on how the crystal system is generated using the crystallographic orientation information and how the grain boundary is treated in lattice particle model. Following this, the model is applied to investigate various microstructural effects on the overall elastic properties and the fracture behavior of a polycrystalline material, including the grain boundary effect and the crystallographic orientation effect. Discussions and conclusions based on this study are drawn.

3.3.2. Theory and Formulation: a review

In this part, we briefly review the basic ideas on the background theory and formulation of the lattice particle model. A detailed derivation can be found in [124].

For a general two-dimensional anisotropic material, six independent components of the material stiffness matrix are required in order to fully characterize its elastic deformation. Using Voigt notation, the material stiffness matrix for the in-plane deformation has following form:

$$\left[C_{ij}\right]=\begin{bmatrix} C_{11} & C_{12} & C_{16} \\ & C_{22} & C_{26} \\ sym & & C_{66} \end{bmatrix} \tag{3.3.1}$$

In order to be consistent with the six degrees of freedom in this continuum model, there are also six independent model parameters in the proposed lattice particle model. The potential energy in lattice particle model was proposed as

$$U_{cell}=\frac{1}{2}\sum_{j=1}^{6}k_{ij}\left(\delta l_{ij}\right)^2+\frac{1}{2}\left(\sum_{j=1}^{6}T_{ij}\delta l_{ij}\right)\left(\sum_{j=1}^{6}\delta l_{ij}\right) \tag{3.3.2}$$

In which k_{ij} are the spring stiffness parameters and T_{ij} are the volume-related parameters for the six springs associated with a unit cell *i*. A typical unit cell with its six normal springs is shown in Fig. 3.3.1. And the corresponding unit normal vectors are shown in Table 3.3.1. Due to symmetry, the springs in opposite directions should have the same local and nonlocal model parameters. Thus, for general two-dimensional anisotropic materials, the total number of model parameters is six in the proposed lattice particle model.

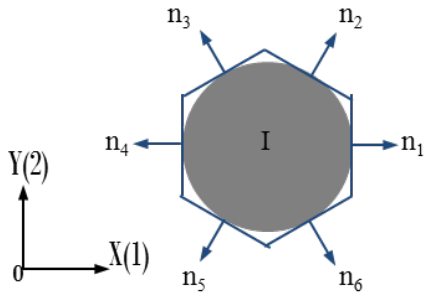

Figure 3.3.1. A Typical Unit Cell and Its Six Normal Vectors

Table 3.3.1. The Normal Vectors for the Six Nearest Neighbors of a Unit Cell

n_1	n_2	n_3	n_4	n_5	n_6
$(1,0)$	$\left(1/2,\sqrt{3}/2\right)$	$\left(-1/2,\sqrt{3}/2\right)$	$(-1,0)$	$\left(-1/2,-\sqrt{3}/2\right)$	$\left(1/2,-\sqrt{3}/2\right)$

Given the unit normal vectors of the six normal springs, the potential function of a unit cell can be rewritten in terms of the components of the strain matrix as

$$U_{cell}=\frac{1}{2}\sum_{b=1}^{6}k_b n_i^b \varepsilon_{ij} n_j^b n_k^b \varepsilon_{kl} n_l^b+\frac{1}{2}\left(\sum_{b=1}^{6}T_b n_i^b \varepsilon_{ij} n_j^b\right)\left(\sum_{b=1}^{6}n_k^b \varepsilon_{kl} n_l^b\right) \tag{3.3.3}$$

Due to the conservation of the potential energy, the material stiffness matrix in terms of the model parameters can be obtained as

$$C_{ijkl}=\frac{1}{V}\frac{\partial^2 U_{cell}}{\partial\varepsilon_{ij}\partial\varepsilon_{kl}} \tag{3.3.4}$$

where V is the volume of a unit cell, $V=2\sqrt{3}hR^2$. For dimensional consistency, the unit thickness h is used. The unit thickness h is omitted in following derivation unless ambiguity arises.

Comparing the derived materials stiffness matrix with the Hooke's law, the relationship between the model parameters and the components of the material stiffness matrix can be uniquely obtained as

$$\begin{Bmatrix} k_1 \\ k_2 \\ k_3 \\ T_1 \\ T_2 \\ T_3 \end{Bmatrix} = \begin{bmatrix} \sqrt{3} & \sqrt{3} & -\frac{4\sqrt{3}}{3} & 0 & 0 & -2\sqrt{3} \\ 0 & 0 & \frac{8\sqrt{3}}{3} & 4 & -4 & 0 \\ 0 & 0 & \frac{8\sqrt{3}}{3} & -4 & 4 & 0 \\ 0 & -\frac{4\sqrt{3}}{9} & \frac{2\sqrt{3}}{3} & 0 & 0 & \frac{2\sqrt{3}}{3} \\ 0 & \frac{2\sqrt{3}}{9} & -\frac{2\sqrt{3}}{3} & -\frac{2}{3} & 2 & 0 \\ 0 & \frac{2\sqrt{3}}{9} & -\frac{2\sqrt{3}}{3} & \frac{2}{3} & -2 & 0 \end{bmatrix} \begin{Bmatrix} C_{11} \\ C_{22} \\ C_{66} \\ C_{26} \\ C_{16} \\ C_{12} \end{Bmatrix} \tag{3.3.5}$$

The above mapping relationship is unique. When the material is isotropic, Eq. (3.3.5) reduces to the special case for isotropic homogeneous materials has been studied in [38].

3.3.3. Generation of the crystal system

An accurate knowledge of the morphological structure of a polycrystalline material is crucial for subsequent modeling and prediction of its physical properties and performance. Many experimental and computational material microstructure characterization techniques are available in the literature, such as x-ray tomography technique [125], lattice-point method [126] , and CAD-based methodology [127]. For illustrative purpose, the polycrystal systems that will be investigated in this study are generated by Voronoi Tessellation technique using MATLAB. The voronoi seeds are generated using a Hard-Particle Monte Carlo method [128]. There are some advantages of using this method to generate the Voronoi seeds, such as controlling the size distribution of the crystallites. Figure 2 shows a 1000 Voronoi seeds generated using the Hard-Particle Monte Carlo method (Fig. 3.3.2(a)) and the associated Voronoi tessellation (Fig. 3.3.2(b)) and cell size distribution (Fig. 3.3.2(c)).

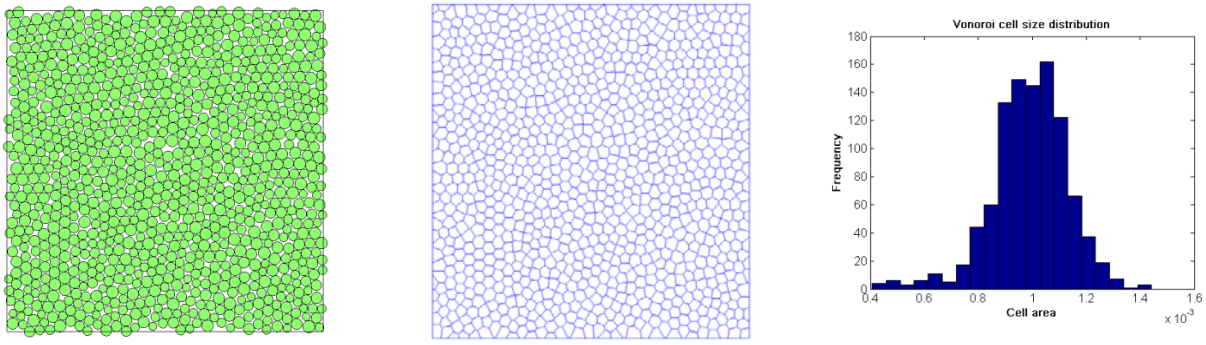

(a) (b) (c)

Figure 3.3.2. The Voronoi Seeds, Tessellation and the Size Distribution

3.3.4. Lattice Rotation and Grain Boundary Generation

Unlike the classical way of treating the crystallographic orientation for different grains by transforming the material stiffness matrix under a reference frame, the proposed model rotates the topological lattice structure consistently with the material crystallographic orientation while keeping the material stiffness matrix intact. This idea is illustrated in Fig. 3.3.3. For a given crystallographic orientation of a specific crystallite, the lattice structure is rotated such that the reference frame for the lattice particle model is coincident with the material crystallographic orientation. The rotation of the lattice structure follows the vector transformation rule as:

$$\mathbf{X}' = \mathbf{Q}\mathbf{X} \tag{3.3.6}$$

where $\mathbf{Q} = \begin{bmatrix} \cos(\alpha) & \sin(\alpha) \\ -\sin(\alpha) & \cos(\alpha) \end{bmatrix}$ is the transformation matrix, and α is positive when the transformation from $\mathbf{X}$ to $\mathbf{X}'$ is counter-clockwise.

By rotating the lattice structure, the material anisotropy is naturally represented in the proposed model. The equivalency between the material stiffness matrix transformation and the lattice rotation has been shown both analytically and numerically in [124].

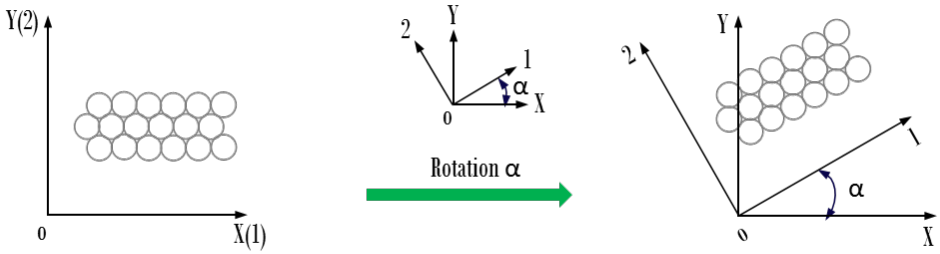

Figure 3.3.3. The Lattice Rotation Scheme Proposed in Lattice Particle Model

For each crystallite, the procedure of rotating the underlying lattice is performed accordingly. And the grain boundary is automatically generated at locations where two crystals meet. A replacing process is used to replace any overlapping-particle clusters whose degree of overlapping is greater than a pre-specified value by a new particle positioned at the center of the cluster. This process is repeated until all of the overlappings are less than the specified value. And the distance between any particles after this process are defined as the un-deformed distance. This is very similar to the deletion [129] and the energy minimization [130] processes in the Molecular Dynamics (MD). Other grain boundary generation processes, such as the simulated solidification process [131] and the devised MD simulation [132] can be applied. The typical grain boundaries generated using the replacing procedures in lattice particle model are shown in Fig. 3.3.4. Crystallites I, II and III have different crystallographic orientations, with values of 15, -15, 0 degrees, respectively. The boundary between crystallite I and II is a twin boundary. The red particles on the grain boundaries are the boundary particles. Fig. 3.3.4 shows the different grain boundary structure with different threshold overlapping distance (i.e., R, 1.2R, and 1.5R, respectively). R is the radius of the particles. It appears that the threshold value of 1.2R gives a satisfactory representation of grain boundaries. In all simulations in the following sections, the critical value of 1.2 R is used to generate the grain boundary between different grains.

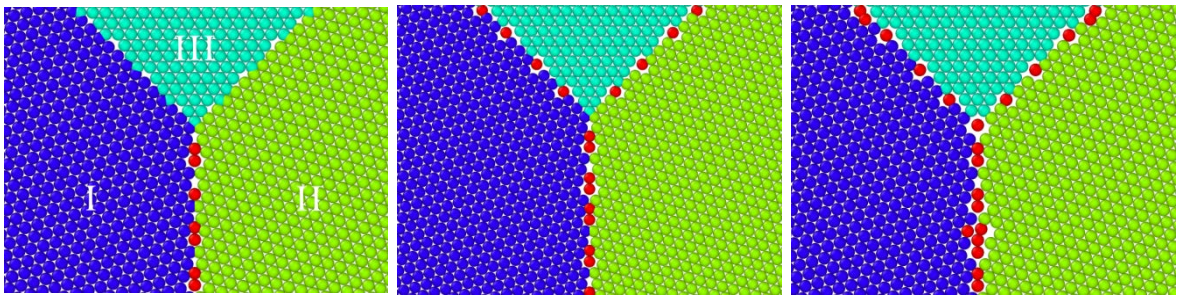

R 1.2R 1.5R

Figure 3.3.4. The Grain Boundaries Generated Using Different Overlapping Degree

3.3.5. Procedures for calculating the effective elastic constants

Procedures on estimating the effective elastic constants of polycrystalline materials in lattice particle model are developed based on the energy of the system. First, a two-step procedure for statistically isotropic materials is derived. After that, an analogical four-step procedure for materials don't possess any material symmetry is formulated. All derivations are based on a square Representative Volume Element (RVE).

Assuming the material to be evaluated is statistically isotropic, an energy-based two-step estimation scheme can be applied to approximate the effective elastic constants in lattice particle model. The two-step estimation procedure is shown below.

1). Subjecting the RVE to a uniform bi-axial extension. The corresponding strain state is $\varepsilon_{xx} = \varepsilon_{yy} = \varepsilon_0, \varepsilon_{xy} = 0$. The total energy $U_{(1)}$ of the RVE is the sum of energies of all unit cells, or particles;

2). Subjecting the RVE to uniform uniaxial extension along one direction and to uniform uniaxial compression along the perpendicular direction. The corresponding strain state is $-\varepsilon_{11} = \varepsilon_{22} = \varepsilon_0, \varepsilon_{xy} = 0$. The total energy is expressed as $U_{(2)}$.

3). In terms of the bulk modulus K and shear modulus G, the energy of a two-dimensional linear elastic isotropic continuum of volume V is

$$U = V\left(\frac{K}{2}\varepsilon_{ii}\varepsilon_{jj} + G\left(\varepsilon_{ij}\varepsilon_{ij} - \frac{1}{2}\varepsilon_{ii}\varepsilon_{jj}\right)\right) \tag{3.3.7}$$

Thus, the two-dimensional bulk and shear moduli can be calculated through these steps as

$$K = \frac{1}{2}\frac{U_{(1)}}{V\varepsilon_0^2}$$
$$G = \frac{1}{2}\frac{U_{(2)}}{V\varepsilon_0^2} \tag{3.3.8}$$

For linear elastic isotropic materials, the two-dimensional bulk and shear moduli can be expressed in terms of the Young's modulus and Poisson's ratio as [133]

$$G = \frac{E}{2(1+\nu)} \tag{3.3.9}$$

For plane stress case,

$$K = \frac{E}{2(1-\nu)} \tag{3.3.10}$$

For plane strain case,

$$K = \frac{E}{2(1+\nu)(1-2\nu)} \tag{3.3.11}$$

For generally anisotropic materials, the procedure to estimate the effective elastic constants is analogous to that of statistically isotropic materials. The strain energy density of a two-dimensional general anisotropic material represented in terms of the elastic constants and components of strain tensor is

$$U = \frac{V}{2}\left(C_{11}\varepsilon_{xx}^2 + C_{22}\varepsilon_{yy}^2 + 2C_{12}\varepsilon_{xx}\varepsilon_{yy} + 4C_{16}\varepsilon_{xx}\varepsilon_{xy} + 4C_{26}\varepsilon_{yy}\varepsilon_{xy} + 4C_{66}\varepsilon_{xy}^2\right) \tag{3.3.12}$$

in which C_{16} and C_{26} are the Constants of Mutual Influence [134].

The four-step estimation procedure is carried out as follows:

1). Subjecting the RVE to a uniform uniaxial tension in x direction while the deformation in y direction is fixed. The corresponding strain state is $\varepsilon_{xx} = \varepsilon_0, \varepsilon_{yy} = 0, \varepsilon_{xy} = 0$. The strain energy of the system is $U_{(1)}$;

2). Subjecting the RVE to a uniform uniaxial tension in y direction while the deformation in x direction is fixed. The corresponding strain state is $\varepsilon_{xx}=0,\varepsilon_{yy}=\varepsilon_0,\varepsilon_{xy}=0$. The strain energy of the system is $U_{(2)}$;

3). Subjecting the RVE to a uniform bi-axial extension. The corresponding strain state is $\varepsilon_{xx}=\varepsilon_0,\varepsilon_{yy}=\varepsilon_0,\varepsilon_{xy}=0$. The strain energy of the system is $U_{(3)}$;

4). Subjecting the RVE to a pure shear. The corresponding strain state is $\varepsilon_{xx}=\varepsilon_{yy}=0,\varepsilon_{xy}=\varepsilon_0$. The strain energy of the system is $U_{(4)}$;

5). Using the strain energy expression given in Eq. (3.3.12), the elastic constants can be calculated using the data from the four-step test. The calculated elastic constants can be expressed as

$$\begin{aligned} C_{11} &= \frac{1}{2}\frac{U_{(1)}}{V\varepsilon_0^2} \\ C_{22} &= \frac{1}{2}\frac{U_{(2)}}{V\varepsilon_0^2} \\ C_{12} &= \frac{U_{(3)}-U_{(2)}-U_{(1)}}{V\varepsilon_0^2} \\ C_{66} &= \frac{1}{8}\frac{U_{(4)}}{V\varepsilon_0^2} \end{aligned} \tag{3.3.13}$$

The above discussion completes the formulation of the lattice particle model, the microstructure and grain boundary generation, and the effective elastic constants estimation procedure in the proposed method. In following section, the proposed lattice particle model will be applied to numerically investigate the microstructural effect on both the elastic and fracture behavior of polycrystalline materials.

3.3.6. Numerical Investigation

Several numerical results from the simulation using the proposed framework are presented in this section. First, the effects of grain boundary properties and the crystallographic orientation

distribution on the effective elastic constants of a polycrystalline material are studied. Special focus is on the effective elastic constants of a polycrystalline material with texture. The degree of texture is defined as the number of crystallites having certain specific orientation by the total number of crystallites of a specimen. Following this, the effects on the brittle fracture behavior of a polycrystalline material are investigated. Parametric studies on the grain boundary properties and crystallographic orientation distribution on the fracture mode and material strength are performed.

For simplicity, the specimens for both elasticity and fracture simulations in this section have the same dimension as shown in Fig. 3.3.5. The only difference is that there is a pre-existing single edge notch in the fracture simulation case, which is not shown in Fig. 3.3.5. The total number of grains is 1000. The material elastic constants of single aluminum crystallite from [135] are utilized in all the simulations, which can be expressed in the matrix format as

$$\mathbf{C} = \begin{bmatrix} 108.24 & 62.16 & 0 \\ 62.16 & 108.24 & 0 \\ 0 & 0 & 28.41 \end{bmatrix} \text{GPa} \tag{3.3.14}$$

According to [135], the Young's modulus calculated by the Hashin-Shtrikman bounds [104] for macroscopically isotropic aggregates produced by the above aluminum crystallites is $E_{HS} = 70.5$ GPa and the Poisson's ratio is $v_{HS} = 0.348$. By Eqs. (3.3.9) and (3.3.11), the corresponding bulk and shear moduli can be calculated as $K_{HS} = 86.0$ GPa and $G_{HS} = 26.1$ GPa.

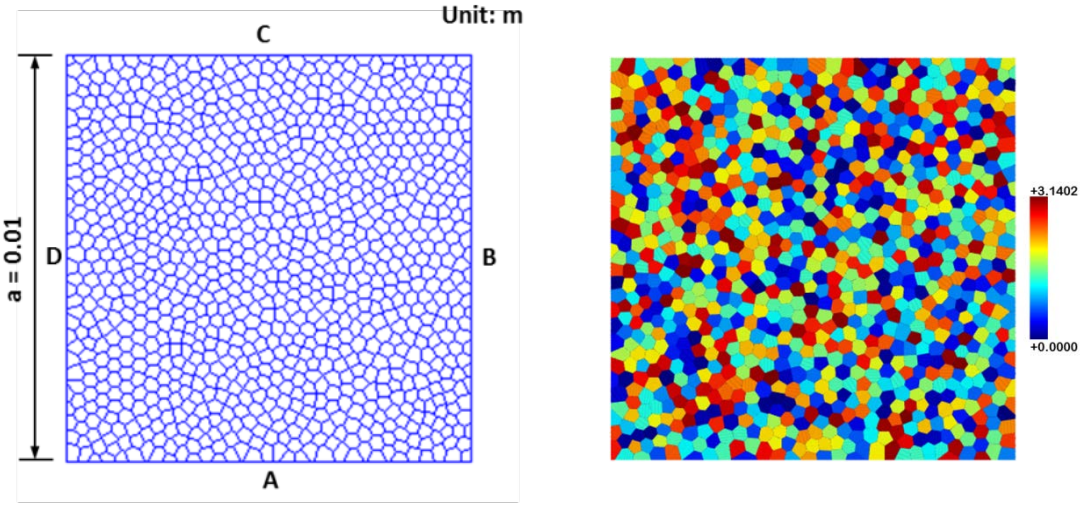

(a). Dimensions (b). The orientation distribution

Figure 3.3.5. The Configuration of the Polycrystalline Specimen

Elasticity

For the numerical method of simulations in this section, the implicit Atomic-scale Finite Element Method (AFEM) developed in [124], [94] is utilized. Details about the AFEM and application of AFEM to lattice particle model can be found in [136] and [94], respectively.

Grain boundary effect

As discussed in previous part, the grain boundaries can be built up in a similar way as in MD simulation. The determination of the grain boundary properties, i.e., spring stiffness and volume-related parameter of particles on the grain boundaries, is an open problem. Similar techniques in the grain boundary theory and engineering [137] may be applied in lattice particle model. For simplification, the spring stiffness and volume-related parameter are assumed to be the same for all boundary particles. Values of arithmetic average, minimum and maximum of the three types of springs are used and the resultant effective elastic constants are compared.

In this simulation, the crystallographic orientation distribution is random and thus the macroscopic behavior is isotropic. Therefore, the two-step evaluation procedure (i.e., for isotropic materials) is used to calculate the effective bulk modulus and shear modulus. The simulation results are

shown in Fig. 3.3.6 for the normalized elastic constants (i.e., simulation results are normalized by the Hashin-Shtrikman solution).

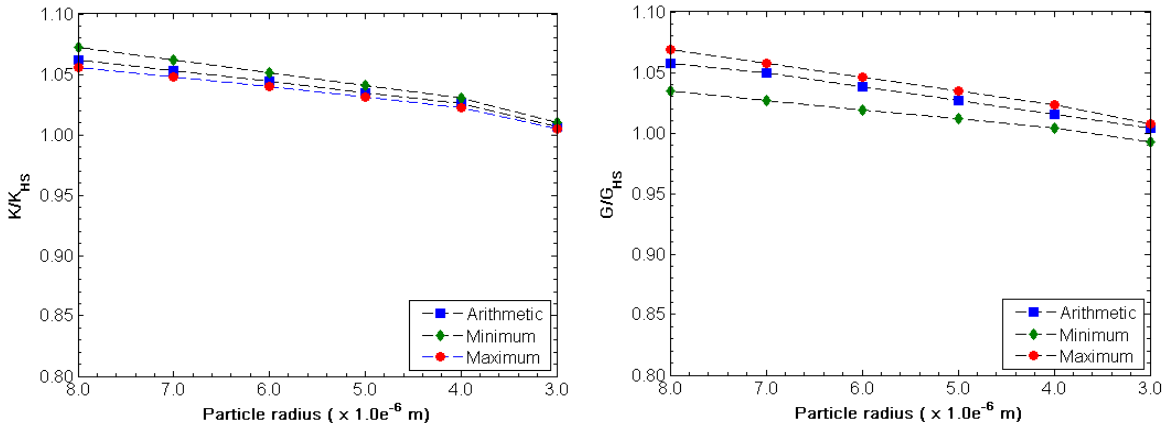

Figure 3.3.6. The Effect of Grain Boundary Properties and the Convergence

As can be seen in Fig. 3.3.6, the bulk and shear moduli obtained from the lattice particle simulation match well with the Hashin-Shtrikman predictions. There exists certain difference in the converged values for different grain boundary properties, i.e., different grain boundary properties will results in different effective elastic constants in the estimation. This difference is grain boundary property dependent. The larger difference between the grain boundary properties, the greater the difference of effective elastic constants. In the given results in Fig. 3.3.6, the relationship between the grain boundary properties is: $GB_{\text{maximum}} > GB_{\text{arithmetic}} > GB_{\text{minimum}}$. The resultant relationship between the bulk modulus is $K_{\text{maximum}} < K_{\text{arithmetic}} < K_{\text{minimum}}$, and for the shear modulus is $G_{\text{maximum}} > G_{\text{arithmetic}} > K_{\text{minimum}}$.

Grain orientation distribution effect

To investigate the grain orientation distribution effect on the effective elastic constants, the fully random distributed crystallographic orientation used in section (a) is modified such that certain degrees of orientation preference, or texture, exist in the material. This is achieved by assigning a specific orientation value to certain amount of random grains which others keep intact. In this case, the specific value is set as *Pi/4*. Since the crystallographic orientation distribution is not completely random, it is assumed that there is no material symmetry in the polycrystalline

materials. Thus, the general four-step procedure is used to estimate the effective elastic constants for each different configuration. The grain boundary properties are assumed to be the arithmetic average.

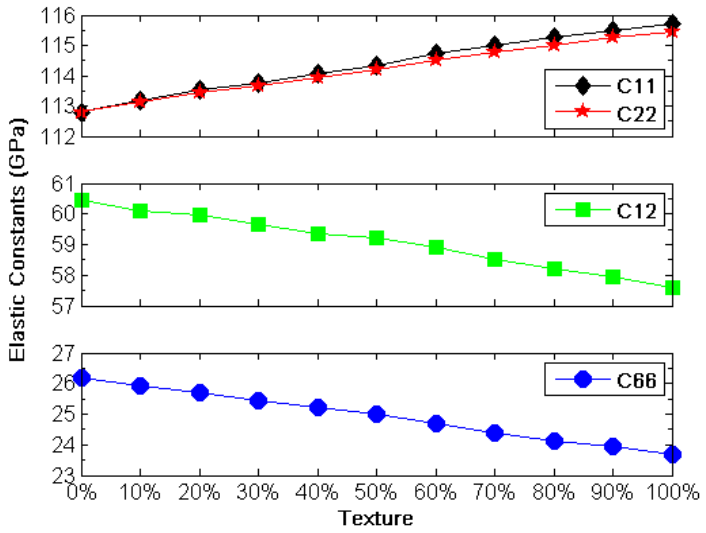

Figure 3.3.7. The Effect of Grain Orientation Distribution

The results for various degrees of texture are shown in Fig. 3.3.7. The horizontal axis is the texture degree. 0% indicates no texture and 100% indicates all grains have the same orientation. As can be seen from the results, the texture can change the elastic constants significantly and consistent with analytical prediction. The difference in the predicted value of C11 and C22 is result from the grain boundary effect.

Fracture

In lattice particle model [124], the fracture behavior of materials is governed by a spring-based critical stretch failure criterion. The crack initiation and propagation are the natural outcome of the spring breakage. No additional external criteria are required. As has been proposed in [124], three calibrated failure parameters are needed in order to simulated the facture behavior of a general two-dimensional anisotropic materials.

$$s_j^{critical} = \alpha_j \cdot R \tag{3.3.15}$$

where $s_j^{critical}$ and α_j is the critical stretch and failure parameter for the jth spring, respectively. R is the particle radius.

For the given materials in this section, i.e., Eq. (3.3.14), according to Eq. (3.3.5), spring 2 and spring 3 are identical since they have the same stiffness parameter and volume-related parameter. Both of them are larger than those of spring 1. Thus, there are only two failure parameters need to be calibrated before carrying out the simulation process. For simplification, the failure parameters are assumed to be

$$\begin{aligned} \alpha_1 &= 0.0005 \\ \alpha_2 &= \alpha_3 = 0.0006 \end{aligned} \tag{3.3.16}$$

For the fracture simulation in this section, a pre-existing crack on edge D is inserted into the specimen shown in Fig. 3.3.5. The initial crack length is 1/10 of the edge length. A uniaxial tensile testing is simulated by applying the displacement boundary condition on edge A and C. The specimen is loaded until the crack propagates through the whole specimen. The particle dynamics solution scheme [52] is utilized in this section. The stiffness and volume-related parameters for springs on the grain boundary are assumed to take the arithmetic average values.

Grain boundary effect

Parametric study on the effect of material strength of the grain boundary springs on the fracture mode is performed. The simulation results of the final crack path are shown in Fig. 3.3.8, and the reaction force profiles on the top edge C are shown in Fig. 3.3.9.

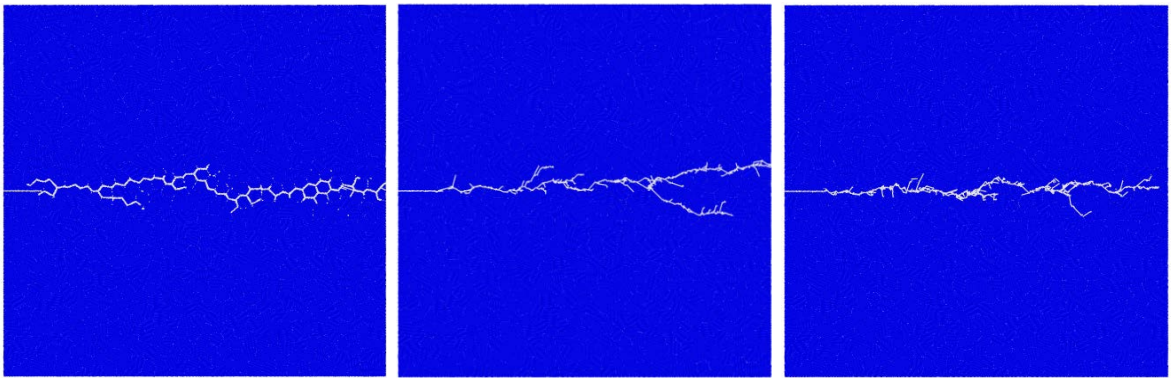

Weak GB ($\alpha_{GB} = 0.0001$) Moderate GB ($\alpha_{GB} = 0.0005$) Strong GB ($\alpha_{GB} = 0.001$)

Figure 3.3.8. The Grain Boundary Effect on the Fracture Behavior: Crack Path

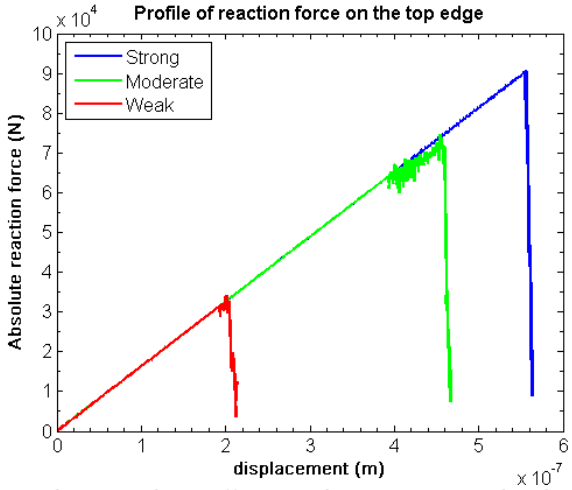

Figure 3.3.9. The Grain Boundary Effect on the Fracture Behavior: Reaction Profile

As can be seen in Fig. 3.3.8, the change of the fracture mode in lattice particle model can be governed by the strength of the grain boundaries. With weak grain boundary strength, e.g., $\alpha_{GB} = 0.0001$, the examined polycrystalline material exhibits intergranular fracture. When the strength of the grain boundary increases, e.g., $\alpha_{GB} = 0.001$, the fracture mode changes to transgranular fracture from the intergranular fracture. For the case of moderate strength, i.e., $\alpha_{GB} = 0.0005$, since we assume isotropic properties for the grain boundary, the fracture mode is transgranular fracture. But the material strength is increased comparing to the case of $\alpha_{GB} = 0.0001$, but not as great as the case of $\alpha_{GB} = 0.001$, as can be seen from Fig. 3.3.9. There is also an interesting arrest-propagate cracking phenomenon in the transgranular fracturing, as shown in Fig. 3.3.9. The crack initiates when the applied force reaches certain level, due to local high strength in front of the crack tip, the crack is arrested after some propagation distance. The crack starts to propagate again after the global applied force reaches another critical value.

Grain orientation distribution effect

For textured polycrystalline materials, since the underlying microstructural information has been changed, the fracture behavior should also be different from the non-textured material, assuming all other factors are the same. In this section, the grain orientation distribution effect of the facture

response of a textured polycrystalline material is investigated. The simulation results for the four cases of texture degrees, i.e., 30%, 50%, 80% and 100%, are shown in Fig. 3.3.10 and Fig. 3.3.11.

As can be seen from Fig. 3.3.10 and Fig. 3.3.11, the general crack path is similar which is governed by the pure mode I loading condition, but both the local crack path and the peak load are changed. With the increase of the degrees of texture, the crack is more likely to branch, for both weak and strong grain boundaries. The material strength for different degrees of texture is also different; with the 100% textured material has the highest strength in the texture direction, as shown in Fig. 3.3.11.

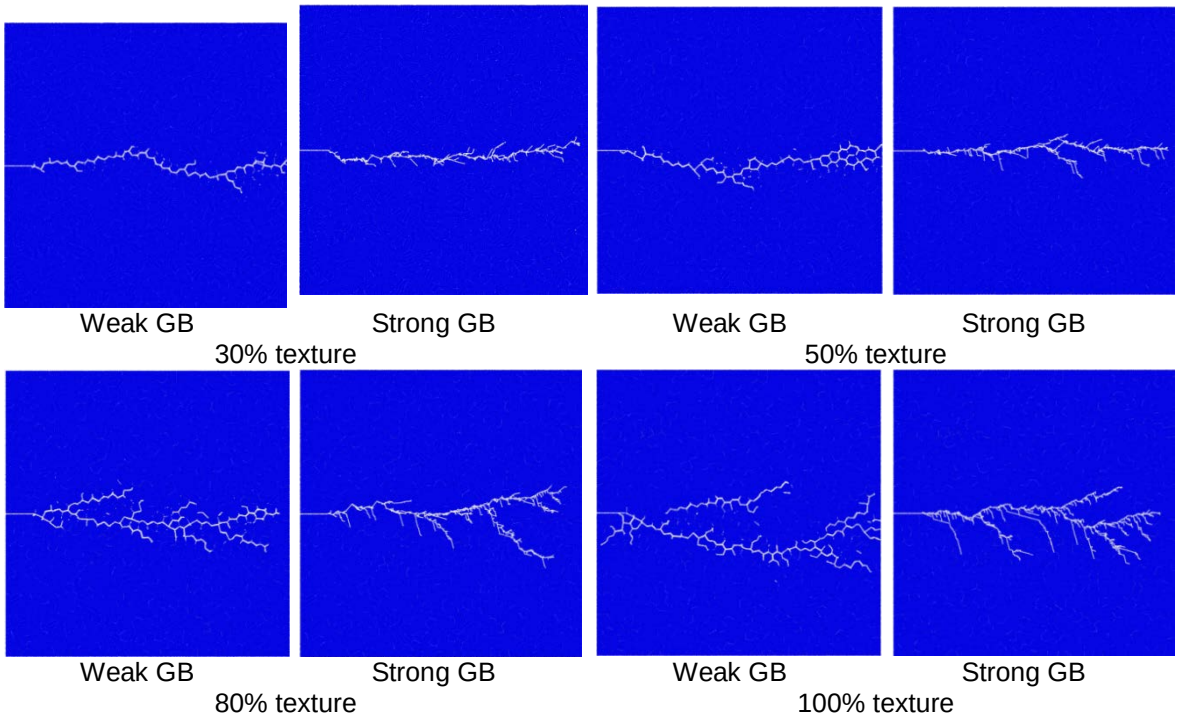

Figure 3.3.10. The Grain Orientation Distribution Effect on the Crack Path

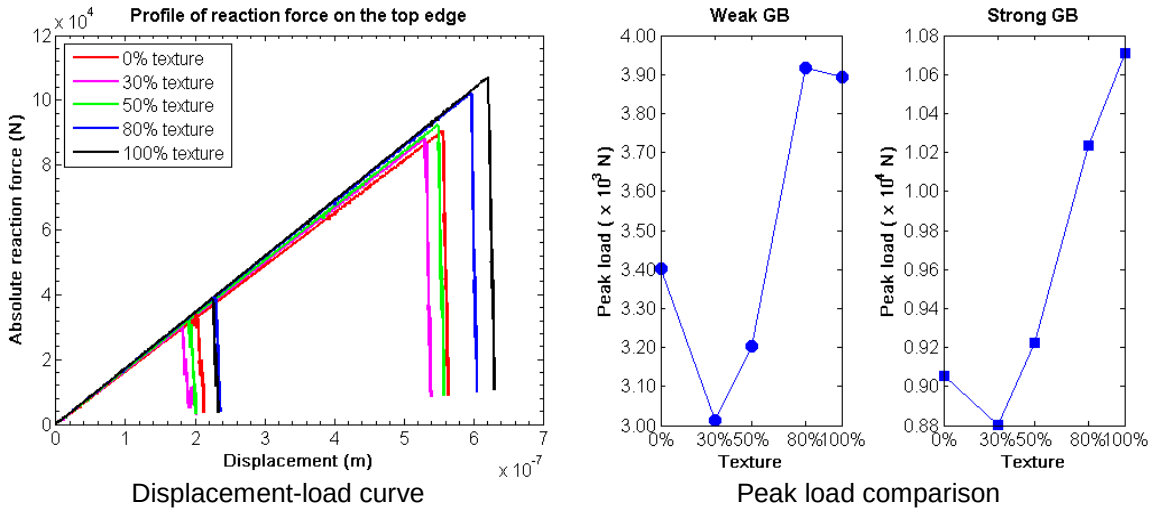

Displacement-load curve Peak load comparison

Figure 3.3.11. The Grain Orientation Distribution Effect on the Reaction Profile

3.3.7. Discussion and Conclusion

In this section, the lattice particle model was applied to model the elastic and fracture behavior of polycrystalline materials. Various microstructural effects, i.e., grain boundary properties and crystallographic orientation distribution, on the performance of a polycrystalline material have been investigated. Without loss of generality, the material properties of single aluminum crystallite have been used throughout all the simulations in this paper. Following general conclusions can be drawn based on the simulation results:

1). The grain boundary properties can affect the macroscopic elastic materials properties. For statistically isotropic material, the stronger the grain boundaries are, the smaller the bulk modulus and the larger the shear modulus;

2). The textured materials have different effective properties than the non-textured ones. With the increase of the degrees of texture, the C11 and C22 components are increasing, while the C12 and C66 components are both decreasing. The difference between the textured and non-textured materials is material property dependent;

3). With other conditions kept the same, the strength of grain boundary will affect the final fracture mode of polycrystalline materials. Weak grain boundaries result in intergranular fracture and low

material strength, while strong grain boundaries produce transgranular fracture and high material strength;

4). For textured materials, the materials strength in the texture direction is higher than the strength in other directions. And among various degrees of texture, the full textured material has the largest strength.

Future work is to extend this concept into 3D cases for materials possessing various material symmetries. Extension of this framework to model crystal plasticity needs additional research work. Comparison with the experimental observation to further validate the proposed model requires additional study.

3.4 3D Cross-ply Laminated Composites

Study of the deformation of cross-ply laminated composite plate using the simple cubic lattice structure is presented in this section. Identical to the case of modeling anisotropic materials using 2D triangular packing, the proposed model in this section considers both the material and geometry orientation by rotating the underlying topological lattice structure consistent with the material orientation, rather than transforming the materials tangent stiffness matrix as in other numerical methods. The advantage of the proposed model lies in the easiness of modeling fracture behavior as the naturally outcome of the breakage of connecting springs. For current study, the focus is on the model development and deformation modeling verification. Future work is to apply the proposed model to fracture and delamination simulation. First, the model formulation for orthotropic materials is presented. Following this, the lattice rotation scheme is discussed. The numerical results are compared with literature findings. Discussion and conclusion are drawn based on current study.

3.4.1 Introduction

Due to the high strength and stiffness to weight ratios and many other superior properties, laminated composite structure has been extensively used in various engineering applications, such as aerospace, automotive and shipbuilding industries. Extensive research works have been doing on understanding the behaviors of these structures both numerically and experimentally. Detailed reviews on computational models for laminated composite plates and shells can be found in [79], [138], [139], [140], [141], [142], [143], [144], [78].

The behaviors of composite laminates can be characterized by complex 3D states of stress. Full 3D elasticity analyses [66], [67], [68], [69], [70], [71] reveal that the interlaminar continuity of transverse normal and shear stresses as well as the layerwise continuous displacement field through the thickness of the laminated structures are the essential requirements for the analysis of laminated structures. The inherent anisotropy and mismatch of material properties, particularly the Poisson's ratio, between plies result in high interlaminar stresses [72], [73], [74], [75], [76],

which is critical to the delamination failure mechanism [77]. These requirements can only be partially fulfilled by other reduced formulations [78]. A drawback of the 3D models is their computational expensiveness. However, these models are essential for an accurate evaluation of the interlaminar stresses at locations such as cutouts, delamination fronts and regions of intense loading. Damage initiation and propagation are likely to occur at such locations, which might lead to the failure of laminate [79]. Moreover, owing to the advent of high-speed computers and the use of parallel computing and GPU computing, this drawback can be underestimated and will not be of concern in the near future.

Comparing to continuum based computational tools, such as FEM [145] and some other meshless methods [146], the discrete formulation based approaches, such as Lattice Spring Model(LSM) [16], [89], [2], Discrete Element Method (DEM) [147], [148], [149] and Peridynamics [150], [151], [152], have certain advantage in failure analysis of composite structures. These models don't require external rules to guide crack initiation, crack propagation and some other more advanced cracking behaviors. A simply bond based failure criterion is sufficient. The crack initiation and propagation can be naturally captured via the breakage of the connecting bonds. Nevertheless, these models have some other limitations. The DEM formulation requires both normal and tangential interactions between elements and the computational procedures are quite involved. Until now, the use of DEM to composite materials is almost restricted to 2D domains. While the available Peridynamic formulations for composites are bond based, and the well-known issue of fixed Poisson's ratio still persist. This will have significant effect on failure analysis, such as delamination modeling as mentioned previously.

Quite recently, Chen et al. [38], [94], [52], [153] has successfully proposed a nonlocal lattice particle model for studying the deformation and fracture behaviors of homogeneous isotropic materials. Later, this approach was extended to anisotropic materials, such as composites [124] and polycrystalline materials [154]. In the lattice particle model, domain of interest is decomposed into regularly packed units or particles whose interaction not only depends on the connecting spring but also has contribution from all its neighbors. Unlike the traditional way of representing

the material orientation by transformation of the material tangent stiffness matrix, lattice particle model rotates the topological lattice structure according to the material's orientation. The equivalency of these two schemes has been shown in [124].

In this study, the methodology is extended to model the deformation behaviors of laminated composite structures. The content of this paper is organized as follows: the formulation and derivation of the Lattice Particle Model for orthotropic materials is discussed in Section 3.4.2. After that, the lattice rotation scheme is presented. The geometric modeling of laminated composite structure in the proposed model is also discussed in Section 3.4.3. Section 3.4.4 is devoted to the numerical results of various laminated composite plates. Conclusions based on current study are given in Section 3.4.5.

3.4.2 Formulation for orthotropic material

In lattice particle model, the domain of interest is decomposed into regularly packed particles. Each particle interacts with its neighbors via linear springs. These interactions are non-local in the sense that they depend not only on the spring connecting these two particles, but also have direct contributions from all their neighbors. In this study, the simple cubic packing is considered, and both the first and the second nearest neighboring particles are considered as the neighbors. A unit cell is defined as the repeating unit identified from the domain decomposition. Different packing will results in different unit cells. A schematic showing the simple cubic packing and the two unit cells is shown in Fig. 3.4.1.

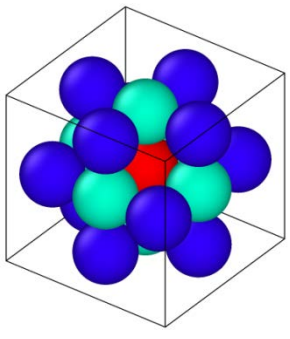

Simple cubic packing

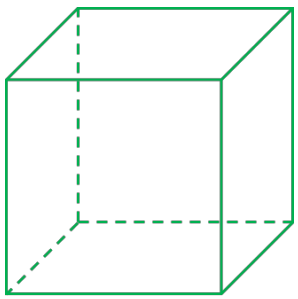

Unit cell 1: Cube

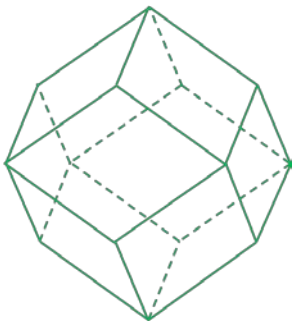

Unite cell 2:

Rhombic dodecahedron

Figure 3.4.1. The Simple Cubic Lattice Structure and the Unit Cells

The volumes of these two unit cells in terms of the particle radius *R* is $V_1 = 8R^3$ and $V_2 = 16R^3$. There are six nearest neighbors associated with unit cell 1 and 12 second nearest neighbors with unit cell 2. The 18 normal unit vectors for each neighbor are given in Table 3.4.1.

Table 3.4.1. The Unit Normal Vectors for Simple Cubic Structure

Neighbors 1 ($N_1 = 6$)					
1	$(1,0,0)$	3	$(0,1,0)$	5	$(0,0,1)$
2	$(-1,0,0)$	4	$(0,-1,0)$	6	$(0,0,-1)$
Neighbors 2 ($N_2 = 12$)					
7	$1/\sqrt{2}(1,1,0)$	11	$1/\sqrt{2}(1,0,1)$	15	$1/\sqrt{2}(0,1,1)$
8	$1/\sqrt{2}(-1,-1,0)$	12	$1/\sqrt{2}(-1,0,-1)$	16	$1/\sqrt{2}(0,-1,-1)$
9	$1/\sqrt{2}(1,-1,0)$	13	$1/\sqrt{2}(1,0,-1)$	17	$1/\sqrt{2}(0,1,-1)$
10	$1/\sqrt{2}(-1,1,0)$	14	$1/\sqrt{2}(-1,0,1)$	18	$1/\sqrt{2}(0,-1,1)$

The key recipe in the formulation of lattice particle model is the potential energy for each particle. This potential energy eventually determines the interactions between particles, i.e., local or non-local. In this study, the potential energy has the following form

$$U_{particle} = \sum_{I=1}^{2} U_{cell\_I} = \sum_{I=1}^{2} \left(U_{s\_I} + U_{v\_I} \right) \tag{3.4.1}$$

where U_{s_I} and U_{v_I} are the local and nonlocal energies.

$$\begin{aligned} U_{s\_I} &= \frac{1}{2} \sum_{J=1}^{N_I} k_J \left(\delta l_{IJ} \right)^2 \\ U_{v\_I} &= \frac{1}{2} \left(\sum_{J=1}^{N_I} T_J \delta l_{IJ} \right) \left(\sum_{J=1}^{N_i} \delta l_{IJ} \right) \end{aligned} \tag{3.4.2}$$

where k_J and T_J are the local and nonlocal spring parameters, δl_{IJ} is the half elongation, I and J is the index of the particles, N_I is the number of neighbors for each unit cell.

Given the local and nonlocal energies, the potential energy for each unit cell can be rewritten in terms of the components of the strain tensor as

$$U_{cell\_I} = U_{s\_I} + U_{v\_I} = \frac{\left(l_0^I\right)^2}{2}\sum_{b=1}^{N_I} k_b n_i^b \varepsilon_{ij} n_j^b n_k^b \varepsilon_{kl} n_l^b + \frac{\left(l_0^I\right)^2}{2}\left(\sum_{b=1}^{N_I} T_b n_i^b \varepsilon_{ij} n_j^b\right)\left(\sum_{b=1}^{N_I} n_k^b \varepsilon_{kl} n_l^b\right) \quad (3.4.3)$$

with $i, j, k, l = 1, 2, 3$, l_0^I is half of the original length between reference particle with its Ith nearest neighbors. n_i^b is the ith component of the spring b given in Table 3.4.1. It should be noted that the springs in opposite directions should have the same parameters.

Due to the conservative of the potential energy, the material tangent stiffness matrix can be obtained by differentiating the total specific energy with respect to the strain tensor twice as

$$C_{ijkl} = \frac{1}{V_1}\frac{\partial^2 U_{cell\_1}}{\partial\varepsilon_{ij}\partial\varepsilon_{kl}} + \frac{V_2}{V_1}\left(\frac{1}{V_2}\frac{\partial^2 U_{cell\_2}}{\partial\varepsilon_{ij}\partial\varepsilon_{kl}}\right) \quad (3.4.4)$$

Plugging in the unit normal vectors given in Table 1, the following correspondence can be obtained by comparing the coefficients of the material tangent stiffness matrices as

$$\begin{aligned}
&C_{11} = \frac{1}{4R}\left(k_1 + k_7 + k_{11} + 2T_1 + 8T_7 + 8T_{11}\right); C_{22} = \frac{1}{4R}\left(k_3 + k_7 + k_{15} + 2T_3 + 8T_7 + 8T_{15}\right)\\
&C_{33} = \frac{1}{4R}\left(k_5 + k_{11} + k_{15} + 2T_5 + 8T_{11} + 8T_{15}\right); C_{13} = \frac{1}{4R}\left(k_{11} + T_1 + T_5 + 4T_7 + 8T_{11} + 4T_{15}\right)\\
&C_{12} = \frac{1}{4R}\left(k_7 + T_1 + T_3 + 8T_7 + 4T_{11} + 4T_{15}\right); C_{23} = \frac{1}{4R}\left(k_{15} + T_3 + T_5 + 4T_7 + 4T_{11} + 8T_{15}\right)\\
&C_{44} = \frac{1}{4R}k_{15}; C_{55} = \frac{1}{4R}k_{11}; C_{66} = \frac{1}{4R}k_7
\end{aligned} \quad (3.4.5)$$

in which the springs in opposite directions have the same parameters, i.e.,

$$k_7 = k_9; T_7 = T_9; k_{11} = k_{13}; T_{11} = T_{13}; k_{15} = k_{17}; T_{15} = T_{17} \quad (3.4.6)$$

In Eq. (3.4.5), there are 12 model parameters. But orthotropic materials only have 9 dependent material constants according to Hooke's Law. The model parameters can be reduced by assuming $T_1 = T_7; T_3 = T_{15}; T_5 = T_{11}$. Thus, the following relationships can be obtained

$$
\begin{aligned}
&C_{11}=\frac{1}{4R}\left(k_1+k_7+k_{11}+10T_1+8T_5\right);C_{22}=\frac{1}{4R}\left(k_3+k_7+k_{15}+8T_1+10T_3\right)\\
&C_{33}=\frac{1}{4R}\left(k_5+k_{11}+k_{15}+8T_3+10T_5\right);C_{13}=\frac{1}{4R}\left(k_{11}+5T_1+4T_3+9T_5\right)\\
&C_{12}=\frac{1}{4R}\left(k_7+9T_1+5T_3+4T_5\right);C_{23}=\frac{1}{4R}\left(k_{15}+4T_1+9T_3+5T_5\right)\\
&C_{44}=\frac{1}{4R}k_{15};C_{55}=\frac{1}{4R}k_{11};C_{66}=\frac{1}{4R}k_7
\end{aligned}
\tag{3.4.7}
$$

The model parameters can be uniquely determined in terms of the material constants as

$$
\begin{bmatrix} k_1\\ k_3\\ k_5\\ k_7\\ k_{11}\\ k_{15}\\ T_1\\ T_3\\ T_5 \end{bmatrix}
= R\begin{bmatrix}
4 & 0 & 0 & -4 & 0 & 0 & -4 & -4 & 4\\
0 & 4 & 0 & 0 & -4 & 0 & 4 & -4 & -4\\
0 & 0 & 4 & 0 & 0 & -4 & -4 & 4 & -4\\
0 & 0 & 0 & 0 & 0 & 4 & 0 & 0 & 0\\
0 & 0 & 0 & 0 & 4 & 0 & 0 & 0 & 0\\
0 & 0 & 0 & 4 & 0 & 0 & 0 & 0 & 0\\
0 & 0 & 0 & 58/189 & 22/189 & -122/189 & -22/189 & 122/189 & -58/189\\
0 & 0 & 0 & -122/189 & 58/189 & 22/189 & -58/189 & -22/189 & 122/189\\
0 & 0 & 0 & 22/189 & -122/189 & 58/189 & 122/189 & -58/189 & -22/189
\end{bmatrix}
\begin{bmatrix} C_{11}\\ C_{22}\\ C_{33}\\ C_{44}\\ C_{55}\\ C_{66}\\ C_{13}\\ C_{12}\\ C_{23} \end{bmatrix}
\tag{3.4.8}
$$

So far, we have derived the model parameters and a unique mapping between these parameters with the material constants is obtained. In next section, the lattice rotation scheme and how the geometry of laminate composite is built in the proposed model will be discussed.

3.4.3 Rotation of topological lattice structure

As has been shown in [124] for 2D case, the rotation of the underlying lattice structure in lattice particle model is equivalent to the stiffness matrix transformation in representing the material orientation in the global coordinate. The same idea is applied here to considering the ply orientation in a laminated composite plate. The equivalency between lattice rotation and transformation of tangent stiffness matrix will be shown numerically in the Numerical Results section.

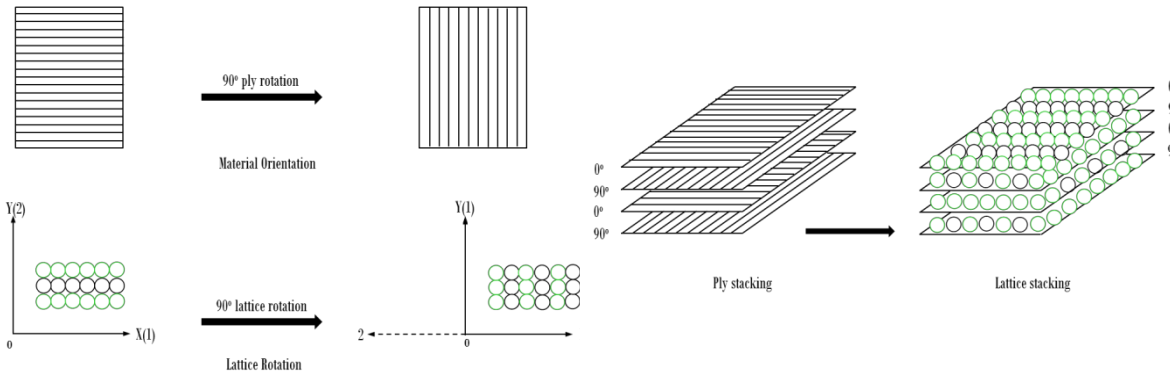

Figure 3.4.2. The In-Plane Lattice Rotation and Out-of-Plane Lattice Stacking

A typical lattice rotation scheme is shown in Fig. 3.4.2. The lattice structure for each ply is rotated according to the ply orientation with respect to the rotation axis. And the rotated lattice structures are then stacked together according to the composite stack sequence. The discretized composite system is built by repeating the rotation and stacking procedure.

3.4.4 Numerical results

In this section, various numerical examples solved using the proposed model are described and discussed. For all the plate bending problems, a simply supported plate with various thickness-to-length ratios is considered for analyses. The transverse loading considered is bidirectional sinusoidal. The accuracy of the solution is established by comparing the obtained results with the solutions wherever available in the literature. The materials properties are given in Table 3.4.2. A general configuration of the laminated plate is shown in Fig. 3.4.3. For nondimensionalized deflection values presented in this section, the following normalization is used:

$$\bar{u}_x = u_x \cdot \frac{h^2 E_2}{P_0 a^3}, \quad \bar{u}_y = u_y \cdot \frac{h^2 E_2}{P_0 a^3}, \quad \bar{u}_z = u_z \cdot \frac{100 h^3 E_2}{P_0 a^4}$$

Unless otherwise specified, the maximum deflection is evaluated at the position of (a/2, a/2, 0). The solution method presented in [153]is used.

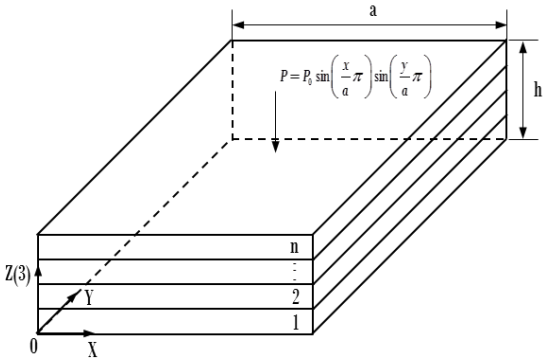

Figure 3.4.3. The Configuration and Dimensions of the Composite Plates

Table 3.4.2. The Various Material Properties for the Tests Presented in the Section

Tests	Source	Material constants		
1, 2, 4	Pagano[67]	$E_1 = 172.4$ GPa $E_2 = 6.89$ GPa $E_3 = 6.89$ GPa	$v = 0.25$	$G_{12} = 3.45$ GPa $G_{13} = 3.45$ GPa $G_{23} = 1.378$ GPa
3, 5	Demasi[155]	Sheet 1		
		$E_1 = 100$ GPa $E_2 = 4$ GPa $E_3 = 40$ GPa	$v = 0.25$	$G_{12} = 2$ GPa $G_{13} = 2$ GPa $G_{23} = 0.8$ GPa
		Sheet 2		
		$E_1 = 100$ GPa $E_2 = 4$ GPa $E_3 = 4$ GPa	$v = 0.25$	$G_{12} = 2$ GPa $G_{13} = 2$ GPa $G_{23} = 0.8$ GPa
		Sheet 3		
		$E = 4$ GPa	$v = 0.25$	$G_{12} = 2$ GPa $G_{13} = 2$ GPa $G_{23} = 0.8$ GPa
6	NAFEMS[156]	$E_1 = 100.0$ GPa $E_2 = 5.0$ GPa $E_3 = 5.0$ GPa	$v_{12} = 0.4$ $v_{13} = 0.3$ $v_{23} = 0.3$	$G_{12} = 3.0$ GPa $G_{13} = 2.0$ GPa $G_{23} = 2.0$ GPa

Directional Young's modulus of homogeneous orthotropic material

The validity of the proposed lattice structure rotation to represent the material orientation is tested in this example. Uniaxial tests are performed using a Representative Volume Element (RVE). The calculated directional Young's modulus on two orthogonal planes, i.e., <010> and <100>, are compared to the analytical solution given by Courtney [157] shown in Fig. 3.4.4.

From the comparison of the prediction with analytical solution shown in Fig. 3.4.4, the lattice rotation scheme can effectively represent the material's orientation. Thus, the equivalency to the transformation of material tangent stiffness matrix is established.

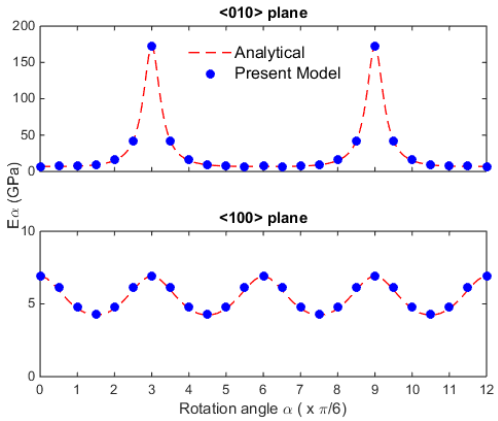

Figure 3.4.4. Variation of the Directional Modulus on <010> and <100> Planes

Simple 2-ply laminated square plate (0/90)

A simply supported two-ply antisymmetric square laminated plate under bidirectional sinusoidal transverse load is considered in this example. The plies have equal thickness and the same material properties but with different ply orientation. Numerical values of nondimensionalized transverse displacement for various aspect ratios (a/h) are shown in Table 3.4.3. A detailed comparison of the in-plane displacement $\bar{u}_x$ is shown in Fig. 3.4.5. The literature results are obtained from [158].

Table 3.4.3. The Nondimensionalized Deflections in a Simple 2-Ply Laminated Square Plate

Model	Nondimensionalized deflection $\bar{u}_z$				
	a/h = 5	a/h = 10	a/h = 20	a/h = 50	a/h = 100
Present	1.7592	1.2509	1.1096	1.0815	1.0745
Pagano [67]	1.7287	1.2318	1.1016	-	1.0742
Kant [159] (model-2)	1.7037	1.2274	1.1078	-	1.0695
Reddy [160]	1.6670	1.2161	1.1018	-	1.0651

The normalized deflections for various length-to-thickness ratios are very accurate compare to the 3D exact solution from [67]. For the detailed comparison of the in-plane displacement $\bar{u}_x$ shown in Fig. 3.4.5, there is no 3D exact solution available in the literature. Instead, a comparison

with Kant's solution [158] is made. But there is some difference for locations at some inner of the top ply. The difference generally is quite small.

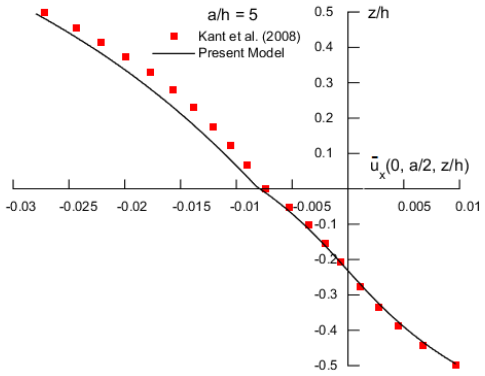

Figure 3.4.5. Variation of Normalized Displacement of a Simple 2-Ply Laminated Plate

Hybrid 2-ply laminated square plate (0/90)

A hybrid 2-ply antisymmetric square laminated plate from Demasi [155] is considered in this example. The plate is simply supported and under transverse bi-directional sinusoidal loading. The top and bottom plies have equal thickness but different material orientation and properties. The top ply has the properties of Sheet 1, while the bottom ply has the properties of Sheet 2. Only the case of length-to-thickness ratio (a/h) equal to 4 is studied. The obtained results using lattice particle model are compared with Demasi's finding [155]. The detailed comparisons of the normalized displacements $\bar{u}_x$ and $\bar{u}_z$ are shown in Fig. 3.4.6.

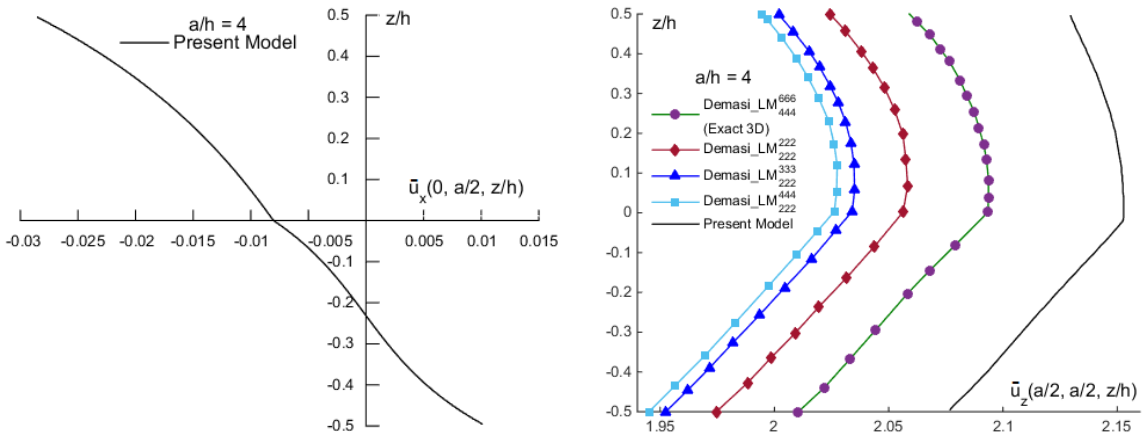

Figure 3.4.6. Variations of the Normalized Displacements of a Hybrid 2-Ply Laminated Plate

For the in-plane displacement $\bar{u}_x$, there is no literature results available. A prediction using the lattice particle formulation is shown in Fig. 3.4.6 (left). The predicted normalized transverse deflection is compared with different mixed theories for plate from Demasi [155]. At current discretization density, there are some errors between the prediction and the 3D exact solution, with maximum of *3%*. The general trend is accurately predicted and consistent with all other predictions from [155].

Simple 3-ply laminated square plate (0/90/0)

A simple 3-ply symmetric square laminated plate is studied in this example. The plate is simply supported and under transverse bi-directional sinusoidal loading. A series of different length-to-thickness ratios are considered. The predicted results are compared with literature results from [159] shown in Table 3.4.4. A detailed comparison of the prediction with 3D exact solution is shown in Fig. 3.4.7.

Table 3.4.4. The Nondimensionalized Deflections in a Simple 3-Ply Laminated Square Plate

Model	Nondimensionalized deflection $\bar{u}_z$				
	a/h = 4	a/h = 10	a/h = 20	a/h = 50	a/h = 100
Present	1.9447	0.7346	0.5081	0.4397	0.4318
Kant [159] (model-2)	1.9261	0.7176	0.5058	0.4433	0.4343
Reddy [160]	1.9218	0.7125	0.5041	0.4430	0.4342

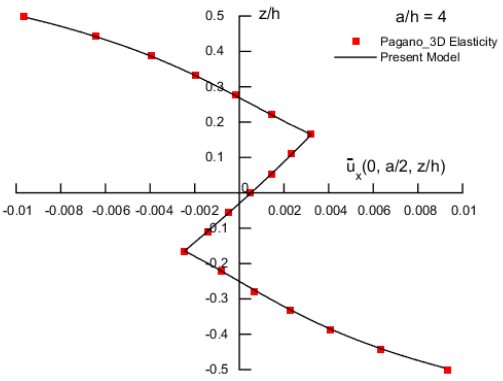

Figure 3.4.7. Variation of Normalized Displacement Ux of a Simple 3-Ply Laminated Plate

As can be seen from Table 3.4.4, there difference between the predictions and the available literature results are very small, with maximum of *3.1%*. The through thickness displacement from 3D exact solution is exactly on top of the predicted curve, shown in Fig. 3.4.7. A pretty good accuracy is obtained in this case.

Hybrid 3-ply laminated square plate (0/90/0)

Another hybrid 3-ply symmetric square laminated plate is studied in this example. The same boundary conditions are applied in this example. The top and bottom plies have the same thickness and material properties of Sheet 1. The thickness for the middle ply is twice of that of the top and bottom plies, and has the properties of Sheet 3.

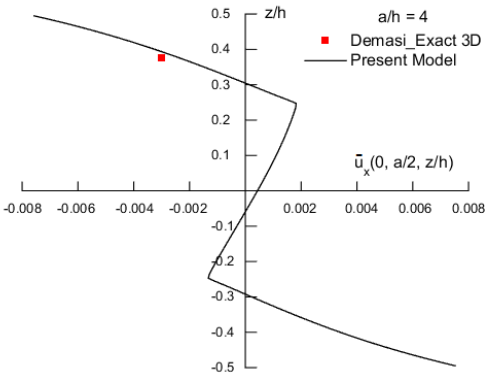

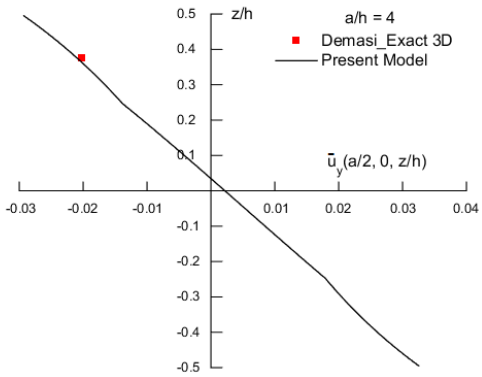

Figure 3.4.8. Variations of Normalized Displacements of a Hybrid 3-Ply Laminated Plate

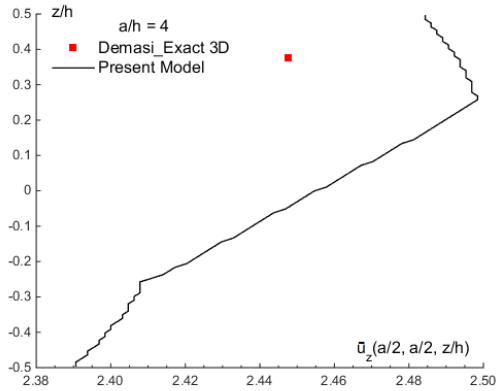

For this problem, only the data for a single point is available from [155], which is indicated using red square shown in Fig. 3.4.8. As can be seen from the comparison, the predicted displacements of $\bar{u}_x$ and $\bar{u}_y$ are very close to the results obtained by Demasi [155] using 3D elasticity formulation. For the case of transverse deflection $\bar{u}_z$, due to current discretization density, there is approximately *2%* difference exists. The general trends for all three displacements are shown in Fig. 3.4.8.

Simple 7-ply laminated rectangular strip ($(0/90)_3/0$)

The deflection of a composite laminated strip under three-point bending configuration is studied in this example. This test is recommended by the National Agency for Finite Element Method and Standards (U.K.) (NAFEMS) [156] for testing the performance of finite elements. The dimensions and configuration of the strip are shown in Fig. 3.4.9. The material properties are given in Table 3.4.2. Due to symmetry, only a quadrant of the plate is modeled.

The deformation distributions are shown in Fig. 3.4.10. The calculated deflection at Point *E* using the proposed model is -1.059 mm, while the reference solution from NAFEMS [156] is -1.06 mm. A very good accuracy is found for the proposed model.

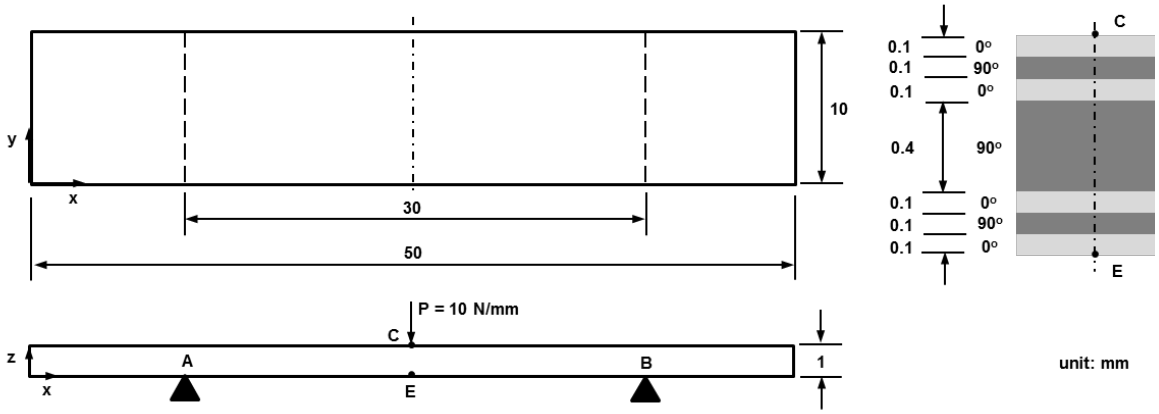

Figure 3.4.9. The Dimensions and Configuration of the Laminated Composite Strip

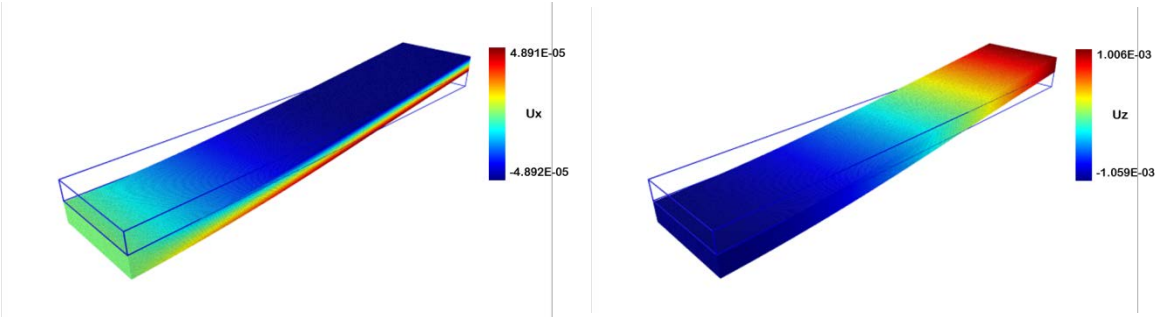

Figure 3.4.10. The Displacement Distributions of the Laminated Composite Strip

3.4.5 Conclusion

A discrete 3D formulation of anisotropic elasticity, the nonlocal lattice particle model, for laminated composite structure is presented in this section. Unlike the traditional way of transforming the material tangent stiffness matrix, an equivalent lattice rotation scheme is used in the proposed model to represent the material orientation. The lattice rotation scheme accounts for not only the material orientation, but also the lamina's fiber orientation. Various numerical benchmark tests prove the validity of the proposed model. Future work is to apply the proposed model to fracture and delamination simulation of laminated composite plate. Generalization of the model to arbitrary angled laminates needs additional work.

3.5 3D Polycrystalline Materials

In this section, a novel top-down coarse-grained non-local lattice particle framework for modeling the elastic behavior of cubic polycrystalline materials is presented. The physical domain of each composing crystallite is discretized into particles which are packed according to the underlying material lattice structure. The crystallographic orientation for each individual crystallite is represented by rotating the topological lattice structure accordingly given the three Euler's angles. Since the real material lattice structure is mimicked, the grain boundaries can be automatically generated in a way similar to the Molecular Dynamics simulation. A nonlocal potential is then proposed to account for the interactions between particles up to the second neighbor. The parameters of the proposed potential are uniquely determined in terms of the corresponding elastic constants of single crystallite via a top-down coarse-graining scheme. The framework is verified with classical elastic solution of single crystallite. Predictions of the elastic constants of polycrystals with or without texture are performed and compared with literature data.

3.5.1 Introduction

Molecular Dynamics (MD) simulation has been widely used to study various physical phenomena of polycrystalline solids, such as grain growth[161], dislocation dynamics [162], [163], [164], crystal plasticity [165], [166] and fracture [167], [168]. However, due to available computing power limitation, simulations of processes on long timescales and large length-scales are prohibitively expensive. According to [169], the largest available molecular system might scale up to one cubic microns by the time of 2025. In order to simulation systems with larger volume and longer temporal domain, reduced representations or coarse-grained models and multi-scale techniques [170] can be used.

A number of coarse-grained methods have been proposed over the years to overcome the severe limitations on both the timescales and length-scales, such as the hyper-dynamics method [171], the parallel-replica dynamics method [172], the temperature accelerated dynamics method

[173], the discrete dislocation dynamics [174], [175], and the lattice models [176], [177], [178], [179]. The coarse-grained methods usually are specific-purpose orientated, such as the discrete dislocation dynamics is developed especially for crystal plasticity. In this letter, we propose a grain level coarse-grained framework to study the mechanical deformation response of crystals or polycrystals.

It's well-known that the macroscopic behavior of polycrystalline aggregates are generally considered as homogeneous and isotropic in terms of the elastic deformation when the materials have random crystallographic and morphologic textures even though the underlying single crystallite exhibits anisotropy and orientation dependent in most materials. Under these assumptions, various theoretical prediction approaches have been proposed for the estimation of the effective elastic properties of materials of this kind, such as the representative work of Voigt [99], Reuss [100], Hill [101], Kröner [102] and Hashin and Shtrikman [103], [104]. Berryman simplified the Hashin-Shtrikman bounds and applied to polycrystal compounds [180] and hcp solids He^4 [181]. However, orientation randomness assumption may not be true when the material does not consist of sufficient number of crystallites or there exists certain material texture. In order to better estimate the properties of materials of these type, it is important to identify local properties, which are the elasticity, crystallographic orientation of each crystallite.

In this letter, a novel nonlocal top-down coarse-grained lattice particle model is proposed to study the mechanical behavior of cubic polycrystalline materials. We restrict ourselves to the scenarios of estimating the effective elastic constants of polycrystalline materials composed by cubic crystallites. For each individual crystallite, the material domain is decomposed into particles packed in the same way as the material's underlying lattice structure. For each decomposed crystal, the particles system is oriented according to the three Euler's angle by rotating the topological lattice structure, in a way similar to the Molecular Dynamics simulation. A nonlocal potential is proposed to account both the pairwise and multi-body interactions. The potential parameters are uniquely determined in terms of the material constant by a top-down coarse-graining process. The model is verified with classical crystal elasticity solution. Predictions on the

effective elastic constants for polycrystals with or without texture are compared with literature results.

3.5.2 Lattice Particle Framework

The nonlocal potential

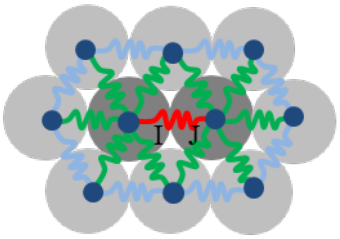

Figure 3.5.1. The Nonlocal Interaction between Particles I and J.

For illustrative purpose, a 2D particle system packed using the triangular lattice is shown in Fig. 3.5.1. From the viewpoint of Physics, the interaction between particle *I* and *J* should not only dependent on the particle pair itself, but also has contribution from its neighboring particles, e.g., at least all the nearest neighbors in Fig.3.5.1. In Molecular Dynamics, usually atoms within the '*cutoff*' radius are interacting with each other. Thus, the potential of a particle should have at least two components,

$$U = U_{pairwise} + U_{multi-body} \tag{3.5.1}$$

In fact, the consideration of only the pairwise potential will results in a fixed Poisson's ratio at the macro level.

In lattice models, the pairwise potential can be written in a scalar form as

$$U_{pairwise} = \frac{1}{2} k \left(\delta l \right)^2 \tag{3.5.2}$$

Based on the pairwise potential, a non-local multi-body potential is proposed as

$$U_{multi-body} = \frac{1}{2} T \left(\sum_{J=1}^{N} \delta l_J \right)^2 \tag{3.5.3}$$

In Eqs. (3.5.2) and (3.5.3), k and T are the local and non-local parameters, δl is the bond elongation, with reference to its original length, N is the number of neighboring bonds.

Energy-based coarse-graining process

In order to connect the parameters of the potential with material constants, a top-down energy-based coarse-graining process is used. The main idea is to equate the potential energy of the particle system with that of the corresponding continuum. Since regular lattice structures are utilized in the proposed model, an energy equivalency at the unit cell level is sought. A unit cell is a smallest repeating unit identified from the lattice structures. This concept will become clearer in Section 2.3.

Assuming there are N_{cell} unit cells identified for a typical particle, then the total potential of such particle has following general form

$$U = \sum_{I=1}^{N_{cell}} U_{cell}^{I} = \sum_{I=1}^{N_{cell}} \left(U_{pairwise}^{I} + U_{multi-body}^{I} \right) \tag{3.5.4}$$

Equating the potential energy to a corresponding continuum, then by the Theory of Hyper-elasticity, the potential can be rewritten in terms of the components of the strain tensor as

$$U = \sum_{I=1}^{N_{cell}} \left(\frac{1}{2} k_I \left(l_I \right)^2 \sum_{b=1}^{N_I} \left(n_i^b n_j^b n_k^b n_l^b \varepsilon_{ij} \varepsilon_{kl} \right) + \frac{1}{2} T_I \left(l_I \right)^2 \left(\sum_{b=1}^{N_I} n_i^b n_j^b \varepsilon_{ij} \right) \left(\sum_{b=1}^{N_I} n_k^b n_l^b \varepsilon_{kl} \right) \right) \tag{3.5.5}$$

where l_I is half of the distance between the center particle with its neighbors for unit cell I. n^b is the unit normal vector for the *b*th neighbor.

By the conservation of the potential energy, the material tangent stiffness tensor can be obtained as

$$\begin{aligned} C_{ijkl} &= \left(\frac{1}{V_1} C_{ijkl}^{1} \right) + \frac{V_2}{V_1} \left(\frac{1}{V_2} C_{ijkl}^{2} \right) + \cdots + \frac{V_{N_{cell}}}{V_1} \left(\frac{1}{V_{N_{cell}}} C_{ijkl}^{N_{cell}} \right) = \frac{1}{V_1} \frac{\partial^2 \left(\sum_{I=1}^{N_{cell}} U_{cell}^{I} \right)}{\partial \varepsilon_{ij} \partial \varepsilon_{kl}} \\ &= \frac{\left(l_I \right)^2}{2V_1} \sum_{I=1}^{N_{cell}} \left(k_I \sum_{b=1}^{N_I} \left(n_i^b n_j^b n_k^b n_l^b \right) + T_I \left(\sum_{b=1}^{N_I} n_i^b n_j^b \right) \left(\sum_{b=1}^{N_I} n_k^b n_l^b \right) \right) \end{aligned} \tag{3.5.6}$$

Comparing the components of the material tangent stiffness matrix, the potential parameters can be solved in terms of the material constants. Generally, the solution is unique, such as [38], but sometimes additional constraint(s) is required, for instance, [52].

Potential parameters for bcc and fcc lattices

Two common cubic lattice structures are considered, the body-centered cubic (bcc) and the face-centered cubic (fcc). For each lattice structure, the "cutoff radius" is the second neighbor. The formulation follows the procedure given in Section II.B.

Body-centered cubic lattice

The unit cells for the body-centered cubic lattice structure are shown in Fig. 3.5.2. The 14 unit normal vectors are given in Table 3.5.1.

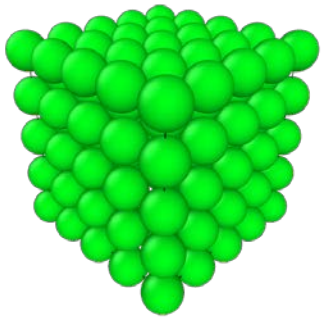

(a). Body-centered cubic lattice

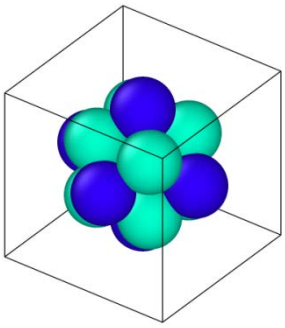

(b). 14 neighbors

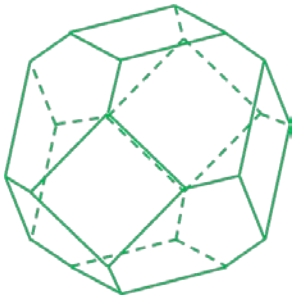

(c). Unit cell 1: Truncated octahedron ($V_1 = 32\sqrt{3}/9\,R^3$)

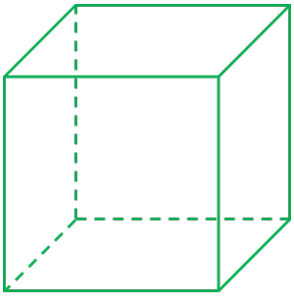

(d). Unit cell 2: Cube ($V_2 = 64\sqrt{3}/9\,R^3$)

Figure 3.5.2. The Body-Centered Cubic Lattice Structure and the Unit Cells

Table 3.5.1. The Unit Normal Vectors for Body-Centered Cubic Lattice Structure

Neighbor 1		
$(1/\sqrt{3},1/\sqrt{3},-1/\sqrt{3})$	$(-1/\sqrt{3},1/\sqrt{3},-1/\sqrt{3})$	$(-1/\sqrt{3},-1/\sqrt{3},-1/\sqrt{3})$

$(1/\sqrt{3},-1/\sqrt{3},-1/\sqrt{3})$	$(1/\sqrt{3},1/\sqrt{3},1/\sqrt{3})$	$(-1/\sqrt{3},1/\sqrt{3},1/\sqrt{3})$
$(-1/\sqrt{3},-1/\sqrt{3},1/\sqrt{3})$	$(1/\sqrt{3},-1/\sqrt{3},1/\sqrt{3})$	
Neighbor 2		
$(1,0,0)$	$(0,1,0)$	$(-1,0,0)$
$(0,-1,0)$	$(0,0,1)$	$(0,0,-1)$

Thus, the potential parameters for bcc lattice structure can be solved as

$$\begin{Bmatrix} k_1 \\ k_2 \\ T \end{Bmatrix} = R \begin{bmatrix} 0 & 0 & 4\sqrt{3} \\ 4\sqrt{3}/3 & -4\sqrt{3}/3 & 0 \\ 0 & 2\sqrt{3}/7 & -2\sqrt{3}/7 \end{bmatrix} \begin{Bmatrix} C_{11} \\ C_{12} \\ C_{44} \end{Bmatrix} \tag{3.5.7}$$

Face-centered cubic lattice

The unit cells for the face-centered cubic lattice structure are shown in Fig. 3.5.3. And the corresponding unit normal vectors are given in Table 3.5.2.

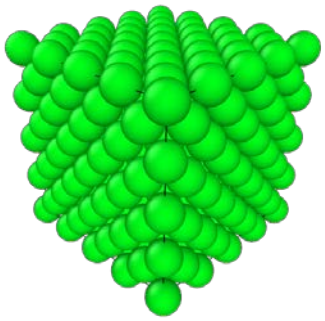

(a). Face-centered cubic lattice

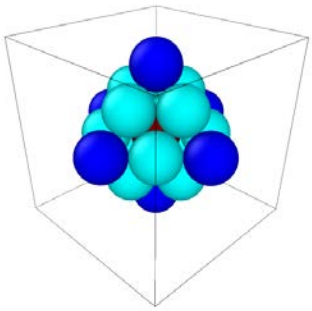

(b). 18 neighbors

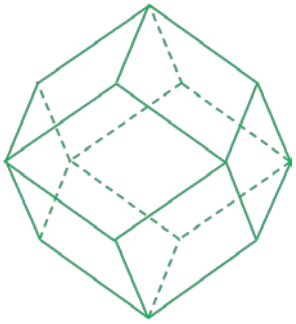

(c). Unit cell 1: Rhombic dodecahedron ($V_1 = 4\sqrt{2}R^3$)

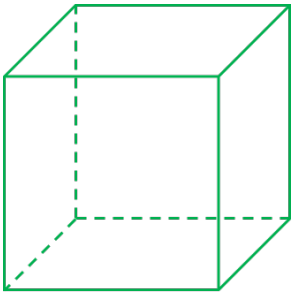

(d). Unit cell 2: Cube ($V_2 = 16\sqrt{2}R^3$)

Figure 3.5.3. The Face-Centered Cubic Lattice Structure and the Unit Cells

Table 3.5.2. The Unit Normal Vectors for Face-Centered Cubic Lattice Structure

Neighbor 1		
$(1/\sqrt{2},-1/\sqrt{2},0)$	$(1/\sqrt{2},1/\sqrt{2},0)$	$(-1/\sqrt{2},1/\sqrt{2},0)$
$(-1/\sqrt{2},-1/\sqrt{2},0)$	$(0,1/\sqrt{2},-1/\sqrt{2})$	$(0,1/\sqrt{2},1/\sqrt{2})$
$(0,-1/\sqrt{2},1/\sqrt{2})$	$(0,-1/\sqrt{2},-1/\sqrt{2})$	$(1/\sqrt{2},0,-1/\sqrt{2})$
$(1/\sqrt{2},0,1/\sqrt{2})$	$(-1/\sqrt{2},0,1/\sqrt{2})$	$(-1/\sqrt{2},0,-1/\sqrt{2})$
Neighbor 2		
$(1,0,0)$	$(0,1,0)$	$(-1,0,0)$
$(0,-1,0)$	$(0,0,1)$	$(0,0,-1)$

Therefore, the potential parameters for fcc lattice structure can be determined as

$$\begin{Bmatrix} K_1 \\ K_2 \\ T \end{Bmatrix} = R \begin{bmatrix} 0 & 0 & 4\sqrt{2} \\ \sqrt{2} & -\sqrt{2} & -\sqrt{2} \\ 0 & \sqrt{2}/6 & -\sqrt{2}/6 \end{bmatrix} \begin{Bmatrix} C_{11} \\ C_{12} \\ C_{44} \end{Bmatrix} \tag{3.5.8}$$

It should be noted that, for uniqueness of the solution for the potential parameters, it was assumed that the nonlocal potential parameter T has the same value for both unit cells. As can been seen in Eq. (2.4.12), a limitation on the proposed framework using the fcc lattice structure is that it can only model materials with $C_{11} > C_{12} + C_{44}$. For fcc materials which do not meet this requirement, the bcc lattice structure model can be used if and only if the material underlying lattice structure can be ignored, such as the elastic properties of polycrystalline materials.

3.5.3 Lattice rotation and grain boundary generation

The way how a simulation model is built in the proposed framework is similar to the procedure employed in MD simulations. The geometrical domain of a crystallite is decomposed into regular particles which are packed according to the material's underlying lattice structure under the global coordinate. The lattice structure then is rotated with the given crystallographic orientation information to account the real crystallite orientation. The particle rotation follows the vector transformation rule. This decomposition-rotation process is repeated for all the crystallites composing the polycrystal. A overlap-deletion scheme [154], [129] is used to generate the grain boundary using the rotated particle system. Any particle whose degree of overlapping with its

neighboring particles is greater than a pre-specified value is deleted. This process is repeated until all of the degrees of overlapping are less than the specified value. And the distance between any particles after this process are defined as the un-deformed distance. Other grain boundary generation processes, such as the energy minimization [130], the simulated solidification process [131] and the devised MD simulation [132] can be applied. A Representative Volume Element (RVE) consisting of *2,000* crystallites represented using the proposed model is shown in Fig. 3.5.4.

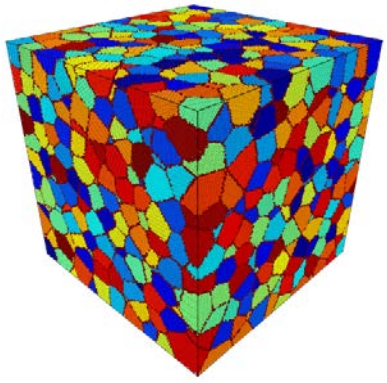

Figure 3.5.4. A Polycrystalline RVE Represented Using bcc Packed Particles

3.5.4 Results

Verification with classical crystal elasticity

The proposed framework is verified with the classical elasticity of a single crystallite. Predictions of the directional Young's modulus and Poisson's ratio are compared with the analytical solution from crystal elasticity [157]. Implicit solution scheme proposed in [94] has been used. The elastic constants (GPa) for selected cubic materials are listed in Table 3.5.3. The values for Al, Cu and Fe are from [182], W from [183]). The anisotropy factor is defined as: $f_0 = 1 - \left(c_{11} - c_{12}\right) / \left(2c_{44}\right)$. The comparisons on the $<010>$ and $<110>$ planes are shown in Figs. 3.5.5 – 3.5.6. The calculation for fcc-structured Copper is carried out using the bcc structure in this example. All the predictions match the analytical solutions very accurately.

Table 3.5.3. Experimental Values for Elastic Constants of Selected Cubic Crystals

Material	c_{11}	c_{12}	c_{44}	f_0
Al	108	62	28.3	0.19
Cu	169	122	75.3	0.69
W	521	202	160.4	0.01
Fe	230	135	117	0.59

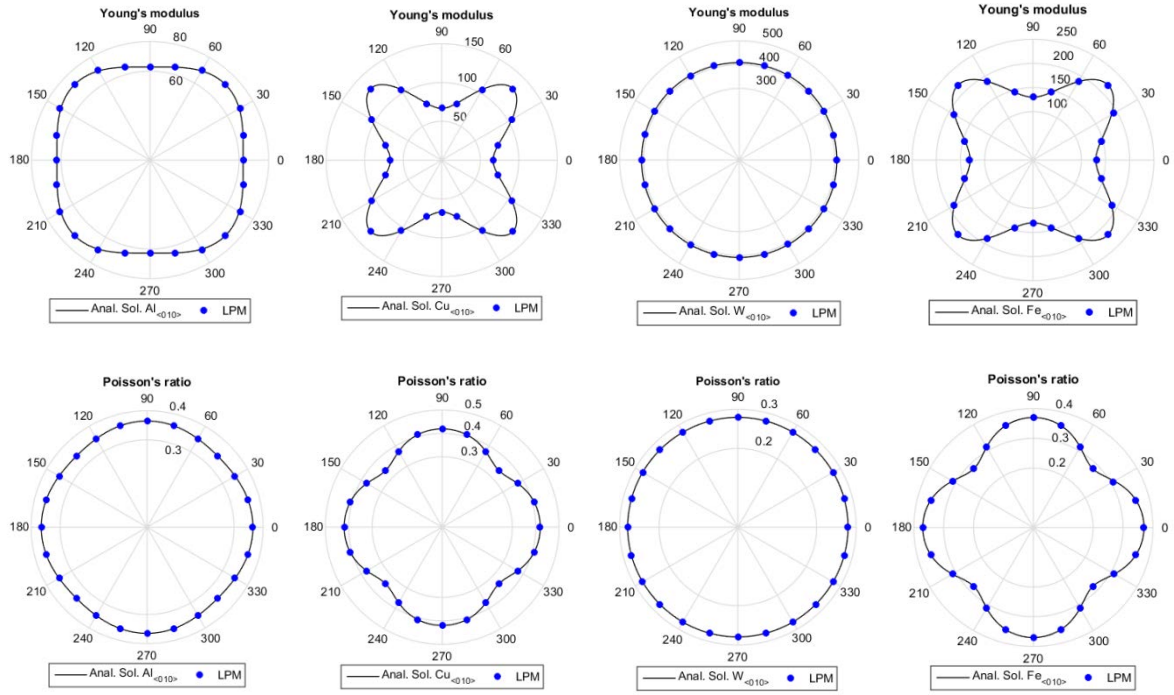

Figure 3.5.5. The Profile of the Young's Modulus and Poisson's Ratio on <010> Plane

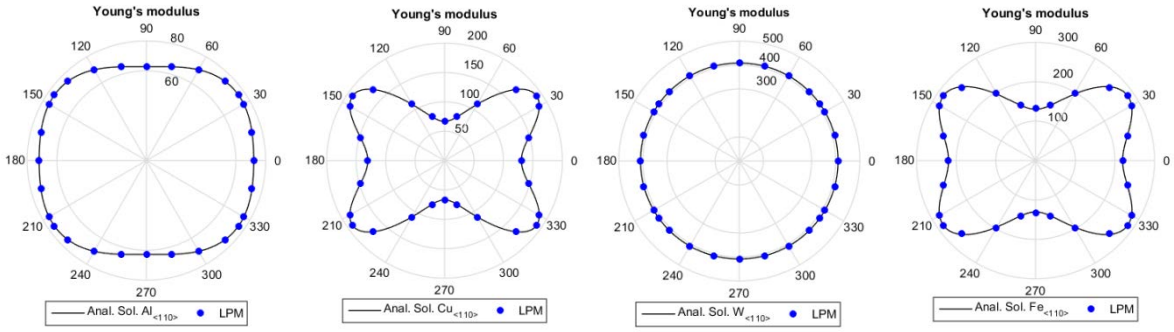

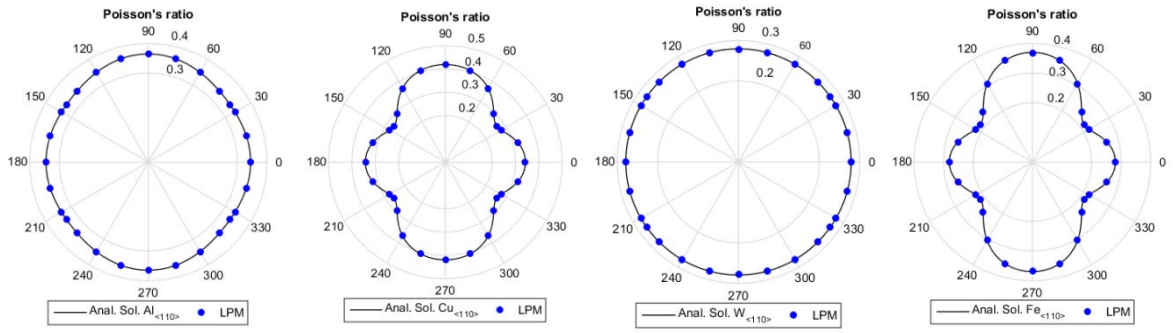

Figure 3.5.6. The Profile of the Young's Modulus and Poisson's Ratio on <110> Plane

3.5.5 Conclusion

One limitation on the proposed framework is that it can only model certain face centered cubic materials with $C_{11} > C_{12} + C_{44}$, i.e., the anisotropy factor $f_0 < 0.5$. This is due to that fact that the local potential parameter K_2 in Eq. (2.4.12) should be positive. But for simulations where the material's underlying lattice structure is not of importance, the body centered cubic structure model can be used, such as the effective elastic constants prediction shown in the result section.

Future work will focus on further investigation of the particle-based volume compensation scheme and application of the VCPM to some other practical problems. The reduction or elimination of the fracture anisotropy can be achieved by including more neighbors.

CHAPTER

4. SOLUTION METHODS AND APPLICATION TO REINFORCED COMPOSITES

4.1 Introduction

Modeling and prediction of the effective elastic, especially the fracture, response of a heterogeneous materials, in particular particulate reinforced composites, remains a very challenging problem in solid mechanics. Analytical and empirical models provide an effective means of predicting bounds on effective elastic properties of the composites from the known properties of its constituents, especially for simple configurations of phases. Many models are available in the literature, such as the Voigt and Reuss approximations; which provides the upper and lower bounds of the estimations. For the fracture properties, there are no analytical results available in the literature.

For multiphase materials, numerical modeling techniques, such as the finite element method (FEM) [184], [185], [186], [187], are more effective than analytical prediction since these materials often lack the structural simplicity such as continuous fiber composites or laminates and hence not readily amenable to closed-form theoretical analyses. Intensive research on using the lattice models to evaluate the effective elastic moduli can be found in the literature. Snyder et al. [188] used the triangular lattice to study the elastic moduli of 2D isotropic composites with circular inclusions. Day et al. [189] applied the same framework to calculate the elastic moduli of a matrix containing circular holes. Ostoja et al. [190], [191], [192] applied the lattice model to study the effective moduli of linear planar Delaunay networks. Garboczi et al. [193] developed a finite element method based algorithm while the simulation domain is represented using square lattice (2D) and simple cubic lattice (3D) for heterogeneous materials. No real lattice models exist in the literature for 3D heterogeneous materials.

In this chapter, the 3D lattice particle model based on simple cubic lattice is applied to calculate the effective elastic properties of particulate reinforced composites. The content of this chapter is organized as follows. In Section 4.2, the implicit solution method based on the Atomistic-scale

Finite Element Method is presented. Details of the resulted AFEM element for each packing is discussed. In Section 4.3, the explicit solution method based on particle dynamics is discussed. Two numerical damping schemes to obtain steady state solution from explicit formulation are discussed. Results for using adaptive dynamics relaxation scheme are provided. In Section 4.4, some basics on coupling the lattice particle model based on implicit solution scheme with finite element method are discussed. Some preliminary results to demonstrate the coupling concept is given. In Section 4.5, as a special application, the lattice particle model is applied to model particulate reinforced composites. Parametric study on the inclusion effects on both the effective elastic and fracture response of the composite is performed.

4.2 The Atomistic-scale Finite Element Method

The implicit solution method is used for model quasi-static response of materials, such as elasticity and plasticity problems. The implicit method used in lattice particle model is derived based on the Atomistic-scale Finite Element Method (AFEM) proposed by Liu et al. [136]. The basic idea in AFEM is system energy minimization. The final discretized equation system shares many similarities with finite element method, which provides an interface for the lattice particle model to be possibly coupled with the finite element methods.

The Atomic-scale Finite Element Method (AFEM) is a general solution method proposed by Liu et al. [136] for molecular statics. It has several advantages over the classical methods, such as conjugate gradient method, for statics in molecular simulation. Some basic and essential concepts in the derivation are given for illustrative purpose, more detailed formulation can be found in [136].

Similar to the Principal of Virtual Work used in deriving the discretized form of the governing equation in finite element methods, the AFEM uses Taylor Expansion of the system energy to obtain the discretized equation system.

The total energy of the particle system is a function of the particle positions

$$E_{total}\left(\mathbf{x}\right)=U_{total}\left(\mathbf{x}\right)-\sum_{I=1}^{N}\overline{\mathbf{f}}_{ext}\cdot\mathbf{x}_I \tag{4.2.1}$$

where $\mathbf{x}=\left(\mathbf{x}_1,\mathbf{x}_2,\cdots\mathbf{x}_N\right)^T$ the position vector of all N particles, $\overline{\mathbf{f}}_{ext}=\left(\overline{\mathbf{f}}_1,\overline{\mathbf{f}}_2,\cdots,\overline{\mathbf{f}}_N\right)^T$ is the external force exerted on the system, and $\mathbf{x}_I=\begin{Bmatrix}x_I\\y_I\end{Bmatrix}$ is the position vector of the particle I.

Omitting the high order terms, the Taylor expansion of E_{total} around an initial guess $\mathbf{x}^{(0)}$ of the equilibrium state gives

$$E_{total}\left(\mathbf{x}\right)\approx E_{total}\left(\mathbf{x}^{(0)}\right)+\left.\frac{\partial E_{total}}{\partial\mathbf{x}}\right|_{\mathbf{x}=\mathbf{x}^{(0)}}\cdot\left(\mathbf{x}-\mathbf{x}^{(0)}\right)+\frac{1}{2}\left(\mathbf{x}-\mathbf{x}^{(0)}\right)^T\cdot\left.\frac{\partial^2 E_{total}}{\partial\mathbf{x}\partial\mathbf{x}}\right|_{\mathbf{x}=\mathbf{x}^{(0)}}\cdot\left(\mathbf{x}-\mathbf{x}^{(0)}\right) \tag{4.2.2}$$

The state of minimal energy corresponds to

$$\frac{\partial E_{total}\left(\mathbf{x}\right)}{\partial \mathbf{x}} = 0 \tag{4.2.3}$$

Based on Eq. (4.2.3), following governing equation for the displacement $\mathbf{u} = \mathbf{x} - \mathbf{x}^{(0)}$ can be obtained

$$\mathbf{K}\mathbf{u} = \mathbf{P} \tag{4.2.4}$$

where

$$\mathbf{K} = \left.\frac{\partial^2 E_{total}\left(\mathbf{x}\right)}{\partial \mathbf{x}\partial \mathbf{x}}\right|_{\mathbf{x}=\mathbf{x}^{(0)}} = \left.\frac{\partial^2 U_{total}\left(\mathbf{x}\right)}{\partial \mathbf{x}\partial \mathbf{x}}\right|_{\mathbf{x}=\mathbf{x}^{(0)}} \tag{4.2.5}$$

is the stiffness matrix and

$$\mathbf{P} = -\left.\frac{\partial E_{total}\left(\mathbf{x}\right)}{\partial \mathbf{x}}\right|_{\mathbf{x}=\mathbf{x}^{(0)}} = \overline{\mathbf{f}}_{ext} - \left.\frac{\partial U_{total}\left(\mathbf{x}\right)}{\partial \mathbf{x}}\right|_{\mathbf{x}=\mathbf{x}^{(0)}} \tag{4.2.6}$$

is the non-equilibrium force vector.

At particle level, the corresponding stiffness matrix for the 2D case can be written as

$$\mathbf{K}_I = \begin{bmatrix} \frac{\partial^2 U_{total}}{\partial x_I \partial x_I} & \frac{\partial^2 U_{total}}{\partial x_I \partial y_I} & \frac{1}{2}\frac{\partial^2 U_{total}}{\partial x_I \partial x_1} & \frac{1}{2}\frac{\partial^2 U_{total}}{\partial x_I \partial y_1} & \cdots & \frac{1}{2}\frac{\partial^2 U_{total}}{\partial x_I \partial x_{18}} & \frac{1}{2}\frac{\partial^2 U_{total}}{\partial x_I \partial y_{18}} \\ \frac{\partial^2 U_{total}}{\partial y_I \partial x_I} & \frac{\partial^2 U_{total}}{\partial y_I \partial y_I} & \frac{1}{2}\frac{\partial^2 U_{total}}{\partial y_I \partial x_1} & \frac{1}{2}\frac{\partial^2 U_{total}}{\partial y_I \partial y_1} & \cdots & \frac{1}{2}\frac{\partial^2 U_{total}}{\partial y_I \partial x_{18}} & \frac{1}{2}\frac{\partial^2 U_{total}}{\partial y_I \partial y_{18}} \\ \frac{1}{2}\frac{\partial^2 U_{total}}{\partial x_I \partial x_1} & \frac{1}{2}\frac{\partial^2 U_{total}}{\partial x_I \partial y_1} & 0 & 0 & \cdots & 0 & 0 \\ \frac{1}{2}\frac{\partial^2 U_{total}}{\partial y_I \partial x_1} & \frac{1}{2}\frac{\partial^2 U_{total}}{\partial y_I \partial y_1} & 0 & 0 & & & 0 \\ \vdots & \vdots & \vdots & & \ddots & & \vdots \\ \frac{1}{2}\frac{\partial^2 U_{total}}{\partial x_I \partial x_{18}} & \frac{1}{2}\frac{\partial^2 U_{total}}{\partial x_I \partial x_{18}} & 0 & & & 0 & 0 \\ \frac{1}{2}\frac{\partial^2 U_{total}}{\partial y_I \partial x_{18}} & \frac{1}{2}\frac{\partial^2 U_{total}}{\partial y_I \partial y_{18}} & 0 & 0 & \cdots & 0 & 0 \end{bmatrix} \tag{4.2.7}$$

The non-equilibrium force matrix is

$$\mathbf{P}_I = \left\{ f_{ext}^{x} - \frac{\partial U_{total}}{\partial x_I} \quad f_{ext}^{y} - \frac{\partial U_{total}}{\partial y_I} \quad 0 \quad 0 \quad 0 \quad 0 \quad 0 \quad 0 \quad 0 \quad 0 \quad 0 \quad 0 \quad 0 \quad 0 \right\}^T \tag{4.2.8}$$

The AFEM elements in the lattice particle model for different lattice packing are shown in Fig. 4.2.1.

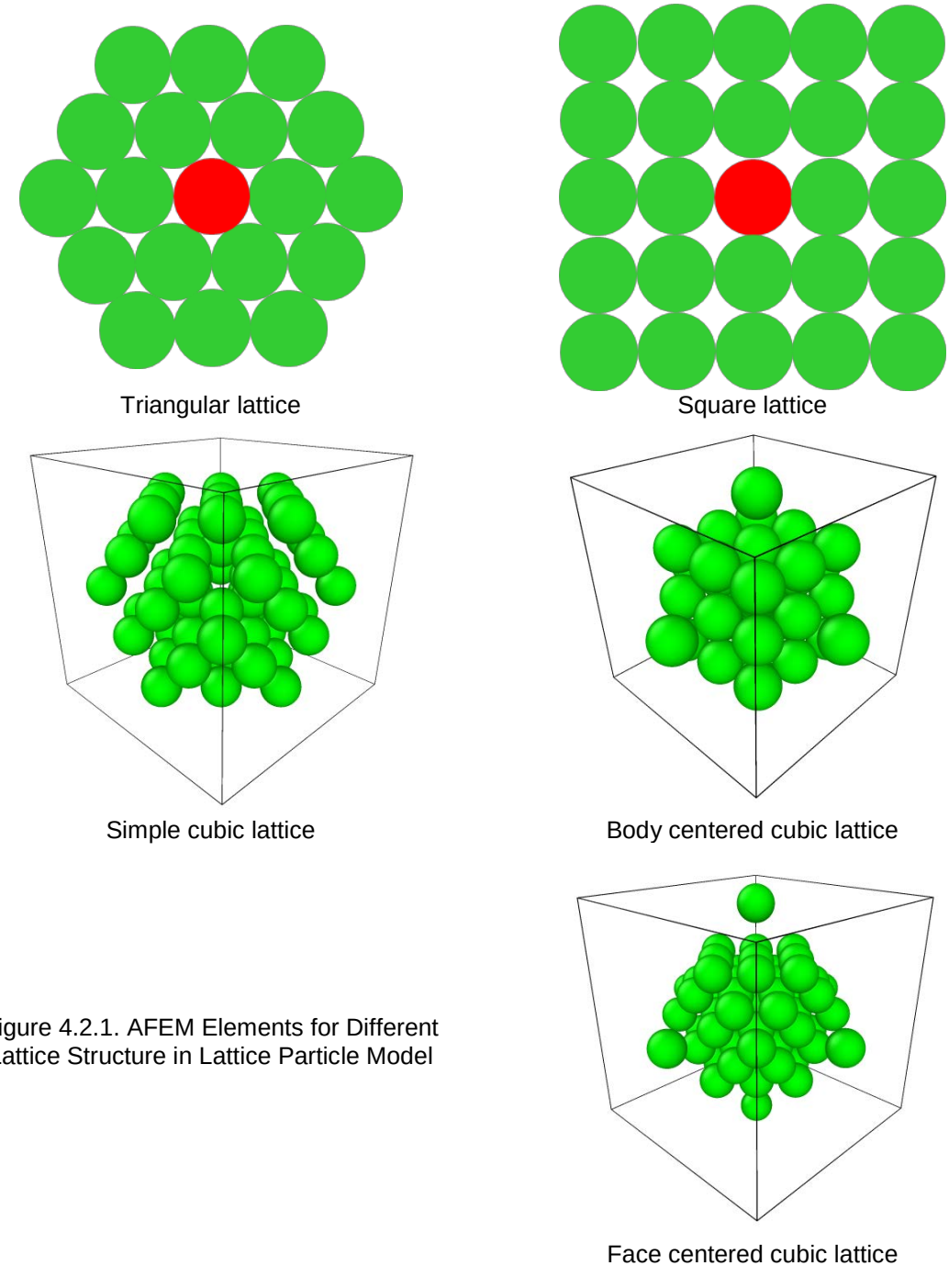

Figure 4.2.1. AFEM Elements for Different Lattice Structure in Lattice Particle Model

4.3 Particle Dynamics

The explicit, or dynamic, solution method aims to model dynamic problems, such as dynamic fracturing and crack propagation problems. It bases on the Newton-Euler's Equation of Motion (EOM) and solves the discrete system as a sequential update of the particle states. One of the frequently used integration schemes in the literature.is the Velocity Verlet integration method [194].

4.3.1. Equation of Motion and Velocity Verlet integration

All particles in the lattice particle model obey the Newton's second law of motion. The Equations of Motion of the entire system is

$$\mathbf{M}\ddot{\mathbf{u}} + \mathbf{f}_{\mathbf{int}} = \mathbf{f}_{\mathbf{ext}} \tag{4.3.1}$$

where $\mathbf{M}$ is the diagonal mass matrix, $\mathbf{u}$ is the position matrix, $\mathbf{f}_{\mathbf{int}}$ is the internal force matrix and $\mathbf{f}_{\mathbf{ext}}$ is the external force matrix. $\ddot{\mathbf{u}}$ is the acceleration matrix needs to be solved. $\mathbf{f}_{\mathbf{int}}$ is a column matrix with the component being the internal resultant force on each particle.

The solution method used in lattice particle model to solve the equations system is the simple Velocity Verlet method [194].

$$\begin{aligned}
\mathbf{x}_i\left(t+dt\right) &= \mathbf{x}_i\left(t\right) + \dot{\mathbf{u}}_i\left(t\right)dt + \frac{\ddot{\mathbf{u}}_i\left(t\right)}{2}dt^2 \\
\dot{\mathbf{u}}_i\left(t+\frac{dt}{2}\right) &= \dot{\mathbf{u}}_i\left(t\right)dt + \frac{\ddot{\mathbf{u}}_i\left(t\right)}{2}dt \\
\ddot{\mathbf{u}}_i\left(t+dt\right) &= \frac{\mathbf{f}_{ext}^{i}\left(t+dt\right) - \mathbf{f}_{int}^{i}\left(t+dt\right)}{m_i} - c\dot{\mathbf{u}}_i\left(t+\frac{dt}{2}\right) \\
\dot{\mathbf{u}}_i\left(t+dt\right) &= \dot{\mathbf{u}}_i\left(t+\frac{dt}{2}\right) + \frac{\ddot{\mathbf{u}}_i\left(t+dt\right)}{2}dt
\end{aligned} \tag{4.3.2}$$

where $\mathbf{x}_i\left(t\right)$ and $\mathbf{x}_i\left(t+dt\right)$ are the position vector of a particle at current time step and next time step, respectively. $\dot{\mathbf{u}}$ is the velocity matrix and c is the damping coefficient.

The solution is conditional stable and the critical time step is determined from the speed of P-wave.

$$\Delta t_{critical} = \frac{2R}{v_p} \tag{4.3.3}$$

where R is the radius of the particles and the P-wave speed is

$$v_p = \sqrt{\frac{K + 4G/3}{\rho}} \tag{4.3.4}$$

where K and G are the bulk and shear moduli of the material.

4.3.2. Kinematic Damping

For quasi-static elastic problems based on dynamic formulation, damping is usually introduced in order to obtain a static solution. Kinetic damping was proposed by Cundall [195] as an alternative damping method to viscous damping. The underlying basis of kinetic damping is that as an oscillating body passes through a minimum potential energy state its total kinetic energy reaches a local maximum. Under this scheme, the total kinetic energy is traced under un-damped motion of the system of particles. Upon detection of a local energy peak, all current particles' velocities are set to zero. The process is then restarted from the current state and continued through generally decreasing peaks until the kinetic energy of the system has been dissipated and the system attains its static equilibrium state. This scheme can be used in lattice particle model for the static solution from dynamics formulation. A schematic for the basic idea in kinetic damping is shown in Fig. 4.3.1.

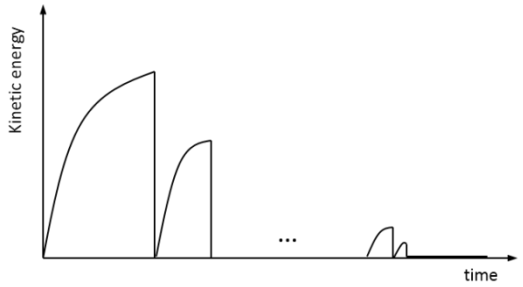

Figure 4.3.1. Dissipation of Kinetic Energy in Dynamic Formulation

4.3.2. Adaptive dynamic relaxation

As has been pointed out by Rayleigh, the static solution of a mechanics system can be referred to as the steady-state part of the transient response of the system to step loadings. This approach was successfully applied to solving linear problems by the pioneer work of Otter [196] and Day [197] independently in the 1960s. Later in early 1980s, Underwood [198] summarized the advances of the dynamics relaxation method and proposed an adaptive dynamic relaxation (aDR) scheme which will be discussed in this section.

Generally, the Equation of Motion (EoM) of a discrete system at step n has following form as

$$\mathbf{M}^n\ddot{\mathbf{u}}^n + \mathbf{C}^n\dot{\mathbf{u}}^n = \mathbf{R}^n \tag{4.3.5}$$

where $\mathbf{M}$ and $\mathbf{C}$ are the fictitious diagonal mass and damping matrices, $\mathbf{u}$ is the displacement vector and $\mathbf{R}$ is the residual force vector.

$$\mathbf{R}^n = \mathbf{F}_{ext}^n - \mathbf{F}_{\text{int}}^n \tag{4.3.6}$$

The central difference integration scheme is used to update the system. Assuming mass-proportional damping, i.e. $\mathbf{C} = c\mathbf{M}$, the fundamental time march equations for updating the velocities and displacements for the next time step are

$$\dot{\mathbf{u}}^{n+1/2} = \left(\frac{2 - c\Delta t}{2 + c\Delta t}\right)\dot{\mathbf{u}}^{n-1/2} + \left(\frac{2\Delta t}{2 + c\Delta t}\right)\mathbf{M}^{-1}\mathbf{R}^n \tag{4.3.7}$$

$$\mathbf{u}^{n+1} = \mathbf{u}^n + \Delta t\dot{\mathbf{u}}^{n+1/2} \tag{4.3.8}$$

The mass matrix $\mathbf{M}$ and time step Δt are not independent and they must satisfy certain relationship in order to make the system stable and convergent. Generally, the time step Δt is taken to be a unity ($\Delta t = 1$) and the inequality based on the Gerschgorin circle theorem for the mass matrix should be satisfied. That is

$$m_{ii}^n \geq \frac{1}{4}\left(\Delta t\right)^2 \sum_j \left|K_{ij}^n\right| \tag{4.3.9}$$

where $\left[K_{ij}^n\right]$ is the stiffness matrix of the system at step n.

Using the mass-stiffness Rayleigh quotient, the damping coefficient c at step n can be approximated as

$$c^n = 2\sqrt{\frac{\left(\mathbf{u}^n\right)^T \mathbf{K}^n \left(\mathbf{u}^n\right)}{\left(\mathbf{u}^n\right)^T \mathbf{M}^n \left(\mathbf{u}^n\right)}} \tag{4.3.10}$$

For the force controlled loading, $\mathbf{u}^0 = \mathbf{0}$, the damping coefficient c^1 is taken to be zero. For displacement controlled loading, the velocities for the particles with applied displacement is nonzero, thus the damping coefficient c^1 can be calculated using Eq.(4.3.10).

For linear problems, the tangent stiffness matrix $\mathbf{K}$ is directly used to approximate the damping ratio, as shown in Eq.(4.3.10). For nonlinear problems, a diagonal estimator $\mathbf{S}$ is commonly used and given by

$$S_{ii}^n = \frac{{}^{\mathrm{i}}F_{\mathrm{int}}^n - {}^{\mathrm{i}}F_{\mathrm{int}}^{n-1}}{\Delta t \dot{u}_i^{n-1/2}} \tag{4.3.11}$$

For non-linear problems exhibit structural instability, the stiffness matrix may lose positive definiteness which results in a negative radicand. Under these conditions, the damping coefficient c is set to be zero as recommended by [198].

As the system marching towards the steady state, a convergence criterion should be used to terminate the simulation process. Different convergence criteria can be used, such as the residual force, the residual kinetic energy. In this study, the kinetic energy convergence criterion is used.

The simulation is terminated when the ratio of the kinetic energy of the system to work done by the internal force is very small to a prescribed tolerance value.

$$\varepsilon = \frac{\frac{1}{2}\left(\dot{\mathbf{u}}^{n-1/2}\right)^T \mathbf{M}\dot{\mathbf{u}}^{n-1/2}}{\frac{1}{2}\left(\mathbf{u}^n\right)^T \mathbf{F}_{\text{int}}^n} \leq \alpha \tag{4.3.12}$$

where α is a very small number such that the whole system can be viewed as under steady state.

Next, a clamped square sectioned beam under traction loading is modeled to assess the performance of the implemented aDR for elastic response of solids in lattice particle model. The 2D configuration of the beam is shown in Fig. 4.3.2.

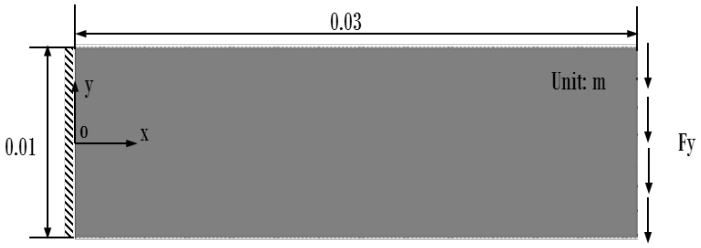

Figure 4.3.2. Cantilever Beam under Traction Force

2D case:

The simulation results of the displacement distribution of the 2D case are shown in Fig. 4.3.3. The profile of the displacement Uy at point (0.03,0) is shown in Fig. 4.3.4. The profile of the system kinetic energy is shown in Fig. 4.3.5. As can be seen from the comparison with FEM solution, the results using ADR solution scheme is very accurate.

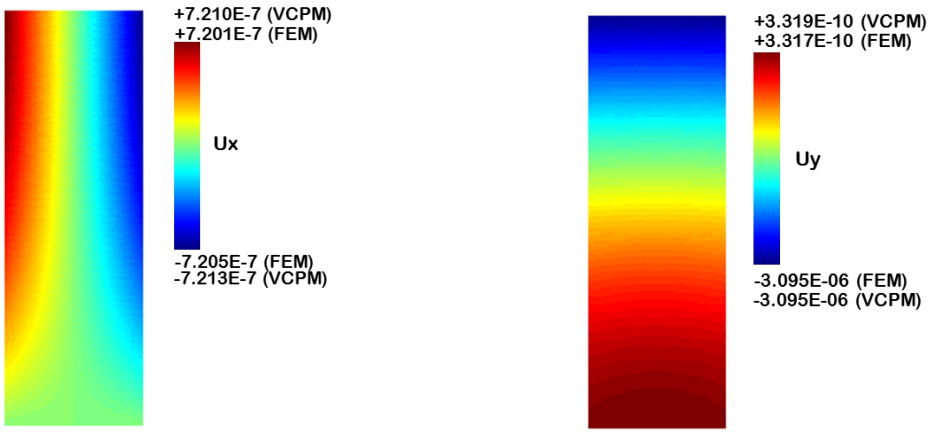

Figure 4.3.3. The Displacements Fields Using the Triangular Llattice

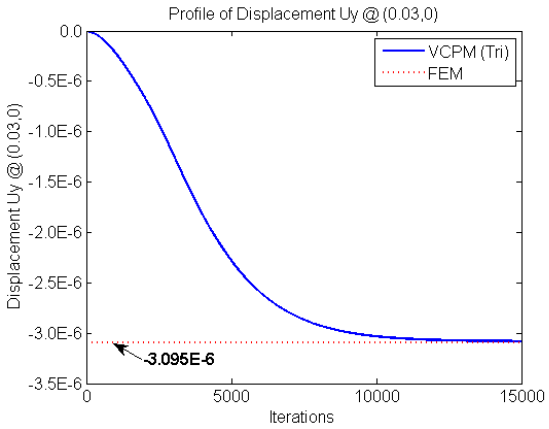

Figure 4.3.4. The Profile of the Displacement Uy at Point (0.03,0)

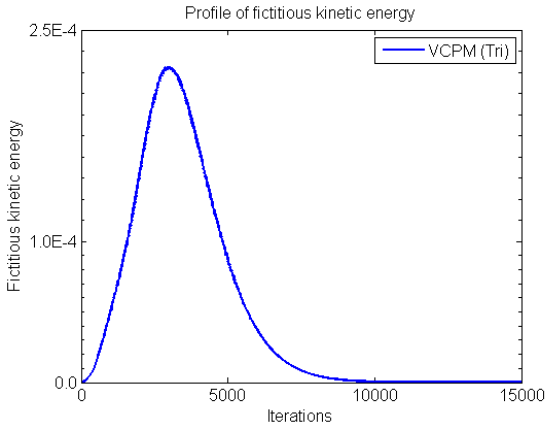

Figure 4.3.5. The Profile of the Fictitious Kinetic Energy of the System (2D)

3D case:

The boundary conditions for 3D case are that the left end is fully clamped and a traction force with value of *2 KN* is applied in the positive *y* direction on the right end surface. The formulation based on body-centered cubic lattice structure is used in this 3D case. The steady state displacement distributions are shown in Fig. 4.3.6. The profile of the displacement Uy at point (0.03,0,0) is shown in Fig. 4.3.7. The kinetic energy profile for the case of simple cubic pack is shown in Fig. 4.3.8.

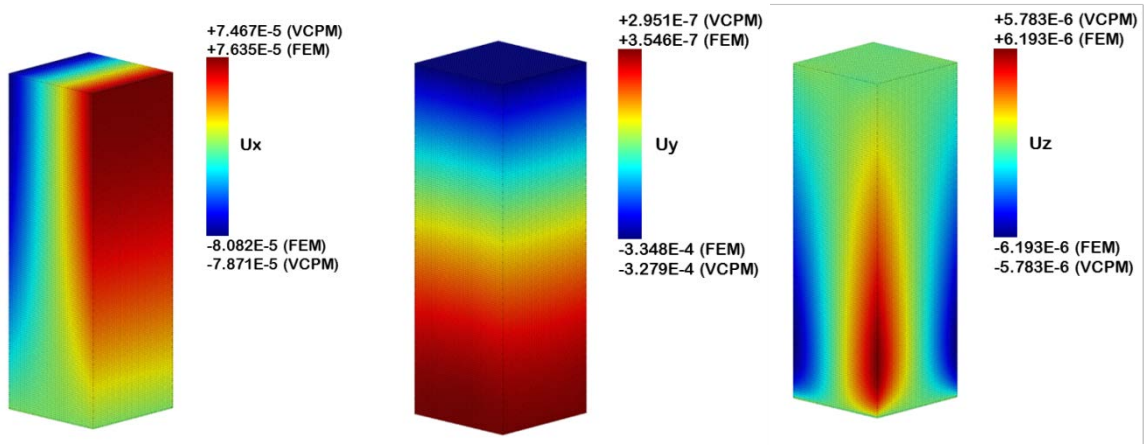

Figure 4.3.6. The displacement fields using the bcc lattice structure

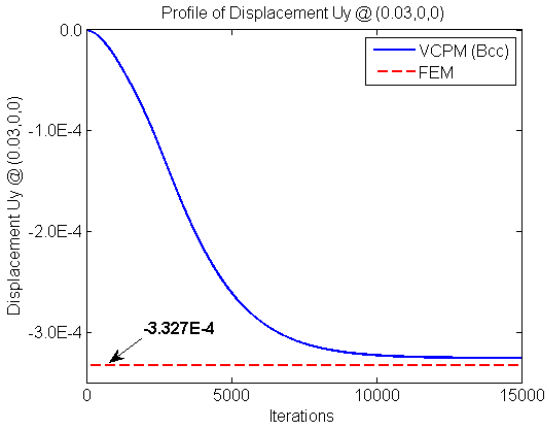

Figure 4.3.7. The Profile of the Displacement Uy at Point (0.03,0,0)

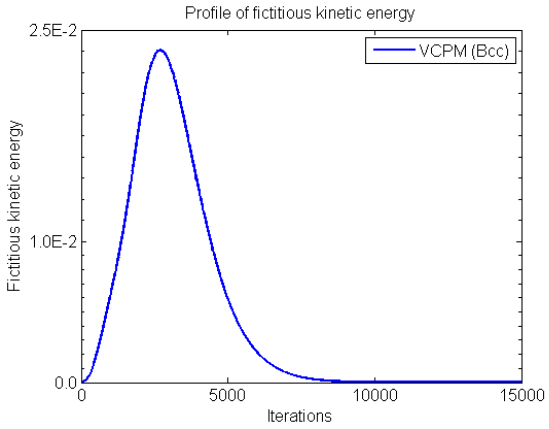

Figure 4.3.8. The Profile of Fictitious Kinetic Energy of the System (3D)

4.4 Coupling between Lattice Particle Model with Finite Element Method

Due to the intrinsic characteristics, discrete models have extensive applications for energetic problems, such as impact simulation. A well-known issue for the discrete models is the computational inefficiency. A relatively large amount of discrete elements must be used in order to achieve certain solution accuracy. This is the case for both static and dynamic formulation. With the fast increase of computation power, this shortcoming will not be of critical concern in simulations using discrete models. It's sometimes still desirable to reduce the computational power requirement by coupling these models with continuum based models, such as finite element methods [199]. This is also sometimes required by model larger structures using the discrete model.

For coupling scheme available in the literature, the domain partition scheme is usually used. The domain of interest is decomposed into several subdomains. For subdomains of special interest, such as crack tip/front, the discrete model is used to take the advantage of modeling discontinuities, while finite element method is used just for the purpose of taking care of general deformation in other subdomain. For some models, a handshake zone is also defined. A handshake zone is a subdomain in which the coupling between two different models is happened and treated only in this area. Sometimes, a bridging zone is also used with the handshake zone. While in some other models, there is no specific zone assigned for the coupling, only the overlapping interface is used.

In this paper, we present some basic concepts for coupling the lattice particle model with finite element method. Preliminary results for applying the coupled model to study the static and dynamic problems are also provided. The content of this section is organized as follows. First, the coupling method between the lattice particle model and finite element method is discussed. Following this, some preliminary results for several benchmarks to examine the accuracy of the coupling methods is presented. Conclusions and future works are drawn at the end of this section.

4.4.1 The lattice particle and finite element interface

In order to couple the lattice particle model with finite element method, the atomistic-scale finite element formulation is used. And since the atomistic-scale finite element formulation shares the same framework with finite element method, the coupling between these two models becomes very trivial. The only concern is how to treat the interface springs. The virtual lattice particles that are centered at the finite element nodes are introduced. A schematic showing the interface coupling is shown in Fig. 4.4.1.

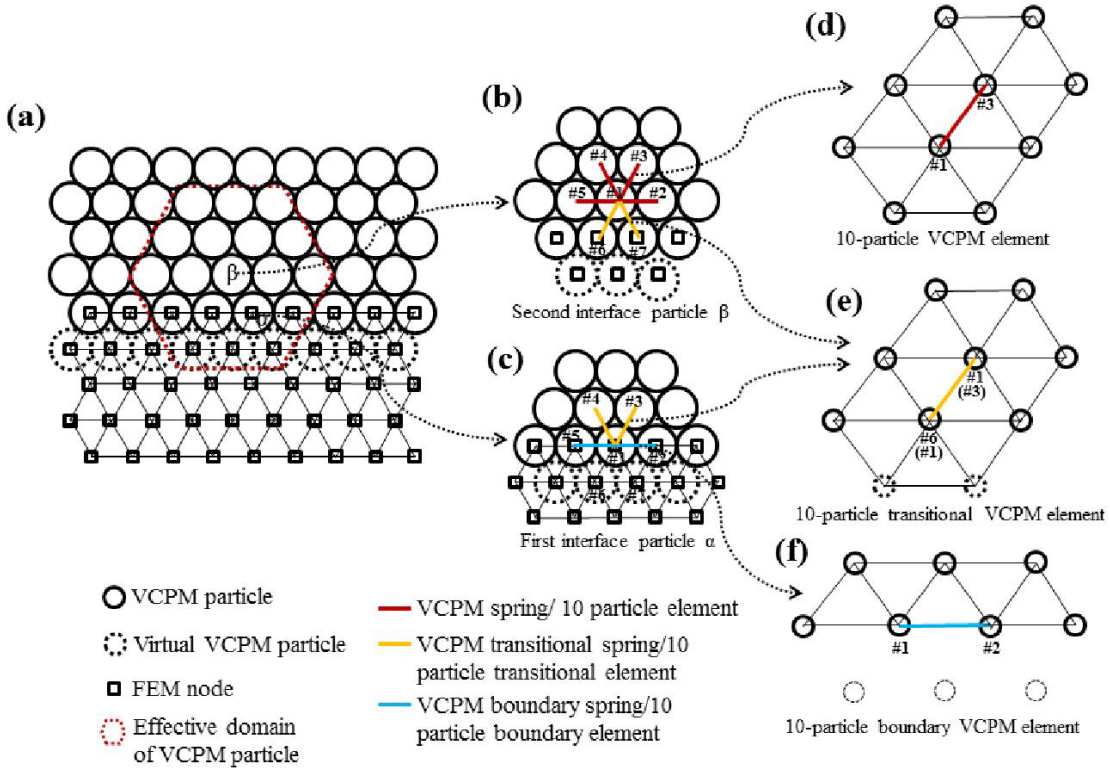

Figure 4.4.1. The Interface Coupling scheme in Lattice Particle Model

4.4.2 Preliminary simulation results

Some preliminary results for applying the coupled model to both static and dynamic problems are presented in this subsection.

Static simulation

Beam bending problems

The geometry and boundary conditions of the static beam bending problem are described in Fig.4.4.2. The beam is fixed in both x- and y- directions at the left and right end. A concentrated load of $5x10^3$ *N* is applied on the center of top edge downward. For modeling, the beam is divided into three sub-regions, where the center region is modeled using the lattice particles with radius equal to $5x10^{-5}$ *m* .The material constants for the beam are Young's modulus *E* = 69 *GPa*, and Poisson's ratios *v* = 0.33.

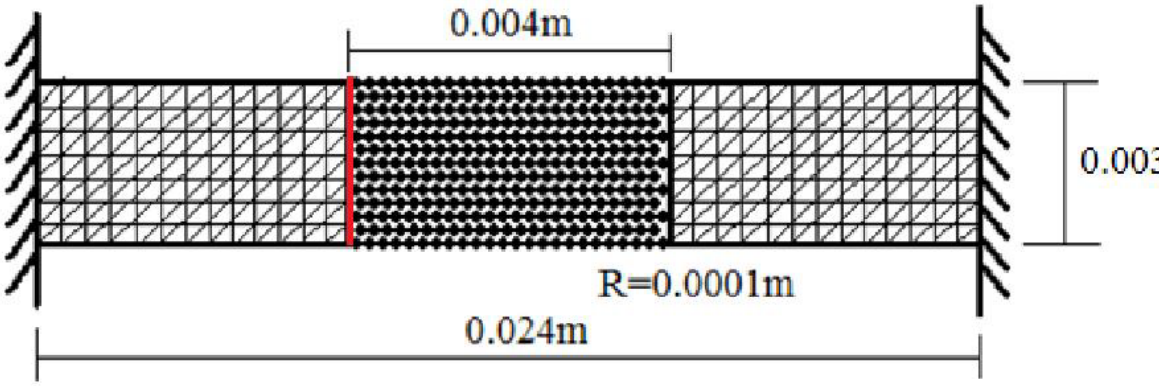

Figure 4.4.2. The Configuration of Clamped Beam for Coupled Model

The displacement distribution is shown in Fig. 4.4.3. The detailed comparison of the reaction force at the two ends and displacements at the bottom edge and the interface are shown in Fig. 4.4.4. From the simulation results, the coupled model can accurately capture the static deformation compared to the finite element solutions from ABAQUS. And there is no displacement discontinuity at the interface.

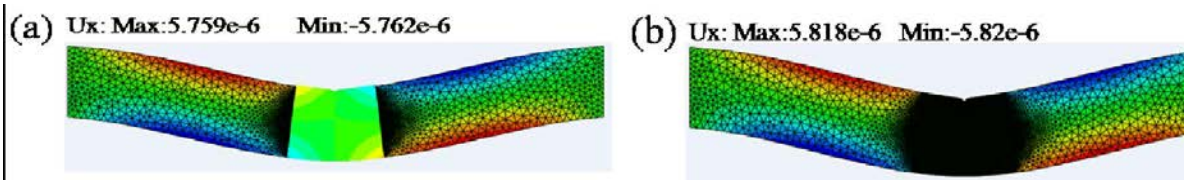

Figure 4.4.3. The Displacements Distribution Using the Coupled Model

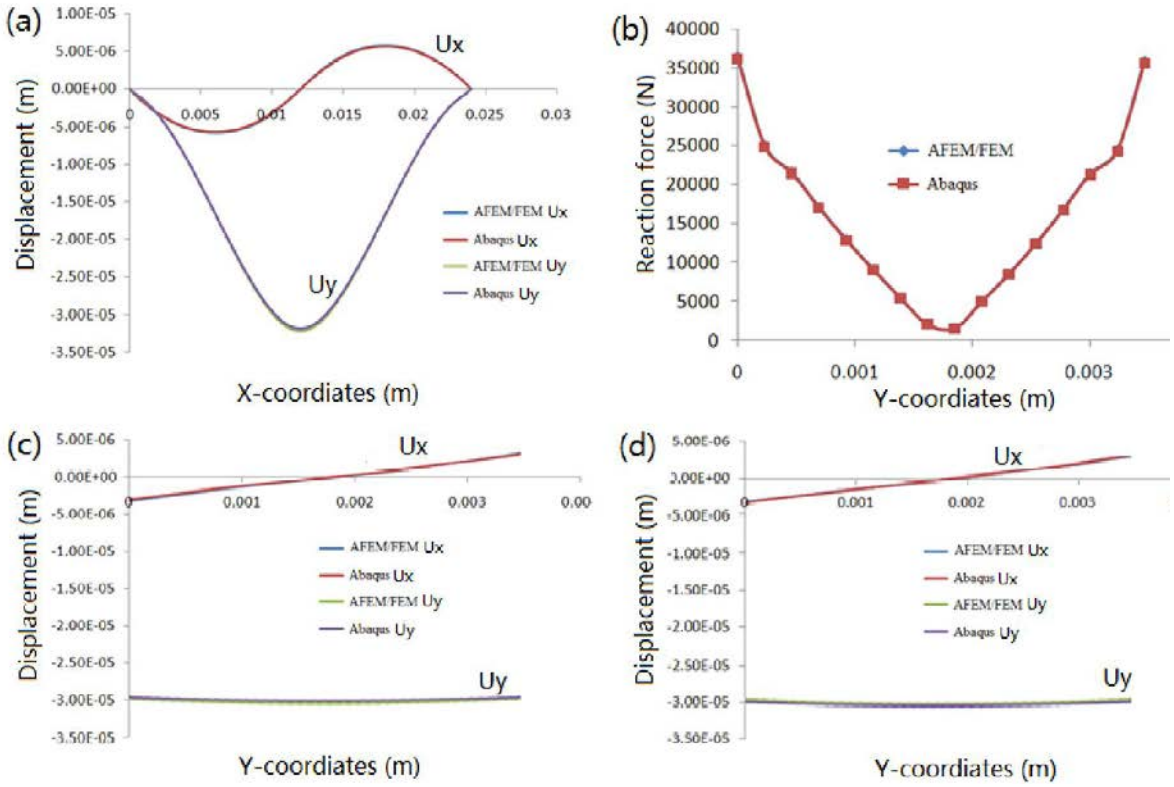

Figure 4.4.4. Detailed Comparison of the End Reaction Force and Interface Deformation

Dynamic simulation

A spall damage simulation is modeled using the lattice particle model. A boundary free beam of size 0.127 x 0.0127 *m* is applied with a rectangular stress wave at the right end. The beam is divided into two subdomains, with the left is modeled using the lattice particle model. The material constants are Young's modulus E = 3.0 *GPa*, Poisson's ratios v = 0.33.and mass density ρ = 1140 kg/m^3.

Three types of input wave with various wave widths are simulated and compared (Fig.4.4.5). From the results, it's clearly show that the spall damage can be captured by the coupled model. The spall zone appears right at the position, where the reflected tension wave meets the wake of the input compression wave.

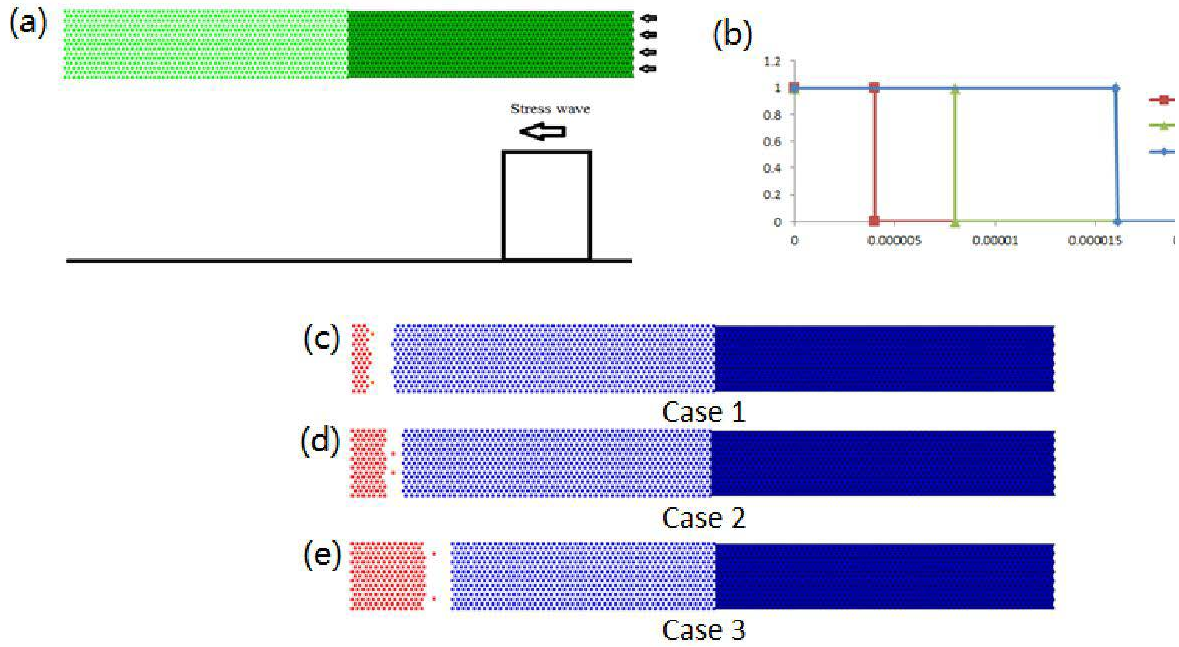

Figure 4.4.5. The Stress Waves and Resulted the Final Failure Patterns

4.4.3. Conclusion

Some basic concepts of coupling the lattice particle method with finite element method are presented in this section. In the developed coupled model, the lattice particle model is applied to the regions of interest, e.g., the regions where the crack initiates and propagates, while finite element model is applied in the remaining regions to take care of the general deformations. The coupling method is based on the atomistic-scale finite element formulation in lattice particle model, which shares the same theoretical framework with the classic finite element method. Some preliminary results of both static and dynamic problems using the coupled model are also provided to test the performance and validity of the coupled model. The results indicate that the coupled model not only significantly improves the computational efficiency, but also well maintains the computational accuracy.

More efforts are required to extend the coupled model to the simulation of more complex problems, e.g., strain rate dependent dynamic failure problems, quasi-static crack propagation problems, etc.

4.5 Particle Reinforced Composites

In this section, the lattice particle model using the simple cubic packing is applied to obtain the effective elastic and fracture properties of bi-phase particulate composite materials. First, the interface problem is discussed in detail. Following this, the representative volume elements for particulate reinforced composite are generated. Finally, simulations for several microstructures are performed. The effective elastic and fracture properties are obtained. Conclusions are drawn based on the current study.

4.5.1 Introduction

Modeling and prediction of the effective elastic, especially the fracture, response of heterogeneous materials, in particular particulate reinforced composites, remains a very challenging problem in solid mechanics. Analytical and empirical models provide an effective means of predicting bounds on effective elastic properties of the composites from the known properties of its constituents, especially for simple configurations of phases. Many models are available in the literature, such as the Voigt approximation; the Reuss approximation, the variational principles model [200], [201], the Mori-Tanaka estimates [202], [203], the self-consistent scheme [204], and the differential method [205], etc. For the fracture properties, there is no analytical result that can be found in the literature.

For multiphase materials, numerical modeling techniques, such as the finite element method (FEM), are more effective than analytical prediction since these materials often lack the structural simplicity such as continuous fiber composites or laminates and hence not readily amenable to closed-form theoretical analyses. Intensive research work have been done in this area, such as[184], [185], [186], [187], to name a few. An important aspect while using the computational approach to approximate the overall properties of a composite material is the determination of the characteristic size of the Representative Volume Element (RVE). The first formal definition of RVE was given by Hill [206] in which a RVE must be structurally entirely typical of whole micro-structure on average and must contain a sufficiently large number of micro-structual

heterogeneities. Later, Drugan and Willis [207] have defined RVE as the smallest volume element of a material for which the usual spatially constant effective modulis are sufficiently accurate to represent overall constitutive response. Torquato [208] has used the correlation function to define the minimum size requirement of a RVE for particulate reinforced system.

In this section, the lattice particle model using the simple cubic packing is applied to study the effective elastic and fracture response of 3D particulate reinforced composites. The content of this section is organized as follow. First, the modeling of interface between different material phases is discussed. Following this, the RVEs generation is presented. Next, parametric studies on the effects of particle volume fraction and size are performed and the calculated effective mechanical properties with interface effect are compared to the analytical estimate. Conclusions are drawn based on current study at the end.

4.5.2 Modeling Interface in lattice particle model

Each phase of composites is assumed to be homogeneous and isotropic. The stiffness of the spring and the volume-related parameter of the particle within a phase are obtained using Eq. (2.4.8) given the material constants, i.e. Young's modulus and Poisson's ratio.

For interfaces between different material phases, the properties of the bonds straddling these two phases can be obtained from experiment. For simplicity, some mathematical averages are used in this study, i.e., the arithmetic mean and the harmonic mean. The arithmetic mean is defined as

$$k_{\text{interphase}}^{\text{arithmetic}} = \frac{k_{\text{phase1}} + k_{\text{phase2}}}{2}; T_{\text{interphase}}^{\text{arithmetic}} = \frac{T_{\text{phase1}} + T_{\text{phase2}}}{2} \tag{4.5.1}$$

while the harmonic mean is defined as

$$k_{\text{interphase}}^{\text{harmonic}} = \frac{2}{\frac{1}{k_{\text{phase1}}} + \frac{1}{k_{\text{phase2}}}}; T_{\text{interphase}}^{\text{harmonic}} = \frac{2}{\frac{1}{T_{\text{phase1}}} + \frac{1}{T_{\text{phase2}}}} \tag{4.5.2}$$

A typical interface in VCPM is shown in Fig. 4.5.1.

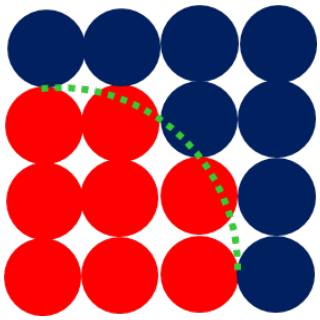

Figure 4.5.1. A Typical Interface in a Two-Phase Material (2D view)

4.5.3 The RVEs

RVEs of different numbers of identical non-overlapping randomly distributed spheres with different volume fractions are created for the investigation of the both effective elastic and fracture properties. Volume fractions of 10%, 20%, 30%, 40%, and 50% are considered. For a fixed volume fraction, 30, 40, and 50 numbers of spheres are considered to study the size effect. The original and the dicretized with periodic boundary condition configurations of the RVEs of the case of 30 spheres, 30% volume fraction are shown in Fig. 4.5.2. The size of these RVE are determined according to [208] using the S2 correlation function. The corresponding S2 correlation function is given in Fig. 4.5.3. From the S2 curve, we can see the RVE size is statistical satisfactory according to [208].

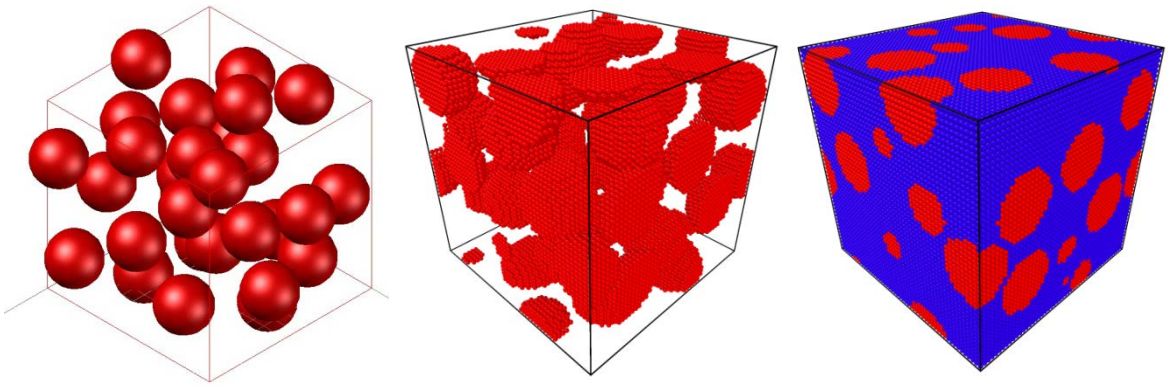

The RVE identified from the composites

The discretized RVE with periodic boundaries (the particles)

The discretized RVE with periodic boundaries

Figure 4.5.2. The RVEs for 30 Particles with Volume Fraction of 30%

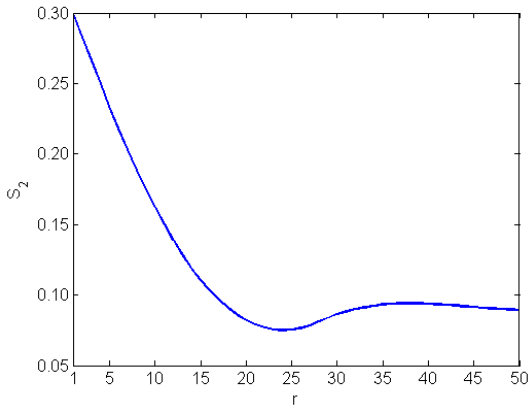

Figure 4.5.3. The S2 for the RVE of 30 Particles with Volume Fraction of 30%

4.5.4 Results and Discussions

The effect of the interface properties, the volume fraction, the inclusion size on both the effective elastic and fracture properties are studied in this section. The material constants are shown in Table 4.5.1.

Table 4.5.1. Material Constants for Bi-Phase Particulate Reinforced Composite

E_{matrix}	70 GPa	E_{particle}	450 GPa
ν_{matrix}	0.3	ν_{particle}	0.17

The calculation of the effective elastic moduli is conducted in three steps:

1). subjecting the cube at its surfaces to a uniform tri-axial extension, corresponding to a strain $\varepsilon_{11} = \varepsilon_{22} = \varepsilon_{33} = \varepsilon_0$, and then calculating the total energy $U_{(1)}$ as a sum of energies of all unit cells, or particles;

2). subjecting the cube at its surface to a uniform extension in y and z directions and a uniform compression in x direction, corresponding to a strain $-\varepsilon_{11} = \varepsilon_{22} = \varepsilon_{33} = \varepsilon_0$, and then calculating the total energy $U_{(2)}$ as before;

3). in terms of the bulk modulus K and shear modulus G, the energy of a three-dimensional linear elastic continuum of volume V is

$$U = V\left(\frac{K}{2}\varepsilon_{ii}\varepsilon_{jj} + G\left(\varepsilon_{ij}\varepsilon_{ij} - \frac{1}{3}\varepsilon_{ii}\varepsilon_{jj}\right)\right) \tag{4.5.3}$$

The bulk modulus and shear modulus can be calculated through these steps as

$$K = \frac{2}{9}\frac{U_{(1)}}{V\varepsilon_0^2}$$
$$G = \frac{1}{24}\frac{9U_{(2)} - U_{(1)}}{V\varepsilon_0^2} \tag{4.5.4}$$

Effective elastic properties

The effects of the interface property, the volume fraction and the inclusion size on the bulk modulus K and shear modulus G are studied in this subsection. The effective value for the bulk and shear moduli are obtained by carry out the outline procedure in lattice particle model. The interface properties are determined using the arithmetic mean and harmonic mean defined in Eqs. (4.5.1) - (4.5.2).

The interface effect

The results showing the effect of the interface properties on the effective bulk and shear moduli are given in Fig. 4.5.4. As can be seen, with the increase of the interface spring stiffness and volume-related parameter (the arithmetic mean is greater than the harmonic mean), both the overall bulk and shear moduli increase. The predicted value also compared with Hashin-Shtrikman's bounds with perfect interface. As can be seen, the predicted values are fall within the bounds.

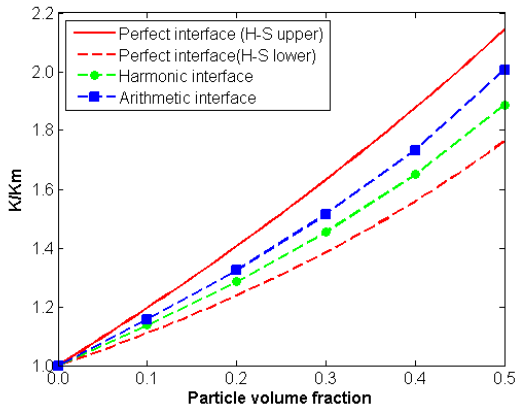

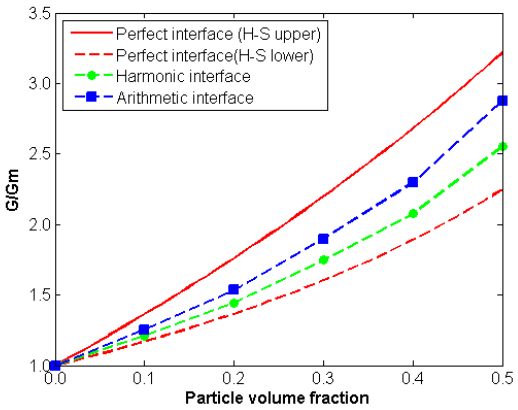

Figure 4.5.4. The Effect of the Interface and Volume Fraction on the Effective Bulk and Shear Moduli

The particle size effect

The results for the particle size effect on the elastic properties, i.e., bulk and shear moduli, are shown in Fig. 4.5.5. As can be seen, for different particle number in a fixed RVE volume, i.e., different particle size, the difference of the predicted values is small. The variance becomes larger with the increase of the particle volume fraction.

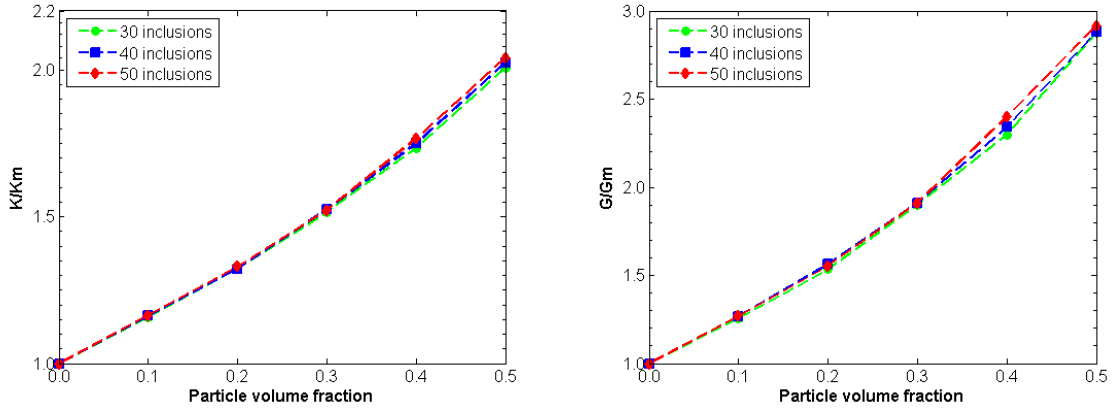

Figure 4.5.5. The Effect of Inclusion Size on the Effective Bulk and Shear Moduli

The volume fraction effect

The results for the effect of particle volume fraction can be seen from Fig. 4.5.4 and Fig. 4.5.5. From Fig. 4.5.4, with the increase of the particle volume fraction, the effective bulk and shear moduli are both increasing. In Fig. 4.5.5, the particle size effect is more obvious with the increase of the particle volume fraction.

The inclusion properties effect

The results of the effects of inclusion properties are shown in Fig. 4.5.6. For a fixed particle volume fraction, the effective shear and bulk moduli increases with the increase of relative Young's modulus of the inclusion over matrix. But for the increase of relative Poisson's ratio of the inclusion over matrix, the effective shear moduli decreases and the effective bulk moduli increases.

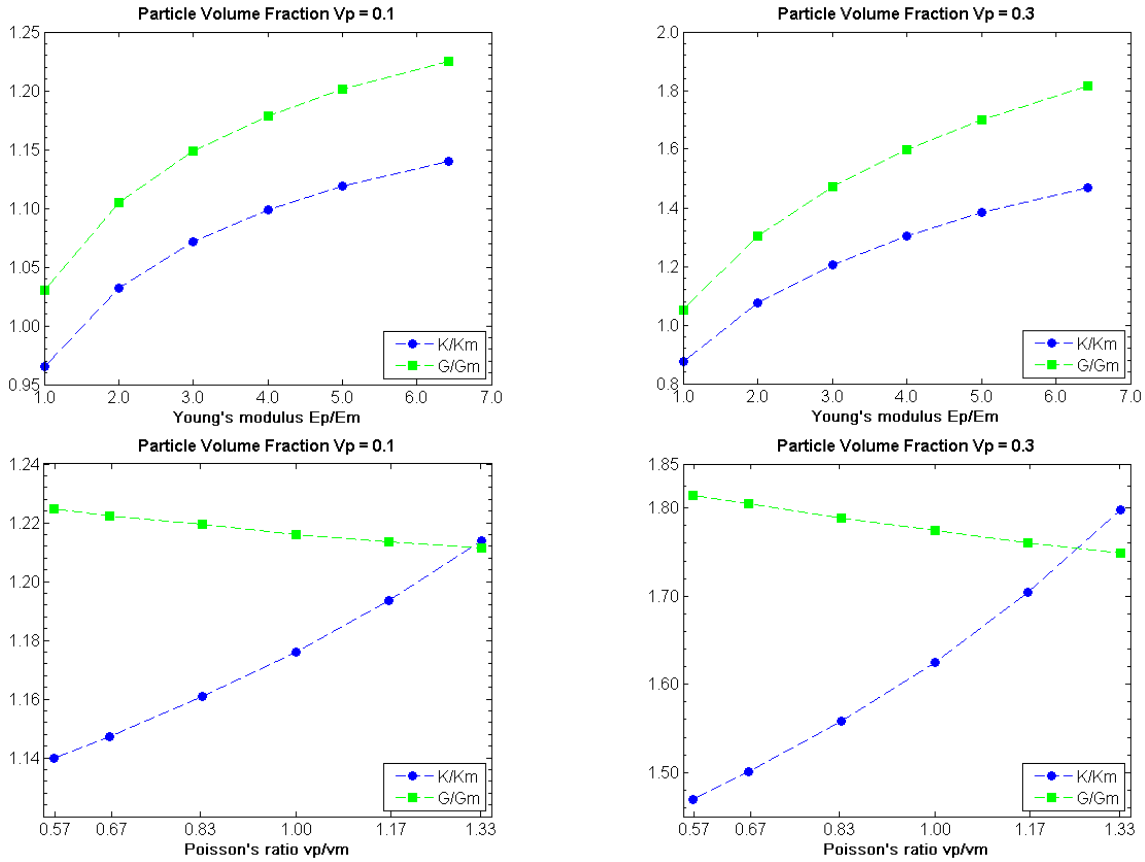

Figure 4.5.6. The Effect of Inclusion Properties on the Effective Bulk and Shear Moduli

Effective fracture properties

As mentioned in the previous section, the model failure parameters can be calibrated from the experimental data. In this study, we investigate qualitatively the effect of interface properties, particle size and particle volume fraction on the overall material strength. Pre-assumed values of different phases are used. As for the interface, the critical stretches are obtained by the arithmetic and harmonic means.

$$\begin{aligned} \alpha_{\text{matrix}} &= 0.0004 \\ \alpha_{\text{particle}} &= 0.0008 \end{aligned} \tag{4.5.5}$$

The interface effect

The results showing the interface effect on the overall material tensile strength using 30 particles are shown in Fig. 4.5.7. As can be seen, the properties of interface play important roles in

determine the effective material tensile strength. Weak interface, i.e., the harmonic mean, will decrease the material tensile strength.

The particle size effect

In this case, the interface properties are assumed to be the arithmetic means. The results of the particle size effect on the material tensile strength are shown in Fig. 4.5.8. As can be seen, generally, the material tensile strength increases with the decrease of the particle size. It should be noted that the analysis is performed with one realization of the microstructure. Statistical averaging for many microstructure realizations is required for a statistical meaningful conclusion.

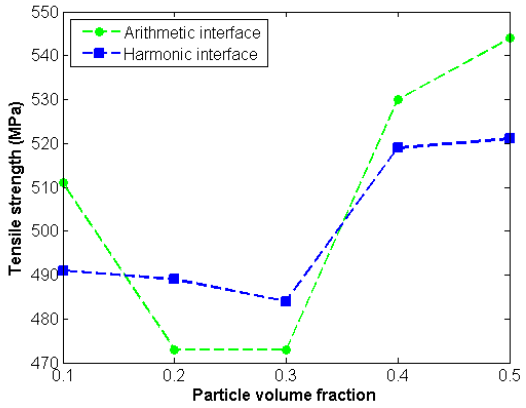

Figure 4.5.7. The Effect of the Interface and Volume Fraction on the Tensile Strength

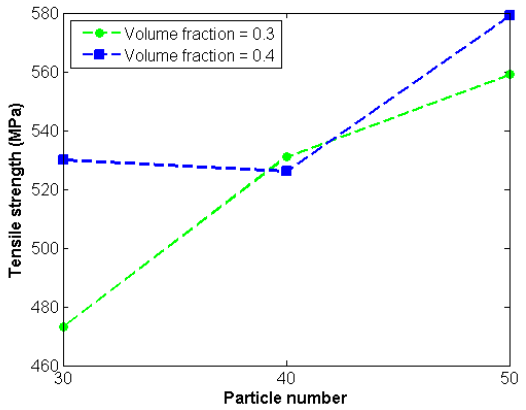

Figure 4.5.8. The Effect of Inclusion Size on the Effective Tensile Strength

4.5.5 Conclusions

The lattice particle model is applied to investigate the inclusion effects, the interface properties, the inclusion volume fraction, the inclusion property and the particle size, on both the effective elastic and fracture properties of a particle reinforced composites. The RVEs' size were determined by the correlation function proposed by Torquato [208]. The following conclusions can be drawn from this investigation:

1). The effective elastic moduli increase with the increase of the particle volume fraction, the interface properties. The decrease of the particle size can also increase the effective elastic moduli.

2). The material tensile strength increases with the increase of the interface properties. For a fixed particle volume fraction, the material tensile strength increases with the decrease of the particle size.

3) It appears that different interface strength hypothesis has large impact on the final marcro level strength estimation, especially for the large particle size based on the current simulation. Large number of statistical averaging is required for confirm this conclusion.

Further work needs to be done to systematically investigate various effects on the material fracture properties. Modification for plasticity effect is required for metallic particle reinforced composites.

CHAPTER

5. CONCLUSION

5.1 Summary

A novel lattice particle framework has been proposed for modeling of solids, including homogeneous isotropic, heterogeneous isotropic and anisotropic materials, under various mechanical loadings. For isotropic materials, it was shown both analytically and numerically that the formulation is frame independent for all the lattice structures have been used. A lattice structure rotation scheme is developed for model anisotropic materials within the proposed lattice particle framework. The equivalency of this lattice structure rotation scheme with the classical tangent stiffness matrix transformation is established both analytically and numerically. A one dimensional spring based criterion is developed for failure analysis within the proposed model for both isotropic and anisotropic materials. The validity of the spring based failure criterion was verified with experimental findings. Benchmark problems have been used to examine the performance and verify the validity of the proposed framework. The simulation results are compared with analytical solution, numerical solution (FEM) and experimental findings. The proposed lattice particle model has following main modeling capacities:

1). The proposed model uses only the axial springs and capable of modeling isotropic materials with arbitrary Poisson's ratio;

3). The proposed model is capable of modeling fracture of isotropic materials without crack path preference;

2). The elasto-plastic materials can be modeled using the proposed model under two dimensional assumptions;

4). The proposed model is capable of modeling anisotropic materials using an effective lattice rotation scheme to represent the material orientation;

5). The proposed model is capable of modeling polycrystalline materials, both 2D and 3D. The real material lattice structure can be accounted for in the proposed model.

A brief comparison of the lattice particle model with some other discrete models is shown in Table 5.1.1.

Table 5.1.1. A Brief Comparison with Some Other Discrete Numerical Models

Discrete Models	Similarities	Distinctions
Discrete Element Method	1). The model parameters are derived from the continuum mechanics in terms of the material constants; 2). Well suited for simulations involving discontinuities, such as damage and fracture problems; 3). One dimensional bond based criteria is used for failure simulation.	1.) Uses both axial and tangential springs in the formulation and no restriction on the effective Poisson's ratio; 2). Considers only the nearest neighboring interactions; 3). Cohesive type of failure criteria is used for failure analysis and the failure parameters need to be calibrated from experiments; 4). Crack path dependent on the element.
Peridynamics		1). Bond based formulation uses only axial spring but the effective Poisson's ratio is fixed to 1/4. State based formulation removes this limitation; 2). The material nonlinearity can be considered but the formulation is based on continuum mechanics; 2). The concept of horizon is used to introduce multiple neighbors; 3). Failure criterion is derived in terms of energy release rate.
Lattice Particle Model		1). Only axial spring is used and no restriction on the effective Poisson's ratio; 2). Able to consider material nonlinearity at the spring level; 3). Multiple neighbor can be considered, and no crack path preference; 4). Material anisotropy can be easily incorporated by the lattice rotation scheme; 5). The real material underlying lattice structures can be considered.

5.2 Scope of Future Work

There are still many future works need to be done in enhancing the proposed lattice particle framework and extending its application. Recommendations of future work are summarized below. It includes but not limited to the following directions:

1). Extension of the lattice particle framework to dynamic contact simulations, such as high velocity impact simulation. The lattice particle model has many advantages over continuum based model specifically for this type of problems.

1). Detailed systematic study on the spring based failure criterion for both isotropic and anisotropic materials, such as considering the spring stiffness degradation effect. This will eventually lead to the time and rate dependent failure criterion in the lattice particle model;

2). Detailed study of the lattice particle model for nonlinear constitutive response of the solids, such as viscoelasticity, elasto-plasticity and visocoplasticity. This will allow the lattice particle model to more efficiently study the nonlinear behavior at microstructural level, such as crystal plasticity;

3). In order to reduce the computational effort for large 3D structures, systematic study on developing the effective coupling mechanism with finite element methods or extended finite element method for both static and dynamic problems is required. Some advantages of the discrete model can be incorporated with classical continuum-based model for failure analysis;

4). Some intrinsic issues due to the regularity of the packing, such as non-smooth boundaries and missing neighbors for boundary particles, also need to be addressed. This problem is common to all discrete models.

REFERENCES

1. Williams, J.R., G. Hocking, and G.G.W. Mustoe, *The Theoretical Basis of the Discrete Element Method*. Numerical Methods of Engineering, Theory and Applications1985, Rotterdam: A.A. Balkema.

2. Ostoja-Starzewski, M., *Lattice Models in Micromechanics.* Applied Mechanics Reviews, 2002. **55**(1): p. 35-60.

3. Silling, S.A., et al., *Peridynamic States and Constitutive Modeling.* Journal of Elasticity, 2007. **88**(2): p. 151-184.

4. Jagota, A. and S.J. Bennison, *Spring-network and finite-element models for elasticity and fracture*, in *Non-Linearity and Breakdown in Soft Condensed Matter*, K. Bardhan, B. Chakrabarti, and A. Hansen, Editors. 1994, Springer Berlin Heidelberg. p. 186-201.

5. Trädegård, A., F. Nilsson, and S. Östlund, *FEM-remeshing technique applied to crack growth problems.* Computer Methods in Applied Mechanics and Engineering, 1998. **160**(1–2): p. 115-131.

6. Elices, M., et al., *The cohesive zone model: advantages, limitations and challenges.* Engineering Fracture Mechanics, 2002. **69**(2): p. 137-163.

7. Belytschko, T., R. Gracie, and G. Ventura, *A review of extended/generalized finite element methods for material modeling.* Modelling and Simulation in Materials Science and Engineering, 2009. **17**(4): p. 043001.

8. Silling, S.A., et al., *Crack nucleation in a peridynamic solid.* International Journal of Fracture, 2010. **162**(1-2): p. 219-227.

9. Beale, P.D. and D.J. Srolovitz, *Elastic fracture in random materials.* Physical Review B, 1988. **37**(10): p. 5500-5507.

10. Keating, P.N., *Effect of the invariance requirements on the elastic moduli of a sheet containing circular holes.* Journal of the Mechanics and Physics of Solids, 1966. **40**: p. 1031-1051.

11. Zhao, S.-F. and G.-F. Zhao, *Implementation of a high order lattice spring model for elasticity.* International Journal of Solids and Structures, 2012. **49**(18): p. 2568-2581.

12. Schlangen, E. and E.J. Garboczi, *Fracture simulations of concrete using lattice models: Computational aspects.* Engineering Fracture Mechanics, 1997. **57**(2–3): p. 319-332.

13. Jirásek, M. and Z. Bažant, *Macroscopic fracture characteristics of random particle systems.* International Journal of Fracture, 1994. **69**(3): p. 201-228.

14. Bolander, J.E. and N. Sukumar, *Irregular lattice model for quasistatic crack propagation.* Physical Review B, 2005. **71**(9): p. 94-106.

15. Monette, L. and M.P. Anderson, *Elastic and fracture properties of the two-dimensional triangular and square lattice.* Modelling and Simulation in Materials Science and Engineering, 1994. **2**(1): p. 53-66.

16. Hrennikoff, A., *Solution of problems of elasticity by the framework method.* Journal of Applied Mechanics, 1941. **8**: p. A619-A715.

17. Bažant, Z., et al., *Random Particle Model for Fracture of Aggregate or Fiber Composites.* Journal of Engineering Mechanics, 1990. **116**(8): p. 1686-1705.

18. Askar, A., *Lattice Dynamical Foundations of Continuum Theories*1985, Singapore: World Scientific.

19. Zubelewicz, A. and Z. Bažant, *Interface Element Modeling of Fracture in Aggregate Composites.* Journal of Engineering Mechanics, 1987. **113**(11): p. 1619-1630.

20. Chen, I.-W.G., N. Hassold, and D.J. Srolovitz, *Computer Simulation of Final-Stage Sintering; I, Model, Kinetics and Microstructure.* Journal of the American Ceremic Society, 1990(73): p. 2857-2864.

21. Born, M. and K. Huang, *Dynamic Theory of Crystal Lattices*1954, Oxford: Oxford Press.

22. P. Grassl, Z.P. Bazant, and G. Cusatis, *Lattice-cell approach to quasibrittle fracture modeling.* Computational Modelling of Concrete Structures: Proceedings of the EURO-C conference 2006, in Mayrhofen, Tyrol, Austria, 2006.

23. van Mier, J.G.M., M.R.A. van Vliet, and T.K. Wang, *Fracture mechanisms in particle composites: statistical aspects in lattice type analysis.* Mechanics of Materials, 2002. **34**(11): p. 705-724.

24. Cusatis, G., Z.P. Bažant, and L. Cedolin, *Confinement-shear lattice CSL model for fracture propagation in concrete.* Computer Methods in Applied Mechanics and Engineering, 2006. **195**(52): p. 7154-7171.

25. Schlangen, E., E.A.B. Koenders, and K. van Breugel, *Influence of internal dilation on the fracture behaviour of multi-phase materials.* Engineering Fracture Mechanics, 2007. **74**(1–2): p. 18-33.

26. Wang, Y. and P. Mora, *Macroscopic elastic properties of regular lattices.* Journal of the Mechanics and Physics of Solids, 2008. **56**(12): p. 3459-3474.

27. Cusatis, G., D. Pelessone, and A. Mencarelli, *Lattice Discrete Particle Model (LDPM) for failure behavior of concrete. I: Theory.* Cement and Concrete Composites, 2011. **33**(9): p. 881-890.

28. Jivkov, A.P. and J.R. Yates, *Elastic behaviour of a regular lattice for meso-scale modelling of solids.* International Journal of Solids and Structures, 2012. **49**(22): p. 3089-3099.

29. Cusatis, G., et al., *Lattice Discrete Particle Model (LDPM) for failure behavior of concrete. II: Calibration and validation.* Cement and Concrete Composites, 2011. **33**(9): p. 891-905.

30. Gao, H. and P. Klein, *Numerical simulation of crack growth in an isotropic solid with randomized internal cohesive bonds.* Journal of the Mechanics and Physics of Solids, 1998. **46**(2): p. 187-218.

31. Volokh, K.Y., Gao, H., *On the modified virtual internal bond method.* Journal of Applied Mechanics, 2005. **72**(6): p. 3.

32. Buxton, G.A., C.M. Care, and D.J. Cleaver, *A lattice spring model of heterogeneous materials with plasticity.* Model. Simul. Mater. Sci. Eng., 2001. **9**(6): p. 485.

33. Thiagarajan, G., Y.Y. Huang, and K.J. Hsia, *Fracture Simulation Using an Elasto-Viscoplastic Virtual Internal Bond Model With Finite Elements.* Journal of Applied Mechanics, 2005. **71**(6): p. 796-804.

34. Foster, J.T., S.A. Silling, and W.W. Chen, *Viscoplasticity using peridynamics.* International Journal for Numerical Methods in Engineering, 2010. **81**(10): p. 1242-1258.

35. Jagota, A. and S.J. Bennison, *Element breaking rules in computational models for brittle fracture.* Modelling and Simulation in Materials Science and Engineering, 1995. **3**(4): p. 485.

36. Wang, G., et al., *Hybrid lattice particle modeling: Theoretical considerations for a 2D elastic spring network for dynamic fracture simulations.* Computational Materials Science, 2009. **44**(4): p. 1126-1134.

37. Timoshenko, S., *Theory of Elasticity*1934, New York: McGraw-Hill.

38. Chen, H., E. Lin, and Y. Liu, *A novel Volume-Compensated Particle method for 2D elasticity and plasticity analysis.* International Journal of Solids and Structures, 2014. **51**(9): p. 1819-1833.

39. Wells, G.N. and L.J. Sluys, *A new method for modelling cohesive cracks using finite elements.* International Journal for Numerical Methods in Engineering, 2001. **50**(12): p. 2667-2682.

40. Belytschko, T., et al., *Meshless methods: An overview and recent developments.* Computer Methods in Applied Mechanics and Engineering, 1996. **139**(1–4): p. 3-47.

41. Gerstle, W., N. Sau, and S. Silling, *Peridynamic modeling of concrete structures.* Nuclear Engineering and Design, 2007. **237**(12-13): p. 1250-1258.

42. Gerstle, W., H.H. Geitanbaf, and A. Asadollahi. *Computational Simulation of Reinforced Concrete using the Micropolar State-Based Peridynamic Hexagonal Lattice Model*. in *8th International Conference on Fracture Mechanics of Concrete and Concrete Structures*. 2013. Barcelona, Spain.

43. Kalthoff, J.F. and S. Winkler. *Failure mode transition at high rates of shear loading*. in *International conference on impact loading and dynamic behavior of materials*. 1987.

44. Ramulu, M. and A.S. Kobayashi, *Mechanics of crack curving and branching — a dynamic fracture analysis.* International Journal of Fracture, 1985. **27**(3-4): p. 187-201.

45. Grah, M., et al., *Brittle intergranular failure in 2D microstructures: Experiments and computer simulations.* Acta Materialia, 1996. **44**(10): p. 4003-4018.

46. Schlangen, E. and E.J. Garboczi, *New method for simulating fracture using an elastically uniform random geometry lattice.* International Journal of Engineering Science, 1996. **34**(10): p. 1131-1144.

47. Silling, S.A. and E. Askari, *A meshfree method based on the peridynamic model of solid mechanics.* Computers & Structures, 2005. **83**(17-18): p. 1526-1535.

48. Song, J.-H., H. Wang, and T. Belytschko, *A comparative study on finite element methods for dynamic fracture.* Computational Mechanics, 2008. **42**(2): p. 239-250.

49. Song, J.-H. and T. Belytschko, *Cracking node method for dynamic fracture with finite elements.* International Journal for Numerical Methods in Engineering, 2009. **77**(3): p. 360-385.

50. Liu, Z.L., T. Menouillard, and T. Belytschko, *An XFEM/Spectral element method for dynamic crack propagation.* International Journal of Fracture, 2011. **169**(2): p. 183-198.

51. Katzav, E., M. Adda-Bedia, and R. Arias, *Theory of dynamic crack branching in brittle materials.* International Journal of Fracture, 2007. **143**(3): p. 245-271.

52. Chen, H., et al., *A Generalized 2D Non-local Lattice Spring Model for Fracture Simulation.* Computational Mechanics, 2014. **54**(6): p. 1541-1558.

53. Monaghan, J.J., *Smoothed particle hydrodynamics.* Reports on Progress in Physics, 2005. **68**(8): p. 1703.

54. Libersky, L. and A.G. Petschek, *Smooth particle hydrodynamics with strength of materials*, in *Advances in the Free-Lagrange Method Including Contributions on Adaptive Gridding and the Smooth Particle Hydrodynamics Method*, H. Trease, M. Fritts, and W.P. Crowley, Editors. 1991, Springer Berlin Heidelberg. p. 248-257.

55. Cundall, P.A. and O.D.L. Strack, *A discrete numerical model for granular assemblies.* Geotechnique, 1979. **29**(1): p. 47-65.

56. Li, S. and W.K. Liu, *Meshfree Particle Methods*2004, New York: Springer.

57. Silling, S.A., *Reformulation of elasticity theory for discontinuities and long-range forces.* Journal of the Mechanics and Physics of Solids, 2000. **48**(1): p. 175-209.

58. Schlangen, E., *Crack Development in Concrete. Part 2: Modelling of Fracture Process.* Key Engineering Materials, 2008. **385-387**: p. 73-76.

59. Chang, C.S., et al., *Fracture modeling using a micro-structural mechanics approach—I. Theory and formulation.* Engineering Fracture Mechanics, 2002. **69**(17): p. 1941-1958.

60. Tadmor, E.B., M. Ortiz, and R. Phillips, *Quasicontinuum analysis of defects in solids.* Philosophical Magazine A, 1996. **73**(6): p. 1529-1563.

61. Chen, H. and A.V. Kumar, *Method for imposing boundary conditions on Reissner–Mindlin plates for analysis using structured background mesh.* Computers & Structures, 2014. **138**(1): p. 1-11.

62. Echter, R., B. Oesterle, and M. Bischoff, *A hierarchic family of isogeometric shell finite elements.* Computer Methods in Applied Mechanics and Engineering, 2013. **254**(0): p. 170-180.

63. Scordelis, A.C. and K.S. Lo, *Computer Analysis of Cylindrical Shells.* American Concrete Institute, 1968. **61**(5): p. 539-560.

64. Macneal, R.H. and R.L. Harder, *A proposed standard set of problems to test finite element accuracy.* Finite Elements in Analysis and Design, 1985. **1**(1): p. 3-20.

65. Ayatollahi, M.R. and M.R.M. Aliha, *Analysis of a new specimen for mixed mode fracture tests on brittle materials.* Engineering Fracture Mechanics, 2009. **76**(11): p. 1563-1573.

66. Srinivas, S. and A.K. Rao, *Bending vibration and buckling of simply supported thick orthotropic rectangular plates and laminates.* International Journal of Solids and Structures, 1970. **6**: p. 1463-1481.

67. Pagano, N.J., *Exact solution for rectangular bidirectional composites and sandwich plates.* Journal of Composite Materials, 1970. **4**(1): p. 20-34.

68. Pagano, N.J. and S.J. Hatfield, *Elastic behavior of multilayered bi-directional composites.* AIAA Journal, 1972. **10**: p. 931-933.

69. Williams, T.O. and F.L. Addessio, *A general theory for laminated plates with delaminations.* International Journal of Solids and Structures, 1997. **34**: p. 2003-2024.

70. Bogdanovich, A.E. and S.P. Yushanov, *Three-dimensional variational analysis of Pagano's problems for laminated composite plates.* Composites Science and Technology, 2000. **60**(12–13): p. 2407-2425.

71. Desai, Y.M., G.S. Ramtekkar, and A.H. Shah, *A novel 3D mixed finite-element model for statics of angle-ply laminates.* International Journal for Numerical Methods in Engineering, 2003. **57**(12): p. 1695-1716.

72. Herakovich, C.T., *On the relationship between engineering properties and delamination of composite materials.* Journal of Composite Materials, 1981. **15**: p. 336-348.

73. Salpekar, S.A. and T.K. O'Brien, *Combined Effect of Matrix Cracking and Free Edge on Delamination*, in *Composite Materials: Fatigue and Fracture (Third Volume)*, T.K. O'Brien, Editor 1991, American Society for Testing and Materials: Philadelphia, PA. p. 287-311.

74. Kim, T. and S.N. Atluri, *Analysis of edge stresses in composite laminates under combined thermo-mechanical loading, using a complementary energy approach.* Computational Mechanics, 1995. **16**(2): p. 83-97.

75. Jones, R.M., *Mechanics Of Composite Materials*. 2nd ed. Materials Science and Engineering Series1998, PA: Taylor & Francis, Inc.

76. Mittelstedt, C. and W. Becker, *Free-Edge Effects in Composite Laminates.* Applied Mechanics Reviews, 2007. **60**(5): p. 217-245.

77. Rybicki, E.F., *Approximate three-dimensional solutions for symmetric laminates under in-plane loading.* Journal of Composite Materials, 1971. **5**: p. 354-360.

78. Khandan, R., et al., *The development of laminated composite plate theories: a review.* Journal of Materials Science, 2012. **47**(16): p. 5901-5910.

79. Reddy, J.N. and J.D.H. Robbins, *Theories and Computational Models for Composite Laminates.* Applied Mechanics Reviews, 1994. **47**(6): p. 147-169.

80. Rinaldi, A., et al., *Lattice models of polycrystalline microstructures: A quantitative approach.* Mechanics of Materials, 2008. **40**: p. 17-36.

81. Griffith, A.A., *The phenomena of rupture and flow in solids.* Phil. Trans. R. Soc. Lond. A, 1921. **221**: p. 163-198.

82. Cotterell, B., *On brittle fracture paths.* International Journal of Fracture Mechanics, 1965. **1**(2): p. 96-103.

83. Sih, G.C., *Strain-energy-density factor applied to mixed mode crack problems.* International Journal of Fracture, 1974. **10**(3): p. 305-321.

84. Erdogan, F. and G.C. Sih, *On the Crack Extension in Plates Under Plane Loading and Transverse Shear.* Journal of Fluids Engineering, 1963. **85**(4): p. 519-525.

85. Takei, A., et al., *Forbidden Directions for the Fracture of Thin Anisotropic Sheets: An Analogy with the Wulff Plot.* Physical Review Letters, 2013. **110**: p. 144301.

86. Tsai, S.W. and E.M. Wu, *A general theory of strength for anisotropic materials* Journal of Composite Materials, 1971. **5**: p. 58-80.

87. Azzi, V.D. and S.W. Tsai, *Anisotropic Strength of Composites.* Experimental Mechanics, 1965. **5**(9): p. 283-288.

88. Hakim, V. and A. Karma, *Crack path prediction in anisotropic brittle materials.* Physical Review Letters, 2005. **95**: p. 235501.

89. Ostoja-Starzewski, M., P.Y. Sheng, and K. Alzebdeh, *Spring network models in elasticity and fracture of composites and polycrystals.* Computational Materials Science, 1996. **7**(1-2): p. 82-93.

90. Pazdniakou, A. and P.M. Adler, *Lattice Spring Models.* Transport in Porous Media, 2012. **93**(2): p. 243-262.

91. Noor, A.K. and M.P. Nemeth, *Micropolar beam models for lattice grids with rigid joints.* Computer Methods in Applied Mechanics and Engineering, 1980. **21**(2): p. 249-263.

92. Okabe, T., M. Nishikawa, and N. Takeda, *Numerical modeling of progressive damage in fiber reinforced plastic cross-ply laminates.* Composites Science and Technology, 2008. **68**(10–11): p. 2282-2289.

93. Wimmer, G. and H.E. Pettermann, *A semi-analytical model for the simulation of delamination in laminated composites.* Composites Science and Technology, 2008. **68**(12): p. 2332-2339.

94. Lin, E., H. Chen, and Y. Liu, *Finite Element Implementation of A Non-local Particle Method for Elasticity and Fracture Analysis.* Finite Elements in Analysis and Design, 2015. **93**(0): p. 1-11.

95. Bailey, J., P. Curtis, and A. Parvizi, *On the transverse cracking and longitudinal splitting behaviour of glass and carbon fibre reinforced epoxy cross ply laminates and the effect of Poisson and thermally generated strain.* Proceedings of the Royal Society of London. A. Mathematical and Physical Sciences, 1979. **366**(1727): p. 599-623.

96. Cox, B. and Q. Yang, *In Quest of Virtual Tests for Structural Composites.* Science, 2006. **314**(5802): p. 1102-1107.

97. Boniface, L., et al., *Transverse Ply Cracking in Cross-Ply CFRP Laminates—Initiation or Propagation Controlled?* Journal of Composite Materials, 1997. **31**(11): p. 1080-1112.

98. Nguyen, V.P., P. Kerfriden, and S.P.A. Bordas, *Two- and three-dimensional isogeometric cohesive elements for composite delamination analysis.* Composites Part B: Engineering, 2014. **60**(0): p. 193-212.

99. Voigt, W., *Theoretische Studien über die Elastizitätsverhältnisse der Kristalle.* Abh. Gött. Akad. Wiss., 1887: p. 48-55.

100. Reuss, A., *Berechnung der Fließgrenze von Mischkristallen auf Grund der Plastizitätsbedingung für Einkristalle.* Zeitschrift für Angewandte Mathematik und Mechanik, 1929. **9**(1): p. 49-58.

101. Hill, R., *The elastic behaviour of a crystalline aggregate.* Proc. Roy. Soc. A, 1952. **65**: p. 349-354.

102. Kröner, E., *Berechnung der elastischen Konstanten des Vielkristalls aus den Konstanten des Einkristalls.* Zeitschrift für Physik, 1958. **151**(4): p. 504-518.

103. Hashin, Z. and S. Shtrikman, *On some variational principles in anisotropic and nonhomogeneous elasticity.* Journal of the Mechanics and Physics of Solids, 1962. **10**(4): p. 335-342.

104. Hashin, Z. and S. Shtrikman, *A variational approach to the theory of the elastic behaviour of polycrystals.* Journal of the Mechanics and Physics of Solids, 1962. **10**(4): p. 343-352.

105. Kneer, G., *Uber Berechnung der elastizitatsmodulu vielkristalliner aggregate mit texture.* Phys. Status Solidi, 1965. **9**: p. K825-838.

106. Morris, P.R., *Elastic constants of polycrystals.* International Journal of Engineering Science, 1970. **8**(1): p. 49-61.

107. Dutta, T., T.K. Ballabh, and T.R. Middya, *Green function calculation of effective elastic constants of textured polycrystalline materials.* Journal of Physics D: Applied Physics, 1993. **26**(4): p. 667-675.

108. Mityushov, E.A., S.A. Berestova, and N.Y. Odintsova, *Effective Elastic Properties of Textured Cubic Polycrystals.* Textures and Microstructures, 2002. **35**(2): p. 99-111.

109. Man, C.-S. and M. Huang, *A Simple Explicit Formula for the Voigt-Reuss-Hill Average of Elastic Polycrystals with Arbitrary Crystal and Texture Symmetries.* Journal of Elasticity, 2011. **105**(1-2): p. 29-48.

110. Sheng, G., et al., *Effective elastic properties of polycrystals based on phase-field description.* Materials Science and Engineering: A, 2012. **554**(0): p. 67-71.

111. Watanabe, T., *An approach to grain boundary design for strong and ductile polycrystals.* Res Mechanica, 1984. **11**: p. 47-84.

112. Watanabe, T. and S. Tsurekawa, *The control of bittleness and develipment of desirable mechanical properties in polycrystalline systems by grain boundary engineering.* Acta Materialia, 1999. **47**(15-16): p. 4171-4185.

113. Sfantos, G.K. and M.H. Aliabadi, *A boundary cohesive grain element formulation for modelling intergranular microfracture in polycrystalline brittle materials.* International Journal for Numerical Methods in Engineering, 2007. **69**(8): p. 1590-1626.

114. Musienko, A. and G. Cailletaud, *Simulation of inter- and transgranular crack propagation in polycrystalline aggregates due to stress corrosion cracking.* Acta Materialia, 2009. **57**(13): p. 3840-3855.

115. Sukumar, N., et al., *Brittle fracture in polycrystalline microstructures with the extended finite element method.* International Journal for Numerical Methods in Engineering, 2003. **56**(14): p. 2015-2037.

116. Simone, A., C.A. Duarte, and E. Van der Giessen, *A Generalized Finite Element Method for polycrystals with discontinuous grain boundaries.* International Journal for Numerical Methods in Engineering, 2006. **67**(8): p. 1122-1145.

117. Lim, L.C. and T. Watanabe, *Fracture toughness and brittle-ductile transition controlled by grain boundary character distribution (GBCD) in polycrystals.* Acta Metallurgica et Materialia, 1990. **38**(12): p. 2507-2516.

118. Qiao, Y. and A.S. Argon, *Cleavage crack-growth-resistance of grain boundaries in polycrystalline Fe–2%Si alloy: experiments and modeling.* Mechanics of Materials, 2003. **35**(1–2): p. 129-154.

119. Ganchenkova, M.G. and V.A. Borodin, *Monte-Carlo simulation of crack propagation in polycrystalline materials.* Materials Science and Engineering: A, 2004. **387–389**(0): p. 372-376.

120. Arafin, M.A. and J.A. Szpunar, *A Markov Chain–Monte Carlo model for intergranular stress corrosion crack propagation in polycrystalline materials.* Materials Science and Engineering: A, 2009. **513–514**(0): p. 254-266.

121. Shenderova, O., et al., *Atomistic modeling of the fracture of polycrystalline diamond.* Physical Review B, 2000. **61**(6): p. 3877-3888.

122. Rudd, R.E. and J.F. Belak, *Void nucleation and associated plasticity in dynamic fracture of polycrystalline copper: an atomistic simulation.* Computational Materials Science, 2002. **24**(1–2): p. 148-153.

123. Crocker, A.G., P.E.J. Flewitt, and G.E. Smith, *Computational Modelling of Fracture in Polycrystalline Materials.* International Materials Reviews, 2005. **50**(2): p. 99-125.

124. Chen, H., Y. Jiao, and Y. Liu, *A Nonlocal Lattice Particle Model for Fracture Analysis of Anisotropic Materials.* 2015(under review).

125. Herman, G.T., *Fundamentals of Computerized Tomography: Image Reconstruction From Projection*. 2nd ed2009, New York: Springer.

126. Jiao, Y. and N. Chawla, *Modeling and characterizing anisotropic inclusion orientation in heterogeneous material via directional cluster functions and stochastic microstructure reconstruction.* J. Appl. Phys., 2014. **115**(9): p. 093511.

127. Ghosh, S., Y. Bhandari, and M. Groeber, *CAD-based reconstruction of 3D polycrystalline alloy microstructures from FIB generated serial sections.* Computer-Aided Design, 2008. **40**(3): p. 293-310.

128. Torquato, S. and Y. Jiao, *Dense packings of polyhedra: Platonic and Archimedean solids.* Phys. Rev. E, 2009. **80**(4): p. 041104.

129. Dahl Jr, R.E., J.R. Beeler Jr, and R.D. Bourquin, *Computer simulation of extended defects in metals.* Computer Physics Communications, 1971. **2**(6): p. 301-321.

130. Smith, D.A., V. Vitek, and R.C. Pond, *Computer simulation of symmetrical high angle boundaries in aluminium.* Acta Metallurgica, 1977. **25**(5): p. 475-483.

131. Cotterill, R.M.J., T. Leffers, and H. Lilholt, *A molecular dynamics approach to grain boundary structure and migration.* Philosophical Magazine, 1974. **30**(2): p. 265-275.

132. Restrepo, S.E., S.T. Giraldo, and B.J. Thijsse, *A generic algorithm for generating grain boundaries.* Modelling Simul. Mater. Sci. Eng., 2013. **21**(5): p. 055017.

133. Jasiuk, I., J. Chen, and M.F. Thorpe, *Elastic Moduli of Two Dimensional Materials With Polygonal and Elliptical Holes.* Applied Mechanics Reviews, 1994. **47**(1S): p. S18-S28.

134. Lekhnitskii, S.G., *Theory of Elasticity of an Anisotropic Elastic Body* Holden-Day Series in Mathematical Physics1963, San Francisco: Holden-Day. 404.

135. Simmons, G. and H. Wang, *Single Crystal Elastic Constants and Calculated Aggregate Properties: A Handbook*. 2nd ed1971, Cambridge, MA: The M.I.T Press.

136. Liu, B., et al., *The atomic-scale finite element method.* Computer Methods in Applied Mechanics and Engineering, 2004. **193**(17–20): p. 1849-1864.

137. Rollett, A.D., et al. *Grain Boundary Property Determination through Measurement of Triple Junction Geometry and Crystallography*. in *International Conference on Grain Growth and Recrystallization*. 2001. Aachen, Germany: Springer-Verlag.

138. Liu, D. and X. Li, *An Overall View of Laminate Theories Based on Displacement Hypothesis.* Journal of Composite Materials, 1996. **30**: p. 1539-1561.

139. Altenbach, H., *Theories for laminated and sandwich plates.* Mechanics of Composite Materials, 1998. **34**(3): p. 243-252.

140. Kant, T. and K. Swaminathan, *Estimation of transverse/interlaminar stresses in laminated composites–a selective review and survey of current developments.* Composite structures, 2000. **49**(1): p. 65-75.

141. Ghugal, Y.M. and R.P. Shimpi, *A Review of Refined Shear Deformation Theories for Isotropic and Anisotropic Laminated Beams.* Journal of Reinforced Plastics and Composites, 2001. **20**: p. 255-272.

142. Carrera, E., *Historical review of Zig-Zag theories for multilayered plates and shells.* Applied Mechanics Reviews, 2003. **56**(3): p. 287-308.

143. Mittelstedt, C. and W. Becker, *Interlaminar Stress Concentrations in Layered Structures: Part I - A Selective Literature Survey on the Free-Edge Effect since 1967.* Journal of Composite Materials, 2004. **38**: p. 1037-1062.

144. Kreja, I., *A literature review on computational models for laminated composite and sandwich panels.* Central European Journal of Engineering, 2011. **1**(1): p. 59-80.

145. Zhang, Y.X. and C.H. Yang, *Recent developments in finite element analysis for laminated composite plates.* Composite Structures, 2009. **88**(1): p. 147-157.

146. Liew, K.M., X. Zhao, and A.J.M. Ferreira, *A review of meshless methods for laminated and functionally graded plates and shells.* Composite Structures, 2011. **93**(8): p. 2031-2041.

147. Sheng, Y., et al., *Microstructure effects on transverse cracking in composite laminae by DEM.* Composites Science and Technology, 2010. **70**(14): p. 2093-2101.

148. Yang, D., et al., *Dynamic simulation of crack initiation and propagation in cross-ply laminates by DEM.* Composites Science and Technology, 2011. **71**(11): p. 1410-1418.

149. Maheo, L., et al., *A promising way to model cracks in composite using Discrete Element Method.* Composites Part B: Engineering, 2015. **71**(0): p. 193-202.

150. Kilic, B., A. Agwai, and E. Madenci, *Peridynamic theory for progressive damage prediction in center-cracked composite laminates.* Composite Structures, 2009. **90**(2): p. 141-151.

151. Oterkus, E., et al., *Combined finite element and peridynamic analyses for predicting failure in a stiffened composite curved panel with a central slot.* Composite Structures, 2012. **94**(3): p. 839-850.

152. Hu, Y.-l., Y. Yu, and H. Wang, *Peridynamic analytical method for progressive damage in notched composite laminates.* Composite Structures, 2014. **108**(0): p. 801-810.

153. Chen, H. and Y. Liu, *A Novel Non-local 3D Lattice Particle Framework for Fracture Simulation.* (Under review), 2015.

154. Chen, H., Y. Jiao, and Y. Liu, *Investigating the Microstructural Effect on Elastic and Fracture Behavior of Polycrystals Using a Nonlocal Lattice Particle Model.* Materials Science and Engineering: A, 2015. **631**: p. 173-180.

155. Demasi, L., *Mixed plate theories based on the Generalized Unified Formulation. Part V: Results.* Composite Structures, 2009. **88**(1): p. 1-16.

156. NAFEMS, *Composite Benchmarks (Test R0031/1).* NAFEMS Publication, 1995.

157. Courtney, T.H., *Mechanical Behavior of Materials*. 2nd ed2005: Waveland Press, Inc.

158. Kant, T., et al., *Elasticity solution for cross-ply composite and sandwich laminates.* Composite Structures, 2008. **83**(1): p. 13-24.

159. Kant, T. and K. Swaminathan, *Analytical solutions for the static analysis of laminated composite and sandwich plates based on a higher order refined theory.* Composite Structures, 2002. **56**(4): p. 329-344.

160. Reddy, J.N., *A Simple Higher-Order Theory for Laminated Composite Plates.* ASME Journal of Applied Mechanics, 1984. **51**(4): p. 745-752.

161. Haslam, A.J., et al., *Stress-enhanced grain growth in a nanocrystalline material by molecular-dynamics simulation.* Acta Materialia, 2003. **51**(7): p. 2097-2112.

162. Yamakov, V., et al., *Dislocation processes in the deformation of nanocrystalline aluminium by molecular-dynamics simulation.* Nat Mater, 2002. **1**(1): p. 45-49.

163. Domain, C. and G. Monnet, *Simulation of Screw Dislocation Motion in Iron by Molecular Dynamics Simulations.* Physical Review Letters, 2005. **95**(21): p. 215506.

164. Gilbert, M.R., S. Queyreau, and J. Marian, *Stress and temperature dependence of screw dislocation mobility in $$\alpha${}$-Fe by molecular dynamics.* Physical Review B, 2011. **84**(17): p. 174103.

165. Dupont, V. and F. Sansoz, *Molecular dynamics study of crystal plasticity during nanoindentation in Ni nanowires.* Journal of Materials Research, 2009. **24**(03): p. 948-956.

166. Ravelo, R., et al., *Shock-induced plasticity in tantalum single crystals: Interatomic potentials and large-scale molecular-dynamics simulations.* Physical Review B, 2013. **88**(13): p. 134101.

167. Holian, B.L. and R. Ravelo, *Fracture simulations using large-scale molecular dynamics.* Physical Review B, 1995. **51**(17): p. 11275-11288.

168. Holland, D. and M. Marder, *Ideal Brittle Fracture of Silicon Studied with Molecular Dynamics.* Physical Review Letters, 1998. **80**(4): p. 746-749.

169. Borhani, D.W. and D.E. Shaw, *The future of molecular dynamics simulations in drug discovery.* Journal of Computer-Aided Molecular Design, 2012. **26**(1): p. 15-26.

170. Horstemeyer, M.F., *Multiscale modeling: a review*, in *Practical Aspects Computational Chemistry*, J. Leszczynski and M.K. Shukla, Editors. 2010, Springer: Netherlands. p. 87-135.

171. Voter, A.F., *Hyperdynamics: Accelerated Molecular Dynamics of Infrequent Events.* Physical Review Letters, 1997. **78**(20): p. 3908-3911.

172. Voter, A.F., *Parallel replica method for dynamics of infrequent events.* Physical Review B, 1998. **57**(22): p. R13985-R13988.

173. Montalenti, F., M.R. Sørensen, and A.F. Voter, *Closing the Gap between Experiment and Theory: Crystal Growth by Temperature Accelerated Dynamics.* Physical Review Letters, 2001. **87**(12): p. 126101.

174. Lépinoux, J. and L.P. Kubin, *The dynamic organization of dislocation structures: A simulation.* Scripta Metallurgica, 1987. **21**(6): p. 833-838.

175. Ghoniem, N.M. and L.Z. Sun, *Fast-sum method for the elastic field of three-dimensional dislocation ensembles.* Physical Review B, 1999. **60**(1): p. 128-140.

176. Onsager, L., *Crystal Statistics. I. A Two-Dimensional Model with an Order-Disorder Transition.* Physical Review, 1944. **65**(3-4): p. 117-149.

177. Ashkin, J. and E. Teller, *Statistics of Two-Dimensional Lattices with Four Components.* Physical Review, 1943. **64**(5-6): p. 178-184.

178. Stanley, H.E., *Dependence of Critical Properties on Dimensionality of Spins.* Physical Review Letters, 1968. **20**(12): p. 589-592.

179. Wu, F.Y., *The Potts model.* Reviews of Modern Physics, 1982. **54**(1): p. 235-268.

180. Berryman, J.G., *Bounds and self-consistent estimates for elastic constants of polycrystals composed of orthorhombics or crystals with higher symmetries.* Physical Review E, 2011. **83**(4): p. 046130.

181. Berryman, J.G., *Bounds and self-consistent estimates for elastic constants of polycrystals of hcp solid He^{4}.* Physical Review B, 2012. **85**(9): p. 094204.

182. Lubarda, V.A., *New estimates of the third-order elastic constants for isotropic aggregates of cubic crystals.* Journal of the Mechanics and Physics of Solids, 1997. **45**(4): p. 471-490.

183. Bolef, D.I. and J. De Klerk, *Elastic Constants of Single-Crystal Mo and W between 77° and 500°K.* Journal of Applied Physics, 1962. **33**: p. 2311-2314.

184. Kouznetsova, V., W.A.M. Brekelmans, and F.P.T. Baaijens, *An approach to micro-macro modeling of heterogeneous materials.* Computational Mechanics, 2001(27): p. 37-48.

185. Segurado, J. and J. Llorca, *A numerical approximation to the elastic properties of sphere-reinforced composites.* Journal of the Mechanics and Physics of Solids, 2002(50): p. 2107-2121.

186. Chawla, N., R.S. Sidhu, and V.V. Ganesh, *Three-dimensional visualization and microstructure-based modeling of deformation in particle-reinforced composites.* Acta Materialia, 2006(54): p. 1541-1548.

187. Kari, S., et al., *Computational evaluation of effective material properties of composites reinforced by randomly distributed spherical particles.* Composite Structures, 2007(77): p. 223-231.

188. Snyder, K.A., E.J. Garboczi, and A.R. Day, *The elastic moduli of simple two-dimensional isotropic composites: Computer simulation and effective medium theory.* Journal of Applied Physics, 1992. **72**(12): p. 5948-5955.

189. Day, A.R., et al., *The elastic moduli of a sheet containing circular holes.* Journal of the Mechanics and Physics of Solids, 1992. **40**(5): p. 1031-1051.

190. Ostoja-Starzewski, M. and C. Wang, *Linear elasticity of planar delaunay networks: Random field characterization of effective moduli.* Acta Mechanica, 1989. **80**(1-2): p. 61-80.

191. Ostoja-Starzewski, M. and C. Wang, *Linear elasticity of planar delaunay networks. Part II: Voigt and Reuss bounds, and modification for centroids.* Acta Mechanica, 1990. **84**(1-4): p. 47-61.

192. Ostoja-Starzewski, M., K. Alzebdeh, and I. Jasiuk, *Linear elasticity of planar Delaunay networks. III: Self-consistent approximations.* Acta Mechanica, 1995. **110**(1-4): p. 57-72.

193. Garboczi, E.J. and A.R. Day, *An algorithm for computing the effective linear elastic properties of heterogeneous materials: Three-dimensional results for composites with equal phase poisson ratios.* Journal of the Mechanics and Physics of Solids, 1995. **43**(9): p. 1349-1362.

194. Swope, W.C., et al., *A computer simulation method for the calculation of equilibrium constants for the formation of physical clusters of molecules: Application to small water clusters.* The Journal of Chemical Physics, 1982. **76**(1): p. 637-649.

195. Cundall, P.A., *Explicit finite-difference methods in geomechanics.* Numer. Methods Eng. (Proceedings of the EF Conference on Numerical Methods in Geomechanics), 1976. **1**: p. 132-150.

196. Otter, J.R.H., *Computations for prestressed concrete reactor pressure vessels using dynamic relaxation.* Nuclear Structural Engineering, 1965. **1**(1): p. 61-75.

197. Day, A.S., *An introduction to dynamic relaxation.* The Engineer, 1965(219): p. 218-221.

198. Underwood, P., *Dynamic Relaxation.* Computational methods for transient analysis, 1983. **1**: p. 245-265.

199. Munjiza, A., *The Combined Finite-Discrete Element Method*2004, Chichester, UK: Wiley. 352.

200. Hashin, Z., *The elastic moduli of heterogeneous materials.* J. Appl. Mech., 1962(29): p. 143-150.

201. Hashin, Z. and S. Shtrikman, *A variational approach to the theory of elastic behavior of multiphase materials.* J. Mech. Phys. Solids, 1963(11): p. 127-140.

202. Mori, T., Tanaka, K., *Average stress in the matrix and average elastic energy of materials with misfitting inclusions.* Acta Metall. Mater., 1973(21): p. 571-574.

203. Benveniste, Y., *A new approach to the application of Mori-Tanaka's theory in composite materials.* Mechanics of Materials, 1987(6): p. 147-157.

204. Hill, R., *A self consistent mechanics of composite materials.* Journal of the Mechanics and Physic of the Solids, 1965(13): p. 213-222.

205. McLaughlin, R., *A study of the differential scheme for composite materials.* Int. J. Eng. Sci., 1977(15): p. 237-244.

206. Hill, R., *Elastic properties of reinforced solids: some theoretical principles.* Journal of the Mechanics and Physics of Solids, 1963. **11**(5): p. 357-372.

207. Drugan, W.J. and J.R. Willis, *A micromechanics-based nonlocal constitutive equations and estimates of representative volume element size for elastic composites.* Journal of the Mechanics and Physics of Solids, 1996(44): p. 497-524.

208. Torquato, S., *Random Heterogeneous Materials: Microstructure and Macroscopic Properties*2002, New York: Springer-Verlag.

APPENDIX

A THE FRAME INVARIANCE OF THE FORMULATION FOR ISOTROPIC SOLIDS

It should be noted that the previous derivation of the model parameters is based on the condition that the lattice coordinate (O123) coincides with the global coordinate (OXYZ). For isotropic materials, the material properties are frame invariant, i.e., not dependent on the direction in which the material properties are measured or observed. Thus, it's very important also to have frame invariant model parameters for modeling isotropic materials. In this appendix, we analytically show that the derived model parameters in lattice particle model for isotropic materials are frame invariant.

Assuming the global coordinate can be obtained by rotating the lattice coordinate by angles (θ_1, θ_2, θ_3) in the sequence of 1, 2, 3. This rotation process is shown in Fig. A.1. Thus, in terms of these three rotation angles, the rotation matrix for coordinate transformation between these two coordinates is

$$\mathbf{Q} = \begin{bmatrix} \cos\theta_2\cos\theta_3 & -\cos\theta_2\sin\theta_3 & \sin\theta_2 \\ \cos\theta_1\sin\theta_3 + \sin\theta_1\sin\theta_2\cos\theta_3 & \cos\theta_1\cos\theta_3 - \sin\theta_1\sin\theta_2\sin\theta_3 & -\sin\theta_1\cos\theta_2 \\ \sin\theta_1\sin\theta_3 - \cos\theta_1\sin\theta_2\cos\theta_3 & \sin\theta_1\cos\theta_3 + \cos\theta_1\sin\theta_2\sin\theta_3 & \cos\theta_1\cos\theta_2 \end{bmatrix} \tag{A.1}$$

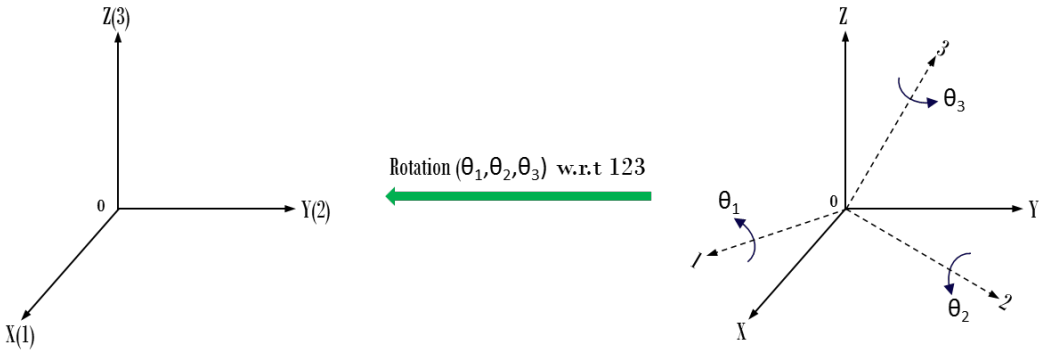

Figure A.1. The Rotations between the Lattice Coordinate and the Global Coordinate

And the vector transformation law under these rotations is

$$\bar{\mathbf{n}}^b = \mathbf{Q}\bullet\mathbf{n}^b \tag{A.2}$$

where $\mathbf{n}^b$ is the unit normal vectors under the lattice coordinate and $\bar{\mathbf{n}}^b$ is under global coordinate.

Without loss of generality, we consider a single arbitrary rotation for each lattice structures, i.e., rotations with respect to 3, 2 and 1 axes for simple cubic structure, body centered cubic and face centered cubic, respectively. The simplified rotation matrices are

$$\mathbf{Q}_3 = \begin{bmatrix} \cos\theta_3 & -\sin\theta_3 & 0 \\ \sin\theta_3 & \cos\theta_3 & 0 \\ 0 & 0 & 1 \end{bmatrix} \tag{A.3}$$

$$\mathbf{Q}_2 = \begin{bmatrix} \cos\theta_2 & 0 & -\sin\theta_2 \\ 0 & 1 & 0 \\ \sin\theta_2 & 0 & \cos\theta_2 \end{bmatrix} \tag{A.4}$$

$$\mathbf{Q}_1 = \begin{bmatrix} 1 & 0 & 0 \\ 0 & \cos\theta_1 & -\sin\theta_1 \\ 0 & \sin\theta_1 & \cos\theta_1 \end{bmatrix} \tag{A.5}$$

Simple Cubic Lattice

The transformed unit normal vectors under the global coordinate system are given in Table A.1.1. The coordinates rotate with respect to the Z(3) axis by an arbitrary angle θ_3. The transformation matrix is $\mathbf{Q}_3$, given in Eq. (A.5).

Table A.1. The Unit Normal Vectors for sc Structure under Global Coordinate

Neighbors 1		
$(\cos\theta_3, \sin\theta_3, 0)$	$(-\sin\theta_3, \cos\theta_3, 0)$	$(0,0,1)$
$(-\cos\theta_3, -\sin\theta_3, 0)$	$(\sin\theta_3, -\cos\theta_3, 0)$	$(0,0,-1)$
Neighbors 2		
$1/\sqrt{2}(\cos\theta_3 - \sin\theta_3, \sin\theta_3 + \cos\theta_3, 0)$	$1/\sqrt{2}(\cos\theta_3, \sin\theta_3, 1)$	$1/\sqrt{2}(-\sin\theta_3, \cos\theta_3, 1)$
$1/\sqrt{2}(\sin\theta_3 - \cos\theta_3, -\sin\theta_3 - \cos\theta_3, 0)$	$1/\sqrt{2}(-\cos\theta_3, -\sin\theta_3, -1)$	$1/\sqrt{2}(\sin\theta_3, -\cos\theta_3, -1)$
$1/\sqrt{2}(\cos\theta_3 + \sin\theta_3, \sin\theta_3 - \cos\theta_3, 0)$	$1/\sqrt{2}(\cos\theta_3, \sin\theta_3, -1)$	$1/\sqrt{2}(-\sin\theta_3, \cos\theta_3, -1)$
$1/\sqrt{2}(-\cos\theta_3 - \sin\theta_3, \cos\theta_3 - \sin\theta_3, 0)$	$1/\sqrt{2}(-\cos\theta_3, -\sin\theta_3, 1)$	$1/\sqrt{2}(\sin\theta_3, -\cos\theta_3, 1)$

Given the transformed unit normal vectors, the energy of a reference particle can be obtained in terms of the strain components as

$$U_{particle}=\frac{R^2}{2}\begin{Bmatrix}\left(\frac{3+\cos 4\theta_3}{2}k_1+\frac{9-\cos 4\theta_3}{2}k_2+36T\right)\left(\varepsilon_{11}^2+\varepsilon_{22}^2\right)+\left(2k_1+4k_2+36T\right)\varepsilon_{33}^2\\+\left(\left(1-\cos 4\theta_3\right)k_1+\left(3+\cos 4\theta_3\right)k_2+72T\right)\varepsilon_{11}\varepsilon_{22}+2k_2\left(\gamma_{13}^2+\gamma_{23}^2\right)\\+\left(\frac{1-\cos 4\theta_3}{2}k_1+\frac{3+\cos 4\theta_3}{2}k_2\right)\gamma_{12}^2+\left(4k_2+72T\right)\left(\varepsilon_{11}\varepsilon_{33}+\varepsilon_{22}\varepsilon_{33}\right)\\+\left(k_1\sin 4\theta_3-k_2\sin 4\theta_3\right)\varepsilon_{11}\gamma_{12}+\left(k_2\sin 4\theta_3-k_1\sin 4\theta_3\right)\varepsilon_{22}\gamma_{12}\end{Bmatrix} \tag{A.6}$$

For isotropic material, there is no coupling between the normal strain and shear strain. Thus, from the above total strain energy there must have

$$k_1\sin 4\theta_3-k_2\sin 4\theta_3=0 \tag{A.7}$$

and

$$k_2\sin 4\theta_3-k_1\sin 4\theta_3=0 \tag{A.8}$$

Therefore, $k_1=k_2$. Given this relationship between the spring stiffness, the above total strain energy can be simplified as

$$U_{particle}=\frac{R^2}{2}\left(\left(6k_1+36T\right)\left(\varepsilon_{11}^2+\varepsilon_{22}^2+\varepsilon_{33}^2\right)+\left(4k_1+72T\right)\left(\varepsilon_{11}\varepsilon_{22}+\varepsilon_{11}\varepsilon_{33}+\varepsilon_{22}\varepsilon_{33}\right)+2k_1\left(\gamma_{12}^2+\gamma_{13}^2+\gamma_{23}^2\right)\right) \tag{A.9}$$

The arbitrary rotation angle θ_3 is cancelled out in the energy given $k_1=k_2$. And this relation, i.e., $k_1=k_2$, is exactly what has been obtained when the lattice coordinate is coincident with the global coordinate, as shown in Eq. (2.4.8). Thus, the derived model parameters for simple cubic packing in lattice particle formulation are frame invariant.

Body Centered Cubic Lattice

The transformed unit normal vectors under the transformation matrix $\mathbf{Q}_2$ are given in Table A.2. The energy for a reference particle in this case is

$$U_{particle}=\frac{R^2}{2}\begin{Bmatrix}\left(\frac{12-4\cos 4\theta_2}{9}k_1+\frac{6+2\cos 4\theta_2}{3}k_2+\frac{112}{9}T\right)\left(\varepsilon_{11}^2+\varepsilon_{33}^2\right)+\frac{8}{9}k_1\gamma_{12}^2+\frac{8}{9}k_1\gamma_{23}^2\\+\left(\frac{8}{9}k_1+\frac{8}{3}k_2+\frac{112}{9}T\right)\varepsilon_{22}^2+\left(\frac{8+8\cos 4\theta_2}{9}k_1+\frac{4-4\cos 4\theta_2}{3}k_2+\frac{224}{9}T\right)\varepsilon_{11}\varepsilon_{33}\\+\left(\frac{4+4\cos 4\theta_2}{9}k_1+\frac{2-2\cos 4\theta_2}{3}k_2\right)\gamma_{13}^2+\left(\frac{16}{9}k_1+\frac{224}{9}T\right)\left(\varepsilon_{11}\varepsilon_{22}+\varepsilon_{22}\varepsilon_{33}\right)\\+\left(\frac{4k_2\sin 4\theta_2}{3}-\frac{8k_1\sin 4\theta_2}{9}\right)\varepsilon_{11}\gamma_{13}+\left(\frac{8k_1\sin 4\theta_2}{9}-\frac{4k_2\sin 4\theta_2}{3}\right)\varepsilon_{33}\gamma_{13}\end{Bmatrix} \tag{A.10}$$

Table A.2. The Unit Normal Vectors for bcc Structure under Global Coordinate

Neighbors 1	
$1/\sqrt{3}\left(\cos\theta_2-\sin\theta_2,1,\sin\theta_2+\cos\theta_2\right)$	$1/\sqrt{3}\left(\cos\theta_2+\sin\theta_2,-1,\sin\theta_2-\cos\theta_2\right)$
$1/\sqrt{3}\left(\sin\theta_2-\cos\theta_2,-1,-\sin\theta_2-\cos\theta_2\right)$	$1/\sqrt{3}\left(-\cos\theta_2-\sin\theta_2,1,\cos\theta_2-\sin\theta_2\right)$
$1/\sqrt{3}\left(\cos\theta_2+\sin\theta_2,1,\sin\theta_2-\cos\theta_2\right)$	$1/\sqrt{3}\left(\cos\theta_2-\sin\theta_2,-1,\sin\theta_2+\cos\theta_2\right)$
$1/\sqrt{3}\left(-\cos\theta_2-\sin\theta_2,-1,\cos\theta_2-\sin\theta_2\right)$	$1/\sqrt{3}\left(\sin\theta_2-\cos\theta_2,1,-\sin\theta_2-\cos\theta_2\right)$
Neighbors 2	
$\left(\cos\theta_2,\sin\theta_2,0\right)$	$\left(0,1,0\right)$ $\left(-\sin\theta_2,\cos\theta_2,0\right)$
$\left(-\cos\theta_2,-\sin\theta_2,0\right)$	$\left(0,-1,0\right)$ $\left(\sin\theta_2,-\cos\theta_2,0\right)$

For isotropic materials, the following must satisfied

$$\frac{4k_2\sin 4\theta_2}{3}-\frac{8k_1\sin 4\theta_2}{9}=0 \tag{A.11}$$

and

$$\frac{8k_1\sin 4\theta_2}{9}-\frac{4k_2\sin 4\theta_2}{3}=0 \tag{A.12}$$

Thus, $2k_1=3k_2$. Given this relationship, the energy in Eq. (A.10) can be simplified as

$$U_{particle}=\frac{R^2}{2}\left(\begin{array}{l}\left(\frac{24}{9}k_1+\frac{112}{9}T\right)\left(\varepsilon_{11}^2+\varepsilon_{22}^2+\varepsilon_{33}^2\right)+\left(\frac{16}{9}k_1+\frac{224}{9}T\right)\left(\varepsilon_{11}\varepsilon_{22}+\varepsilon_{22}\varepsilon_{33}+\varepsilon_{11}\varepsilon_{33}\right)\\+\frac{8}{9}k_1\left(\gamma_{12}^2+\gamma_{23}^2+\gamma_{13}^2\right)\end{array}\right) \tag{A.13}$$

When $2k_1=3k_2$, the arbitrary rotation angle θ_2 is cancelled out in the energy, as shown in Eq. (A.13). This relationship, i.e., $2k_1=3k_2$, is exactly what has been obtained when the lattice coordinate is coincident with the global coordinate, as shown in Eq. (2.4.10). Thus, the derived model parameters for body centered cubic packing in lattice particle formulation are also frame invariant.

Face Centered Cubic Lattice

The transformed unit normal vectors for this case by the transformation matrix $\mathbf{Q}_1$ are given in Table A.1.3. The energy of a reference particle for this lattice packing is

$$U_{particle}=\frac{R^2}{2}\begin{pmatrix}\left(2k_1+4k_2+24T\right)\varepsilon_{11}^2+\left(\left(\frac{9-\cos 4\alpha}{4}\right)k_1+\left(3+\cos 4\theta_1\right)k_2+24T\right)\left(\varepsilon_{22}^2+\varepsilon_{33}^2\right)\\+\left(\left(\frac{3+\cos 4\theta_1}{4}\right)k_1+\left(1-\cos 4\theta_1\right)k_2\right)\gamma_{23}^2+\left(2k_1+48T\right)\left(\varepsilon_{11}\varepsilon_{22}+\varepsilon_{11}\varepsilon_{33}\right)\\+\left(\left(\frac{3+\cos 4\theta_1}{2}\right)k_1+2\left(1-\cos 4\theta_1\right)k_2+48T\right)\varepsilon_{22}\varepsilon_{33}+k_1\left(\gamma_{12}^2+\gamma_{13}^2\right)\\+\left(2k_2\sin 4\theta_1-\frac{k_1\sin 4\theta_1}{2}\right)\varepsilon_{22}\gamma_{23}+\left(\frac{k_1\sin 4\theta_1}{2}-2k_2\sin 4\theta_1\right)\varepsilon_{33}\gamma_{23}\end{pmatrix} \tag{A.14}$$

Table A.3. The Unit Normal Vectors for fcc Structure under Global Coordinate

Neighbors 1		
$1/\sqrt{2}\left(1,\cos\theta_1,\sin\theta_1\right)$	$1/\sqrt{2}\left(1,-\sin\theta_1,\cos\theta_1\right)$	$1/\sqrt{2}\left(0,\cos\theta_1-\sin\theta_1,\sin\theta_1+\cos\theta_1\right)$
$1/\sqrt{2}\left(-1,-\cos\theta_1,-\sin\theta_1\right)$	$1/\sqrt{2}\left(-1,\sin\theta_1,-\cos\theta_1\right)$	$1/\sqrt{2}\left(0,\sin\theta_1-\cos\theta_1,-\sin\theta_1-\cos\theta_1\right)$
$1/\sqrt{2}\left(1,-\cos\theta_1,-\sin\theta_1\right)$	$1/\sqrt{2}\left(1,\sin\theta_1,-\cos\theta_1\right)$	$1/\sqrt{2}\left(0,\cos\theta_1+\sin\theta_1,\sin\theta_1-\cos\theta_1\right)$
$1/\sqrt{2}\left(-1,\cos\theta_1,\sin\theta_1\right)$	$1/\sqrt{2}\left(-1,-\sin\theta_1,\cos\theta_1\right)$	$1/\sqrt{2}\left(0,-\cos\theta_1-\sin\theta_1,\cos\theta_1-\sin\theta_1\right)$
Neighbors 2		
$(1,0,0)$	$\left(0,\cos\theta_1,\sin\theta_1\right)$	$\left(0,-\sin\theta_1,\cos\theta_1\right)$
$(-1,0,0)$	$\left(0,-\cos\theta_1,-\sin\theta_1\right)$	$\left(0,\sin\theta_1,-\cos\theta_1\right)$

For isotropic materials, the following must satisfied

$$2k_2\sin 4\theta_1-\frac{k_1\sin 4\theta_1}{2}=0 \tag{A.15}$$

and

$$\frac{k_1\sin 4\theta_1}{2}-2k_2\sin 4\theta_1=0 \tag{A.16}$$

Therefore, $k_1=4k_2$. The energy can be simplified as

$$U_{particle}=\frac{R^2}{2}\begin{pmatrix}\left(3k_1+24T\right)\left(\varepsilon_{11}^2+\varepsilon_{22}^2+\varepsilon_{33}^2\right)+\left(2k_1+48T\right)\left(\varepsilon_{11}\varepsilon_{22}+\varepsilon_{22}\varepsilon_{33}+\varepsilon_{11}\varepsilon_{33}\right)\\+k_1\left(\gamma_{12}^2+\gamma_{23}^2+\gamma_{13}^2\right)\end{pmatrix} \tag{A.17}$$

When $k_1=4k_2$, the arbitrary rotation angle θ_1 is cancelled out in the energy, as shown in Eq.(A.17). This relationship, i.e., $k_1=4k_2$, is exactly what has been obtained when the lattice coordinate is coincident with the global coordinate, as shown in Eq. (2.4.12). Thus, the derived model parameters for face centered cubic packing in lattice particle formulation are also frame invariant.

In conclusion, the lattice particle model parameters for the three cubic lattice structures are frame invariant for isotropic material.

APPENDIX

B EQUIVALENCE OF LATTICE ROTATION AND STIFFNESS TRANSFORMATION

For modeling anisotropic materials in FEM, the material stiffness tensor is usually transformed according to the material coordinate rotation with respect to the global. In the proposed method, the lattice rotation rather than the stiffness matrix transformation is used to accommodate this coordinate rotation. In this section, the equivalence of the two approaches for the anisotropic elasticity will be shown. We begin with a counter-clockwisely rotated lattice orientation, as show in Fig. B.1, with respect to the global coordinates XOY by an angle α. For this configuration, the six normal vectors for a unit cell are given in Table B.1.

Table B.1. The Normal Vectors of the New Configuration of a Unit Cell

n_1	n_2	n_3
$\left(\cos(\alpha),\sin(\alpha)\right)$	$\left(\cos\left(\alpha+\frac{\pi}{3}\right),\sin\left(\alpha+\frac{\pi}{3}\right)\right)$	$\left(\cos\left(\alpha+\frac{2\pi}{3}\right),\sin\left(\alpha+\frac{2\pi}{3}\right)\right)$
n_4	n_5	n_6
$\left(\cos(\alpha+\pi),\sin(\alpha+\pi)\right)$	$\left(\cos\left(\alpha+\frac{4\pi}{3}\right),\sin\left(\alpha+\frac{4\pi}{3}\right)\right)$	$\left(\cos\left(\alpha+\frac{5\pi}{3}\right),\sin\left(\alpha+\frac{5\pi}{3}\right)\right)$

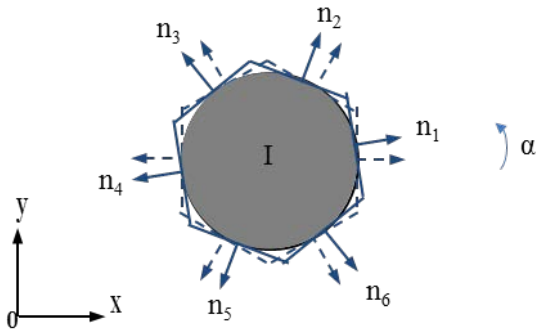

Figure B.1. Rotation of Lattice Orientation

We first consider the case of rotating underlying lattice. Using the same procedure as has been described in previous section and the normal vectors in Table B.1, the general mapping relationship between the components of the material stiffness tensor and the model parameters for an arbitrary material coordinate rotation can be obtained as

$$\begin{Bmatrix} C_{11} \\ C_{22} \\ C_{66} \\ C_{26} \\ C_{16} \\ C_{12} \end{Bmatrix} = \left[A_{ij} \right] \begin{Bmatrix} k_1 \\ k_2 \\ k_3 \\ T_1 \\ T_2 \\ T_3 \end{Bmatrix} \tag{B.1}$$

where

$$\left[A_{ij} \right] = \begin{bmatrix} \frac{\sqrt{3}}{3}\cos^4(\alpha) & A_{12} & A_{13} & \sqrt{3}\cos^2(\alpha) & A_{15} & A_{16} \\ \frac{\sqrt{3}}{3}\sin^4(\alpha) & A_{22} & A_{23} & \sqrt{3}\sin^2(\alpha) & A_{25} & A_{26} \\ \frac{\sqrt{3}}{3}\sin^2(\alpha)\cos^2(\alpha) & A_{32} & A_{33} & 0 & 0 & 0 \\ \frac{\sqrt{3}}{3}\sin^3(\alpha)\cos(\alpha) & A_{42} & A_{43} & \frac{\sqrt{3}}{4}\sin(2\alpha) & A_{45} & A_{46} \\ \frac{\sqrt{3}}{3}\sin(\alpha)\cos^3(\alpha) & A_{52} & A_{53} & \frac{\sqrt{3}}{4}\sin(2\alpha) & A_{55} & A_{56} \\ \frac{\sqrt{3}}{3}\sin^2(\alpha)\cos^2(\alpha) & A_{62} & A_{63} & \frac{\sqrt{3}}{2} & \frac{\sqrt{3}}{2} & \frac{\sqrt{3}}{2} \end{bmatrix}$$

$$A_{12} = \frac{\sqrt{3}}{3}\cos^4\left(\alpha + \frac{\pi}{3}\right); \qquad A_{22} = \frac{\sqrt{3}}{3}\sin^4\left(\alpha + \frac{\pi}{3}\right)$$

$$A_{32} = \frac{\sqrt{3}}{3}\sin^2\left(\alpha + \frac{\pi}{3}\right)\cos^2\left(\alpha + \frac{\pi}{3}\right); \qquad A_{42} = \frac{\sqrt{3}}{3}\sin^3\left(\alpha + \frac{\pi}{3}\right)\cos\left(\alpha + \frac{\pi}{3}\right)$$

$$A_{52} = \frac{\sqrt{3}}{3}\sin\left(\alpha + \frac{\pi}{3}\right)\cos^3\left(\alpha + \frac{\pi}{3}\right); \qquad A_{62} = A_{32}$$

$$A_{13} = \frac{\sqrt{3}}{3}\cos^4\left(\alpha + \frac{2\pi}{3}\right); \qquad A_{23} = \frac{\sqrt{3}}{3}\sin^4\left(\alpha + \frac{2\pi}{3}\right)$$

$$A_{33} = \frac{\sqrt{3}}{3}\sin^2\left(\alpha + \frac{2\pi}{3}\right)\cos^2\left(\alpha + \frac{2\pi}{3}\right); \qquad A_{43} = \frac{\sqrt{3}}{3}\sin^3\left(\alpha + \frac{2\pi}{3}\right)\cos\left(\alpha + \frac{2\pi}{3}\right)$$

$$A_{53} = \frac{\sqrt{3}}{3}\sin\left(\alpha + \frac{2\pi}{3}\right)\cos^3\left(\alpha + \frac{2\pi}{3}\right); \qquad A_{63} = A_{33}$$

$$A_{15}=\left(\frac{\sqrt{3}}{2}-\frac{3}{4}\sin(2\alpha)-\frac{\sqrt{3}}{4}\cos(2\alpha)\right);\quad A_{25}=\left(\frac{\sqrt{3}}{2}+\frac{3}{4}\sin(2\alpha)+\frac{\sqrt{3}}{4}\cos(2\alpha)\right)$$

$$A_{45}=\left(\frac{3}{8}\cos(2\alpha)-\frac{\sqrt{3}}{8}\sin(2\alpha)\right);\qquad A_{55}=A_{45}$$

$$A_{16}=\left(\frac{\sqrt{3}}{2}+\frac{3}{4}\sin(2\alpha)-\frac{\sqrt{3}}{4}\cos(2\alpha)\right);\quad A_{26}=\left(\frac{\sqrt{3}}{2}-\frac{3}{4}\sin(2\alpha)+\frac{\sqrt{3}}{4}\cos(2\alpha)\right)$$

$$A_{46}=\left(-\frac{3}{8}\cos(2\alpha)-\frac{\sqrt{3}}{8}\sin(2\alpha)\right);\qquad A_{56}=A_{46}$$

When rotation angle α = 0, the previous derivation is recovered.

Next, the lattice structure is not rotated but the stiffness matrix is transformed for the mapping solution of the lattice particle parameters. The transformation for the material stiffness matrix is

$$\bar{\mathbf{C}}=\mathbf{Q}^{-1}\mathbf{C}\mathbf{Q}^{-T} \tag{B.2}$$

where $\mathbf{C}$ and $\bar{\mathbf{C}}$ are the original untransformed and transformed material stiffness matrix, respectively, $\mathbf{Q}$ is the transformation matrix which is defined as

$$\mathbf{Q}=\begin{bmatrix}\cos^2\theta & \sin^2\theta & 2\sin\theta\cos\theta\\ \sin^2\theta & \cos^2\theta & -2\sin\theta\cos\theta\\ -\sin\theta\cos\theta & \sin\theta\cos\theta & \cos^2\theta-\sin^2\theta\end{bmatrix} \tag{B.3}$$

with θ is the rotation angle from the rotated material coordinate to the global coordinate. Apparently, θ = - α in the case shown in Fig. B.1.

From Eq. (B.2), we have the original untransformed material stiffness matrix in terms of the rotation angle and the transformed material stiffness matrix as

$$\mathbf{C}=\mathbf{Q}\bar{\mathbf{C}}\mathbf{Q}^{T} \tag{B.4}$$

The mapping relationship between the component of the transformed material stiffness matrix and the model parameters using the un-rotated lattice structure is

$$\begin{Bmatrix} \bar{C}_{11} \\ \bar{C}_{22} \\ \bar{C}_{66} \\ \bar{C}_{26} \\ \bar{C}_{16} \\ \bar{C}_{12} \end{Bmatrix} = \begin{bmatrix} \frac{\sqrt{3}}{3} & \frac{\sqrt{3}}{48} & \frac{\sqrt{3}}{48} & \sqrt{3} & \frac{\sqrt{3}}{4} & \frac{\sqrt{3}}{4} \\ 0 & \frac{3\sqrt{3}}{16} & \frac{3\sqrt{3}}{16} & 0 & \frac{3\sqrt{3}}{4} & \frac{3\sqrt{3}}{4} \\ 0 & \frac{\sqrt{3}}{16} & \frac{\sqrt{3}}{16} & 0 & 0 & 0 \\ 0 & \frac{3}{16} & -\frac{3}{16} & 0 & \frac{3}{8} & -\frac{3}{8} \\ 0 & \frac{1}{16} & -\frac{1}{16} & 0 & \frac{3}{8} & -\frac{3}{8} \\ 0 & \frac{\sqrt{3}}{16} & \frac{\sqrt{3}}{16} & \frac{\sqrt{3}}{2} & \frac{\sqrt{3}}{2} & \frac{\sqrt{3}}{2} \end{bmatrix} \begin{Bmatrix} k_1 \\ k_2 \\ k_3 \\ T_1 \\ T_2 \\ T_3 \end{Bmatrix} \tag{B.5}$$

Substituting Eq. (B.4) to (B.5), we finally have the mapping relationship between the components of the original untransformed material stiffness and the model parameters as

$$\begin{Bmatrix} C_{11} \\ C_{22} \\ C_{66} \\ C_{26} \\ C_{16} \\ C_{12} \end{Bmatrix} = \left[B_{ij} \right] \begin{Bmatrix} k_1 \\ k_2 \\ k_3 \\ T_1 \\ T_2 \\ T_3 \end{Bmatrix} \tag{B.6}$$

with

$$\left[B_{ij} \right] = \begin{bmatrix} \frac{\sqrt{3}}{3}\cos^4(\alpha) & B_{12} & B_{13} & \sqrt{3}\cos^2(\alpha) & B_{15} & B_{16} \\ \frac{\sqrt{3}}{3}\sin^4(\alpha) & B_{22} & B_{23} & \sqrt{3}\sin^2(\alpha) & B_{25} & B_{26} \\ \frac{\sqrt{3}}{3}\sin^2(\alpha)\cos^2(\alpha) & B_{32} & B_{33} & 0 & 0 & 0 \\ \frac{\sqrt{3}}{3}\sin^3(\alpha)\cos(\alpha) & B_{42} & B_{43} & \frac{\sqrt{3}}{4}\sin(2\alpha) & B_{45} & B_{46} \\ \frac{\sqrt{3}}{3}\sin(\alpha)\cos^3(\alpha) & B_{52} & B_{53} & \frac{\sqrt{3}}{4}\sin(2\alpha) & B_{55} & B_{56} \\ \frac{\sqrt{3}}{3}\sin^2(\alpha)\cos^2(\alpha) & B_{62} & B_{63} & \frac{\sqrt{3}}{2} & \frac{\sqrt{3}}{2} & \frac{\sqrt{3}}{2} \end{bmatrix}$$

$$B_{12}=\left(\frac{3\sqrt{3}}{16}-\frac{\sqrt{3}}{6}\cos^4(\alpha)-\frac{3}{8}\sin(2\alpha)+\frac{1}{4}\sin(2\alpha)\cos^2(\alpha)\right)$$

$$B_{22}=\left(\frac{3\sqrt{3}}{16}+\frac{1}{4}\sin(2\alpha)+\frac{1}{16}\sin(4\alpha)-\frac{\sqrt{3}}{6}\sin^2(\alpha)+\frac{\sqrt{3}}{24}\sin^2(2\alpha)\right)$$

$$B_{32}=\left(\frac{\sqrt{3}}{16}-\frac{1}{16}\sin(4\alpha)-\frac{\sqrt{3}}{24}\sin^2(2\alpha)\right);\qquad B_{62}=B_{32}$$

$$B_{42}=\left(\frac{1}{8}\cos(2\alpha)+\frac{1}{16}\cos(4\alpha)+\frac{\sqrt{3}}{48}\sin(4\alpha)-\frac{\sqrt{3}}{24}\sin(2\alpha)\right)$$

$$B_{52}=\left(\frac{1}{8}\cos(2\alpha)-\frac{1}{16}\cos(4\alpha)-\frac{\sqrt{3}}{48}\sin(4\alpha)-\frac{\sqrt{3}}{24}\sin(2\alpha)\right)$$

$$B_{13}=\left(\frac{3\sqrt{3}}{16}-\frac{\sqrt{3}}{6}\cos^4(\alpha)+\frac{3}{8}\sin(2\alpha)-\frac{1}{4}\sin(2\alpha)\cos^2(\alpha)\right)$$

$$B_{23}=\left(\frac{3\sqrt{3}}{16}-\frac{1}{4}\sin(2\alpha)-\frac{1}{16}\sin(4\alpha)-\frac{\sqrt{3}}{6}\sin^2(\alpha)+\frac{\sqrt{3}}{24}\sin^2(2\alpha)\right)$$

$$B_{33}=\left(\frac{\sqrt{3}}{16}+\frac{1}{16}\sin(4\alpha)-\frac{\sqrt{3}}{24}\sin^2(2\alpha)\right);\qquad B_{63}=B_{33}$$

$$B_{43}=\left(-\frac{1}{8}\cos(2\alpha)-\frac{1}{16}\cos(4\alpha)+\frac{\sqrt{3}}{48}\sin(4\alpha)-\frac{\sqrt{3}}{24}\sin(2\alpha)\right)$$

$$B_{53}=\left(-\frac{1}{8}\cos(2\alpha)+\frac{1}{16}\cos(4\alpha)-\frac{\sqrt{3}}{48}\sin(4\alpha)-\frac{\sqrt{3}}{24}\sin(2\alpha)\right)$$

$$B_{15}=\left(\frac{3\sqrt{3}}{4}-\frac{3}{4}\sin(2\alpha)-\frac{\sqrt{3}}{2}\cos^2(\alpha)\right);\qquad B_{25}=\left(\frac{3\sqrt{3}}{4}+\frac{3}{4}\sin(2\alpha)-\frac{\sqrt{3}}{2}\sin^2(\alpha)\right)$$

$$B_{45}=\left(\frac{3}{8}\cos(2\alpha)-\frac{\sqrt{3}}{8}\sin(2\alpha)\right);\qquad B_{55}=B_{45}$$

$$B_{16}=\left(\frac{3\sqrt{3}}{4}+\frac{3}{4}\sin(2\alpha)-\frac{\sqrt{3}}{2}\cos^2(\alpha)\right);\qquad B_{26}=\left(\frac{3\sqrt{3}}{4}-\frac{3}{4}\sin(2\alpha)-\frac{\sqrt{3}}{2}\sin^2(\alpha)\right)$$

$$B_{46}=\left(-\frac{3}{8}\cos(2\alpha)-\frac{\sqrt{3}}{8}\sin(2\alpha)\right);\qquad B_{56}=B_{46}$$

When rotation angle α = 0, the previous derivation is recovered.

After simplification, it is shown that $\mathbf{A} = \mathbf{B}$. Thus, the underlying lattice rotation in the proposed framework is equivalent to the material stiffness tensor transformation for anisotropic elastic materials.

BIOGRAPHICAL SKETCH

Hailong Chen was born and brought up in Jiangxi, China. He graduated with the degree of Bachelor of Science in mechanical engineering from Shanghai Normal University, Shanghai, China on July 1, 2010. He received his Master of Science degree in Mechanical Engineering from University of Florida on May 1, 2012. His master research focuses on application of Implicit Boundary Finite Element Method for modeling of plate and shell structures. In August, 2012, he joined Professor Yongming Liu's group to pursue his PhD degree at Arizona State University. His area of interest includes, not limited to, non-local particle methods and finite elements for mechanical analysis of engineering materials.